Study of capture and annihilation of a few GeV WIMPs inside the Sun by using an underground neutrino detector

Koun Choi

Division of Particle and Astrophysical Science,
Nagoya University

January 18, 2015

Abstract

Dark matter has an enigmatic invisible existence contributing most of the gravity in the universe. Weakly interacting massive particles (WIMPs) are favored as particle candidates for non-baryonic cold dark matter, since their interaction strength can explain the thermal relic abundance of dark matter. Recent event excesses or annual modulation signals reported by direct detection experiments such as DAMA/LIBRA, CoGeNT, CRESST and CDMS II Si would suggest possible evidence for WIMPs with light masses of a few to a few tens of GeV/c^2. However, they conflict with null results from other experiments such as XENON100, LUX and SuperCDMS. A promising way to identify a WIMP particle is to search for excess of a high-energy neutrino flux coming from the Sun, often referred to as the "solar WIMP search". WIMPs in the dark matter halo could scatter off nuclei inside the Sun and be captured, then pair-annihilate producing neutrinos from decays of the annihilation products which propagate through the Sun and may finally be detected in neutrino detectors on the earth. Thanks to the hydrogen-rich composition and huge gravity of the Sun, tight limits on the scattering cross section of WIMPs to protons by spin-dependent interaction have been placed by neutrino telescopes such as Super-Kamiokande, IceCube, Baksan and ANTARES.

For a critical interpretation of indirect searches by neutrino detectors and comparisons to direct detection experiments, astrophysical uncertainties are key issues. This is especially true for the light WIMP region, where the velocity distribution of WIMPs in the dark matter halo are known to be a large uncertainty source for direct detection searches. The effect of the uncertainties from the velocity distribution of WIMPs in the solar WIMP search are precisely evaluated. We examine various sources of uncertainties including local circular speed of the Sun, high-velocity cut of halo, halo shapes from cosmological simulations and the possible existence of the dark disc. We conclude that the impacts of the uncertainties on the velocity distribution on the solar WIMP search are not significant. The estimated size of the total uncertainty is found to be less than 24% for 20 GeV/c^2 WIMPs for scenarios without the dark disc. For heavier WIMPs, the uncertainties are larger but still below about 50%.

Super-Kamiokande (SK), a water Cherenkov neutrino observatory located in Kamioka mine in Japan, is used to search for light WIMPs. The signal acceptances for a few GeV/c^2 WIMPs are improved by one to two orders of magnitude by using vertex-contained type of neutrino events. To discriminate signal from the overwhelming atmospheric neutrino background events, we perform a least-squares fit on event bins finely defined by using angle, energy and flavor information. By fitting 3,903-days of

SK I-IV data, we examine the best-fit contribution of WIMP-induced neutrino events added to back-ground events.

As a result, much better sensitivity for spin-dependently coupling WIMPs than any other direct detection experiment is achieved. For the tested 4–200 GeV/c^2 WIMP masses and several annihilation channels, the data is in agreement with a no-WIMP contribution and new constraints on WIMP-nucleon cross-sections are obtained. We set the current best limit on the spin-dependent (SD) WIMP-proton cross section for WIMP masses below 200 GeV/c^2 (at 10 GeV/c^2, 1.49×10^{-39} cm^2 for $\chi\chi \to b\bar{b}$ and 1.31×10^{-40} cm^2 for $\chi\chi \to \tau^+\tau^-$ annihilation channel), also eliminating $\tau^+\tau^-$ dominantly annihilating WIMPs with spin-independent (SI) coupling as a candidate for DAMA and CoGENT claimed signals. We also rule out some new parameter space for SI coupling WIMPs below 6 GeV/c^2 by $\tau^+\tau^-$ annihilation channel.

In this thesis, astrophysical uncertainties, including uncertainties from the velocity distribution, are quantified and reflected on the new limits from the SK for the first time. The upper limits on SD or SI WIMP-nucleon scattering cross sections obtained in this work carry an uncertainty of about 30% for 4 GeV/c^2 WIMP, which increases for higher WIMP masses and resulting up to 60% (100%) for SD (SI) coupling WIMPs of 200 GeV/c^2 mass. We also find that the contradistinctive responses of direct and indirect detections to the velocity distribution tell us that a solar WIMP search can be a good complementary method to entangle uncertainties afflicting direct detection. In terms of not only good sensitivity for signal but also unique sensitivities and insensitivities to astrophysical properties, the usefulness of this result and the searches from future neutrino detectors are highlighted.

Acknowledgements

Firstly I'd like to thank my supervisor, Prof. Yoshitaka Itow without whose effort this dissertation would be in very awful shape. I appreciate his advising in the past four years of my Ph.D studies, for being a big wallet of ideas to which I could always access and take as much as I could invest, for always (and I select this word with enough statistics) considering my future as an experimentalist, and for almost always listening to what I want to do in advance to judging my capability.

I also appreciate Prof. Carsten Rott for having suggested me a great experience to work under his guidance, for his patience on the project and warm supports in general. Many thanks to Piotr Mijakowski, Roger Wendell and Takayuki Tanaka for their great helps when I first started my research. Thanks for taking your time to answer my naive questions, and also for being good friends.

Many thanks to my colleagues and friends in the Super-K. Thanks to people who are always there and maintaining the detector; Hayato san, Miura san, Moriyama san, Hide san, Tomura san, Kameda san, Sekiya san, Nakano kun, Nakahata san, Suzuki san, and many people whom I can't recall now, and the officers, security guards and the observatory and dormitory labourers. I especially appreciate the solar WIMP paper committee members' effort in the revision of the analysis. And thanks to Ed for encouraging me to finish and move on.

I also thank Bish san, Lluis, Okumura san, SKanadians and especially Hiro for always being a good drinking guru and for his wise advices. I also thank my father, Goya and Stefan, Ssal, Cris, and my muse Jia. Special thanks to my mother for always supporting me. Also thanks to my defence committee - especially Shiozawa san, who is going to come to Nagoya for my defence on Christmas day!

Finally, thanks to Nagoya university GCOE program for giving me a lot of opportunities.

Contents

To Lily, Ola and Oksu

Chapter 1

Dark matter and WIMP

1.1 Overview

The existence of cold non-baryonic dark matter is suggested from its gravitational effects. Weakly interacting massive particles (WIMPs) are prominent candidates to explain the cold non-baryonic dark matter particle. They naturally arise in Super Symmetry (1) or models with large extra dimensions (2). By crossing symmetry, they could be searched through the scattering cross section with ordinary matters in the Standard Model.

In Chap. 1.2, the observation history of dark matter is briefly summarised. In Chap. 1.3, the distribution of the dark matter in the Galaxy will be described. In Chap. 1.4, a short introduction of WIMP will be given. Finally in Chap. 1.5, methods to detect the WIMPs and the current achievements will be briefly described.

1.2 The gravitational existence of dark matter

1.2.1 The history of dark matter discovery

Dark matter was first postulated due to the discovery of the discrepancy between the mass deduced from gravitational potential and the mass estimated from luminous matter. In 1933, Fritz Zwicky observed the radial velocities of eight galaxies in the Coma galaxy cluster, and found that the observed velocity dispersion was much larger than that expected from the gravitational field due to the visible matter. His explanation for this observation was that some “dark” matter is present with a much greater mass than luminous matter (3), and it might be regarded as the first reference to dark matter (4).

Subsequently, another evidence of dark matter arose in 1939 by Horace Babcock (5). He measured the Doppler shifts of star lights at various places around the outer edge of the galaxy M31 and found they showed unexpected behaviors: the speed of stars orbiting around the galactic center did not decrease following the expected Keplerian dynamics, but instead remained roughly constant to far distances from the galactic center. Today Babcock's result is interpreted as evidence of dark matter, whose massive gravitational field holds the stars more strongly than the visible field would do. But at that time, he suggested either the possible foreground for the light propagation or the modification of the Keplerian dynamics as an explanation.

Despite several related results obtained by others, until the 1970's the scenario of the existing dark matter was not accepted as a standard idea. In the 1970's Rubin and Ford measured the Doppler shifts of star lights in the external parts of the spiral galaxies (6). The observation was very clear and straightforward that it was enough to convince the community with the idea that the luminous stars are probably only the visible tracers of a invisible massive volume in the galaxy. This observation was extended to larger radius by Roberts and Whitehurst (7) using 21-cm line observations made with the 300-ft radio telescope, that reached to 30 kpc as shown in Fig. 1.1.

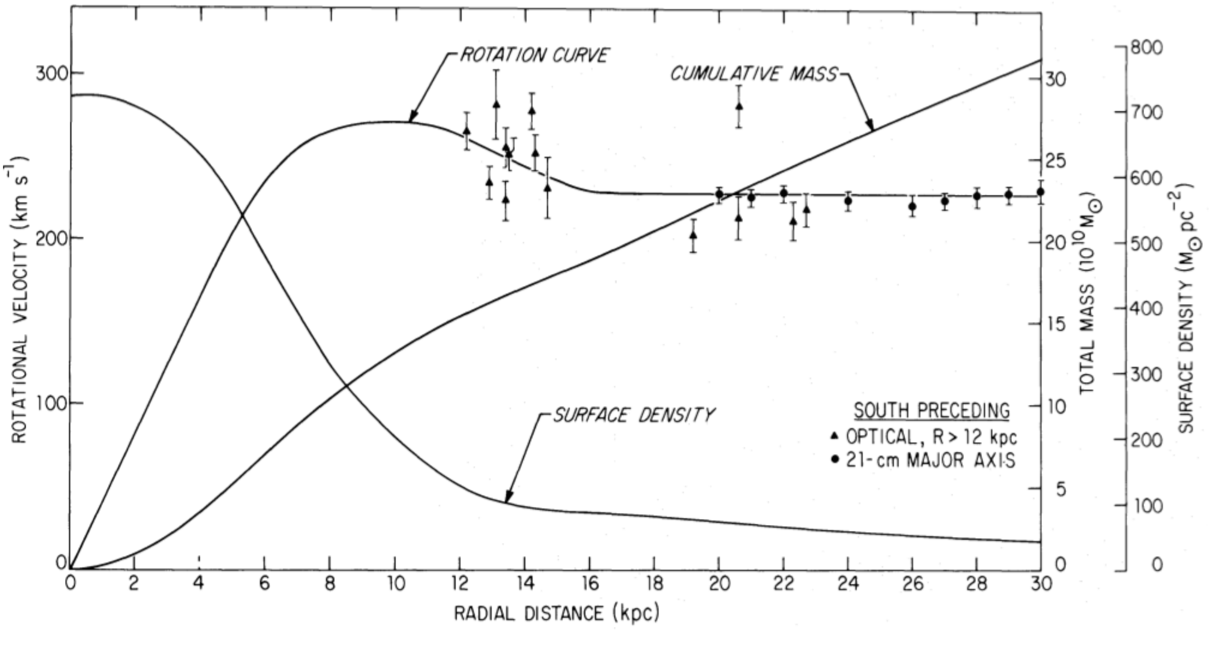

Figure 1.1: The rotation curve of M31. The triangles beyond 12 kpc show the optical observation by Rubin & Ford (1970), the circles at the outer edge show the 21-cm line observations by Roberts & Whitehurst. Note that the rotational curve appears to be flat beyond $\sim$ 15 kpc. Image is taken from (7).

A good visual and direct evidence for dark matter was the observation of the Bullet cluster by both gravitational lensing and X-ray. The idea of directly estimating the mass of an object by observing gravitational lensing effect by foreground galaxy clusters was first suggested by Zwicky (3). The first observation of the gravitational lensing was done by the Hubble Space Telescope in the 1990's. The distorted galaxy images taken were used to calculate approximately how much mass should present behind the "lens". On the other hand, the observation of X-rays emitted by very hot gas in the cluster could be used to derive the mass profile of the baryonic matter. In the Bullet cluster, the mass which is in charge of gravitational lensing, and the baryonic mass which is in charge of X-ray emission, were observed to be in separated locations, in a shape of a bullet. It was interpreted that the two clusters of galaxies were colliding and the passing gas particles belonging to each cluster were slowed down by electromagnetic interactions, where much of the mass of the two clusters passed through each other without interactions. The observation of the Bullet cluster by Clowe et al. (8) is shown in the Fig. 1.2.

Figure 1.2: The 'Bullet cluster', also known as 1E 0657-56. The pink-colored region represents hot gas observed by the Chandra X-ray space telescope, the blue region represents dark matter seen through its gravitational effects. Image is taken from (8).

1.2.2 The non-baryonic dark matter

By the end of 1970's, the idea of the existence of the dark matter had been largely accepted. But still its property was hidden in a veil until its shady property first started manifesting in the Big Bang nucleosynthesis (BBN).

When the atomic nuclei heavier than hydrogen were primordially formed in the early universe, the expansion rate of the universe which is related to the total matter density would have determined the population of each light element. The BBN prediction matches the observed populations only when the baryonic matter accounts for 4∼5% of the critical density of the universe as shown in Fig. 1.3. This was the first notice that we are clueless about the left 95% of the energy budget of the universe.

The next strong evidence of the existence of non-baryonic dark matter came from the observed discrepancy between the total cosmological density of matter and the density of baryonic matter.

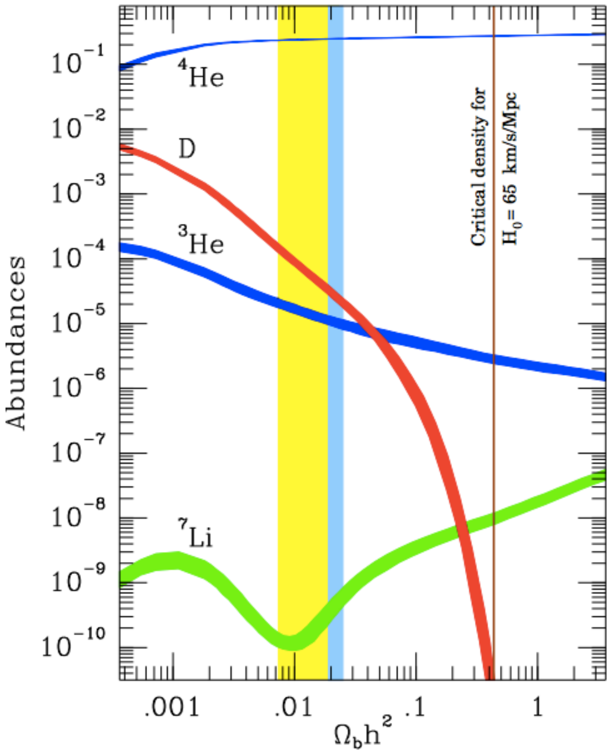

Figure 1.3: The BBN prediction of the light elements. Predicted abundances of each element, with the width of the curve indicating the 2σ theoretical uncertainties, are in agreement with the measurements in the consistency interval (vertical band, Copi et al (9)) of baryon density. The blue consistency interval band corresponds to Tytler et al (10)'s determination of the deuterium abundance. Image is taken from (11) and the courtesy of K. Nollett.

In 1964, Cosmic Microwave Background (CMB) was detected and brought a doubt to the presumption of baryonic dark matter. To form the currently observed structures as galaxies, clusters and superclusters from the density evolution of the baryonic matters, the theoretical calculation said that the initial density fluctuation of the universe at the epoch of decoupling ("recombination") of the CMB was required to be above $\sim 10^{-3}$. And it was expected that we could find the footprint of it on the CMB, as fluctuations of the temperature. The early observations of the CMB couldn't find this but the upper limits were set to be much lower than the predicted limit of 10^{-3}. When the COBE satellite finally measured the temperature fluctuation of the CMB, it appeared to be two orders of magnitude lower than expected; only about 30 μK where the average temperature of the CMB was 2.7K. The COBE result showed a need for a electrically neutral (which is non-baryonic) mass which could avoid the radiation pressure slowing down the gravitational growth of density fluctuations, so that it could already initialise the structure formation in advance to the recombination.

Later on, more precise analyses on the anisotropy of CMB were carried on and gave us stronger constraints on the abundance of non-baryonic matter. The typical angular scales of the oscillations of radiation in the early universe were measured as a angular power spectrum of the CMB anisotropies, which revealed the effects of baryonic matter and dark matter. By measuring the first three peaks with good precision, the analysis of the WMAP nine-years results (12) estimated that 4.6% of the total energy of the current universe is made up with baryonic matter, and the total matter density is about 28.6% of the total energy density, which indicated that about 24% of the energy was composed of non-baryonic dark matter. Figure 1.4 shows the all-sky picture and a pie chart of the energy budget of the current universe, obtained from nine years of WMAP data.

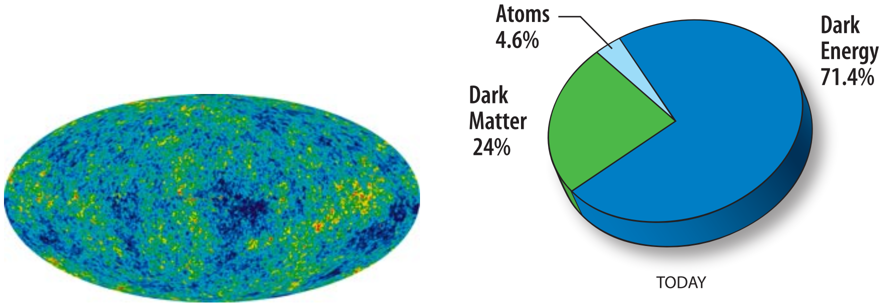

Figure 1.4: Left: The all-sky picture from nine-years WMAP data. The colors correspond to temperature fluctuations. Right: The contents of the energy source of the current universe revealed by nine-years WMAP observation (13).

The evidence for that the majority of dark matter can not consist of baryons further emerged from lensing observations. Gravitational lensing surveys excluded nearly all the plausible baryonic objects such as the Massive Compact Halo Object (MaCHO)s hiding in our galactic halo as candidate of dark matter.

Baryonic acoustic oscillation (BAO) provided stricter constraint on the total matter density and baryonic matter density of the universe. BAO characterizes acoustic density perturbations in the early universe. In early stage of the universe, photons and baryons were bound together until the universe expanded and cooled enough to form hydrogen. In this recombination epoch, photons decoupled from baryons and quickly diffused away leaving the baryon wave crests stalled. The remaining over-dense baryon shells are predicted to be observed at approximately $100h^{-1}$Mpc, where h is defined by the Hubble constant H_0 as $h = H_0/100$ km s^{-1} Mpc^{-1}. As baryonic matter and dark matter might have affected the oscillations by their gravities in different effects, the amout of total matter and barionic matter could be derived from the power spectrum of galaxies. The final study of the 2dFGRS found $\Omega_m = 0.231 \pm 0.021$ and Ω_b / Ω_m = 0.185 ± 0.046 (14); a study based on the SDSS data with the combination of Union supernova result (15) yielded the total matter content $\Omega_m = 0.286 \pm 0.018$ and the baryonic matter content $\Omega_b h^2 = 0.02267 \pm 0.00058$ at 68% confidence limit (16), where $\Omega_i = \rho_i/\rho_c$ with ρ_c, the critical density which was defined as $3H^2/8\pi G$.

1.2.3 The cold dark matter

It is natural to consider the neutrino as a candidate of dark matter due to its nature of being non-baryonic and electrically neutral. However, a simple calculation shows that their total relic density is predicted to be

$$\Omega_\nu h^2 = \sum_{\nu_i=1}^{3} \frac{m_{\nu_i}}{93eV}. \tag{1.1}$$

The best laboratory constraint on neutrino mass comes from tritium β-decay experiments at Troitsk and Mainz (17) as

$$m_\nu < 2.05 \text{ eV} \tag{1.2}$$

with 95% C.L.. This implies an upper bound on the total neutrino relic density of

$$\Omega_\nu h^2 < 0.07. \tag{1.3}$$

A more stringent constraint on the neutrino relic density comes from the analysis of CMB anisotropies, combined with large-scale structure data, suggesting $\Omega_\nu h^2 < 0.0067$ (95% C.L.). Thus the abundance of neutrinos is insufficient to be the dominant component of dark matter.

Furthermore, observations imply that the majority of the dark matter can not be composed of relativistic ("hot") matter. In the middle of 1970's, the first red-shift observation of bright galaxies showed that the galaxies are not distributed randomly as supposed in early days, but they formed filaments and voids in a scale of up to several tens of Mpc. N-body simulations of large scale cosmic structure found that without dark matter, it could not form the large structures with filaments and voids observed by SDSS and other surveys in the proper time scale. Additionally, in the scenarios with relativistic dark matter, the small-scale, i.e. galaxy-sized initial density fluctuations would have been washed out by the free-streaming of the dark matter (18; 19; 20). As a result, relativistic neutrinos are ruled out as a main component of dark matter.

When photons decoupled from baryons at the recombination epoch, the distance that a photon could diffuse became much greater. The photons would free-stream from high to low density regions while dragging protons and electrons with them. This process, known as Silk damping or diffusion damping is also known to have wiped out fluctuations; it would have erased all the perturbations existed under $\sim 10^{13} M_\odot$. However, in the scenarios with non-relativistic ("cold") dark matter, the problem can be solved. If the dark matters were already cold during the period of structure formation, as they were pressure-less, they might not have experienced Silk damping and stayed with the original size of the perturbations. At the end of recombination where the small-scale anisotropies in the baryons had been all removed away by damping photons, the baryons rapidly fell into the potential wells of dark matter perturbations. As a result, in the scenario of the universe where the cold dark matter is the dominant form of the matter, the Silk damping observed in CMB data is irrelevant for galaxy formation (21).

As a result, non-baryonic cold dark matter is needed to take the role of the seed for perturbation in the evolution of the universe. This "bottom up" model of structure formation with cold dark matter has been proved by observations; the structure formation in the universe started from the smallest structures and then the gravitational merging processes have formed the clusters of galaxies and so on, hierarchically.

1.3 Dark matter distribution in the Milky way

As summarised above, there are plenty of evidences that most of the matter of the universe is in the form of non-baryonic cold dark matter. During the structure formations of cosmological history, massive halos of dark matter are expected to have been formed within which the visible part of the Galaxies (disk and bulge) are immersed. During gravitational collapse and subsequent Virialization ("violent relaxation"), the collisionless dark matter would have formed a halo that is roughly spherical in shape (22).

The fact that the Sun rotating around the galactic center has the speed of ~220 km/s allows us to infer the depth of the potential well of the Milky way. The local dark matter halo density near the Sun, ρ_0, is estimated to be 0.3 GeV/cm^3 (23).

1.3.1 Modeling of dark matter distribution, and the standard halo model

For a phase space distribution function of collisionless particles:

$$f(x_i, v_i, t), \tag{1.4}$$

the steady-state solution is given by the collisionless Boltzmann equation (24):

$$\frac{\partial f}{\partial t} + \sum_{i=1}^{3}(v_i \frac{\partial f}{\partial x_i} - \frac{\partial \Phi}{\partial x_i}\frac{\partial f}{\partial v_i}) = 0 \tag{1.5}$$

where the density distribution generates the potential:

$$\nabla^2 \Phi = 4\pi G \int f d^3 v. \tag{1.6}$$

For a spherical isotropic system, there's a unique relationship between $\rho(r)$ and $f(v)$ given by Eddington's equation (25):

$$f(E) = \frac{1}{\sqrt{8}\pi^2} \int_0^E \frac{d^2\rho}{d\Phi^2} \frac{d\Phi}{\sqrt{E - \Phi}}, \tag{1.7}$$

where Φ is the relative potential as a function of radius, and E is the relative energy, $E = \Phi - mv^2/2$.

The flat rotational curve of the Milky way implies the choice of density profile

$$\rho(R) = \rho_0(\frac{R_0}{R})^2, \tag{1.8}$$

in which case the resultant velocity distribution function is the Maxwell-Boltzmann distribution:

$$f(v)d^3v = \frac{e^{-v^2/v_{rms}^2}}{\pi^{3/2}v_{rms}^3}d^3v. \tag{1.9}$$

The value of v_{rms} can be obtained from the observation of rotational speed. For example, using the condition of hydrostatic equilibrium for an isothermal sphere:

$$-4\pi R^2 dp = G\frac{MdM}{R^2} \tag{1.10}$$

with $p = \frac{1}{3}\rho v_{rms}^2$ and $v_{rot}^2 = \frac{GM}{R}$, one can get the relation between v_{rms} and v_{rot},

$$\frac{v_{rms}^2}{v_{rot}^2} = -3\frac{d\ln R}{d\ln\rho} = \frac{3}{2}. \tag{1.11}$$

The observed value of the circular speed in the solar position $v_\odot$ is about 220 km/s, which leads the local velocity dispersion of the dark matter halo v_{rms} to be $\simeq \sqrt{3/2}v_\odot \simeq$ 270 km/s.

High-velocity dark matters might escape from the Milky Way leaving a cut off in the Velocity Distribution Function (VDF) at the galactic escape speed. The equation formally derived extends to infinity, therefore velocity distribution is usually truncated at escape velocity by hand as:

$$f(v)d^3v = \frac{e^{-v^2/v_{rms}^2}}{\pi^{3/2}v_{rms}^3}\Theta(v - v_{esc})d^3v. \tag{1.12}$$

The above description of the dark matter distribution is called the Standard (Maxwellian) Halo Model or SHM, and is commonly used as a canonical model in the dark matter searches.

However, some important departures from the SHM are observed, and supported by analytic calculations and numerical simulations. For example Hansen et al. (26) shows that the velocity distribution function (VDF) derived numerically through the Eddington's formula with power-low density profiles matches well to the analytical derivation of non-extensive statistical mechanics (27; 28). The authors suggest that self gravitating collisionless particles don't obey the rule of extensivity, so they can't be described by the statistical mechanics derived from the Boltzmann entropy but the non-extensive statistical mechanics from the generalized entropy should be applied.

Among many choices of analytically derivable dark matter profiles, the NFW profile is a suitable choice to the spherical halos simulated in N-body simulations:

$$\rho(r) = \frac{\rho_0}{\frac{r}{r_s}(1 + \frac{r}{r_s})^2}, \tag{1.13}$$

where ρ_0 is the normalization parameter for the density and r_s is the scale radius of the halo. When $r \ll r_s$, $\rho(r) \propto r^{-1}$ therefore the profile is cuspy at the core.

Recent high-resolution N-body simulations show that three-parameter profiles, for example Einasto profile, fits better to the wide range of simulated dark matter halos. It has a form of:

$$\rho(r) \propto \exp(-\mathrm{Ar}^{\alpha}). \tag{1.14}$$

The parameter α defines the steepness in a power law, and by choice of it, the Einasto profile gets a flat or slow central slope, which doesn't diverge at the center of the core.

1.3.2 N-body simulations

Cosmological N-body integration is a promising way to understand the dark matter properties within a framework of the standard ΛCDM model. N-body simulations have been successful in showing large scale structure, growth of structure and dark matter halo properties, evolution of the distribution and clustering of halos, accretion history of halos and other halo statistics (29) in agreement with observations.

Despite their successes, there have been claimed several critical discrepancies between the observations and the N-body simulations. The "cuspy halo problem" arises from cosmological simulations that seem to indicate sharply peaked (cuspy) density distribution at the center of the galaxies, whereas the observations likely have no cusps there. The discussions have been done on the possibility of that high-resolution CDM-only simulations may be being misinterpreted and maybe baryons strongly modify the structure of subhalos, therefore it needs better understanding of the effcts of baryonic physics.

Hydrodynamic galaxy formation simulations involving baryons, with adequate resolution and realistic feedback mechanisms, appear to be able to reproduce the evolution of galaxies, formation of galactic spheroids via mergers, and galaxy images over wide ranges in wavelength including stellar evolution and dust. So far, adding baryons in galaxy formation simulations has been resulting in problems such as "angular momentum catastrophe" in galaxy formation, overcooling therefore disks becoming too small and resulting in too high baryon-to-dark matter ratio, no bulge-less galaxies, too many stars overall, and so on. But by recent progresses at different mass scales with better resolution and more realistic feedback mechanisms, the angular momentum catastrophe appears to be resolved (30).

Recently, N-Body simulations of smoothed-particle hydro-dynamics including explicit H_2 and metal cooling, star formation and supernovae driven gas outflows (31) show that the cusp can be removed by starbursts blowing out central gas; Starting at high redshift, rapid and repeated gas outflows following bursty star formation transfer energy to the dark matter component and significantly flatten the originally cuspy central dark matter mass profile of galaxies with present day stellar masses. “The missing satellite problem” which means that much smaller number of dwarf galaxies are observed than expected from simulation, and the “too big to fail (32) problem” which means that the observed dwarf spheroidal galaxy masses are much smaller than expected for the most massive subhalos from simulations, are also possibly solved by future N-body simulations including baryons (33). Figure 1.5 shows an example of a N-body simulation including baryon (34).

By several cosmological simulations of hierarchical structure formation including baryons, it is suggested that the merger history of the Milky Way probably allows the existence of a co-rotating structure made from materials accreted from merged satellites, known as the dark disc (34; 35; 36; 37; 38). In those simulations the pre-existing baryonic disc perturbs the merger process of the host galaxy with satellites, as it draws satellites to the disc plane by dynamical friction and disrupts them by tidal force. As a result, the accreted materials settle around the galactic disc of the host halo and produce a co-rotating equilibrium structure of dark matter, as well as the hot stellar disc.

1.4 WIMP, a particle candidate of cold dark matter

To be a good dark matter candidate in terms of explaining gravitational observations, the abundance in each epoch of the universe, speed in early universe, decay life time and annihilation cross-section etc. would be considered. However, the non-baryonic nature of dark matter forces us to consider it, not only as a phenomenon solely appearing in cosmology, but as a possible evidence of new physics beyond the Standard Model. In that vein, most attempts of modeling and detecting dark matter have been made for target particles which are motivated by existing physics problems.

There are numbers of candidates for non-baryonic cold dark matter particle beyond the Standard Model. Among the candidates, WIMPs, Weakly Interacting Massive Particles, are most favored as they arise from Super Symmetry (SUSY) or extra dimension scenarios. Axions are also favored as a candidate of cold dark matter as they are a possible solution for the strong-CP problem.

WIMPs do not interact via electromagnetism, nor do they interact with strong force, but only with weak force. When the universe was at very high temperature, WIMPs were in thermal equilibrium with the radiation. After the temperature dropped below the mass of the WIMP as the universe expanded, its number density froze out, and a substantial number of WIMPs have been left. The remarkable fact is that thermal relics with electroweak interactions can give us relic abundance of WIMPs in agreement with concordance model, thus it is called the “WIMP miracle”.

In some extension of the Standard Model, there can be found particle models for

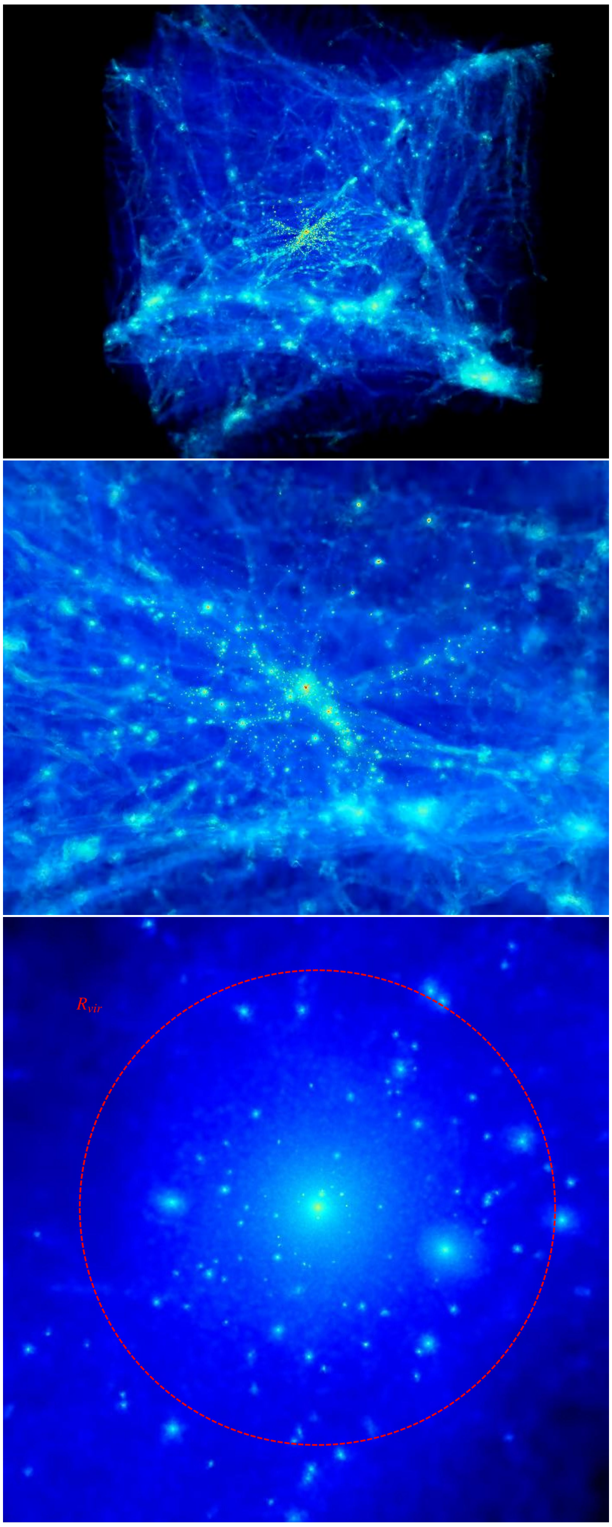

Figure 1.5: The 20 Mpc/h-sized box of a N-body simulation including baryons (34) (top), for zoomed view on the central region (middle) and the galaxy in the center of it (bottom). In the bottom plot, the red circle shows its Virial radius (264 kpc) and the halo is concentrated in the center and has many subhalos, as expected. Figures are taken from (34).

WIMP such as a fourth generation of Dirac neutrino, a Majorana neutrino or a scalar-coupled WIMP. But what made WIMP most famous is that it naturally arises from SUSY theory which is highly motivated to explain the hierarchy problem in the Standard Model. The most popular candidate, neutralino, is the LSP (lightest Symmetric Particle) in SUSY models. In the Minimal Supersymmetric extension of the Standard Model (MSSM), the R-parity is conserved and sparticles (superpartners of SM particles) can only decay into an odd number of sparticles plus Standard Model particles. The LSP is therefore stable and can only be destroyed via pair annihilation, making it an excellent dark matter candidate (39; 40). They are predicted to have masses ranging from a few GeV to a few TeV (41).

1.5 Current experimental searches for WIMPs

1.5.1 Overview

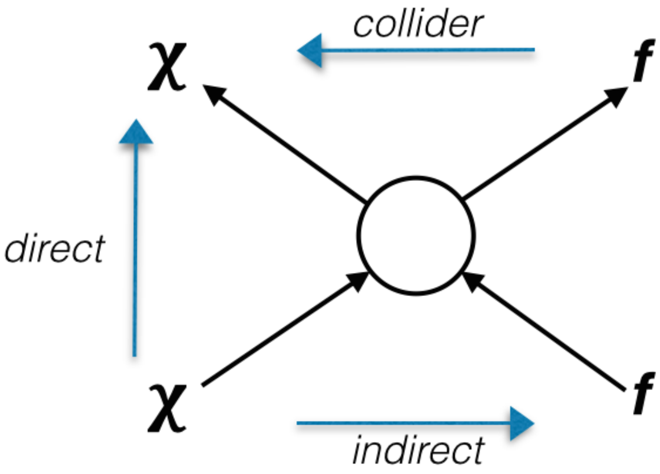

Figure 1.6: WIMP interactions with ordinary matter and corresponding detection strategies.

If WIMPs are to have a cosmological density of order unity, they must have some small but finite coupling to ordinary matter; otherwise, they would not have annihilated in the early universe and would be unacceptably overabundant today. By crossing symmetry as shown in Fig. 1.6, the amplitude for WIMP annihilation to quarks is related to the amplitude for scattering of WIMPs off quarks. Therefore, WIMPs are generically expected to have small but nonzero coupling to nuclei through the coupling to quarks as well as self-annihilation.

Dark-matter searches mostly rely on the non-gravitational interactions with the Standard Model particles - weak interactions in the majority of the searches. By the type of the interaction between WIMPs and the Standard Model particles used in a search, the WIMP searches can be categorised in big three methods as illustrated in

Fig. 1.6. The Feynman diagram following the arrow from right to left shows the production of dark-matter particles from the Standard-Model particles. This strategy is used in the WIMP searches in hadron colliders by using mono-jet and mono-photon signatures. The WIMP-nucleon scattering cross section can be deduced by these searches, however, these searches employ effective field theories and depend on masses of mediating particles. The other Feynman diagram following the arrow from left to right indicates WIMP annihilation. The annihilation cross-section allows us to search for WIMPs by its annihilation products. “Indirect detection searches” aim at detecting the final products as Standard-Model particles among which, gamma rays, neutrinos and anti-particles are particularly targeted because of its strong back-ground discriminating power or directional information. Target objects are in various places of the universe wherever it is expected have WIMP population; Galactic Center, Milky Way halo, dwarf galaxies and the Sun and the Earth. Dense regions are favored as the annihilation rate goes as the square of the density, but diffuse components from all directions are also promising because of their competing abundances. Note that the general definition of “indirect” comes from the fact that they search for secondary products. In this sense, the search for decay products which doesn’t appear in the diagram also falls into indirect detection category.

Finally, the Feynman diagram directing from bottom to top shows the scattering interactions of dark-matter particles with the Standard-Model particles, which are strategies widely used in commonly called “direct detection”.

Detection of WIMPs in the Sun using neutrino detectors has sensitivity to both annihilation and scattering cross sections. It is categorised in “indirect detection” in the sense that it searches for neutrinos from those secondary annihilation products, however, it is sensitive to WIMP interaction with Standard-Model particles same as direct detections, by the mean that will be explained in the next chapter (Chap. 2).

In this chapter, methods and current status of the WIMP searches by direct detection and for the neutrinos coming from the WIMP annihilation in the Sun are discussed.

1.5.2 WIMP-nucleon scatterings

As the elastic scattering of WIMPs off nuclei occurs in the non-relativistic limit in both direct detection and solar WIMP detection using neutrinos, the simplifications can be made: the axial-vector current becomes a “spin-spin interaction”, while the vector and tensor currents take the same form as the scalar interaction (42; 43). As a result, two types of interactions are considered for WIMP search; spin-spin interaction and scalar interaction. In the case of the spin-spin interaction, WIMPs couple to the spin of the nucleus with spin-dependent (SD) scattering cross-section; in the case of the scalar interaction, WIMP couples to the mass of the nucleus with spin-independent (SI) scattering cross-section.

The WIMP-nucleon spin-dependent scattering cross-section at zero momentum transfer can be written as

$$\sigma^{SD} = 32\frac{G_F^2\mu_N^2}{\pi}(a_p < S_{p(N)} > +a_n < S_{n(N)} >)^2\frac{J+1}{J}, \tag{1.15}$$

where G_F is the Fermi constant, μ_N is the reduced mass $m_\chi m_N/(m_\chi + m_N)$ of the mass of WIMP m_χ and the mass of target nucleus m_N. $a_p(a_n)$ is the coupling constant for proton(neutron), $< S_{p(i)} >(< S_{n(i)} >)$ is the expectation value of the spin content of the proton (neutron) group in the nucleus and J is the total angular momentum. The SD scattering can be efficient when a nucleus has large number of unpaired protons or neutrons.

Figure 1.7 shows possible tree level SD scattering diagrams.

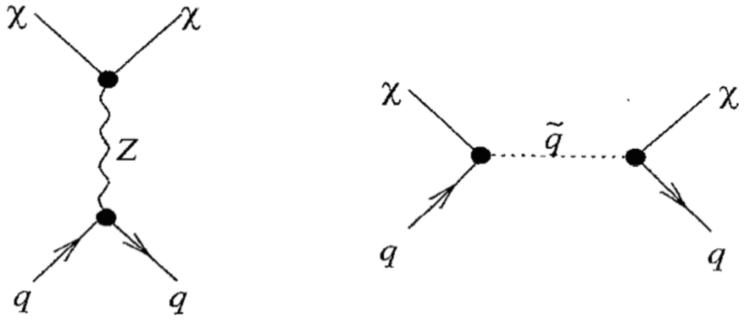

Figure 1.7: Feynman diagrams contributing to spin-dependent elastic scattering of neutralinos off quarks. Squark exchanges are allowed for SUSY neutralinos. Figure is taken from (42).

In the spin-independent interaction, the WIMP-nucleon scattering cross-section can be written as

$$\sigma^{SI} = \frac{4\mu_N^2}{\pi}(Zf_p + (A-Z)f_n)^2, \tag{1.16}$$

where f_p and f_n are coupling constants to the proton and neutron, respectively, A is the mass number and Z is the atomic number of the target nucleus. The cross sections for each nucleus is calculated with f_p and f_n defined for individual model of WIMP candidate. However, a simplification can be made: assuming $f_p \simeq f_n$, the cross section can be written as

$$\sigma^{SI} = \frac{4m_N^2\mu_N^2}{\pi}\frac{f_p^2}{m_p^2} \tag{1.17}$$

$$= \sigma_0^{SI}A^2\frac{\mu_N^2}{\mu_p^2}, \tag{1.18}$$

where m_p is proton mass and μ_p is the WIMP-proton reduced mass. Note that all the information about a specific model is encoded in f_p inside σ_0^{SI}, where σ_0^{SI} is the SI WIMP-nucleon (equally to proton and neutron) scattering cross-section.

Figure 1.8 shows possible tree level diagrams contributing to SI scattering. For SI scattering, one-loop amplitudes for interactions with gluons are also important (42).

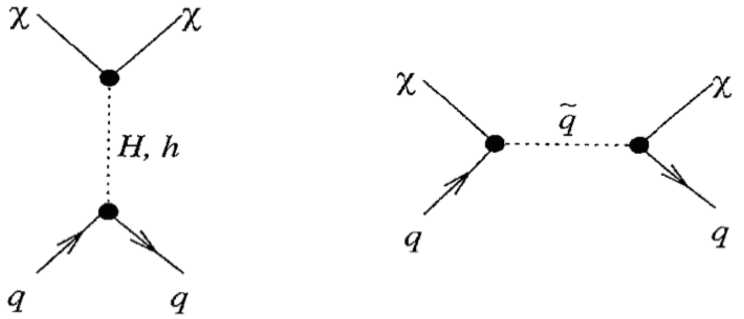

Figure 1.8: Feynman diagrams contributing to spin-independent elastic scattering of neutralinos off quarks. Squark exchanges are allowed for SUSY neutralinos. Figure is taken from (42).

1.5.3 Direct detection searches on WIMP-nucleon scatterings

The basic idea of direct detection is waiting for dark matter scattering off a material which is buried in the deep underground to reduce background for a very weak signal. When WIMPs pass through the material, they may experience weak scattering and transfer a small amount of kinetic energy to a nucleus. The recoil energy of the nucleus is:

$$E_R = \frac{1}{2}m_\chi v^2 \times \frac{4m_\chi m_N}{(m_\chi + m_N)^2} \times \frac{1+cos\theta}{2}. \tag{1.19}$$

The first part is the kinetic energy of incoming WIMP, the middle part is the "mass-matching factor" between the WIMP mass m_χ and the target nucleus mass m_N and the last part is the angular factor, with the θ being a scattering angle in the center-of-mass frame. Maximal energy transfer happens for head-on recoil (when θ=0). For the case of the WIMP and the target have the same mass,

$$E_R^{max} \sim \frac{1}{2}m_\chi v^2. \tag{1.20}$$

It indicates that it is a good choice to select a material to have similar mass with the target WIMP. The WIMPs distributed in the dark matter halo in the Galaxy will get boosted in the coordinate of the detector as the solar system moves in the Galaxy with the speed ∼220km/s. The typical incoming velocity of the WIMPs thus will be $v \sim 10^{-3}c$, as a result the expected maximal recoil energy is about:

$$E_R^{max} \sim \frac{1}{2}(\frac{m_\chi}{\mathrm{GeV}})\mathrm{keV}, \tag{1.21}$$

resulting tens to hundreds of keV signal for tens to hundreds GeV mass of WIMPs. Observing this tiny amount of deposited energy is the challenge of direct detection experiments.

The expected event rate is:

$$\frac{dR}{dE_R} = N_T \frac{\rho_\chi}{m_\chi} \int_{v_{min}} f(v) v \frac{d\sigma}{dE_R} d^3\vec{v} \tag{1.22}$$

with N_T as the number of nuclear targets.

Typically a very low event rate is expected; for $\sigma \sim 10^{-46}$ cm^2, the event rate of ∼1 count/day/kg is expected for the most effective target nucleus, thus usually ton-scale detectors are demanded. Typically detectors have a finite energy threshold set at around a few to few tens of keV which cut off sufficient amount of signal, therefore have more sensitivity to energetic WIMPs. Many sources of backgrounds, some of them having a similar exponential spectrum to the signal, are also a challenge for direct detection experiments.

To observe the recoil energy signal, various signal channels are used such as scintillation lights, ionization yields, thermal energy and bubbles. Most of the current detectors use one of these channels or a combination of them to efficiently reduce backgrounds of for instance γ's, electrons and nucleons. In Fig. 1.9, the various direct detection techniques and experiments are shown.

As for target materials; heavy nuclei are widely used to enhance the SI cross section. Liquid noble gases, such as Xe or Ar, form a dense and homogeneous target with self-shielding and allow large detector masses at moderate costs. They also yield high light (40 photons/keV) and charge. Noble gases usually can produce signals in two ways; scintillation and ionization processes. Single phase liquid noble gas detectors which are sensitive to scintillation yield such as XMASS, CLEAN and DEEP generally have advantage that they can be built larger without high-voltage eletrodes, resulting less radioactive background. Double phase detectors using the time projection chamber technique can further discriminate background events reading both charge and scintillation signals. XENON100, LUX, PandaX, ArDM, DarkSide are on data-taking or in the R&D process.

Another type of detectors use cryogenic materials such as Ge (CDMS, EDELWEISS), CaWO4 (CRESST). They typically detect phonons and have a high yield. CRESST uses a calcium tungstenate crystal as the target, and detects both a phonon signal and the scintillation lights. By 730 kg-days of data taking, they observed event excess over known backgrounds at more than 4 σ significance in 2011 (45). CDMS is a semiconductor detector measuring signal by ionization and phonons. With Si target of low atomic mass, they have claimed the observation of three WIMP-candidate events

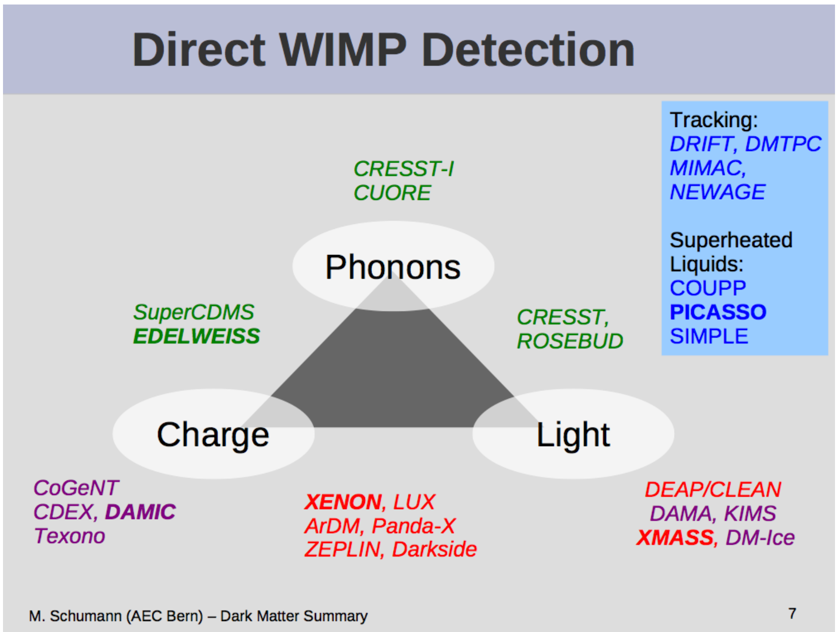

Direct WIMP Detection

CRESST-I
CUORE

Phonons

SuperCDMS
EDELWEISS

CRESST,
ROSEBUD

Tracking:
DRIFT, DMTPC
MIMAC,
NEWAGE

Superheated
Liquids:
COUPP
PICASSO
SIMPLE

Charge

Light

CoGeNT
CDEX, ***DAMIC***
Texono

XENON*, LUX*
ArDM, Panda-X
ZEPLIN, Darkside

DEAP/CLEAN
DAMA, KIMS
XMASS*, DM-Ice*

M. Schumann (AEC Bern) – Dark Matter Summary 7

Figure 1.9: The direct detection techniques and the experiments categorised by the techniques being used. Image is taken from M. Schumann's slides in ICRC 2013 (44).

in the 140.2 kg-days of data taken, which is consistent with low mass WIMP signal at 3 σ C.L. (46).

Because of the relative velocity of the Earth to the Sun added to the motion of the Sun in the Galactic frame, the event rate is expected to have annual modulation. The modulation amplitude in the region of maximal sensitivity is expected to be $\simeq$ 7% for halo distributions which are commonly used (47). So far DAMA (DAMA/NaI and DAMA/LIBRA) and CoGENT have reported annual modulation signals observed. DAMA has been taking data for 13 years using NaI crystal measuring scintillation lights, and observed an annual modulation signal interpreted as WIMP interactions with 8.9 σ significance. By a year-data taking of CoGENT, a P-type Point Contact Germanium Detector measuring ionization, it is showed 2.8 σ annual modulation (48).

However, their allowed signal regions are completely rejected by recent results from XENON100 (49), LUX (50) and SuperCDMS (51). The current best constraints are made by two phase Xe detectors, i.e., XENON100 (49) and LUX (50), and are rapidly rejecting the theoretically profound WIMP parameter space around the scattering cross section of 10^{-45}cm^2. Figure 1.10 shows the current best limits from direct detection searches.

Recently, direct detection experiments are making steep gains in sensitivity and achieving nearly zero-background searches. In the near future, the experiments will reach the irreducible solar-neutrino background at around the sensitivity of SI WIMP-nucleon cross-section $\sim 10^{-48}\text{cm}^2$.

Some detectors have a sensitivity for SD interactions as well. Natural isotopes with some unpaired protons or neutrons are used as a target. Si and Ge are almost composed of spin-less isotopes, however, ^{73}Ge (7.8% of natural Ge) and ^{29}Si (4.67% of natural Si) contribute to the sensitivity to spin-dependent coupling WIMPs in spite of their small abundance. Superheated fluids are also used; COUPP is a bubble chamber using CF_3I and PICASSO, SIMPLE are superheated droplets made of C_4F_{10}.

Figure 1.10 shows the current limits from WIMP detection experiments on spin-independent WIMP-nucleon cross section and spin-dependent WIMP-proton cross section.

1.5.4 Constraints by indirect detection searches on WIMP-nucleon scatterings

Indirect solar WIMP searches have strong sensitivity to spin-dependent coupling WIMPs as the Sun is mainly composed of protons. Tight limits on the SD scattering cross section of WIMPs on protons have been placed by neutrino telescopes such as Super-Kamiokande (56), AMANDA (57), IceCube (54), BAIKAL (58), Baksan (59) and ANTARES (60).

Super-Kamiokande (SK) is a 50 kton Water Cherenkov neutrino observatory located in Kamioka mine in Japan. The Super-Kamiokande collaboration has analysed their accumulated data and reported the result in 2004 (61) and 2011 (56). The analysis done in 2004 used a dataset of 1679.6 days of SK-I muons which pass through the detector. The updated analysis in 2011 increased the dataset to SK I-III (3109.6 days). In addition, it introduced a new event categorization of muons to use the neutrino energy information to reduce background, in order to improve the limits especially for lower mass WIMPs. As muon events dominate the observed events in SK above 10 GeV, the signal acceptance for WIMPs with mass above 10 GeV was good, also the good angular resolution of muon events allowed an efficient way to distinguish signal from background. As a result, the search resulted the best limit for WIMPs in the mass range from 10 GeV to a few hundreds of GeV at the moment.

The IceCube is a large Cherenkov detector situated in the ice at the South Pole. Spanning a surface area of roughly 1 km^2 and depths between 1450 and 2450 m, IceCube has strong sensitivity for heavy WIMPs. Current report (54) provides the world best limit for spin-dependent coupling cross section for WIMP masses above 20 GeV, which eliminates the cross sections of about 10^{-40}cm^2 and the MSSM parameter space which is not reached by direct detection experiments.

Figure 1.11 shows the current best limits from searches for the neutrinos coming from the WIMP annihilation in the Sun.

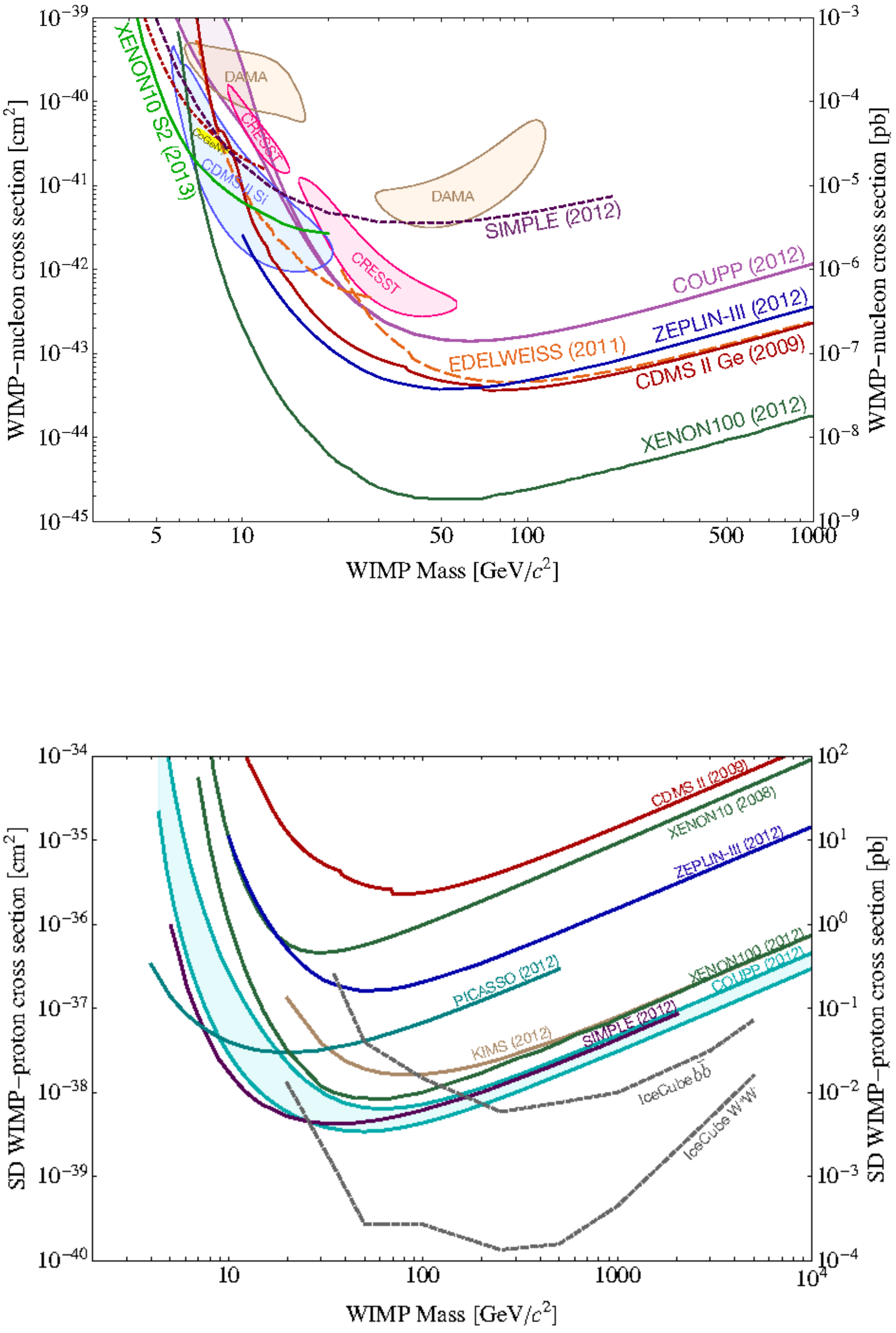

Figure 1.10: Top: Constraints and signal claims on spin-independent WIMP-nucleon cross sections as a function of WIMP mass (52; 49; 53). Bottom: Constraints on spin-dependent WIMP-proton cross sections as function of WIMP mass for direct detection experiments (IceCube (54) result is shown in comparison). Figure is taken from (55).

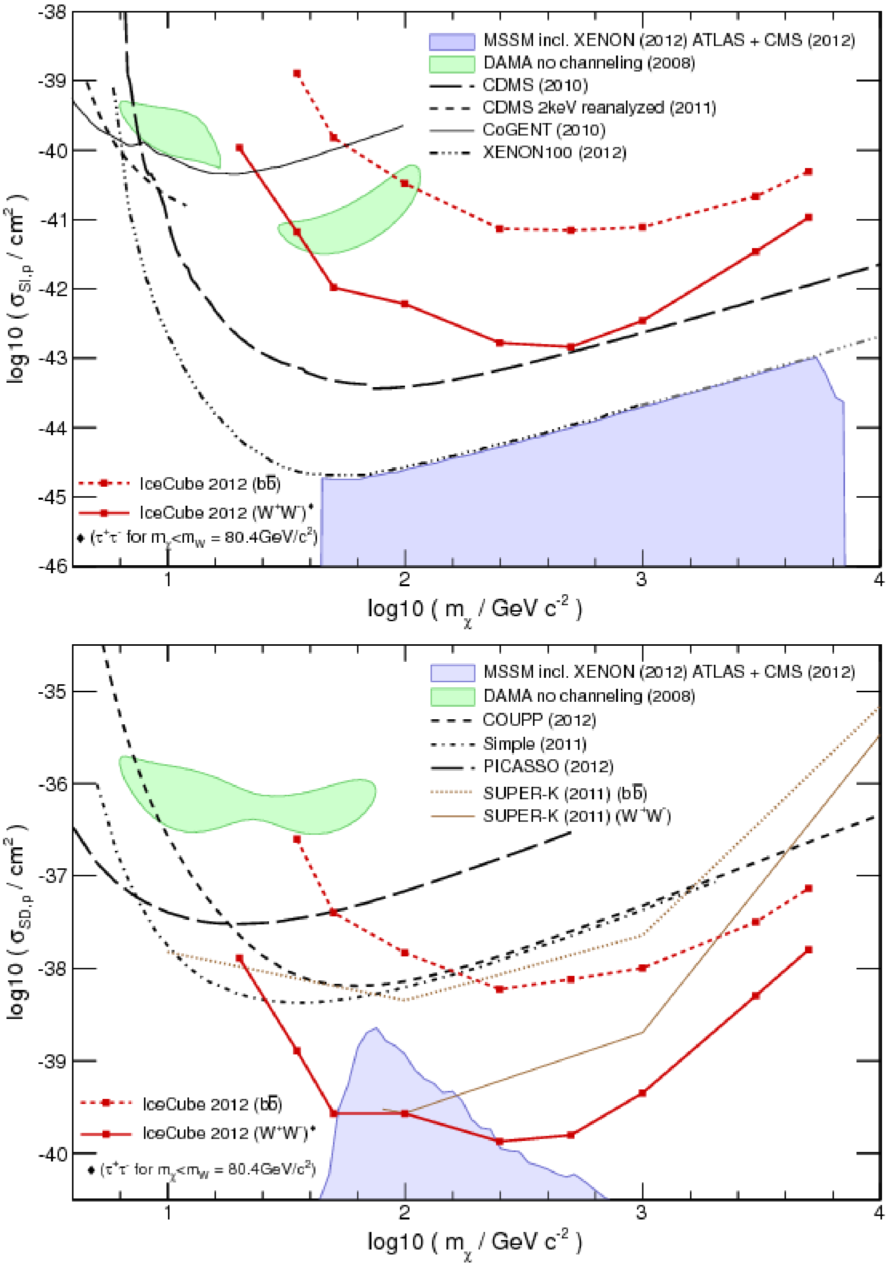

Figure 1.11: 90% C.L. upper limits on spin-independent scattering cross-section (top) and spin-dependent one (bottom) as function of mass from solar WIMP searches are shown. The shaded regions indicate allowed MSSM parameter spaces. Results from direct detection experiments are shown for comparison. Figure is taken from (54).

1.6 Prediction of sensitivity of the Super-Kamiokande for light WIMPs

As mentioned above, recently, there have been possible signals claimed by direct detection experiments such as DAMA/LIBRA (62), CoGeNT (48), CRESST (45) and CDMS (46), mostly for light WIMP mass below 30 GeV, but these claims conflict with many other experimental results (52; 49; 50; 51). Investigation with an independent detection method and uncertainties on this region will be therefore appreciated.

As typical neutrino energy resulting from WIMP annihilation in the Sun is roughly 1/3 to 1/2 of the WIMP mass (42), the SK's sensitivity to few-GeV neutrinos makes it suitable for this search. The huge gravity and hydrogen-rich composition of the Sun combined with high sensitivity of SK allow promising sensitivity to light WIMPs (63; 64; 65; 66), especially for spin-dependent coupling case.

Recent theoretical works (64; 65; 66) have calculated the expected power of SK data to test light WIMPs. Kappl et al.'s work shows that using SK-I fully-contained type of neutrino events, it can be proved that spin-dependently coupling WIMPs annihilating even subdominantly into neutrinos, taus, bottoms or charms will fail to explain the DAMA signal region (65). Fig. 1.12 shows their work on SD WIMP-nucleon scattering cross section and the result of a sensitivity study using 200 kton contained type of events done by Carsten et al. (66).

The sensitivity of Super-Kamiokande for SI WIMP-nucleon cross section for light WIMPs is also expected to be competitive with direct detection. The huge size of the Sun allows sizable contribution even from less abundant elements than hydrogen, and heavier elements scatter energetic WIMPs more efficiently. Kappl et al.'s study (65) shows that spin-independently coupling WIMPs which annihilate dominantly into neutrino or tau pairs will be inconsistent with the DAMA and CoGENT favored regions. The upper limit on SI WIMP-nucleon scattering cross section in case of using SK I fully-contained events studied by Kappl et al. is shown in Fig. 1.13.

Motivation for considering isospin violating dark matter (IVDM) arises from recent CDMS (46) result which can be "reconciled" with conflicting results by introducing destructive interference $f_n/f_p < 0$ (67; 68). The IVDM model is also motivated by current accelerator searches that low mass ($<$ 20 GeV) WIMPs have been essentially ruled out in the context of the MSSM. But we can find theoretically well-motivated light WIMPs for example in nMSSM (next-to-Minimal Supersymmetric Standard Model) scenarios and generally light WIMP candidates found in those scenarios do not necessarily always conserve isospin (68).

As the Sun is composed of relatively light elements, the Super-Kamiokande is expected to have strong sensitivity to IVDM with destructive interference (69; 70). Figure 1.14 shows the sensitivity study done by Chen et al. (69) assuming 1679.6 live-days data of the SK. Most of the DAMA and CoGeNT signal regions are expected be excluded assuming $b\bar{b}, \tau^+\tau^-$ or cc annihilation channels.

Previous Super-Kamiokande solar WIMP search (56) used upward-going muons produced in the surrounding rock. The new sensitivity for the light WIMPs can be achieved by increasing signal acceptance to a few-GeV neutrinos, whose interaction vertices are expected to be contained inside the detector. However, the atmospheric neutrino background events increase as $\propto E^{-2.7}$ at low energy. Also angular correlation between the parent neutrino and daughter lepton becomes worse for low-energy events. Therefore for light WIMP search, introducing large background in the solar WIMP search is inevitable. Developing an analysis tool to increase signal acceptance and to improve the sensitivity to signal against the increased background is a goal of this work.

Another challenge the solar WIMP search faces, while confirming results of direct-detection searches, is to understand the effect of astrophysical uncertainties. The phase-space distribution of WIMPs in the Galaxy is a large source of uncertainty for WIMP searches. Uncertainty in the local WIMP density will make a similar overall shift of the limits for direct detection and solar WIMP searches. However, the velocity distribution of WIMPs will affect the direct detection and the solar WIMP search in different ways. In the existing literature there have been extensive discussions about the impact of the velocity distribution on direct detection (see e.g. (71; 72) and references therein), but for the solar WIMP search, there have been no overall quantitative investigation on the size of the uncertainties except for specific scenarios (73; 74; 75; 76; 77; 66; 78; 79).

In Chap. 2, details of scattering and annihilation processes inside the Sun, neutrino production and the propagation to the detector will be described. In Chap. 3, the uncertainties in the WIMP velocity distribution and its effect on the solar WIMP search will be discussed. In Chap. 4, we briefly introduce the SK detector and its calibration procedure. In Chap. 5 and 6, MC simulations and event reduction, reconstruction and categorization of data and MC will be summarised. In Chap. 7, the analysis method of the SK solar WIMP search and results will be shown. In Chap. 8, the uncertainties in the analysis will be summarised. Finally, the conclusion and the future prospect are given in Chap. 9.

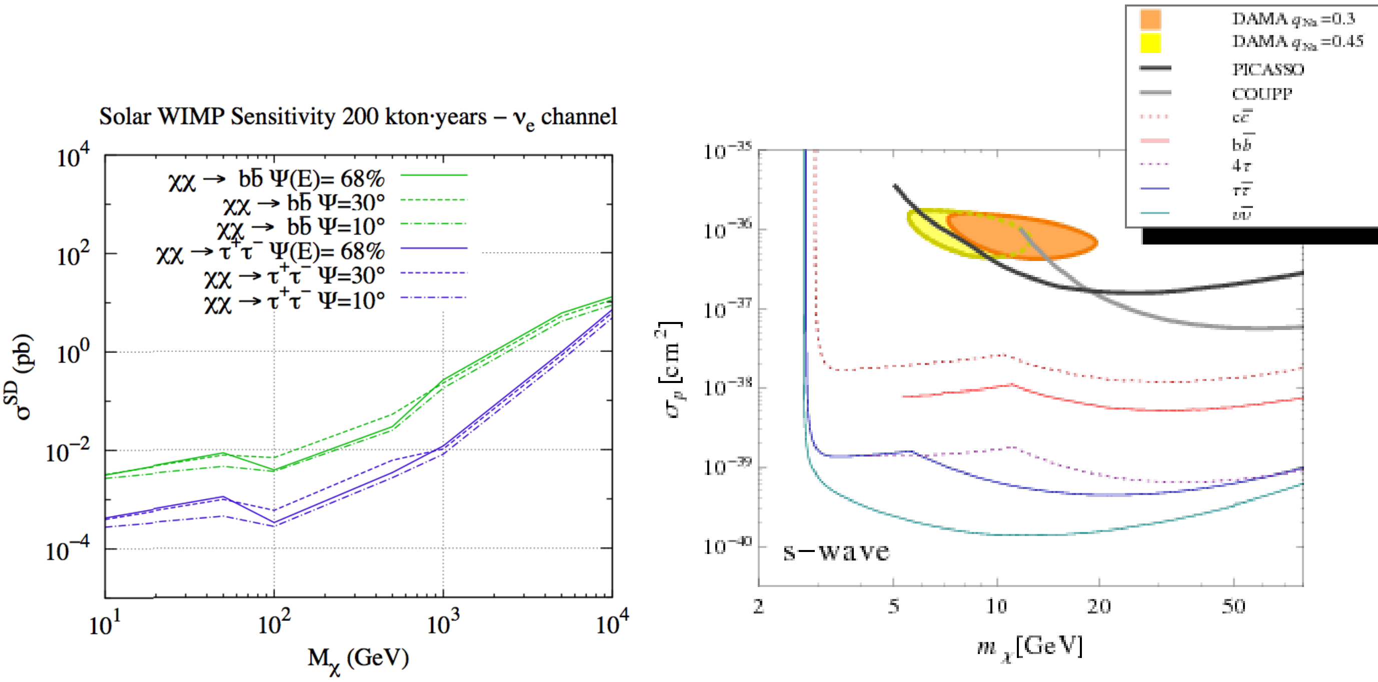

Figure 1.12: Left: Sensitivity study done by Rott et al. (66) of 200 kton-years neutrino detector data on SD WIMP-proton scattering cross section for annihilations into $\tau^+\tau^-$ (blue) and $b\bar{b}$ (green). Here FC ν_e events with three different direction cuts are used. Figure is taken from (66). Right: Sensitivity study (65) of the SK-I data on SD WIMP-proton cross section for various annihilation channels. The limits are obtained by using fully contained events at low mass region. Also shown are results from direct detection experiments. Figure is taken from (65).

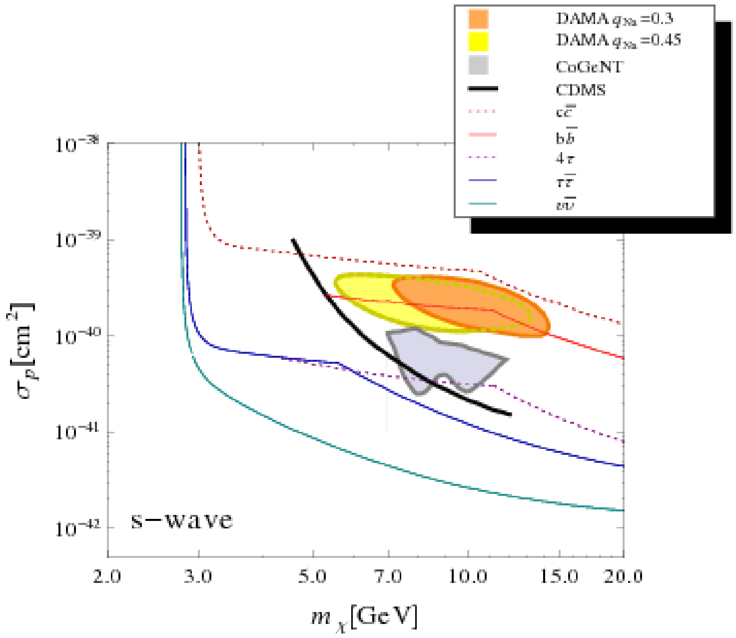

Figure 1.13: Sensitivity study done by kappl et al. (65) of the SK-I data on SI WIMP-nucleon cross section for various annihilation channels. At lower WIMP mass region FC events contribute to the sensitivity. Also shown allowed regions and upper limits claimed by various direct detecation expriments. Figure is taken from (65).

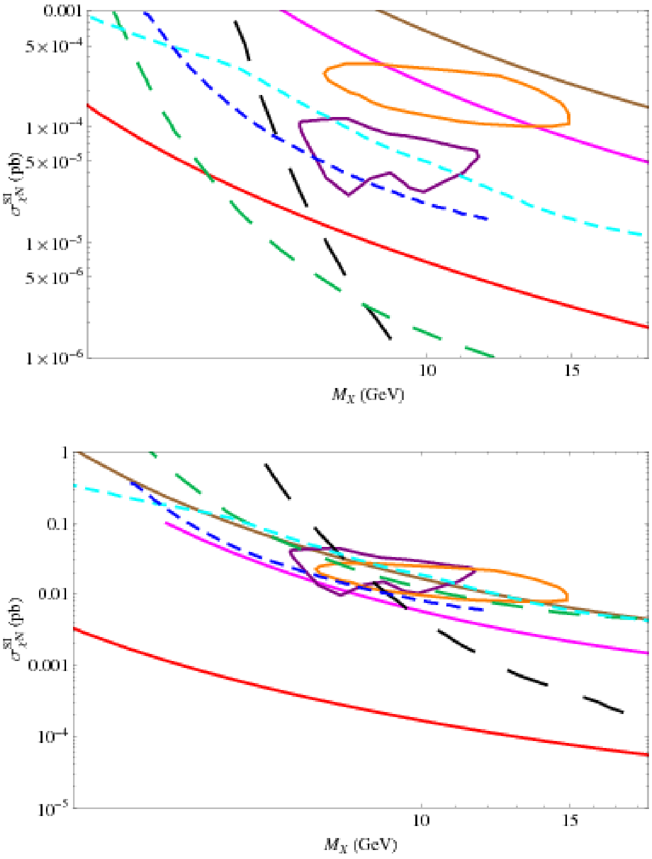

Figure 1.14: Sensitivity study done by Chen et al. (69) of the SK solar WIMP analysis (solid curves) in isospin conserving case (upper panel) and violating (lower panel) case with $f_n/f_p = 0.7$. DAMA (orange circle) and CoGeNT (purple circle) signal regions and the limits from other direct detection experiments (dashed line) are shown together. Figure is taken from (69).)

Chapter 2

Capture of WIMPs in the Sun and the search for it in a neutrino detector

2.1 Overview

As the solar system travels on the Milky Way arm, WIMPs in the dark matter halo could occasionally become gravitationally captured to the Sun after losing energy by scattering off nuclei within the Sun. Once captured, WIMPs may lose energy in subsequent scatters and settle at the center of the gravitational well and thermalize. The WIMPs would then pair-annihilate in the deep solar core, after which produced neutrinos propagate outward through the Sun and may be detected in terrestrial neutrino detectors.

The first WIMP detection attempts using neutrinos were motivated by the work done in 1985 by Press and Spergel, who calculated the capture rate of heavy particles by the Sun (80). In 1988, Gould refined the calculations of Press and Spergel and derived exact formulae for the capture rates (81; 82) which have been used in many subsequent studies including this work.

In section 2.2, we will review the WIMP capture process in the Sun. In Chap. 2.3, the WIMP number density evolution in the core of the Sun will be briefly reviewed and in Chap. 2.4, it will be linked to the assumption on equilibrium between the capture rate and the annihilation rate. In Chap. 2.5, the annihilation of WIMPs and the production of neutrinos will be introduced. Throughout the dissertation, calculations of the capture of WIMPs are done by using the numerical package for neutralino dark matter calculations, DarkSUSY (83). In Chap. 2.6, brief explaination of the usage of the DarkSUSY in this work will be given.

2.2 WIMP capture in the Sun

WIMPs that are abundant in the dark matter halo of the Milky Way can scatter off a nucleus in the Sun as it revolves around the Galactic center. The WIMPs may lose enough energy by elastic scattering off a nucleus to fall below the escape velocity of the Sun at the point of the scatter, and then be gravitationally captured. The differential WIMP capture rate on nucleus i per unit shell volume dV at distance r from the center takes the following form :

$$\frac{dC_i}{dV} = \frac{\rho_H}{m_\chi} \int_0^\infty du \frac{f_\eta(u)}{u} \Omega_i(q), \tag{2.1}$$

where ρ_H is the local dark matter halo density set to be 0.3 GeV/cm^3 (23; 84) and m_χ is the mass of the WIMP. $f_\eta(u)$ is the Velocity Distribution Function (VDF) seen in the reference frame of the Sun. For isotropic VDF, $f_\eta(u)$ can be simply calculated from the original VDF in the Galactic frame, $f_o(v)$, as

$$f_\eta(u) = \int_{-1}^{1} f_o(\sqrt{v^2 + v_\odot^2 + 2vv_\odot cos\theta})\ dcos\theta, \tag{2.2}$$

where $\vec{u} = \vec{v} + \vec{v_\odot}$ and θ is the angle between $\vec{v}$, WIMP velocity in the Galactic frame, and $\vec{v}_\odot$, the speed of the Sun in the Galactic frame. The bound velocity of a WIMP in the gravitational field of the Sun, w, and the escape velocity at the scattered position, $u_{esc}(r)$, are related via $w^2 = u^2 + u_{esc}(r)^2$. A WIMP can be captured when w drops below $u_{esc}(r)$ after losing kinetic energy through scattering off a nuclei. The capture probability $\Omega_i(q)$ can be written as (82)

$$\Omega_i(q) = \sigma_i n_i \frac{m_i}{2\mu_i^2} \int_{q_{min}}^{q_{max}} F^2(q) dq, \tag{2.3}$$

where σ_i is the WIMP-nucleus i elastic-scattering cross-section at zero-momentum transfer, n_i is the number density of nucleus i in the Sun, m_i is the mass of nucleus i, μ_i is the reduced mass of nucleus i and the WIMP, q is the recoil energy where

$$q_{\min} = \frac{1}{2} m_\chi u^2 \tag{2.4}$$

is the minimum recoil energy required to be captured,

$$q_{\max} = \frac{1}{2} \beta_+ m_\chi w^2, \tag{2.5}$$

is the kinematically determined maximal recoil energy with

$$\beta_\pm = \frac{4 m_i m_\chi}{(m_i \pm m_\chi)^2}, \tag{2.6}$$

and $F^2(q)$ is a nuclear form factor taken to have exponential form from (82). The σ_i^{SD} and σ_i^{SI} shown in Chap. 1 are not the real total cross sections used in the calculation

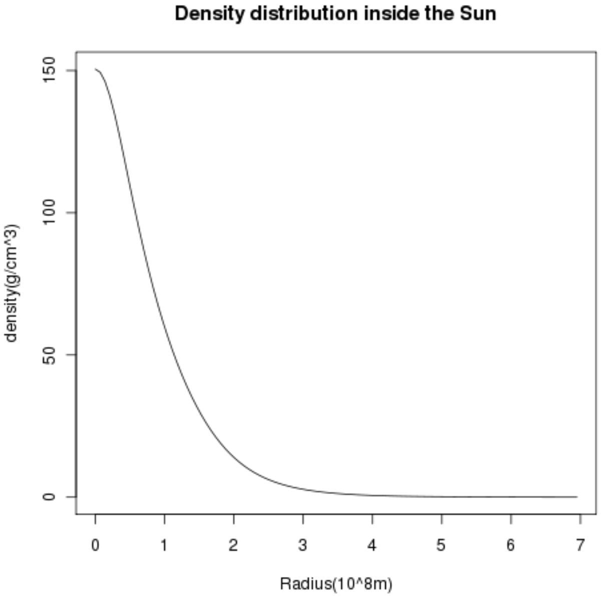

Figure 2.1: Density distribution inside the Sun as a function of radius.

of the capture rate. The actual cross section is obtained by integrating $\frac{d\sigma(q)}{dq^2}$ over dq^2 considering nuclear form factor $F^2(q)$. Where actual differential cross sections are used in the analysis, we define the 'zero-momentum transfer cross section' that are denoted by σ_i^{SD} and σ_i^{SI} and can be regarded to be total cross sections assuming $F^2(q) = 1$. This allow us to reduce them into σ_0^{SD} and σ_0^{SI}, which are the fiducial variables compared between models and various detection methods.

For SD WIMP capture, we neglect contributions from elements heavier than hydrogen. For the SI coupling case, we assume isospin-conserving scattering and use the SI zero-momentum transfer cross section as shown in Eq. 1.5.2.

To calculate the total capture rate, Eq. 2.1 must be summed over all relevant nuclear species inside the Sun and integrated over the distance r from the center as,

$$C_C = \int_0^{R_\odot} 4\pi r^2 dr \sum_i \frac{dC_i}{dV}, \tag{2.7}$$

where $R_\odot$ is the radius of the Sun.

Depending on the WIMP scattering nature with ordinary matter which is described in the previous chapter, the total capture rate is decided. The sun is mostly composed of hydrogen (∼74% of total mass) and helium (∼25% of total mass), then oxygen, carbon, iron, and so on. The capture rate also depends on the solar composition. The radial distribution of each element inside the Sun is adopted from the BS2005-OP model in the DarkSUSY. An example of radial distribution of total mass is shown in Fig. 2.1.

In the case when the strength of the interaction cross sections are the same, spin-independent coupling is more efficient to capture WIMPs than spin-dependent coupling

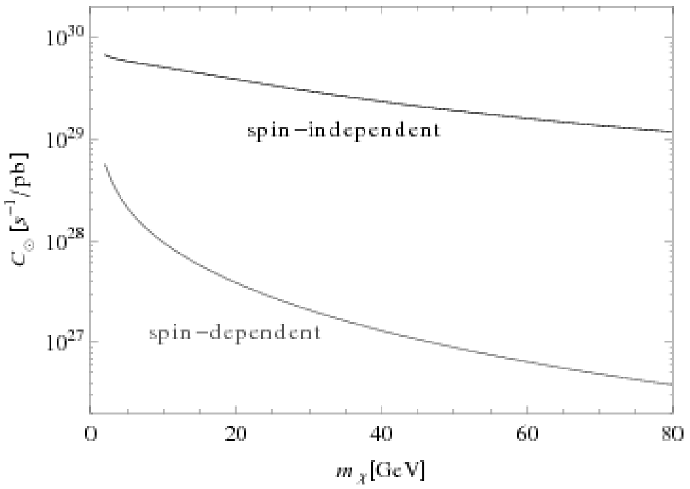

Figure 2.2: Capture rates of WIMPs in the Sun divided by interaction strength [pb] for spin-independent and spin-dependent coupling cases, as a function of WIMP mass. Figure is taken from (65).

for most of the WIMP masses. An example of the capture rates from both scatterings are shown in Fig. 2.2.

For the spin-independent coupling case, the contributions come from several elements. In the case of heavy elements with A$\gg$1 such as iron, besides coherent enhancement $\propto$A^2, the mass-matching factor becomes approximately $\propto$A^2, resulting in the capture rate being boosted $\propto$A^4. Therefore, despite being the fifth most abundant element, iron could capture the WIMPs most efficiently. However, because of the form-factor suppression, the capture from scattering off iron can be suppressed by several orders of magnitude for WIMPs with mass of several hundred GeV (42). Therefore the capture of heavy WIMPs through spin-independent coupling is dominated by scattering off oxygen (82). Figure 2.3 visualises the capture rates from several elements for spin-independent coupling WIMPs.

2.3 WIMP thermalization inside the Sun

Once captured, WIMPs bound in the gravitational potential well of the Sun will experience further rescatterings by solar nuclei through which they could lose more energy. As they lose energy, they can move to smaller orbits and finally settle at a dense core of the Sun and thermalize. The thermalization time depends on the WIMP-nucleon cross section which governs the rescattering rate. It also depends on the WIMP mass, as the mass governs the number of scatters required for the WIMP to be completely embedded in the Sun (86). Once they are embedded in the solar radius, they will quickly reach thermal equilibrium with the solar medium. Figure 2.4 shows the mass dependence of the number of scatters required to bring the WIMP orbit within the two times solar radius, calculated by A. Peter (86).

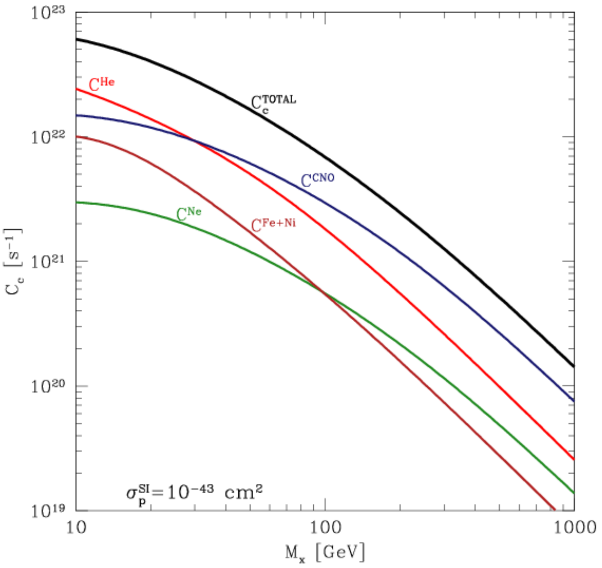

Figure 2.3: Capture rate of WIMPs in the Sun with assumed interaction strength of $\sigma_{SI} = 10^{-43}\text{cm}^2$. The total capture rate (C_{total}) and the contribution from several most important elements are shown together, as a function of WIMP mass: He (C_{He}), the sum of C, O and N (C_{CNO}), the sum of Fe and Ni (C_{Fe+Ni}), and Ne (C_{Ne}). Figure is taken from (85).

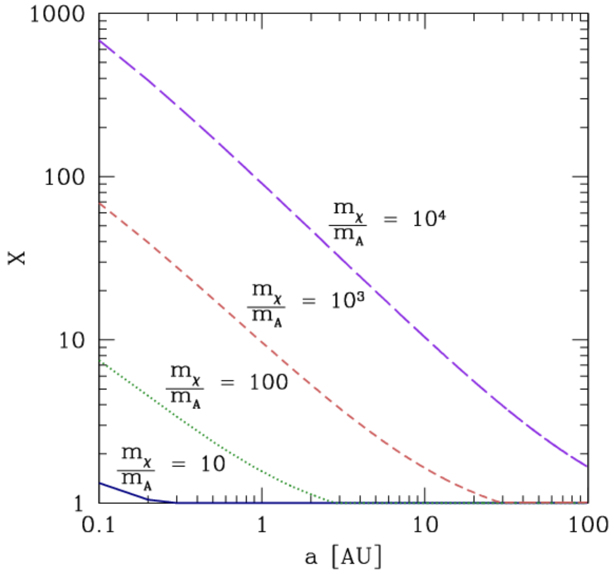

Figure 2.4: The number of scatters X, required to bring a WIMP orbiting with a semi-major axis a after first scattering down to orbiting with $a_f = 2R_\odot$, as a function of the WIMP-nucleus mass ratio m_χ/m_A. Figure is taken from (86).

Considering those effects, the estimated lower limit on the elastic scattering cross section for which the median thermalization time of captured WIMPs is less than the age of the solar system is calculated (86). In the spin-dependent (spin-independent) scattering case, the thermalization time exceeds the age of the solar system if σ_{SD} (σ_{SI}) $< 10^{-48}$ cm^2 (10^{-51} cm^2) for $m_\chi = 100$ GeV. These limits are low enough compared to the expected sensitivity of indirect detection with existing neutrino detectors, so it is safe to assume that WIMPs "instantly" achieve thermal equilibrium with solar medium.

The WIMPs that are in thermal equilibrium will spatial distribution described by the global temperature and the local gravitational potential. At the radial distance from the center of the Sun r, the equilibrium number density, $n_e(r)$ will be described as:

$$n_e(r) = n_0 e^{-m_\chi \Phi(r)/k_B T}, \tag{2.8}$$

where n_0 is a normalization factor, m_χ is the WIMP mass, $\Phi(r)$ is the gravitational potential of the Sun, i.e. $\int_0^r drGM(r)/r^2$, k_B is the Bolzmann factor and T is the temperature to which WIMPs are thermalized. Typically the temperature of the WIMPs are assumed to be constant at the temperature at the center of the Sun, $T_\odot$.

Assuming that the density of highly condensed ordinary matter within a sphere of radius r is constant and equal to the central density, $\rho_\odot$ for simplicity, then with the gravitational potential $\Phi(r) = 2\pi G\rho r^2/3$ with Newton's constant G, one can find that the WIMPs are concentrated in the center of the Sun with the typical radius of r_χ, as (87):

$$n_\chi(r) = n_0 e^{-r^2/r_\chi^2}, \text{with} \tag{2.9}$$

$$r_\chi = (\frac{3T_\odot}{2\pi G\rho_\odot m_\chi})^{1/2} \sim 0.01 R_\odot \sqrt{\frac{100GeV}{m_\chi}}. \tag{2.10}$$

The thermalized WIMPs are predicted to distribute within 1% of the radius of the Sun. Thus it is safe to assume that the annihilations of WIMPs happen at the center of the Sun.

WIMPs can eventually be accumulated in the center of the Sun in this fashion and be ready to annihilate. The WIMP annihilation rate is proportional to N^2 as a pair of WIMP annihilate together. Also it is proportional to the thermally averaged annihilation cross section $< \sigma v >$. The annihilation rate is described as:

$$\Gamma_A = \frac{1}{2} C_A N^2 \tag{2.11}$$

where

$$C_A = \frac{1}{N^2} \int 4\pi r^2 dr n_e^2(r) < \sigma v > \tag{2.12}$$

with N being the total number of WIMPs.

Using the equations 2.9 and 2.10, C_A is calculated as a function of $< \sigma v >$, WIMP mass and the density and the temperature of the solar core (87):

$$C_A =< \sigma v > (\frac{G m_\chi \rho_\odot}{3 T_\odot})^{3/2}, \tag{2.13}$$

with the solar core density $\rho_\odot$ of about 151 g/cm^3 and the solar core temperature $T_\odot$ of about 15.5 E^6 K around the center of the Sun.

2.4 WIMP density evolution inside the Sun and the equilibrium condition

Considering capture and annihilation described above together, the evolution of the total number of WIMPs in the Sun, N, can be described by the following differential equation

$$\frac{dN}{dt} = C_C - C_A N^2 - C_E N, \tag{2.14}$$

where C_C is the capture rate, C_A is linked to the annihilation rate Γ_A as described in the previous chapter, and C_E is the evaporation rate. WIMPs could also become unbound from the Sun in scatters, in a process known as 'evaporation'. The evaporation process is not considered and the discussion on it will be given in Chap. 8.

Neglecting the evaporation effect, the equation can be solved and the current annihilation rate can be written as

$$\Gamma_A = \frac{C_C}{2} \tanh^2(t_\odot/\tau), \tag{2.15}$$

where $t_\odot$ is the age of the Sun, τ is $(C_C C_A)^{-1/2}$. In the literature, τ is often regarded as "equilibrium time" because when $t_\odot \gg \tau$, or when equilibrium between capture and annihilation has been achieved, the time dependence of the annihilation rate will be removed as:

$$\Gamma_{\mathrm{A}}^{\mathrm{equi}} = \frac{1}{2} C_C \tag{2.16}$$

and the capture rate, C_{C}, regulates the annihilation rate, $\Gamma_{\mathrm{A}}^{\mathrm{equi}}$. Some discussion about the equilibrium condition will be given in Chap. 8.

2.5 Production of neutrinos inside the Sun

The captured WIMPs in the core of the Sun can self-annihilate in a pair and create the Standard Model particles. By hadronization and decays of the annihilation products, neutrinos and anti-neutrinos can be produced as final products and escape the Sun, then be detected by the detectors on the Earth.

The three-flavor neutrino and anti-neutrino fluxes at production in the core of the Sun are shown in Fig. 2.5. For the $b\bar{b}$ channel, WIMPs hadronize and produce B mesons, which interact in the solar medium before decay. This channel is considered to represent the “softest” spectrum among the channels considered in this and other typical analyses. For the W^+W^- channel, the high-energy and the low-energy peaks correspond to the prompt decay of the W boson and decay products of hadrons, respectively. For larger WIMP masses, i.e. for larger boosts of the primary W, this feature is smeared into a smooth spectrum as seen in Fig. 2.6. The $\tau^+\tau^-$ channel produces far more tau neutrinos than electron neutrinos and muon neutrinos. Annihilation to $\nu\bar{\nu}$ pair is helicity-suppressed for Majorana particle (39) whereas it is not the case for general dark matter candidates such as those found in extra dimension scenarios. This channel is not studied in this analysis, therefore the $\tau^+\tau^-$ channel represents the most energetic (“hardest”) spectrum. The figures are generated using WIMPsim (88) and more plots of the neutrino fluxes from WIMP annihilation at various distances can be found in (89).

The propagation of the neutrinos experiences both vacuum and matter oscillations with three-flavor mixing. Also neutrino interactions in the solar medium are considered. A charged current (CC) interaction would reduce the amount of the flux, and a neutral current (NC) interaction will reduce the energy of the neutrino. When a muon or electron (anti-) neutrino interacts through charged current, produced electrons are stable and muons are stopped before decay. But when a tau neutrino interacts, the produced tau lepton can decay and produce secondary neutrinos which can propagate to the detector. Figure 2.7 shows the three flavor neutrino and anti-neutrino fluxes at the surface of the Sun.

After passing through the Sun, neutrinos propagate in the vacuum as it is oscillating. The electron neutrinos, which remained almost without mixing throughout the solar medium with high electron number density, now is efficiently mixed with the muon and tau neutrinos. As a result all three flavors of neutrino and anti-neutrinos end up having similar spectrum at 1AU. Figure 2.8 shows the three flavor neutrino and anti-neutrino fluxes at 1AU.

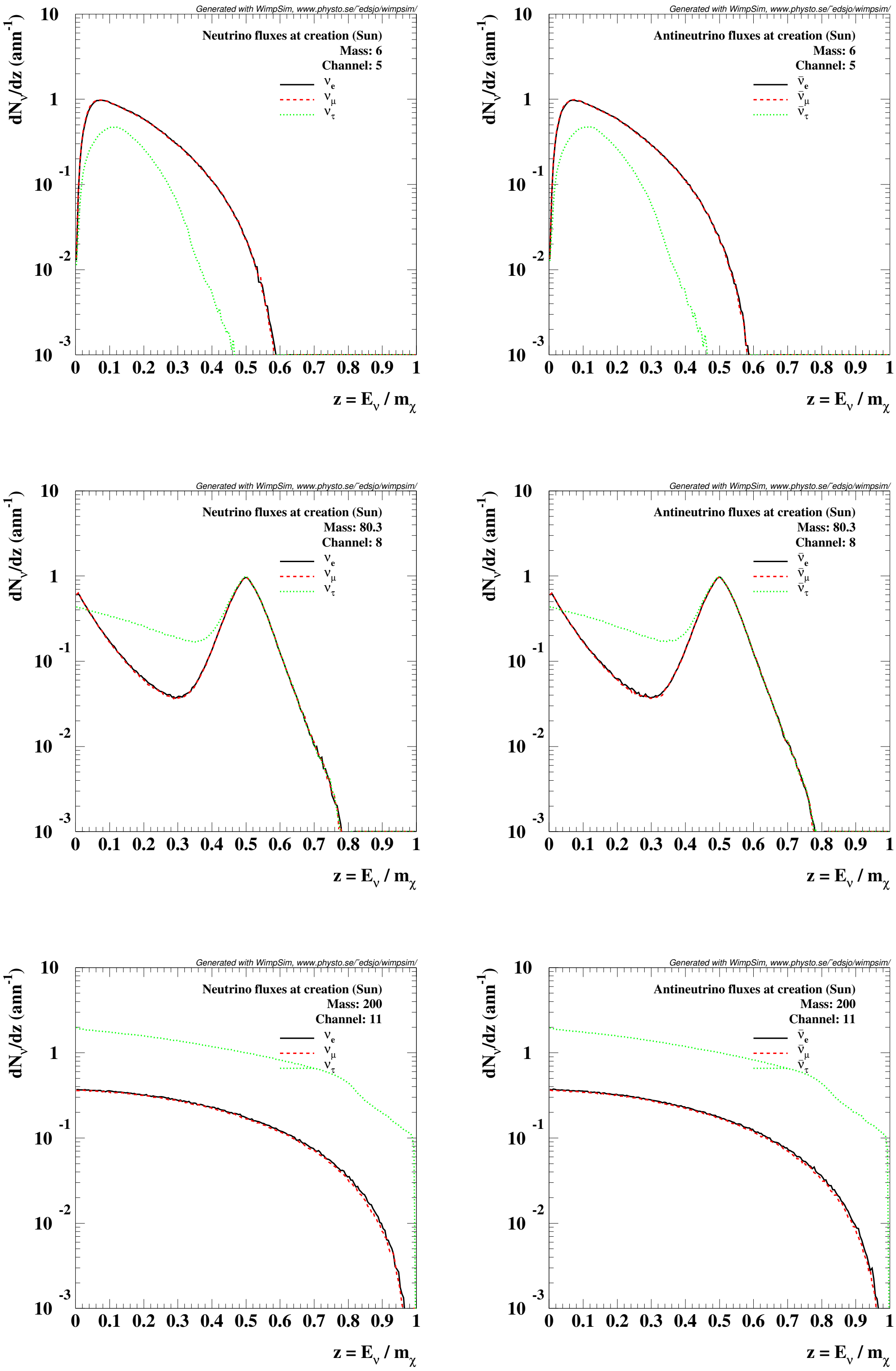

Figure 2.5: The WIMP-induced neutrino fluxes at the production at the center of the Sun for $m_\chi = 6$ GeV $b\bar{b}$ channel, 80.3 GeV W^+W^- channel, and 200 GeV $\tau^+\tau^-$ channel. Fluxes are shown as a function of neutrino energy normalized to WIMP mass (z) for neutrino (left column) and anti-neutrino fluxes (right column).

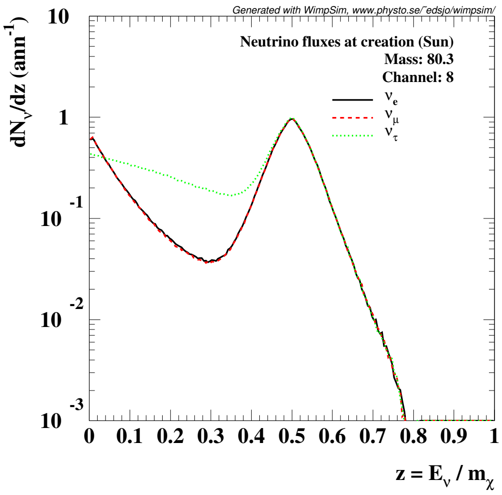

Figure 2.6: The WIMP-induced left-handed neutrino fluxes at the production at the center of the Sun for W^+W^- channel for $m_\chi = 80.3$ GeV (left) and $m_\chi = 100$ GeV (right) are compared. The flux is shown as a function of neutrino energy normalized to WIMP mass (z).

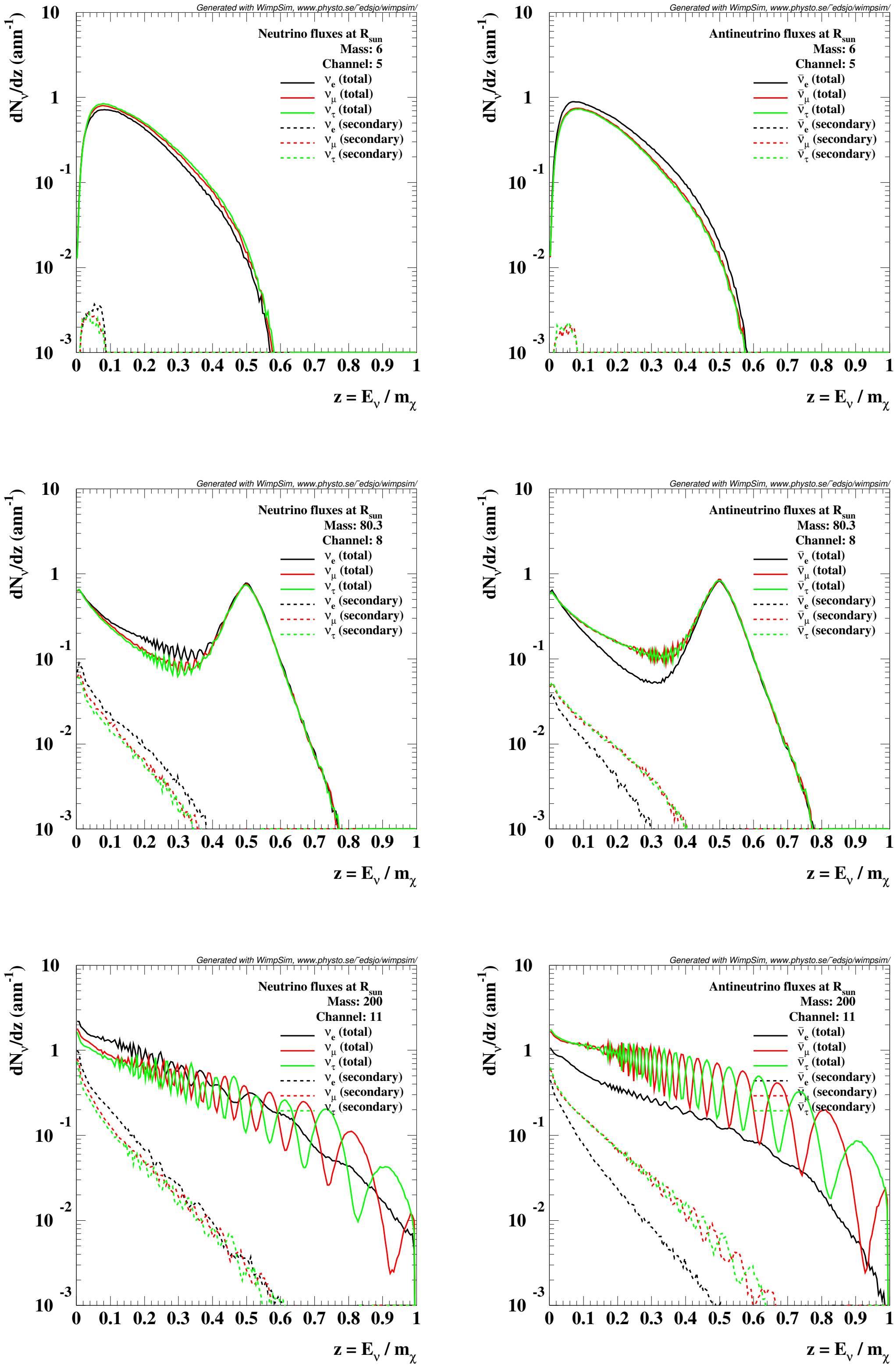

Figure 2.7: The WIMP-induced neutrino fluxes at the surface of the Sun for m_χ = 6 GeV $b\bar{b}$ channel, 80.3 GeV W^+W^- channel, and 200 GeV $\tau^+\tau^-$ channel. The flux is shown as a function of neutrino energy normalized to WIMP mass (z) for neutrino (left column) and anti-neutrino flux (right column). Three-flavor oscillation with parameters: $\theta_{12} = 33.461°, \theta_{13} = 9.097°, \theta_{23} = 40.686°, \delta = 300, \Delta m^2_{21} = 0.766 \times 10^{-4}$ eV^2, $\Delta m^2_{32} = 0.274 \times 10^{-2}$ eV^2 are used assuming normal mass hierarchy.

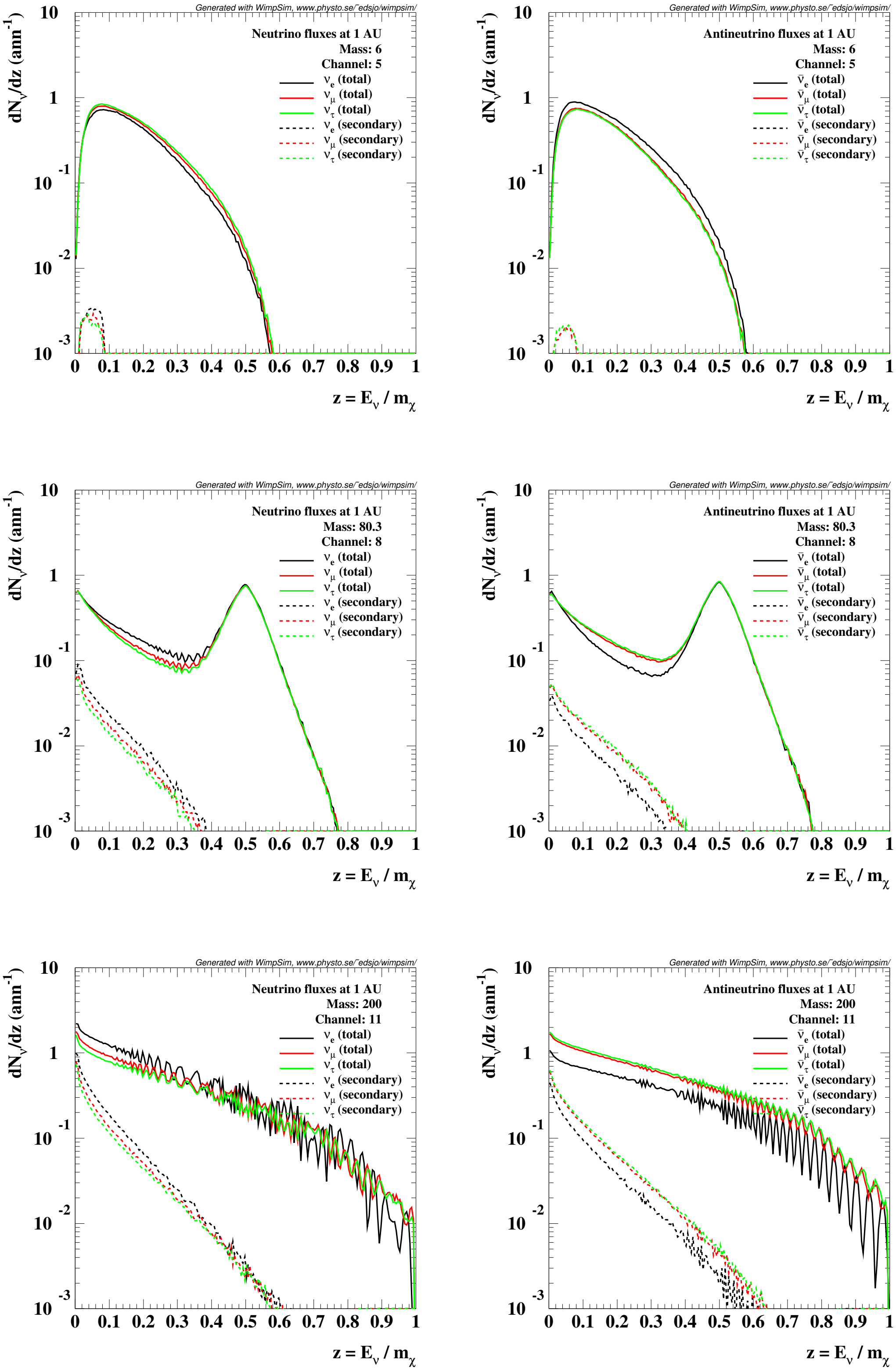

Figure 2.8: The WIMP-induced neutrinos flux at 1AU for m_χ = 6 GeV $b\bar{b}$ channel, 80.3 GeV W^+W^- channel, and 200 GeV $\tau^+\tau^-$ channel. The flux is shown as a function of neutrino energy normalized to WIMP mass (z) for neutrino (left column) and anti-neutrino flux (right column). Three-flavor oscillation with parameters: $\theta_{12} = 33.461°, \theta_{13} = 9.097°, \theta_{23} = 40.686°, \delta = 300, \Delta m^2_{21} = 0.766 \times 10^{-4}$ eV^2, $\Delta m^2_{32} = 0.274 \times 10^{-2}$ eV^2 are used assuming normal mass hierarchy.

2.6 Utilization of DarkSUSY

DarkSUSY (83) is a simulator written in Fortran language which can be utilized for calculations of expected WIMP signal in direct detections and indirect detections of various annihilation products such as gamma rays, antimatter, solar and Earth neutrinos, and so on. DarkSUSY version 5.0.6 is used for this work. It is a voluminous program, but for the use in solar WIMP neutrino detection, the functionalities that DarkSUSY provides can be categorized as follows:

1. Scans parameter space of SUSY scenarios and predict WIMP candidate properties
2. For a given WIMP model, calculates the capture rate
3. Calculates the annihilation rate accordingly
4. For a determined annihilation rate, read WIMPsim output files and delivers the neutrino flux to the user.

Here is a brief sketch of the usage of the DarkSUSY in this work for each process.

1) In DarkSUSY, we can define the model space that we want to scan by setting ranges of SUSY parameters directly, and indirectly introducing bounds from recent accelerators and CMB measurements. For this analysis, we set the rough range of SUSY parameters for CMSSM and released the other constraints as much as possible. When one runs DarkSUSY in 'random model mode', DarkSUSY will automatically scan possible WIMP scenarios which are randomly chosen within the model space we set. We ran it for about 5,000,000 scenarios first, and among the results we collected the models which have WIMP masses close to our region of interest (4, 6, ... GeV). For the selected models, we made the 'mode' files which are a summary of SUSY parameters for each WIMP hypothesis.

2) The next step is running DarkSUSY in 'read model mode' for each WIMP hypothesis. In running in the read model mode, according to the SUSY parameters read from mode file, DarkSUSY analytically calculates the capture rate as described in the previous chapter. We let DarkSUSY calculate the capture rate for spin-dependent coupling WIMPs and spin-independent coupling WIMPs separately. In calculation of the capture rate for SD coupling WIMP, SI scattering inside the Sun is ignored by setting it to be zero, and vice versa. With setting the local dark matter density, the velocity distribution of dark matter in the halo and other nominal parameters, DarkSUSY allows the precise calculation of the capture rate for a selected WIMP mass and scattering cross section. For inputting the velocity distribution of dark matter, both analytic equations and numerical tables can be used.

3) DarkSUSY also decides how many annihilations are allowed to happen for the scenario. In this analysis, to achieve equilibrium for any chosen model, we manipulated the age of the Sun to be very old. In this way, the model-dependent annihilation rate calculated by DarkSUSY is ignored and the result is equivalent to solving Eq. 2.16.

4) If we don't choose a particular annihilation channel, DarkSUSY will run for multiple channels with branching ratio decided by the set of SUSY parameters in the mode file. Otherwise, it can force the annihilation into a specified channel. We used this function to run DarkSUSY for a single channel.

We can also feed the type of yield of interest, which are differential neutrino/anti-neutrino fluxes in this analysis. Then DarkSUSY reads the selected type of yield from the tabulated output of WIMPsim, and interpolates or extrapolates the flux and magnifies it by the ratio between the calculated annihilation rate and the WIMPsim nominal annihilation rate. After that, DarkSUSY adjusts it in the finer format that user specified; it applies the energy threshold, cuts the angular size from the Sun and chooses the flavor. In this analysis, the energy threshold is set to be zero. Also the angular size of the flux is turned off as the source is regarded to be point-like. In summary, the resultant neutrino flux we get from DarkSUSY is the neutrino flux whose differential spectrum and flavor ratio are calculated by WIMPsim, and for which the absolute normalization is calculated by DarkSUSY for a certain mass and scattering cross section.

In summary, we get a neutrino flux corresponding to a certain WIMP mass, annihilation channel and WIMP-nucleus scattering cross section $\sigma_0^{SD/SI}$ using DarkSUSY.

Chapter 3

The velocity distribution and the capture rate of WIMPs

3.1 Overview

Under the assumption of equilibrium between the capture rate and the annihilation rate, the uncertainty on the annihilation is directly given by the uncertainty on the WIMP capture in the Sun. This capture mechanism is theoretically well understood so that we can study the impacts of the various effects that contribute to its uncertainty and is the subject of this chapter.

In this chapter, we will give a comprehensive and general treatment of uncertainties from the dark matter velocity distribution in indirect solar WIMP search. We will discuss the general response of solar WIMP search to the change of the velocity distribution which will be helpful to understand the effect on capture rate from individual source of uncertainties. The uncertainties will be quantified and given as a function of WIMP mass, making it easy to incorporate in future experimental and theoretical works. We study the effect of the velocity distribution of dark matter on capture rate in the Sun considering four sources of uncertainties: circular speed of the Sun, galactic escape speed of dark matter, departures from a Maxwellian distribution and existence of the dark disc.

In chapter 3.2 we show how solar WIMP search responds to the velocity distribution in comparison to direct detection. In Chap. 3.3, we introduce the velocity distributions of dark matter halo, for which we discuss the impact on the capture rate in Chap. 3.4. In the final chapter 3.5, we conclude and summarise the chapter.

3.2 Uncorrelated and anti-correlated uncertainties in direct and indirect detections

The local velocity distribution of dark matter impacts on direct and indirect searches very differently. First, WIMPs in the Sun have been accumulating over a very long time period. Even though there is no evidence for very large density fluctuations or changes in the velocity distribution, we point out that direct detection rates are only sensitive to the present local dark matter density and velocity distribution, while indirect solar WIMP search rates are a result of the dark matter halo density and velocity distribution that has been sampled by the Sun over the equilibration time scale. Hence, indirect detection rates are related to the average dark matter density and velocity distribution at the solar orbit.

Secondly, as opposed to direct detections looking for energetic scattering of WIMPs, the less energetic ones are easier to be captured by the Sun. Thus direct detections are sensitive to WIMPs with higher velocity, by contrast, indirect detections are sensitive to the lower part of the velocity distribution. This contrast in the responses of direct and indirect detections to the velocity distribution will manifest in anti-correlated size and sign of the uncertainties; i.e. whereas the direct detection event rate is largely affected by any source of uncertainty, the size of the effect on capture rates can be marginal; or whereas direct detection event rate is boosted, the capture rate can be reduced, and so on.

The maximum velocity of a WIMP to be captured by nucleus i at distance r from the centre of the Sun is given when q_{min} (Eq. 2.4) equals to q_{max} (Eq. 2.5), where

$$u_{max}(i) = \sqrt{\beta_-} u_{esc}(r). \tag{3.1}$$

The escape velocity at the surface of the Sun is $\sim$ 618 km/s. In the case of $\sqrt{\beta_-} \sim 1$, $u_{max}(i)$ is large enough compared to the mean velocity of the WIMPs in the galactic halo being $\sim$ 300 km/s, so to allow an efficient capture process. However, when the mass-matching between the WIMP and the nucleus fails then β_- becomes smaller than 1, the capture of high-velocity WIMPs will be suppressed.

To estimate u_{max} for the total capture rate, we have to consider contributions from multiple elements with their radial distribution inside the Sun. Figures 3.1 and 3.2 visualise the relative capture rate for several WIMP masses as a function of the dark matter velocity in the local reference frame at the Sun, whereas the Sun rotates around the galactic center with $v_\odot = 220$ km/s, and in the Galactic frame which is defined such that the plane of our Galaxy has a latitude of zero, respectively. Capture rates are calculated using delta function for VDF and are relatively normalised to the highest capture rate for the mass. Because the capture in the Sun is dominated by the most abundant hydrogen and other light elements, for the light WIMPs good mass-matching will allow the capture to be efficient up until the high-velocity tail, where for heavy WIMPs it starts losing its efficiency in the lower-velocity region. Compared to capture by SD interactions, capture by SI interaction keeps high efficiency longer until ~50 GeV, which is the 'resonance range' (82; 42), helped by mass-matching scatterings with heavier elements such as He, O, Si and Fe.

Meanwhile, the u_{min}, the minimum velocity detectable in direct detections, is determined when the maximal recoil energy $q_{\max} = \beta_+ \frac{1}{2} m_\chi u^2$ is the same as the energy

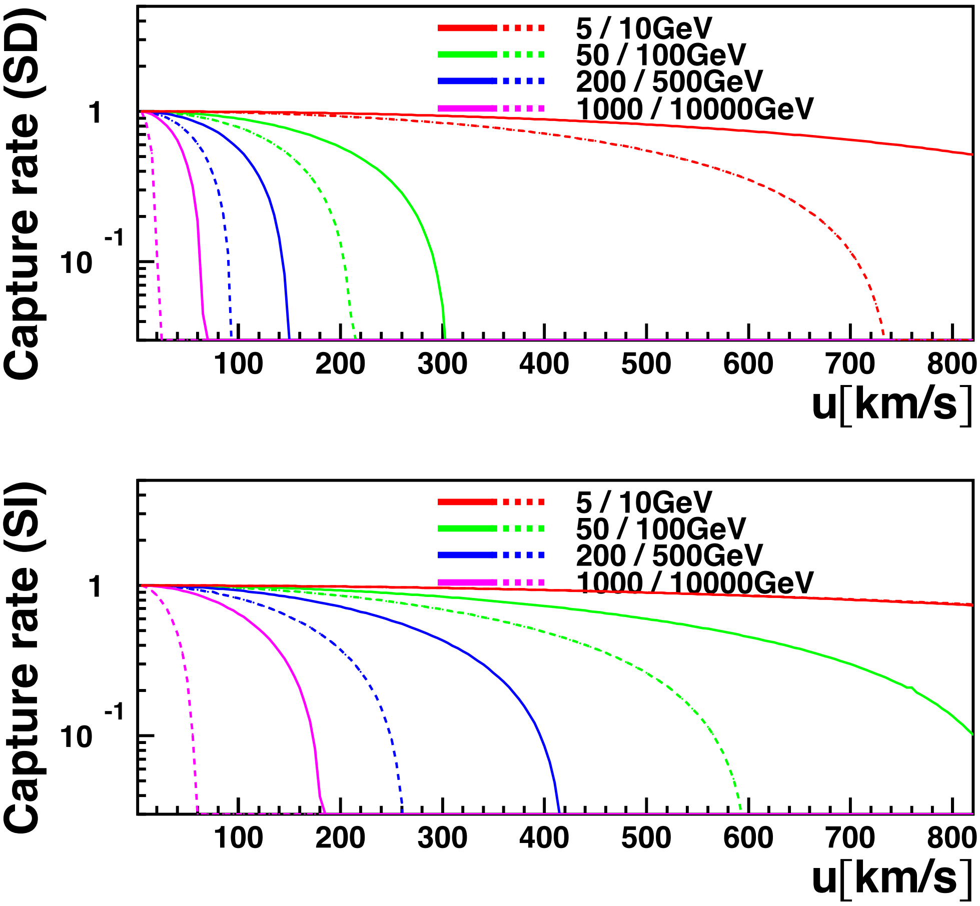

Figure 3.1: The capture rate for sample WIMP masses as a function of the relative velocity to the Sun. The rates are normalised to the rate when $u = 0$. We show the SD case (top) compared to the SI case (bottom) for eight sample masses of 5 (red solid) / 10GeV (red dashed), 50 (green solid) / 100GeV (green dashed), 200 (blue solid) / 500GeV (blue dashed), 1000 (magenta solid) /10000 GeV (magenta dashed).

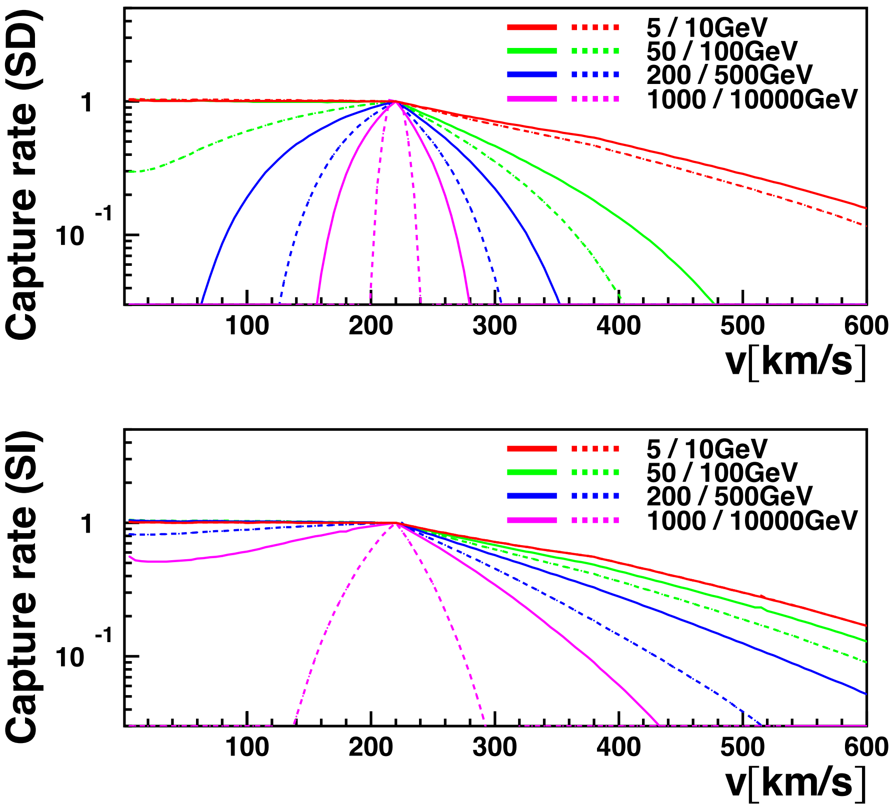

Figure 3.2: The capture rate for various WIMP mass as a function of the velocity in the galactic frame is given relative to the capture rate for $v = 220$ km/s. We show the SD case (top) compared to the SI case (bottom) for eight sample masses of 5 (red solid) / 10GeV (red dashed), 50 (green solid) / 100GeV (green dashed), 200 (blue solid) / 500GeV (blue dashed), 1000 (magenta solid) /10000 GeV (magenta dashed).

threshold for the detector, E_{th},

$$u_{min} = \sqrt{\frac{2E_{th}}{\beta_+ m_\chi}}. \tag{3.2}$$

Below u_{max} and above u_{min}, the capture efficiency or detection efficiency are not 100% because typically WIMPs cannot transfer q_{max} to nucleus. As a result, indirect detection will more efficiently capture WIMPs at low-velocity, while direct detections will have strong favor to the high-velocity region. Helped by Fig. 3.1 to estimate u_{max}, and keeping in mind that u_{min} is dependent on the energy threshold and nuclear used in individual direct detectors, we will follow the simple notation of 'high-velocity' and 'low-velocity' hereafter.

Figure 3.1 shows that the heavier the WIMP is, the smaller u_{max} will be due to mass-matching with light nuclei inside the Sun. In the calculation of u_{min}, there is an additional m_χ besides the mass-matching factor in the denominator of Eq. 3.2, therefore for a type of direct detection experiments, the u_{min} for heavier WIMPs will be smaller until $m_\chi \gg m_N$.

Taking the above into account; light WIMP direct detection is sensitive to high-velocity tail, while light WIMP capture comes from wide range of VDF (starting from the low-velocity tail). In contrast, heavy WIMP indirect detection can only see the low-velocity part of the VDF, while direct detection for heavy WIMPs can see a wide range (starting from the high-velocity tail). Be aware that u_{min} and u_{max} are defined in different ways, so the regions to which direct and indirect detection are sensitive are not always separated. For example, for a liquid Xe detector with an energy threshold of 10 keV, the typical u_{min} required to produce a nuclear recoil is of the order of $\sim$300 km/s for 100 GeV WIMPs, while in indirect detection for 400 km/s WIMPs are still possible to be captured with spin independent coupling.

The contrasts in the responses of direct and indirect detections to VDF would manifest clearly when the uncertainty only affects the high or the low velocity tail. In this case, when either indirect detection or direct detection is strongly affected by an uncertainty in VDF, the other detection method would possibly be blind to the change or affected to a minor degree. As a result, the effects of the uncertainties in both detection methods might be uncorrelated. It is also interesting to interpret some type of uncertainties as a 'shift of WIMP population from one (low or high) region to another', which makes the changes in low and high velocity regions anti-correlated. Because of the contrasts in the responses of direct and indirect detections to the velocity distribution, the sign of the effect in direct and indirect detections might be anti-correlated; i.e. whereas capture rate will be decreased, direct detection event rate will be increased (76). With the situations above, we will be able to interpret the response of capture rates to the uncertainties in velocity distribution which will be discussed in following chapters.

3.3 The dark matter velocity distribution

In this section we survey the dark matter velocity distribution in the galactic dark matter halo. We introduce VDFs obtained from various simulations. We also shortly discuss about the dark disc. These VDFs are later used as benchmark scenarios for which we compute capture rates of WIMPs in the Sun.

The SHM serves as a useful benchmark model, but recent cold dark matter N-body simulations indicate the significant deviation of the VDF of dark matter halos from the SHM (90; 34; 91; 92). We choose three benchmark VDFs from recent works as shown in the left plot of Fig. 3.3 and show them in the local reference frame at the Sun as shown in the right plot of Fig. 3.3. VDFs in the local reference frame at the Sun are shown in the form of $f(u)/u$ as this term is inserted in the capture rate as shown in Eq. 2.1.

Our benchmark distributions are taken from three recent N-body hydrodynamical simulations: the Aquarius (93) project; an N-body simulation with Baryons (34) carried with the cosmological Adaptive Mesh Refinement (AMR) code RAMSES (94); the Rhapsody cluster re-simulation project (95).

Name & Reference	Description of simulation	Description of VDF	Source
Vogelsberger et al. (90)	Largest dark matter only simulation of a Milky Way-sized dark matter halo	Median of the velocity modulus distributions for 2 kpc boxes centred between 7 and 9 kpc from the galactic centre, with a broad bump at $v \simeq 250$ km/s	Fig.2
Ling et al. (34)	A Milky Way-sized galaxy from high-resolution N-body simulation with baryons	Velocity modulus in a spherical shell $7 < R < 9$ kpc around the galactic centre, with platykurtic shape (K = 2.39) and high velocity dispersion (v_0 = 267.2 km/s)	Fig.4(d)
Mao et al. (92)	Cluster re-simulation project	Stacked velocity distribution for 96 halos at $r/r_s = 0.15$, peaks at low-velocity	Fig.1

Table 3.1: The sources and descriptions of the benchmark VDFs used in this chapter are summarised.

The green line in Fig. 3.3 shows the VDF from the result of Aquarius project, taken from Fig.2 in Vogelsberger et al. (90). It shows the median of the velocity modulus

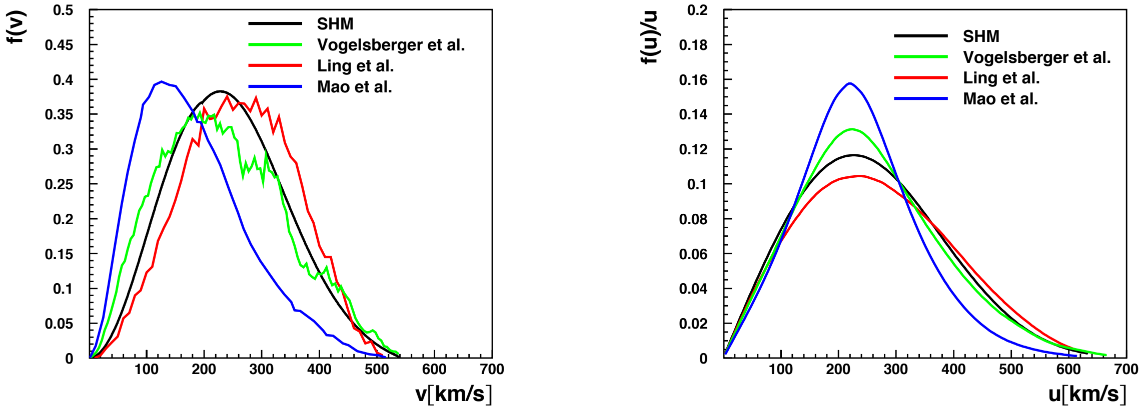

Figure 3.3: The VDFs of dark matter halo from simulations are shown together with the standard Maxwellian halo (SHM). Left panel shows the normalised VDF $f(v)$s in the galactic frame and right panel shows the VDFs in the local reference frame at the Sun in the form of $f(u)/u$ in eq. 2.1. Detailed descriptions for Vogelsberger et al. (90) (green), Ling et al. (34) (red), Mao et al. (92) (blue) simulated halos are given in the text.

distributions for 2 kpc boxes centred between 7 and 9 kpc from the centre of simulated halo, Aq-A-1 (93). The broad bump above 250 km/s originates from bumps in each single box at approximately the same velocity, with similar amplitude. They found that these features appear in all six of simulated halos, which suggests that they do not reflect local structures but rather a global property of the inner halo, possibly a consequence of real dynamical structure. We take this VDF as a representative VDF with bumpy structures.

The velocity modulus in a spherical shell $7 < R < 9$ kpc around the galactic center shown in Fig.4(d) of Ling et al. (34) is taken in the red line in Fig. 3.3. The VDF is platykurtic, i.e. fatter than a Gaussian distribution with the same standard deviation. Equilibrated self-gravitating collisionless structures can be described by non-extensive statistical mechanics, which gives theoretical support to the use of the Tsallis distribution for describing gravitational structures such as galactic halos (26). For the particles in this shell they showed the VDF is indeed well fit by the Tsallis distribution and the best fit kurtosis parameter K = 2.44 agrees well with the observational value K = 2.39. This agreement is better than the one from the best-fit generalised Maxwellian, which is K = 2.71. The best-fit Tsallis distribution gives the velocity dispersion parameter $v_0 = 267.2$ km/s. This VDF will serve as a representative of a realistic description of a galaxy, considering interactions between the baryonic and the dark components.

The third benchmark velocity distribution is taken from Fig.1 of Mao et al. (92), which is the stacked VDF for ninety-six halos from the Rhapsody simulations (95). They argue that the largest current theoretical uncertainty in the VDF arises from the unknown radial position of the solar system relative to the dark matter halo scale radius, r/r_s. In the range of current observations ((92) and its references) r/r_s is

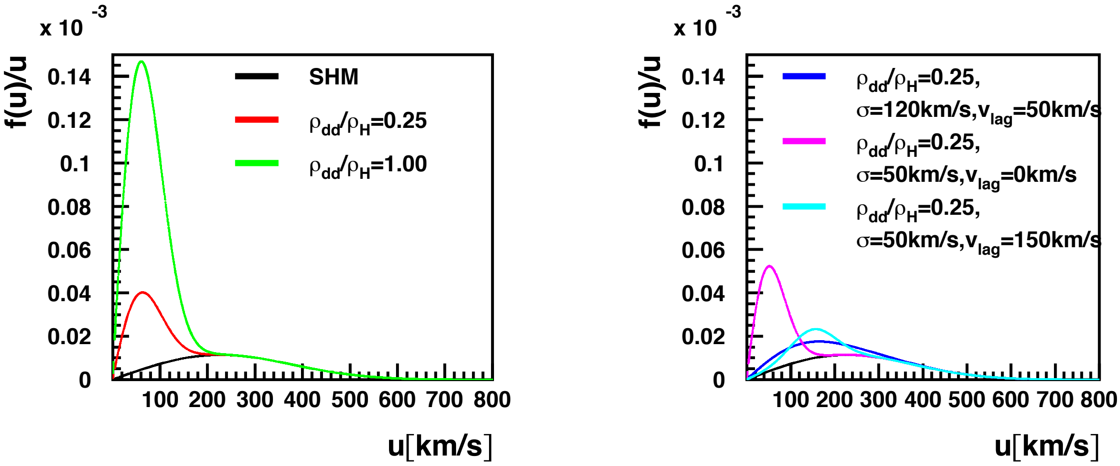

Figure 3.4: The dark disc velocity distributions added to dark matter halo in the local reference frame at the Sun are shown in the form of $f(u)/u$. red: with $\rho_{dd}/\rho_H = 0.25$, $\sigma = 50$ km/s, $v_{lag} = 50$ km/s, green: $\rho_{dd}/\rho_H = 1$, blue: $\sigma = 120$ km/s, magenta: $v_{lag} = 0$ km/s, cyan: $v_{lag} = 150$ km/s. Unless otherwise specified in the legend, parameters are fixed to $\rho_{dd}/\rho_H = 0.25$, $\sigma = 50$ km/s, $v_{lag} = 50$ km/s and $\rho_H = 0.3$ GeV/cm^3. Note that the total dark matter density is increased to $\rho_{dd} + \rho_H$. The SHM with no dark disc is shown for comparison (black).

suggested to be within $0.15 \sim 6$. Here we picked the marginal value of $r/r_s = 0.15$. This halo will represent the halo model peaking at low-velocity.

Descriptions of our benchmark VDFs are summarised in Tab. 3.1. Note that VDFs are regarded to be isotropic throughout our discussion to simplify the argument.

Simulations show that the local density of the dark disc ρ_{dd} could range from a few percent (38) up to ~ 1.5 times (36) of the local dark matter halo, ρ_H. We consider scenarios with the mild dark disc (ρ_{dd}=$0.25\rho_H$) and the strong dark disc ($\rho_{dd} = \rho_H$) assuming Maxwellian VDF with fiducial parameters for VDF; $v_{rms} = 50\sqrt{3}$ km/s and the relative circular velocity to the Sun, $v_{lag} = 50$ km/s following (96) and (75). However, the VDF of the dark disc also contains large uncertainties. The velocity dispersion is likely to be substantially larger (37) and more realistic values can be provided by full cosmological hydrodynamics simulations (75). The uncertainty of v_{lag} is discussed in (36). In order to test properties of the dark disc velocity distribution, we varied v_{rms} to $120\sqrt{3}$ km/s, and v_{lag} to 0 and to 150 km/s fixing the density to $\rho_{dd} = 0.25\rho_H$. Figure 3.4 shows the distributions of combined dark matter halo and dark disc in the local reference frame at the Sun. Note that for the dark matter halo we fix the total local density to the standard value $\rho_H = 0.3$ GeV/cm^3 and allow the additional contribution from the dark disc.

3.4 The effect of WIMP velocity distribution to the capture rate of WIMPs

In this section we discuss uncertainties associated with WIMP capture in the Sun. We evaluate the impact of the local circular speed of the Sun, the halo escape speed, various VDFs for the dark matter halo and the dark disc introduced in the previous section on capture rate, respectively.

For our evaluation we use DarkSUSY (83) with which we can precisely compute capture rates as explained in Chap. 2. We modify VDFs parameters or introduce new VDFs in the DarkSUSY and calculate the capture rate for various WIMP masses for SD or SI coupling cases.

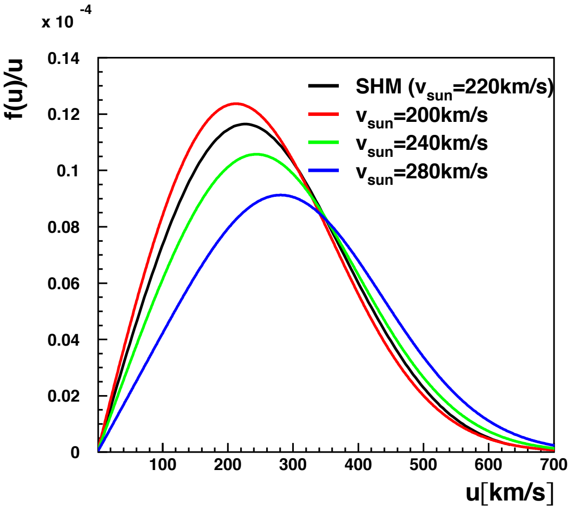

Figure 3.5: The VDFs in the local reference frame at the Sun with varied $v_\odot$ are shown together with the standard Maxwellian halo (SHM) in the form of $f(u)/u$, for $v_\odot =$ 200 km/s (red), 240 km/s (green) and 280 km/s(blue).

We first investigate how the WIMP capture rate in the Sun changes with respect to the local circular speed of the Sun $v_\odot$. We took the range 200 $\sim$ 280 km/s from McMillan et al. (97) and fixed v_{rms} to 270 km/s. In Fig. 3.5 we show the VDFs with varied $v_\odot$ in the local reference frame at the Sun and the effect on capture rate in Fig. 3.6 as a function of WIMP mass. The size of the uncertainty in capture rate can be well visualised by showing the relative change compared to the SHM with fiducial value $v_\odot = 220$ km/s. For this purpose we introduce a boost factor, which is defined by the ratio of the capture rate of the assumed velocity distribution (C) divided by the capture rate of SHM (C_{SHM}) as C/C_{SHM}. Results are separately shown for WIMPs that undergo a SD or SI interaction only as each process experiences different effective capture from the multiple nuclei inside the Sun. It appears that higher v_{rms} reduces

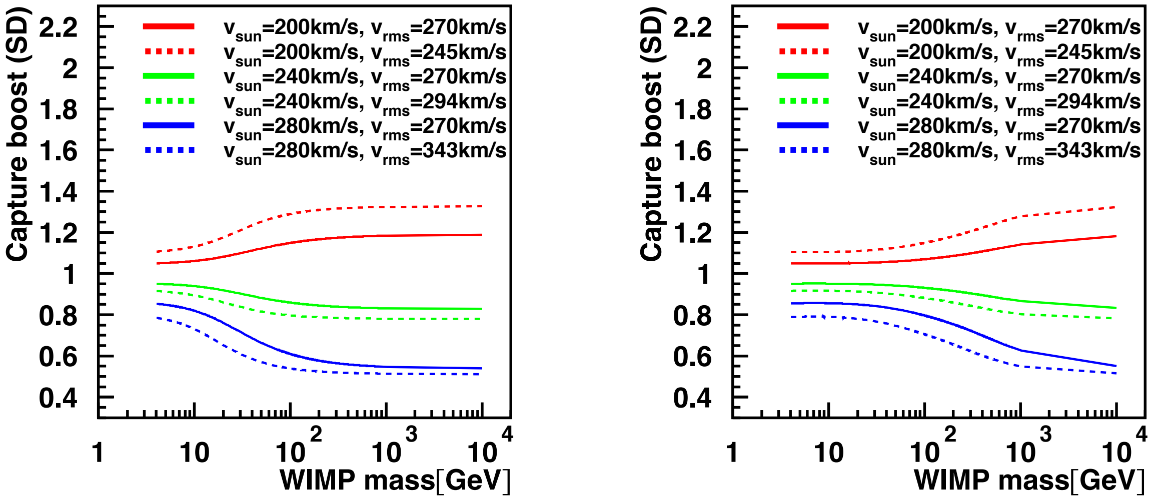

Figure 3.6: The capture boosts defined as $C/C_{\rm SHM}$ are shown as a function of WIMP mass for the SD (left) and SI (right) couplings assuming an orbital speed of the Sun of $v_\odot = 200$ km/s (red solid), 240 km/s (green solid) and 280 km/s(blue solid) with fixed $v_{rms} = 270$ km/s, dashed lines for varied $v_{rms} = \sqrt{3/2}v_\odot$ with same color scheme.

the capture rate and the size of the uncertainty appears larger for heavy WIMPs. For example, for a 20 GeV WIMP with SD (SI) coupling the capture rate changes as much as -24 % (-15 %) when $v_\odot = 280$ km/s, whereas for a 1000 GeV WIMP with SD (SI) coupling the change will be -45 % (-38 %).

This result, in agreement with previous studies (66) for SD coupling, is easily understood; the higher the relative speed between the WIMPs in the halo and the Sun, the stronger the WIMPs in the local reference frame at the Sun get boosted and become harder to be captured. This is especially true for the capture of heavy WIMPs that are sensitive to the low-velocity tail and thus experience more significant diminution. On the other hand, the shift of WIMPs to the high-velocity region will increase the signal rate in direct detection of light WIMPs (71). As a result direct and indirect detections will get opposite signs in the change, thus they are 'anti-correlated'. However, Fig. 3.5 gives us a hint that this can be reversed for the high mass region, because the capture rate and the scattering rate are calculated by integrating over $f(u)/u$ (see also (76)).

In Fig. 3.7, we show the relative changes in capture rate for the set of our benchmark velocity distributions. Several comments are in order here.

The small structures in Vogelsberger et al. (90) dark matter halo seen in the galactic frame (Fig. 3.3 right) are washed out in the local reference frame at the Sun (Fig. 3.3 left). Because the circular speed of the Sun is almost 1/3 of the size of the typical VDF of dark matter halo, we expect that any structure of the size smaller than this will be easily spread out. The SD (SI) coupling capture of 10 GeV WIMPs that come from the entire range of the VDF, including the bumpy shape above 250 km/s in Vogelsberger et

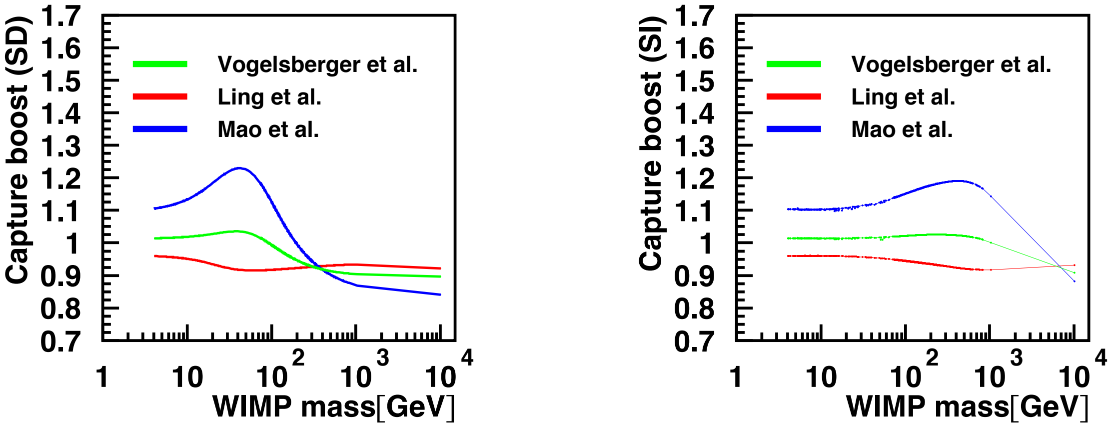

Figure 3.7: The capture boosts for SD (left), SI (right) coupling WIMPs as a function of WIMP mass for VDFs of the dark matter halo in Vogelsberger et al. (90) (green), Ling et al. (34) (red) and Mao et al. (92) (blue) compared to SHM. Detailed descriptions of VDFs can be found in Chap. 3.3.

al. (90), gives ∼2 (1)% change compared to the SHM. In the same simulation (90), they found that the contributions from either unbound streams or sub-halos are likely subdominant. For ultra-fine structures beyond the highest resolution of the current N-body simulations, it is studied to have negligible impact on direct detections (98; 99; 100). Note that the effect of these properties on the capture rate in the Sun is expected to be more suppressed because of the larger size and the longer time scale of the capture.

The transformation from the halo frame to the local reference frame at the Sun also changes the overall characteristics of VDF. Because the capture rate is not sensitive to specific changes in the structure of the VDF, we can simply interpret the overall effect as another source of anti-correlation between the low-velocity and high-velocity populations. Simply, either a high velocity dispersion or high kurtosis will result in a tendency to enrich the high-velocity region at the local reference frame of the Sun. In Fig. 3.1, we can see that for 50 (500) GeV WIMPs the SD (SI) capture process is efficient for velocities below 300 km/s. The highly peaked $f(u)/u$ in this region of Mao et al. (92) halo seen in the right plot of Fig. 3.3 brings 23 (19)% increase of SD (SI) capture rate for 50 (500) GeV WIMP and keeps more efficient capture than SHM for lighter WIMPs. As opposed to it, in Fig.6 in Mao et al.(92), the blue line shows the negative boost for our adopted halo benchmark model of Mao et al. (92) for 10 GeV above 300 km/s ($u_{min}/u_{esc} > 0.55$), which manifests the anti-correlated responses of direct and indirect detections discussed previously. We also found that Ling et al. (34) dark matter halo with broad shape and high velocity dispersion gives relatively small abundance in this velocity range, resulting in ∼8 (8)% decrease of the SD (SI) capture rate for 50 (500) GeV WIMP and keeps the negative boost for lighter WIMPs.

By investigating three characteristic halos, we conclude that the capture rate is not

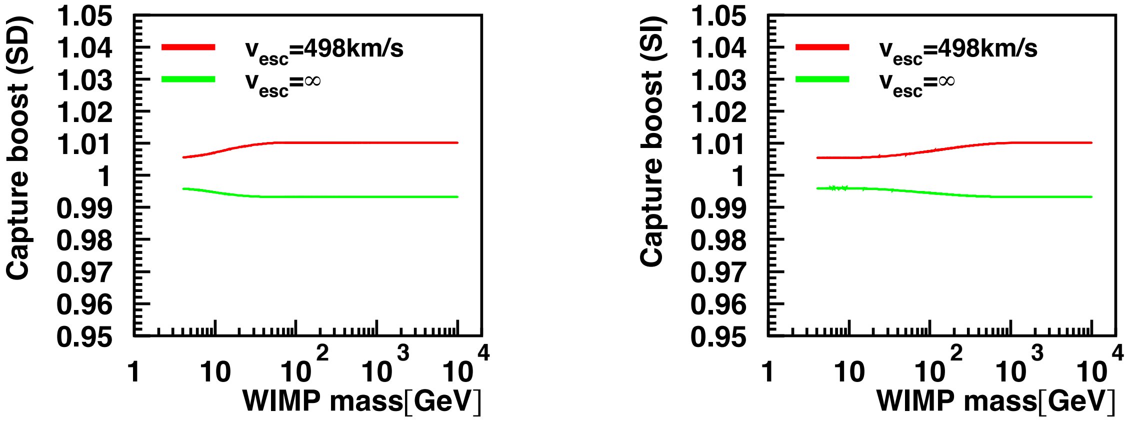

Figure 3.8: The capture boosts for SD (left), SI (right) coupling WIMPs with the escape speed of the Milky Way of red : 498 km/s, green : infinity, compared to 544 km/s in SHM as a function of WIMP mass. The normalisation of the VDFs are kept to unity for different truncations.

significantly affected by the VDF itself. This is also found to be the case in direct detections (101), generally the size of uncertainty from VDF is discussed to be within 10 $\sim$ 20% (90; 102).

Some changes in the halo models or astrophysical assumptions will give rise to an overall shift of the WIMP population from the high-velocity to the low-velocity region or vice versa. In this case, the expected change in event rates for both direct and indirect searches are rather moderate. For the orbital speed of the Sun, the uncertainty is found to be less than ~40% in this work and ~20% for various direct detector set-ups examined (76). The expected change in capture rate due to the halo VDF is found to be less than ~20% in this work and a similar magnitude is expected for direct detection experiments in general (90; 101; 76; 102). The effect is smaller for direct detection in the heavy WIMP scenarios and for indirect detection in light WIMP scenarios, as for those cases a wide range of the velocity distribution contributes. For example, even if the WIMP distribution has shifted from the low-velocity to the high-velocity region which is harder to be captured, they can still contribute to the indirect neutrino signal in a light WIMP scenario, although not in a heavy WIMP scenario. While the different response to these type of uncertainties is a limiting factor in the comparison between direct and indirect detection (76) it also stresses the complementarity between the two methods.

N-body simulations of galactic halos show a steeper fall-off at high-velocity tail than what is expected for a Maxwell-Boltzmann distribution (103; 104). Figure 3.8 examines the cases with different velocity cuts varied to 498 km/s (105) or infinity (106; 107), compared to the SHM with the fiducial value v_{esc}=544 km/s. Since the normalization of the VDF is kept to be 1 for different truncations, the low and high parts of VDF are not completely uncorrelated, but it can be regarded to be approximately uncorrelated. The indirect detection of heavy WIMPs is blind to the reduction of the WIMP population

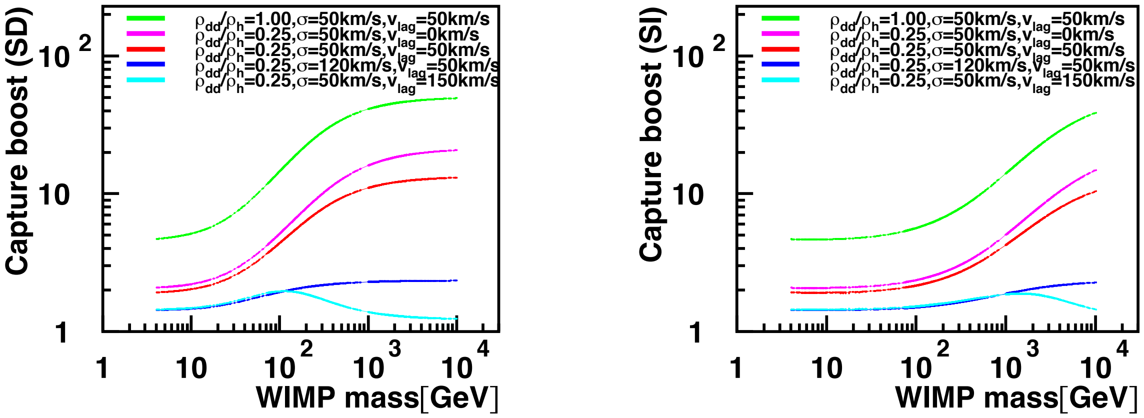

Figure 3.9: The capture boosts for SD (left), SI (right) coupling WIMPs for dark disc scenarios. green: with $\rho_{dd}/\rho_H = 1$, magenta: $v_{lag} = 0$ km/s, red: $\rho_{dd}/\rho_H = 0.25$, $\sigma = 50$ km/s, $v_{lag} = 50$ km/s, blue: $\sigma = 120$ km/s, cyan: $v_{lag} = 150$ km/s. Unless otherwise specified in the legend, parameters are fixed to $\rho_{dd}/\rho_H = 0.25$, $\sigma = 50$ km/s, $v_{lag} = 50$ km/s and $\rho_H = 0.3$ GeV/cm^3 (Note that the total dark matter density is increased to $\rho_{dd} + \rho_H$). The boosts in capture rate as a function of WIMP mass are given relative to a scenario without the dark disc.

in the high-velocity tail, while the marginal changes at the high mass come from the renormalization of the low-velocity part. Also the changes in the low mass region are mild, because the WIMP population in the high-velocity tail is originally small and kinematically hard to capture. As a result the uncertainty from a high-velocity cut is less than 1% for indirect detection for any WIMP masses.

In light WIMP scenarios the uncertainty on the high-velocity tail requires a careful interpretation of direct detection experiments (75; 71; 102; 103; 108), while the size of the effect on capture rate in the Sun as studied here will be marginal. Note that several studies have pointed out the large uncertainty in modeling of the high-velocity tail of the dark matter halo (103; 102; 77; 72), therefore it requires a careful interpretation of direct detection results in the low mass region (75; 71; 102; 103; 108). This merits the complementarity of direct and indirect searches.

In a heavy WIMP scenario the opposite effect will occur; indirect detection results need to be interpreted in a careful manner as the capture will be governed by the low-velocity part of the VDF. Luckily, sources of uncertainties in the low-velocity tail of simulated halos are expected to be small (79).

Another example of uncertainty, which would change the VDF in an uncorrelated manner, is the existence of the dark disc. Figure 3.9 shows the capture boosts for the previously discussed dark disc scenarios. The mean relative velocity of co-rotating dark disc with respect to the Sun is smaller than that of the non-rotating dark matter halo. Hence, the dark disc primarily populates the low-velocity region. We consider SD and

SI couplings exclusively, which was not done previously.

The first thing we notice is that the boost effect appears more dramatically in the spin-dependent coupling case. This is because SD capture is more sensitive to the low-velocity region. Figure 3.4 shows that the dark disc contribution is mainly contained below 200 km/s. In Fig. 3.1, we can see that for WIMP masses above 100 GeV (1000 GeV) for SD (SI) coupling, efficient captures are allowed for WIMPs with relative velocity to the Sun below 200 km/s. Taking these facts into account, the boost factor is as much as 15 (6) for SD (SI) coupling at 100 GeV for the strong ($\rho_{dd}/\rho_H = 1$) dark disc model, and larger in the higher mass region.

Secondly, our result for the strong dark disc on SI coupling is in agreement with the previous study done by Ling (75). A study by Bruch et al. (73) has discussed CMSSM models that define the ratio between SI and SD couplings for specific scenarios and found boost factors as much as an order of magnitude for 100 GeV WIMPs. By running DarkSUSY (83), we confirm that some 100 GeV neutralinos in CMSSM can result in an order of magnitude boost for the strong dark disc. We point out that this high boost can only be realised in scenarios with large SD contributions.

Lastly, we confirm that the capture boost can be limited with larger values of relative velocity or velocity dispersion used for modeling dark disc (75).

In manner contrary to the uncertainty of escape speed, enhancement of low-velocity region due to the dark disc will significantly affect heavy WIMP indirect detection, whereas direct detections also get a sizeable effect, with a factor $2 \sim 3$ for WIMP masses above 50 GeV (96) for recoil energies of $5 - 20$ keV. Below this mass direct detections are hardly altered, for example the so called channeling region of the DAMA annual modulation signal is not changed (75). In summary, the uncertainty coming from the dark disc on capture rates can be orders of magnitude depending on the WIMP mass and coupling type. But for the reason that the dark disc only adds an extra contribution to which indirect detection is more sensitive, it makes the interpretation of null results from indirect detections more conservative.

Possible sources of uncertainty in the low-velocity tail have been extensively discussed in the literature (109; 110; 111; 112; 113; 86; 114; 115). The phase space of low-velocity WIMPs could be influenced by the gravitational fields of the Sun and the planets. Recently, Sivertsson et el. (78) concluded that the loss of the weakly captured population by the Sun due to Jupiter depletion, which has been known to substantially reduce the capture of WIMPs heavier than a TeV, can be compensated with gravitational diffuse components. As a result, the simple free-space approximation in (109) turned out to be accurate (78).

3.5 Summary

We conclude that the uncertainties for light WIMPs are mild; for 20 GeV WIMP, they are 18 (14)% from local circular speed, 1 (1)% from high-velocity cut for the tested range for SD (SI) couplings. We also found that even though the form of the dark matter halo VDF is unknown the impact on the capture rate of light WIMP is suppressed because the effect is entirely integrated, which is consistent with the discussion in (116); it is up to 16 (10)% for the examined dark matter halos from cosmological simulations. In summary, the estimated sizes of the uncertainties from possible sources in VDF are found to be less then 24% (17%) for 20 GeV SD (SI) coupling WIMPs, if there was no dark disc.

For heavier WIMPs, the uncertainties are larger because of their sensitivity to the low-velocity tail, but it still is in the level of 50%; they are 45 (32)% from local circular speed, 1 (1)% from high-velocity cut for the tested range, up to 11 (16)% from the deviation of the VDF from Maxwellian for SD (SI) coupling 500 GeV WIMP.

The results are summarised in Tab. 3.2.

WIMP mass (GeV)	$v_\odot$ (%)	v_{esc} (%)	VDF (%)	Total (%)
20	18 (14)	1 (1)	16 (10)	24 (17)
500	45 (32)	1 (1)	11 (16)	46 (36)

Table 3.2: Summary of the size of the uncertainty for each source; $v_\odot$ is the local circular speed of the Sun, v_{esc} is the high-velocity cut, VDF is model of velocity distribution functions. Also total sum of them are shown for two cases of WIMP mass, for SD coupling (SI coupling) cases.

By quantitative research of the uncertainties, we concluded that the size of uncertainties in the solar WIMP search are moderate, which ensure the interpretation of their results within 50% error. This result will be taken into account for the result of the Super-Kamiokande data analysis together with other uncertainties, in Chap. 8. The existence of the dark disc enriching the low-velocity population could result in a significant increase in capture rate especially for heavy WIMPs, but the interpretation of the indirect searches compared to direct searches will become more conservative with its consideration.

Chapter 4

The Super-Kamiokande detector

4.1 Overview

The Super-Kamiokande (SK) is a cylindrical water Cherenkov detector located in the Kamioka mine in Japan. The Super-Kamiokande observes Cherenkov lights which are emitted by the relativistic charged particles travelling in the water by photomultiplier tube (PMT)s. Figure 4.1 shows a display of a neutrino event observed in the Super-Kamiokande detector. The Cherenkov light produces characteristic ring pattern on the finely aligned PMTs on the wall of the water tank.

The Super-Kamiokande, whose name stands for “Super-Kamioka Nucleon Decay Experiment”, was first proposed to search for nucleon decays and various studies of neutrinos. The Super-Kamiokande sets the world best limits on lifetimes of various nucleon decay modes. The studies of neutrino in the Super-Kamiokande target various sources such as the Sun, atmosphere and the human-maid neutrino beams; it has been used as a far detector for long-baseline neutrino oscillation experiments such as K2K and T2K. The Super-Kamiokande has been contributing significantly to our understanding of neutrino physics including the first evidence of neutrino oscillation by analysing atmospheric neutrinos, the confirmation of the solar neutrino oscillation and the high-precision measurement of the mixing angle θ_{13} using the neutrino beam. Various astrophysical sources, such as supernovae, gamma ray bursts and dark matter are studied using neutrinos as well.

Super-Kamiokande was commissioned after a great success of the Kamiokande experiment in neutrino physics and astrophysics. The construction was started in 1991 and finished in 1995, and the operation was started in April 1996. After about five years (1678 days) of operation which is called “SK-I”, it was shut down for maintenance and upgrade in July 2001. On November 12, 2001, a terrible accident occurred during refilling water after maintenance work is done. An implosion of a PMT destroyed more than a half of PMTs by a chain reaction. The operation was resumed (called “SK-II”) from October 2002 with temporary PMT coverage which was about a half of that of SK-I. SK-II continued measurement for three years and paused in October 2005 to recover the photo coverage. After recovering, it resumed operation (called “SK-III”) in

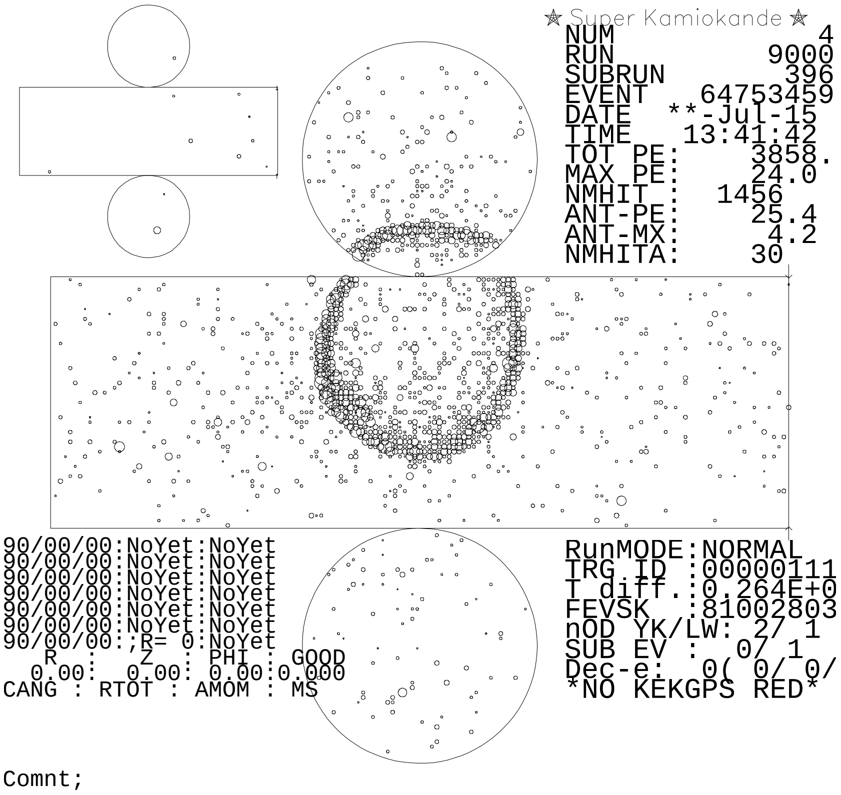

Figure 4.1: The development view of the Super-Kamiokande detector taken with an observed neutrino event. The size of the small circles correspond to the Cherenkov photons detected in each PMT, and the larger circle indicates the Cherenkov ring pattern.

June 2006 with similar PMT coverage to the original design and that of SK-I period. In September 2008 new electronics modules were developed and installed. After the upgrade of electronics, the running period is changed once again (called "SK-IV") and being continued until now.

This chapter will start with a brief introduction of Cherenkov radiation in Chap. 4.2. In Chap. 4.3, the detector site and facilities will be introduced. In Chap. 4.4, photomultiplier tubes installed in the SK is explained roughly. Chap. 4.5 summarises the electronics system of the SK-IV. In Chap. 4.6, short summary of the SK calibration system will be given.

4.2 Cherenkov radiation

When a charged particles travel with velocity v in medium with refraction index n, if $v \gg c/n$, the Cherenkov photons are emitted. Passing through the medium, the electromagnetic field of the charged particle excites the atoms and molecules which quickly return to ground state by emitting Cherenkov photons. The geometry of the emitted photon with speed of c/n, being slower than the charged particle with speed of $v = \beta c$, results in a cone-shaped shock wave front as shown in Fig. 4.2.

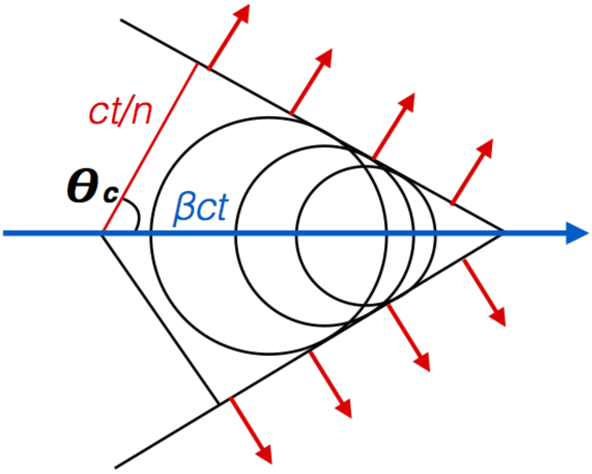

Figure 4.2: Image explaining Cherenkov photon propagation.

The characteristic half opening angle θ_C ("Cherenkov angle") between the direction of the traveling particle and the Cherenkov photon is determined as:

$$\cos\theta_C = \frac{c/n}{\beta c} = \frac{c}{nv}. \tag{4.1}$$

For a particle traveling with $v \sim c$, the Cherenkov angle has a maximum angle being about 42°.

A momentum threshold to generate Cherenkov radiation is:

$$p = mv \geq \frac{mc}{n}. \tag{4.2}$$

With the refractive index of water being ∼1.34, the thresholds for e, μ, $\pi^{\pm}$ and p are 0.57, 118, 156 and 1051 MeV/c respectively.

The number of photons emitted by a charged particle of charge ze per unit path length x per wavelength λ is written as a function of λ:

$$\frac{d^2N}{dxd\lambda} = \frac{2\pi\alpha z^2}{\lambda^2}(1 - \frac{c^2}{n(\lambda)^2 v^2}), \tag{4.3}$$

where α is the fine structure constant. Around 340 photons/cm are emitted for λ ranging 300 ∼ 600 nm.

4.3 The detector

Super-Kamiokande is located in the Mozumi mine of the Kamioka Mining and Smelting Company near the village of HigashiMozumi, Gifu, Japan. Geographic coordinate is 36°25'N and 137°18'E, with the altitude of about 370 m. The detector lies under the peak of Mt. Ikenoyama so it is beneath 1000 m of rock, which corresponds to 2700 m-water-equivalent overburden. The reduced cosmic ray muon even rate is ∼ 2.7 kHz in the detector. Figure 4.3 shows the schematic view of the detector and its location. The coordinate system of the detector used throughout this work and found other SK publications is drawn in Fig. 4.4.

The Super-Kamiokande is a cylindrical tank with a diameter of 39.3 m and a height of 41.4 m filled with 50 kilo ton of purified water.

Clean and abundant water supplied by the Kamioka mine is continuously circulated in the SK tank through water purification system in the flow rate of 35 ton/hour. To maximize water transparency and to remove radioactive materials, the water used to fill the SK tank is highly purified by a multi-step system including filtration, reverse osmosis (RO) and degasification.

The radon background present in the mine is in relatively high level. In order to reduce back-ground radioactive events which is a background source for the solar neutrino observation in the MeV energy region, also to keep low radon level around the experimental area, fresh air pumped in from a site outside and well away from the mine entrance is purified and is continuously pumped to inside the SK tank at a positive pressure with flow rate about 18 m^3/hour (119).

Within the tank, stainless-steel frameworks are spaced approximately 2 ∼ 2.5 m inside the tank wall to support PMTs. The remaining PMT glass envelopes, rest spaces are covered with black opaque polyethylene sheet which optically separates the tank to two concentric cylindrical regions. The inner and the outer part of the frames are called the inner detector (ID) and the outer detector (OD) respectively.

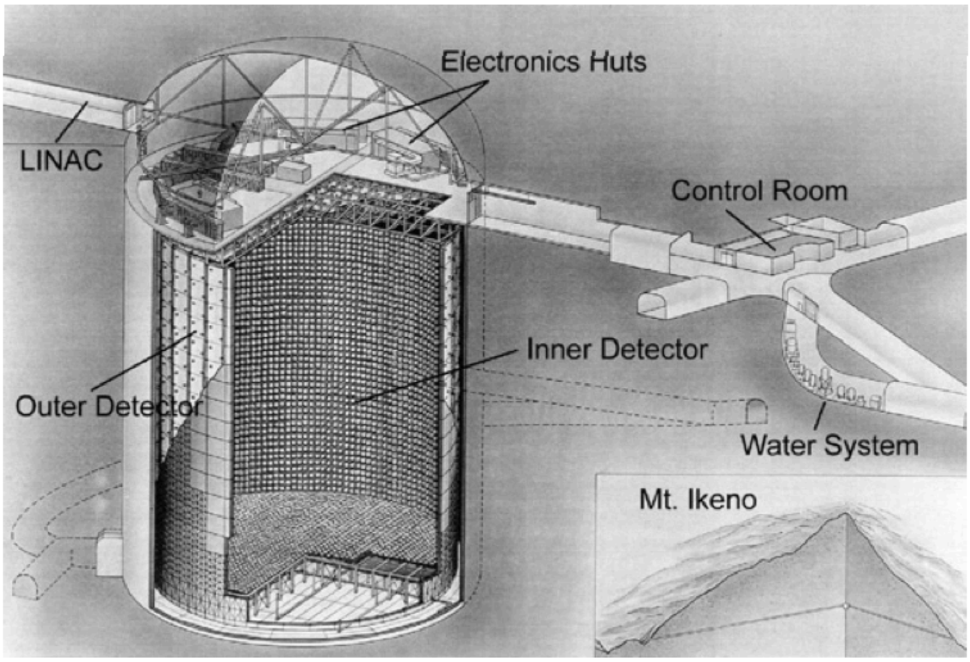

Figure 4.3: A sketch of the Super-Kamiokande detector and its location. Figure is taken from (117).

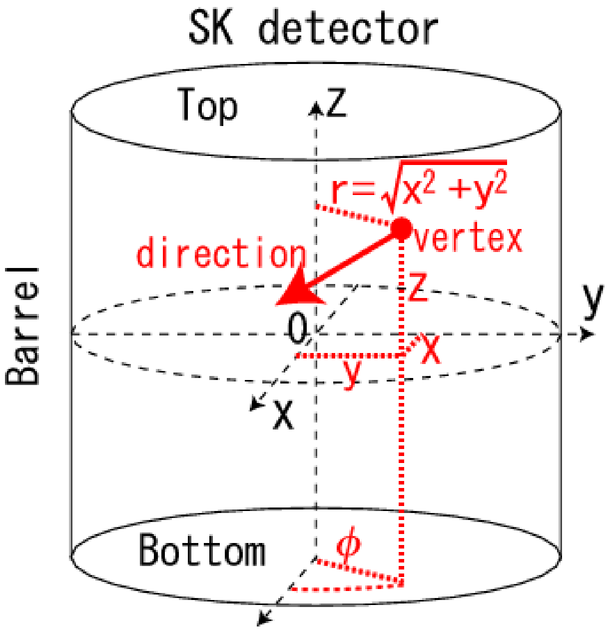

Figure 4.4: A sketch of the definition of detector coordinate system. Figure is taken from (118).

The inner detector is instrumented with approximately 11,100 (5200 for SK-II) 20-inch Hamamatsu photomultiplier tubes (PMTs). The outer detector is instrumented with $\sim$ 1,880 8-inch PMTs for use as veto counter for incoming and outgoing muons. The OD acts as a passive shield for low energy particles such as neutrons and γ rays from the surrounding rocks as well. The drawing of ID and OD is shown in Fig. 4.5.

PMTs are connected to high voltage supplies and electronics via cables which are brought up to the tank top and distributed to four huts which contain electronics racks and front-end DAQ computers. Another electronics hut is built at the center of the four huts to contain electronics and associated computers for triggering, housekeeping, and Global Positioning System (GPS) time synchronization systems. The details of the detector can be found elsewhere (117).

4.4 The photomultiplier tubes

The ID PMTs were mounted approximately every 70 cm on the side wall, top and bottom of the tank. The photocathode coverage of the ID surface is 40% for SK-I,III and IV and about 47% of it for SK-II. 50 cm PMTs (Hamamatsu R3600) are developed by Hamamatsu Photonics in collaboration with Super-Kamiokande (120) and used for ID. The bialkali (Sb-K-Cs) coated photo-cathode has peak quantum efficiency of about 21% at 360 $\sim$ 400 nm wavelength as shown in Fig. 4.7. The neck of each PMT was

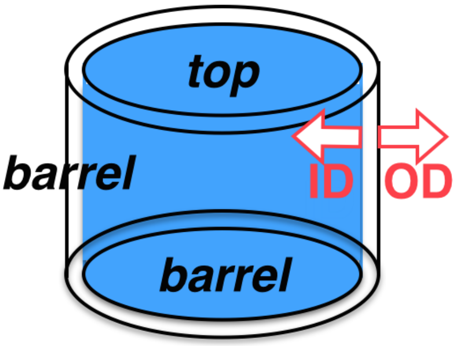

Figure 4.5: A sketch of the ID, OD regions in the SK detector.

coated with a silver reflector to block external light. Figure 4.6 shows a schematic view of the ID PMT. The collection efficiency at the first dynode is over 70%. The dynamic range covers from 1 to 300 photoelectron (p.e.). The transit time spread for a single p.e. signal is about 2.2 ns. The average dark noise rate at the 0.25 p.e. threshold is about 3 kHz. The ID PMTs were operated with a gain of 10^7 at a supply high voltage ranging from 1700 to 2500 V. Fig. 4.8 shows the charge distribution for single p.e., obtained from the calibration measurement with nickel source (121). A clear single p.e. peak can be seen.

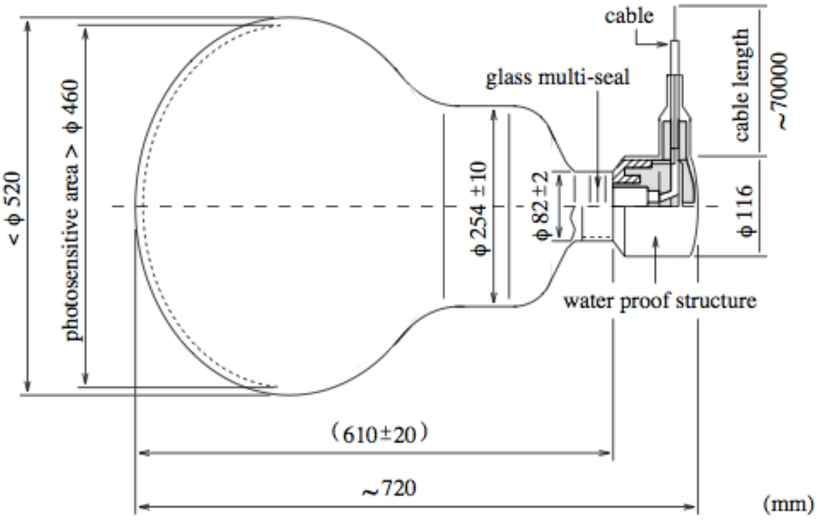

Figure 4.6: Schematic view of a 50 cm PMT used for ID. Figure is taken from (117).

After the accident in 2001, the PMTs have been instrumented with acrylic covers to

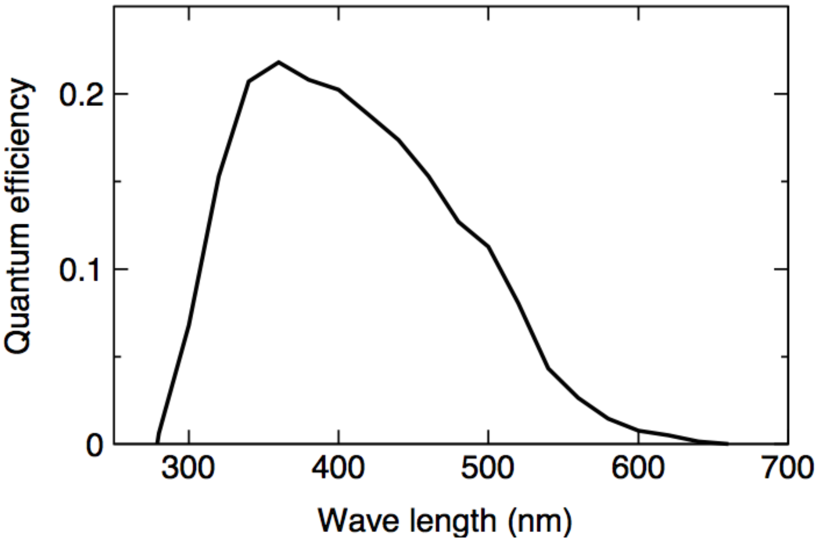

Figure 4.7: quantum efficiency of the bialkali (Sb-K-Cs) coated photocathode as a function of wavelength. Figure is taken from (117).

avoid chain reaction of implosions since SK-II period. A 12 mm thick UV-transparent acrylic dome is used to cover the photocathode of each PMT, and the side of the PMT is protected with Fiber-Reinforced Plastic (FRP) shield with holes letting water flows through inside the case. Transparency of the acrylic cover in water is more than 96% above wavelength 350 nm.

To prevent the geomagnetic field affecting the PMT response, 26 horizontal and vertical Helmholtz coils are implemented around the detector, which reduce the magnetic field from 450 mG to 50 mG.

The OD is implemented with 20 cm PMTs (Hamamatsu R1408) facing outward. The photocathode of the OD PMT is covered with a 60 cm × 60 cm × 1.3 cm wavelength shifter plate, in order to increase light collection efficiency.

4.5 Electronics and data acquisition system in SK-IV period

After 12 years of operation without a major upgrade, the detector data acquisition (DAQ) system was upgraded in 2008. In the designing of the new system, the main goal was to implement the system able to use software trigger instead of hardware trigger used for SK-I,II and III. The new system is developed that all the data of PMT hits can be sent to the online PCs, and then various software trigger can be applied in order to pick up the events for each science goal. In this way, more advanced science goals can be examined such as: more precise determination of oscillation parameters and the

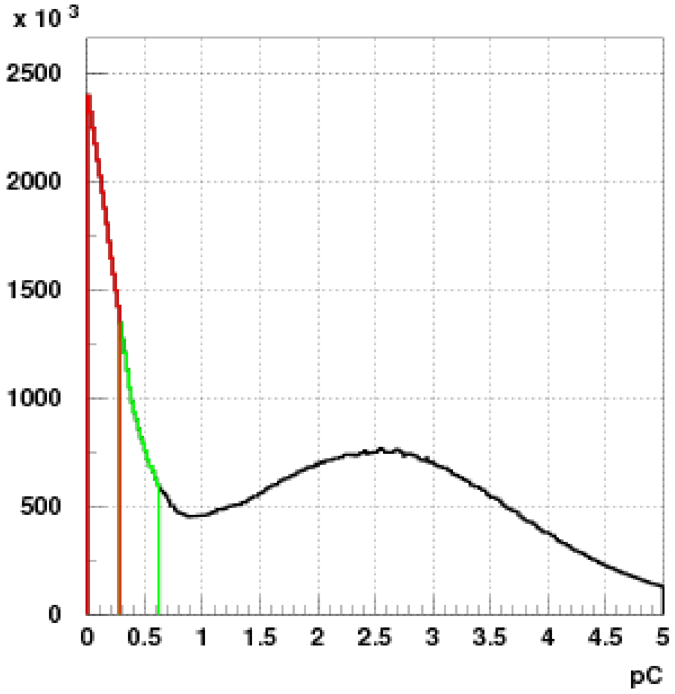

Figure 4.8: The single p.e. distributions in pC unit from the calibration data with nickel source in SK-III. The black line shows the data with normal set up of SK PMTs, the green line shows the data with double gain and half threshold and the red line is linear extrapolation. Figure is taken from (121).

observation of energy dependence of neutrino oscillation in the low energy region using solar neutrinos by the decreased energy threshold, fully detecting nearby supernova burst by the increased size of the storing data, detecting relic supernova neutrinos by tagging 2.2 MeV gamma ray from neutrons.

The newly developed front-end electronics is called QBEE, which stands for “QTC (charge (Q) to Time Converter) Based Electronics with Ethernet”. The QBEE has 24 analog input channels - a board is equipped with eight QTC chips which have three input channels each - which can collect signals from 24 PMTs. A custom application-Specific Integrated Circuit (ASIC) is developed as a high-speed QTC. It integrates the input charge and issues an output pulse whose width is proportional to the amount of charge. Figure 4.9 shows the block diagram of the QTC.

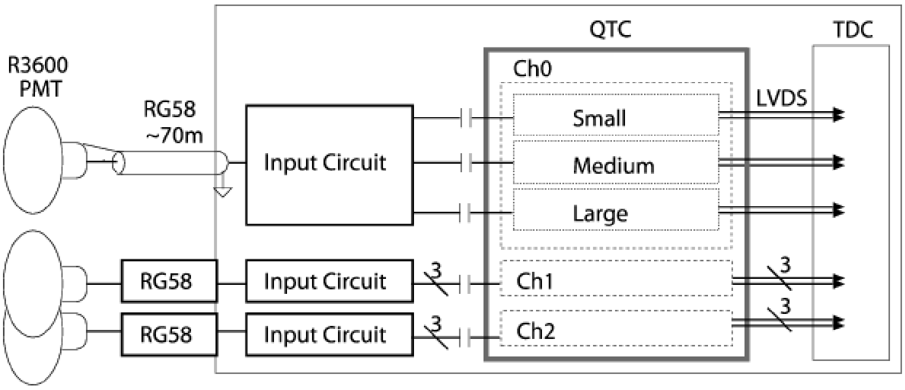

Figure 4.9: Block diagram of a QTC. Each channel has three gain ranges: small, medium and large. Figure is taken from (122).

The output of QTC is sent to the multi-hit Time-to-Digital converter (TDC) called AMT-3. The TDC measures the width of QTC output pulse by detecting the time of leading and falling edges. Then the data of the width and arrival timing of the leading edge is sent to a Field-Programmable Gate Array (FPGA) and then finally to the front-end PC. The front-end PC passes the data to 10 merger PCs in which the software triggers for physics analyses are applied to select events. One front-end PC receives the data from 30 QBEE boards. The data transfer is greatly improved by adopting Ethernet for transferring data to online PCs; 11.8 MB/s per QBEE board has been achieved.

Figure 4.10 shows the block diagram of the new DAQ system. Detailed descriptions are found in (123). In the merged data, the software trigger searches the events satisfying the trigger conditions for physics analyses. The basic trigger is applied by calculating the number of PMT hits in a 200ns sliding window, which is the same as the hardware trigger of the previous system for SK I-III. In SK-IV, there are used four types of basic trigger - Super Low Energy (SLE), Low Energy (LE), High Energy (HE) and special high energy (SHE) triggers. The different event widths are stored

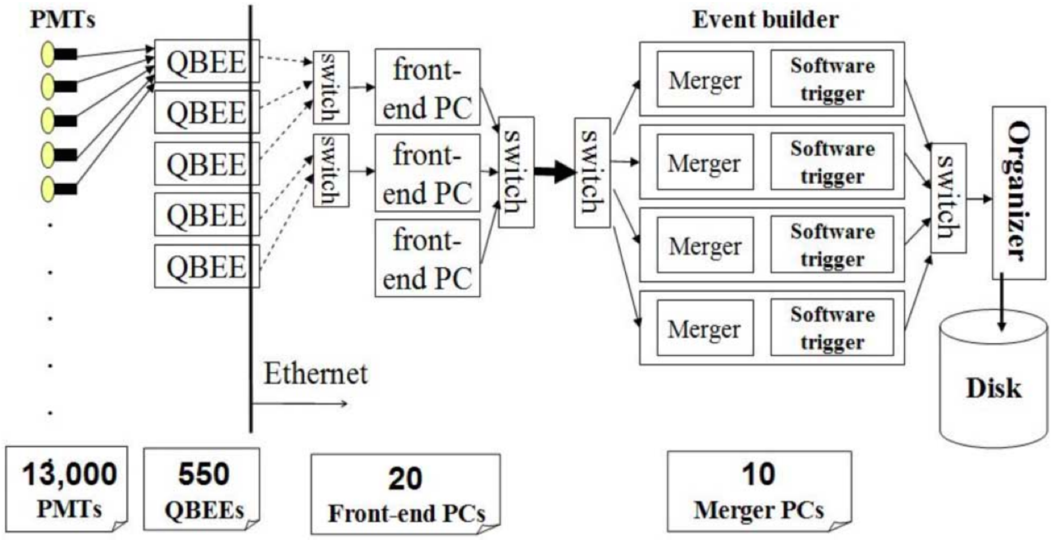

Figure 4.10: The schematic view of the data acquisition system in SK-IV. In the left part, newly developed front-end electronics boards connected with PMTs are shown. In the right part, components of the new online system are shown. Figure is taken from (123).

for different trigger types; SLE trigger can be set to save 1.5μs of data and the much less frequently triggering LE and HE triggers can save data for like 40μs. SHE has been introduced with a threshold of 58 hits since September 2011. The thresholds and event widths for these triggers are shown in Tab. 4.1. In addition to the basic trigger, special triggers, for example for neutrino tagging, for the detector calibration with an external source and for the T2K data are implemented.

More information of the new electronics and online system can be found in (123).

4.6 Detector calibration

4.6.1 PMT calibration

High-voltage setting

Setting appropriate HV for each PMT was performed in order to achieve same output charge for the same incident light intensity for all PMTs. At the center of the detector, an isotropic light source, the “scintillator ball”, which is a 5 cm diameter acrylic ball containing a diffuser is deployed. Lights from a Xe lamp are passed through a UV filter and then injected to the scintillator ball. To control the incident light yields to each PMT at different locations, 420 pre-calibrated “standard PMTs” are

Trigger	Threshold (hits)	Event Width (μs)
OD	22	
SLE	34	$-0.5 \sim 1.0$
LE	47	$-5 \sim 35$
HE	50	$-5 \sim 35$
SHE	70 → 58 (from Sep, 2011)	$-5 \sim 35$
AFT	SHE, no OD	$35 \sim 535$

Table 4.1: The thresholds and event widths for OD and various ID triggers.

mounted in the ID and served as references for other neighbor PMTs. The HV values of the standard PMTs are initially adjusted so that they give the same ADC values for incident light of ~ 30 p.e.'s. The HV settings of other PMTs are adjusted so that the observed charges match those for the neighbor standard PMTs. After determining the HV setting for all PMTs, the reproducibility is checked and confirmed to be within 1.3% RMS as seen in Fig. 4.11.

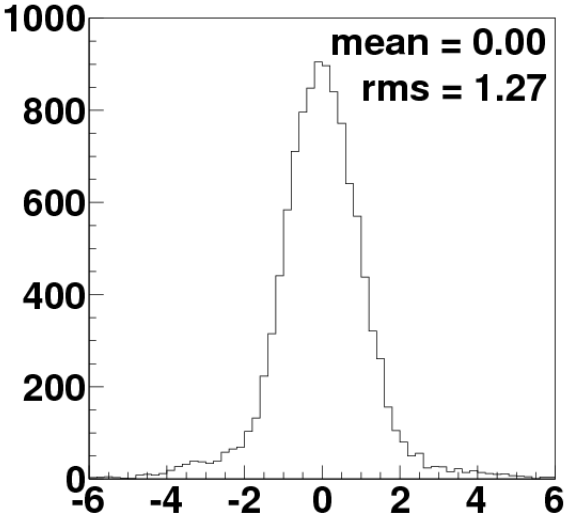

Figure 4.11: The percent differences in observed charge from the respective reference value are accumulated for all PMTs. Figure is taken from (121).

Relative gain

To measure the relative gain difference for each PMT, a nitrogen-laser-driven dye laser is used as a light source. The measurements are done in two ways: first, the light source flashes at high-intensity, I_w, from which every PMT gets a sufficient number of photons and create an average charge $Q_{obs}(i)$ in repeated events. Secondly, the measurement uses flashes at low-intensity, I_s, in which only a few PMTs are hit by the number of times, $N_{obs}(i)$, in repeated events, and each of them can be safely assumed to be a single-p.e. hit. $Q_{obs}(i)$ and $N_{obs}(i)$ have following factors involved:

$$Q_{obs}(i) \propto I_s \times a(i) \times \epsilon_{qe}(i) \times G(i), \tag{4.4}$$

$$N_{obs}(i) \propto I_w \times a(i) \times \epsilon_{qe}(i), \tag{4.5}$$

where $a(i)$ is the acceptance at the i-th PMT, $\epsilon_{qe}(i)$ is the quantum efficiency of the i-th PMT and $G(i)$ is the gain of the i-th PMT.

By comparing two measurements, $G(i)$ can then be derived as:

$$G(i) \propto \frac{Q_{obs}(i)}{N_{obs}(i)}. \tag{4.6}$$

By normalizing with the average gain over all PMTs, $G = \overline{Q}_{obs}/\overline{N}_{obs}$, the relative gain of each PMT can be obtained. Figure 4.12 shows the accumulated relative gain for all PMTs. The RMS of the distribution was found to be 5.9%. After adjusting HV to have the same gain for all PMTs, this deviation is inferred to come from different QEs among PMTs. The relative gain differences among PMTs are made as table and are used as fine corrections.

Absolute gain

For a uniform and stable source of single-p.e. level light, the "nickel source" that isotropically emits $\sim$9 MeV γ-rays from thermal neutron capture by Ni is used. The nickel source consists of Ni wires stored in a container with Cf-252 neutron sources. The nickel source is deployed at the center of the tank and generates about 100 Cherenkov photons per capture, assuring more than 99% of observed signals are from single p.e..

Applying the relative gain corrections obtained in the previous chapter, the cumulative single-p.e. distribution are measured for all PMTs. The resulting charge distribution is shown in Fig. 4.8. The sharp peak near zero is caused by electrons which punch-through the first dynode, and the second round peak corresponds to single p.e. signal. The averaged pC over the whole distribution was defined as the conversion factor from pC to single p.e.; the obtained value of this conversion factor for SK-I, SK-II, SK-III and SK-IV are 2.044 pC/p.e., 2.297 pC/p.e., 2.243 pC/p.e. and 2.658 pC/p.e., respectively.

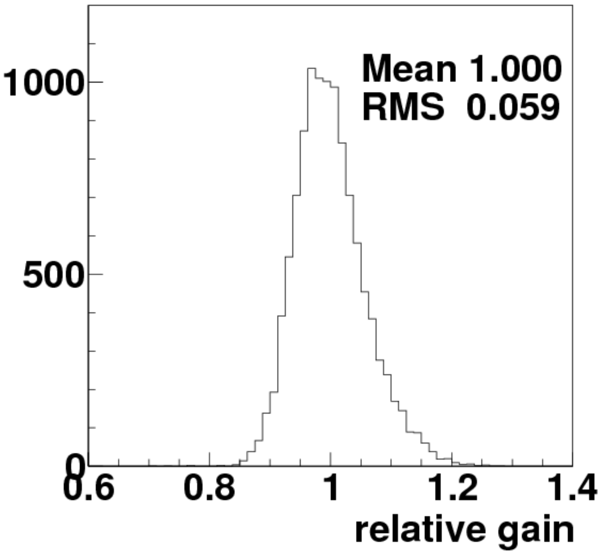

Figure 4.12: Accumulated relative gains of all PMTs. Figure is taken from (121).

Relative differences in QEs

We used the nickel source data to be compared with MC simulation which predicts the number of photons arriving at each PMT. After correcting the distance from the source position to the PMT position, the acceptance as a function of incident angle and light propagation in the water, the remaining differences in observed number of hits are attributed to come from the QE differences of PMTs. Figure 4.13 shows the difference between number of hits from the calibration data and MC, after correcting the distance and the angle-dependent acceptance. The obtained relative QEs of the PMTs are tabulated and used in the MC simulations.

Relative timing

The timing response of a PMT depends on length of the cable, time walk of PMT pulses at the discriminator, and processing time of electronics. The overall effect on timing can be calibrated by injecting fast light pulses at various intensities. The laser light from a fast Nitrogen laser is injected to a diffuser ball located at around the center of the tank.

The TQ-map, timing as a function of the pulse height is fitted with a polynomial function. Each PMT has its own TQ-map. Figure 4.14 shows an example of TQ distribution for a PMT. The parameters resulting from the fitting are used to correct the time response for each PMT as a function of charge.

The timing resolution is evaluated for each Qbin by accumulating all PMT timing distributions after correction by their TQ-maps. The timing resolution is measured

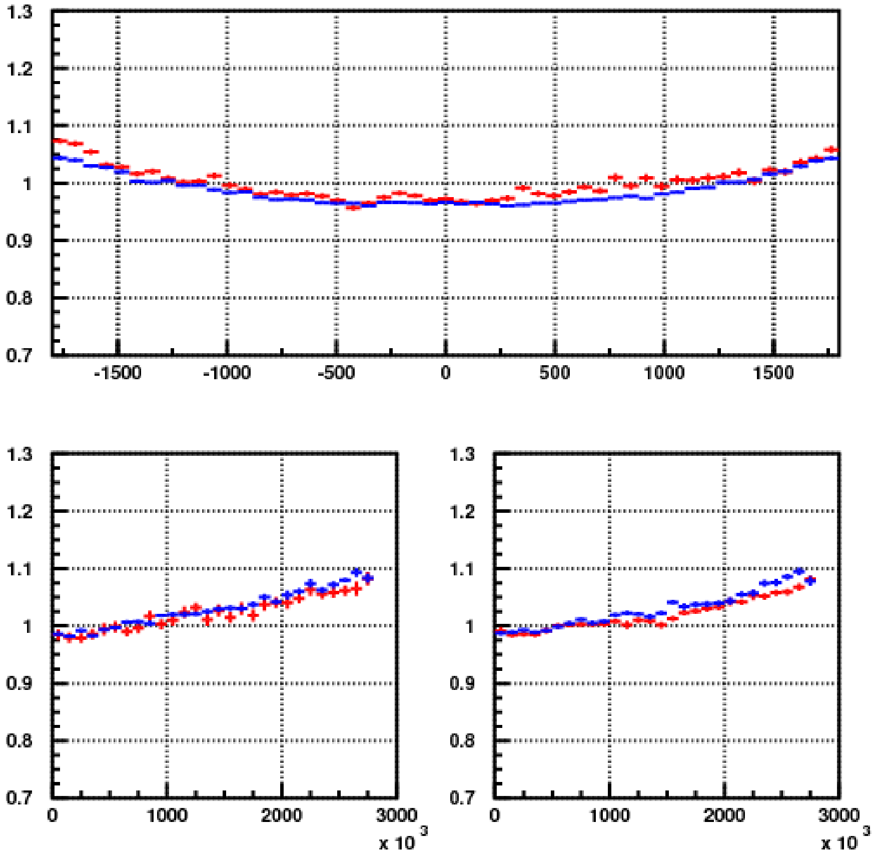

Figure 4.13: Hit probability as a function of PMT position, after normalising by average value of all the PMTs for data (red line) and MC (blue line). For the barrel PMTs shown in top figure, the horizontal axis denotes the z (cm) position of PMTs. The lower figures show top (left) and bottom (right) PMTs, where the horizontal axis shows the square of the distance from the center (cm^2). Figure is taken from (121).

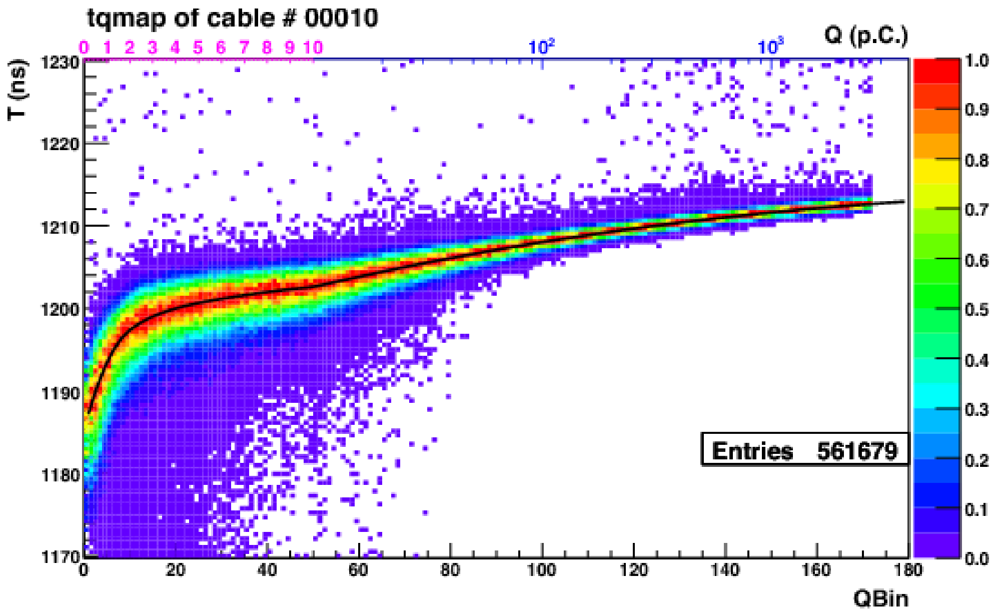

Figure 4.14: Typical scatter plot of TQ distribution for a single PMT for charge versus hit timing after time-of-flight-correction. Larger T corresponds to earlier hits. Figure is taken from (121).

to be 2.1 ns at single p.e. level and 0.5 ns at 100 p.e. level. Figure 4.15 shows the timing distribution together with the fitted function resulting from the fit for Qbin = 14, which corresponds to ∼1 p.e..

The stability of the time-response of PMTs during SK detector operation is monitored in real-time and correction is applied to the TQ-map. As a result, it is checked to be stable within ± 0.1 ns for a few years.

4.6.2 Water quality and light reflection

By injecting a collimated laser beam with the wavelength at 337, 375 405, 445 and 473 nm vertically through the SK tank, the PMT hit timing distributions are obtained for PMTs mounted at top and five barrel parts of the SK tank as shown in Fig. 4.16. While the sharp peak in later timing (right region of plots) represents photons reflected by the bottom PMTs or black sheets, the hits in the left region are from photons scattered by the water. The total number of scattered photons and the shape of the time distribution are used to tune scattering and absorption properties for the water.

The intensity of the light traveling in water exponentially decreases as:

$$I(\lambda) = I_0(\lambda) e^{\frac{-1}{L(\lambda)}}, \tag{4.7}$$

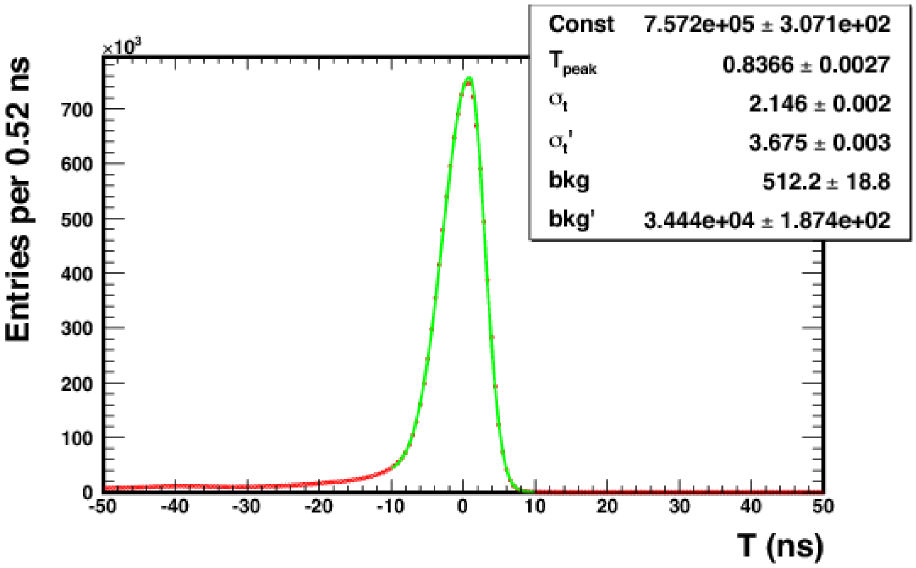

Figure 4.15: Accumulated timing distribution of all the PMTs in Qbin=14. The fitted asymmetric Gaussian distribution is shown by the green solid curve. Figure is taken from (121).

where $L(\lambda)$ is the attenuation length. Attenuation length in water is described as $L = (\alpha_{abs} + \alpha_{scat.sym} + \alpha_{scat.asym})^{-1}$ in the SK MC, where α_{abs}, $\alpha_{scat.sym}$ and $\alpha_{scat.asym}$ are absorption, symmetric scattering and asymmetric scattering coefficients respectively. Physically, the symmetric scattering may consist of Rayleigh and symmetric Mie scattering and the asymmetric scattering may consist of forward Mie scattering. Though in the MC, forms of these parameters are empirically determined and the coefficients are tuned by fitting the laser beam data with the least-χ^2 method. The results of the fit are shown in Fig. 4.17.

The laser-beam data for water transparency is continuously measured and the time variations are monitored at several wavelengths. Figure 4.18 shows time variations of the water parameters in SK-IV from October 2008 to November 2012. The symmetric scattering coefficient is relatively stable, being about 3% for August 2008 to November 2012. The absorption and asymmetric scattering coefficients have relatively larger time dependence, being about 20 $\sim$ 40% and 20 $\sim$ 60% in the same time period, respectively.

4.6.3 Energy scale calibration

The energy scale is determined by vertical cosmic-ray through-going muons which stop in the bottom OD layer. The accuracy of the absolute energy scale is checked with four sources covering wide momentum range from a few tens of MeV/c to about 10 GeV/c.

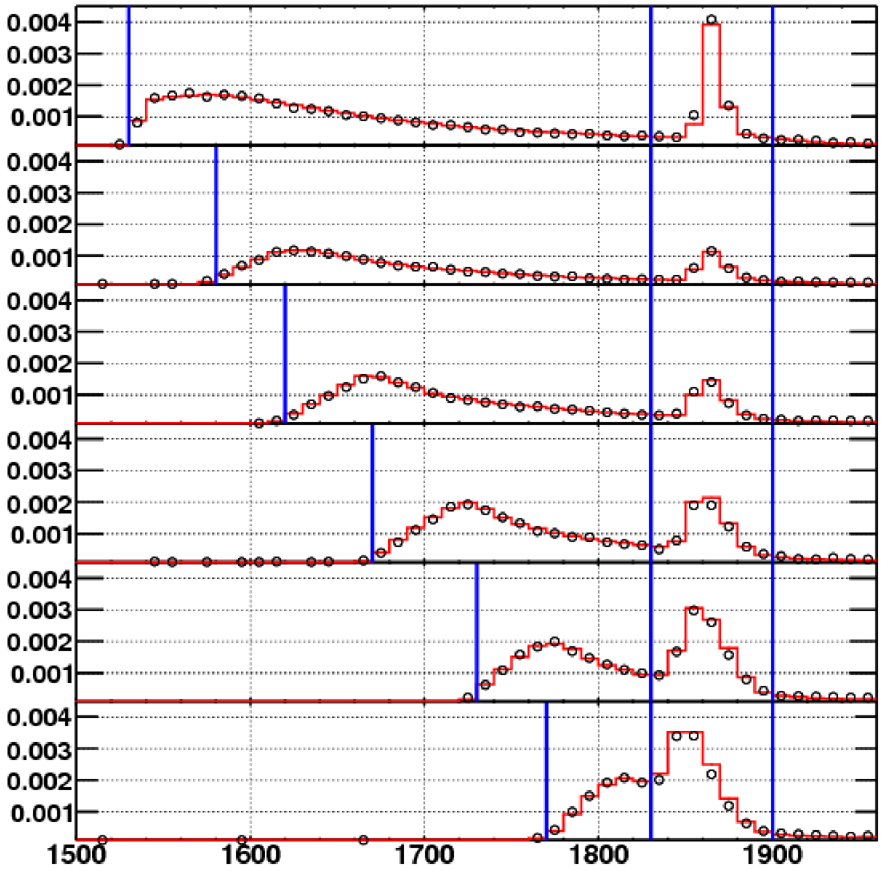

Figure 4.16: Typical hit PMT timing distributions of after time-of-flight correction for the wavelength at 405 nm, for data (black circle) and MC (red solid line) normalized by total p.e.'s. The top plot is for the PMTs mounted at the tank top, and the following five plots are for the PMTs on the divided regions on the barrel, from the top to the bottom. The hits within the first two blue lines are used to estimate the absorption and scattering properties, and the hits between the last two blue lines are used for the measurement of reflection, for which readers are referred to see (121). Figure is taken from (121).

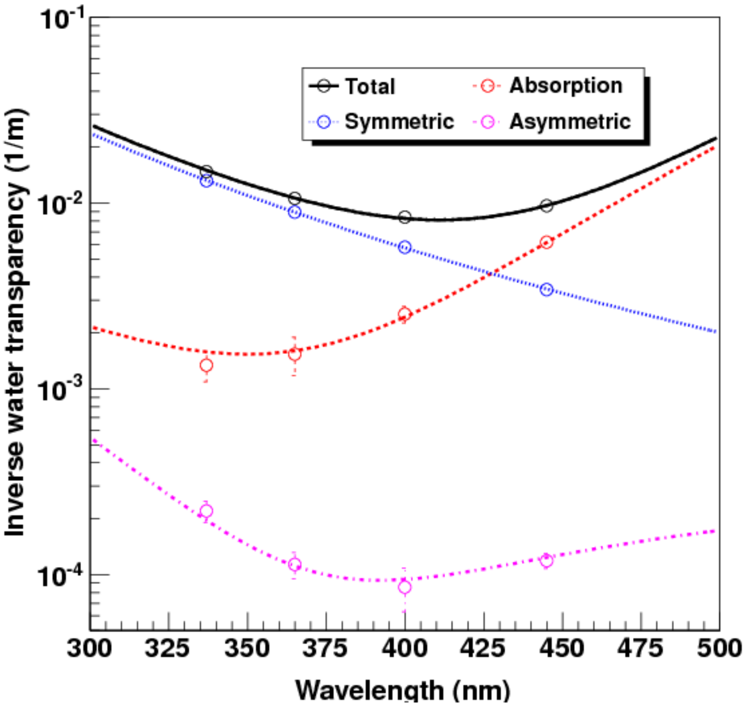

Figure 4.17: The water coefficient functions (lines) fitted to data obtained in April 2009 (circles). The asymmetric (pink) and symmetric (blue) scattering coefficients, the absorption (red) coefficients are shown together with the all fitted functions added (black). Figure is taken from (121).

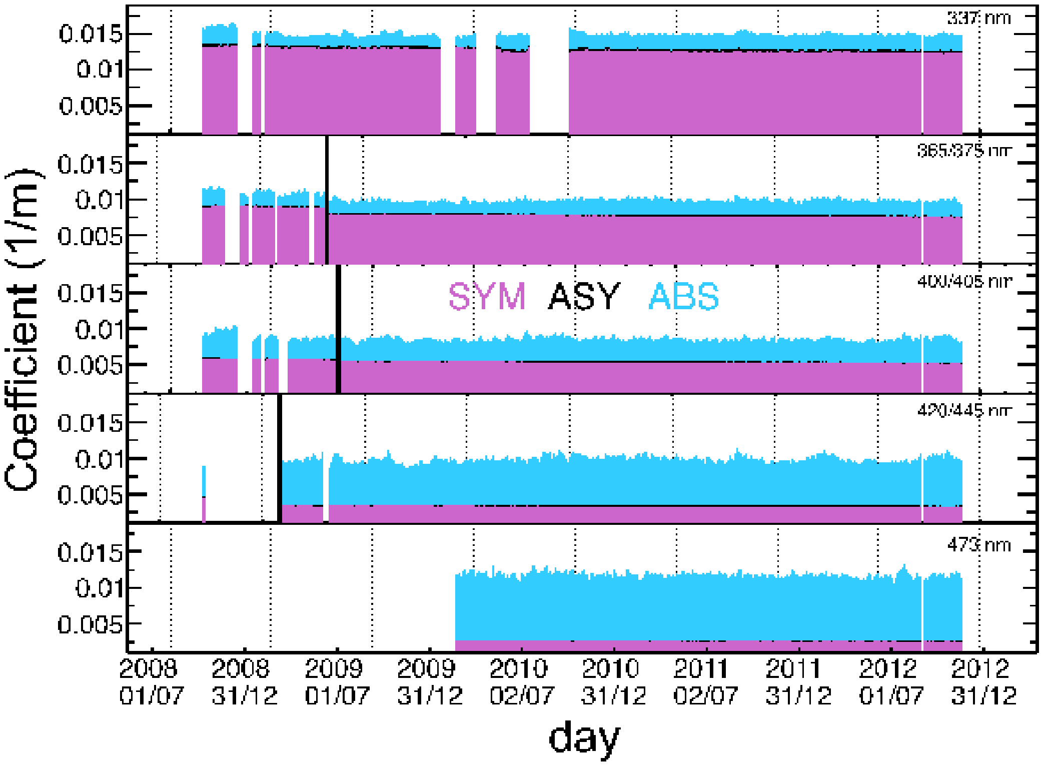

Figure 4.18: Time variation of the asymmetric (black) and symmetric scattering (purple) parameters, and the absorption (blue) parameter in SK-IV, for several wavelengths. Figure is taken from (121).

Track lengths of high energy stopping muons

The first source of energy scale calibration covering 1 ∼ 10 GeV/c of momentum range is high energy muons. Muons entering the detector from the top, traveling downward and stopping inside the detector are selected to be used. With the known energy loss being about 2.3 MeV per cm, the reconstructed muon track length is compared with total p.e.'s. The track of stopping muon is reconstructed by connecting the entering position at the detector and the vertex position of the subsequent decay electron. The accuracy of the absolute energy scale is checked by comparing calibration data and Monte Carlo simulation. As a result, data and MC agree within 0.7%, 1.1%, 2.0% and 2.2% for SK-I, SK-II, SK-III and SK-IV, respectively. Figure 4.19 shows the agreement between data and MC for SK-I.

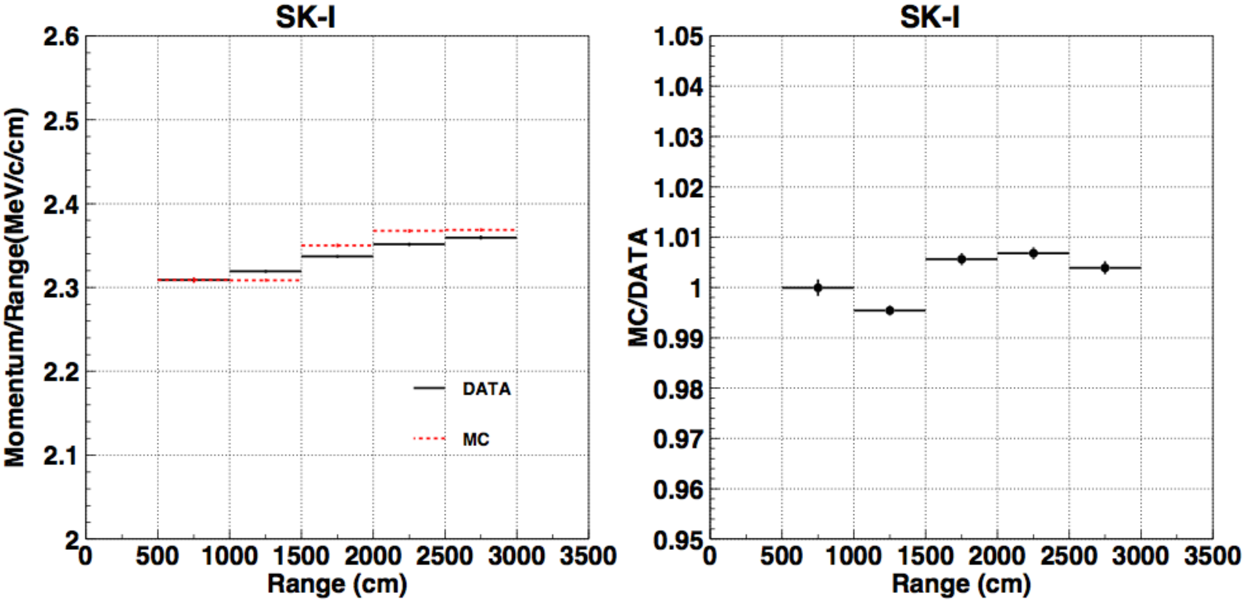

Figure 4.19: The averaged $P_{p.e.}/P_{mom}$ where P_{mom} is the momentum estimated with muon track for SK-I data (solid) and MC (dashed) (left), and the ratio between MC and data (right). Figure is taken from (124).

Cherenkov angles of low energy stopping muons

Cherenkov angles of low energy cosmic ray muons are used for lower momentum ($<$ 400 MeV/c) calibration. The Cherenkov angle has momentum dependence as following:

$$cos\theta_C = \frac{1}{n\beta} = \frac{1}{n}\sqrt{1 + \frac{m^2}{p^2}}. \tag{4.8}$$

Selection of sample muons have same criteria as above, and total p.e.s are required to be less than 1500 (750 for SK-II) which correspond to $pc <$ 380 MeV/c in addition to them. The data and MC agree within 0.7%, 1.3%, 2.1% and 2.1% for SK-I, SK-II, SK-III and SK-IV respectively. Figure 4.20 shows the agreement between data and MC for SK-IV.

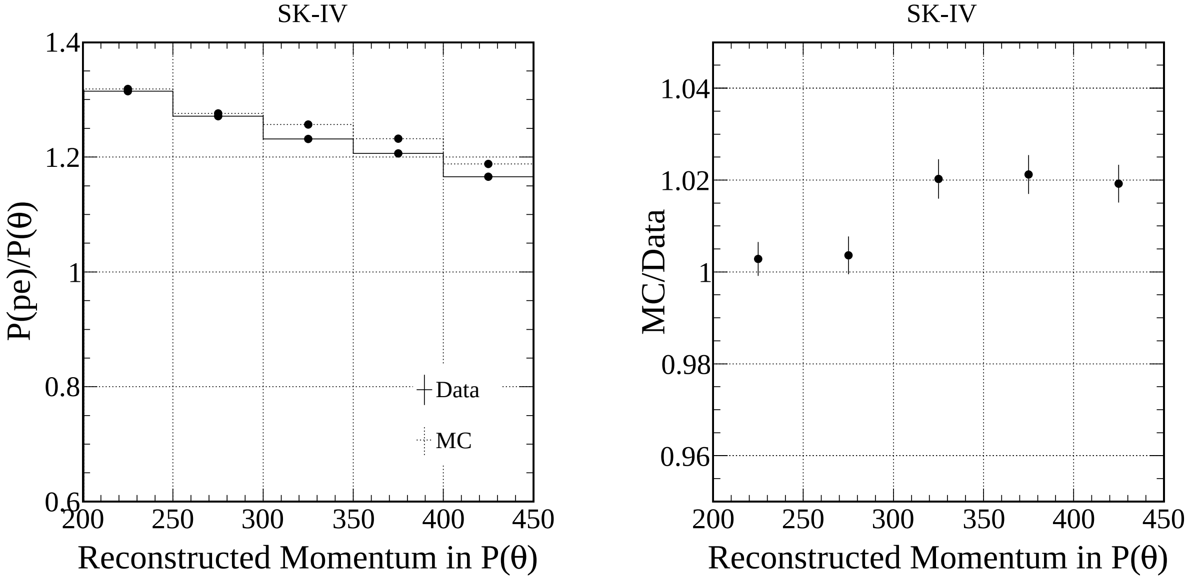

Figure 4.20: The averaged $P_{p.e.}/P_\theta$ where P_θ is the momentum estimated with θ_C for SK-IV data (solid) and MC (dashed) (left), and the ratio between MC and data (right). Figure is taken from (125).

Invariant mass of pions

Pions produced by neutrino interactions can also be a source of calibration as the invariant mass of π^0 can be reconstructed from two γ rays. The distribution of the invariant mass peaking around 135 MeV is compared to MC as shown in Fig. 4.21. The peak positions obtained by Gaussian fitting of data and MC agree within 0.7%, 1.3%, 0.3% and 1.7% for SK-I, SK-II, SK-III and SK-IV respectively.

Momentum spectra of decay electrons

Decay electrons produced from decay of cosmic-ray stopping muons are abundant and their momentum spectra are well understood. To reject ~6 MeV γ rays produced from μ^- capture on nucleons, events whose NHIT_{50} is greater than 60 (30 for SK-II) are

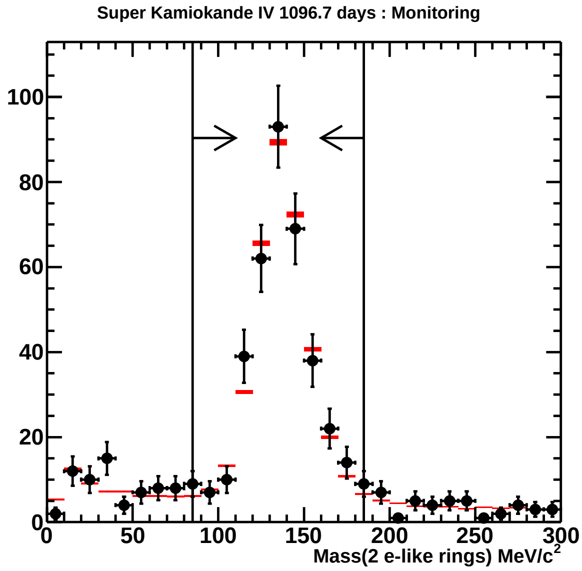

Figure 4.21: Invariant mass distribution of neutrino induced π^0 events (black dot) in comparison to MC (red box). Figure is taken from (125).

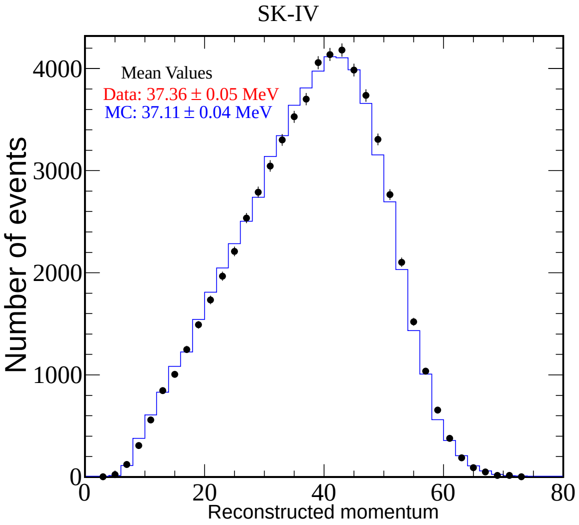

Figure 4.22: Momentum spectrum of decay electrons (black dot) in comparison to MC (blue solid line) for SK-IV. Figure is taken from (125).

selected. Figure 4.22 shows the momentum spectra of decay electrons in comparison to the MC. The mean value of the spectrum agrees with MC within 0.6%, 1.6%, 0.8% and 1.6% for SK-I, SK-II, SK-III and SK-IV respectively.

The stopping muons and decay electrons are used to check long-term variation of energy scale. The RMS of the mean reconstructed momentum of stopping muons divided by muon track length, and the mean reconstructed momentum of decay electron are calculated. The size of the fluctuations are estimated to be 0.74%, 1.60%, 2.08% and 0.39% for SK-I, SK-II, SK-III and SK-IV, respectively.

Combining the size of the uncertainties in energy scale calibration with the time variation of them in quadrature, the total uncertainty in the energy scale is estimated to be 1.1%, 1.7%, 2.7% and 2.3% for SK-I, SK-II, SK-III and SK-IV, respectively. Figure 4.23 shows the estimated uncertainty of each source for SK I-IV.

As decay electron events are expected to uniformly occur, the averaged momentum of decay electrons are compared to the MC for five zenith angles. The detector gains are uniform over zenith angles within ±0.6%, ±0.6%, ±1.3% and ±1.3% for SK-I, SK-II, SK-III and SK-IV respectively. They are also uniform over azimuthal angles within ±1%.

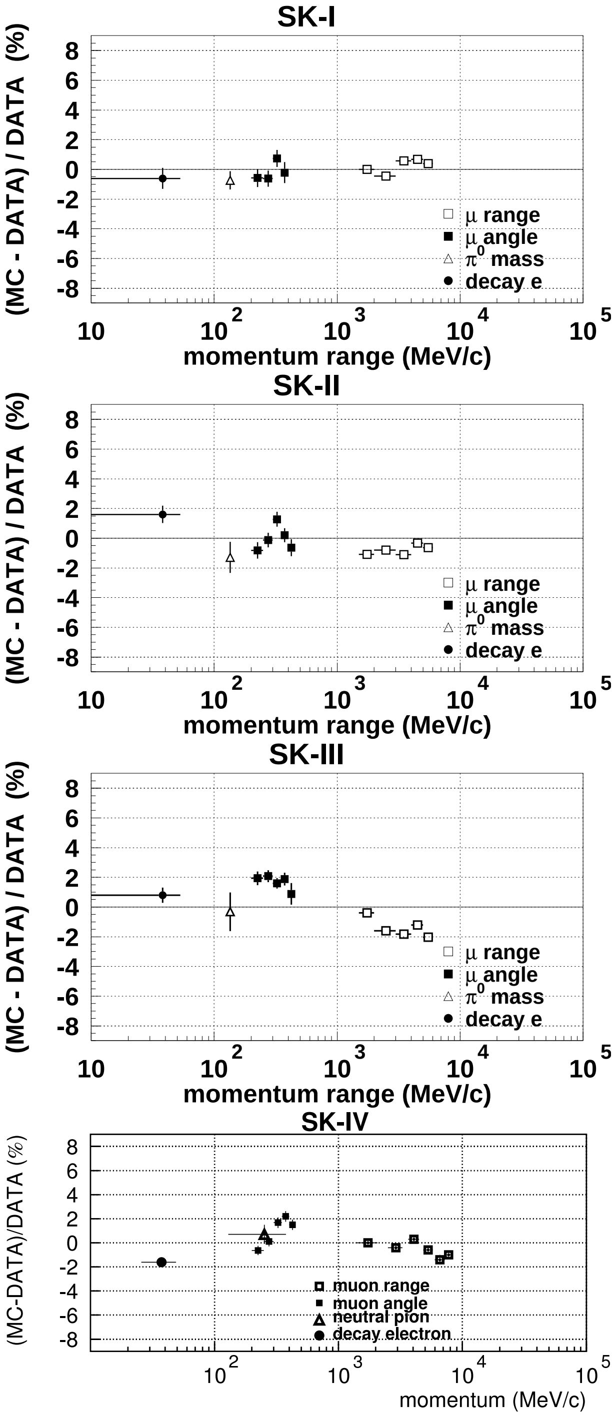

Figure 4.23: Estimated energy scale uncertainties for four sources in their momenta ranges, for SK I-IV are shown. Figure is taken from (125).

Chapter 5

Simulation of WIMP neutrinos and atmospheric neutrinos at SK

5.1 Overview

Neutrino events in the Super-Kamiokande are simulated by Monte-Carlo method. The simulation is composed of three parts: expectation of neutrino flux, neutrino interactions and particle tracking including Cherenkov photons in the detector.

For the calculation of the WIMP-neutrino flux at SK, the WIMPsim (88) simulator is used. The atmospheric neutrinos originated from the cosmic ray interactions are background of the WIMP search. For the atmospheric neutrino flux, calculation by M. Honda et al. (Honda flux) (126; 127; 128; 129) is mainly adopted to predict the flux at SK.

By the neutrino interaction simulation code "NEUT" (130) (131), secondary particles are produced at the SK detector and surroundings considering several types of neutrino interactions. With the detector simulation, Cherenkov photons are produced, tracked and then finally recorded in electronics simulation.

In Chap. 5.2, the simulation of the WIMP-neutrino flux at SK site by WIMPsim is described. Following chapter 5.3 will show the resulting WIMP-induced events detected in SK. In Chap. 5.4, the atmospheric neutrino flux will be described and in Chap. 5.5 its oscillated feature will be explained. The neutrino interactions in the simulation is summarised in Chap. 5.6. After that, events are propagated through the detector response simulations, about which it is briefly described in Chap. 5.7. The information of simulated events are recorded in the same structure as the observed data that can be later processed by common reconstruction and reduction software programs.

5.2 The simulation of WIMP-neutrino flux by WIMPsim

For expecting the WIMP-neutrino spectrum at SK, the WIMPsim (88) version 3.01 is used. WIMPsim calculates the annihilation process of WIMPs inside the Sun then tracks produced neutrinos all the way from the center of the Sun to a detector in an event-based scenario. The propagation of the neutrinos includes vacuum and matter oscillations with the full three-flavor mixing and neutrino interactions on the way through the Sun such as absorption, energy losses and regeneration from tau decays.

We ran WIMPsim for WIMP mass 4, 6, 10, 20, 50, 80.3 (only for W^+W^- channel), 100 and 200 GeV for $\chi\chi \to b\bar{b}$, $\chi\chi \to W^+W^-$ and $\chi\chi \to \tau^+\tau^-$ annihilation channels assuming 100% brunching fraction of annihilation. For $b\bar{b}$ and W^+W^- channels they started from 6 GeV and 80.3 GeV, respectively instead of 4 GeV due to kinematical restrictions. For each mass and annihilation channel, we simulated 10^6 annihilations. WIMPsim calls the simulator Pythia to simulate the hadronization and decay of the annihilation products at the center of the Sun. And then it collects the produced neutrinos and anti-neutrinos. WIMPs are predicted to be thermalized before annihilation and the initial momenta are neglected. As a result, a neutrino properties at the creation simply are regulated by WIMP mass and annihilation channel.

After that, WIMPsim let all the emerged neutrinos propagate outwards through the solar medium treating neutrino oscillations and interactions simultaneously. Using neutrino-nucleon interaction cross-section, WIMPsim randomizes the frequency of the interaction in the solar medium, which decides the interaction point or let the neutrino pass through without any interaction. On the way to the interaction point, neutrinos are oscillated with total Hamiltonian including MSW potential term, which is calculated for each density layer from the center along the radial direction sliced in reasonable size: a width of 0.3 % of the radius of the Sun. Three-flavor oscillation with parameters: $\theta_{12} = 33.461°, \theta_{13} = 9.097°, \theta_{23} = 40.686°, \delta = 300, \Delta m^2_{21} = 0.766 \times 10^{-4}$ $\text{eV}^2, \Delta m^2_{32} = 0.274 \times 10^{-2}$ eV^2 are used assuming normal mass hierarchy. These values are consistently applied in the treatment of the oscillation effect on both WIMP neutrinos and background (BG) atmospheric neutrinos.

The tracking of neutrinos is once stopped at 1AU from the Sun, then with respect to the time and location of the detector, WIMPsim let the flux propagate forward or backward to the exact distance to the detector, considering the matter effect in the Earth. We generated the flux at the SK location averaging from the spring equinox to the autumn equinox. The final neutrino spectrum delivered at the SK site is shown in Fig. 5.1. Note that the fast oscillating pattern seen in Fig. 2.8 is washed out due to eccentricity of the Earth's orbit, i.e. the variation of the Sun-Earth distance.

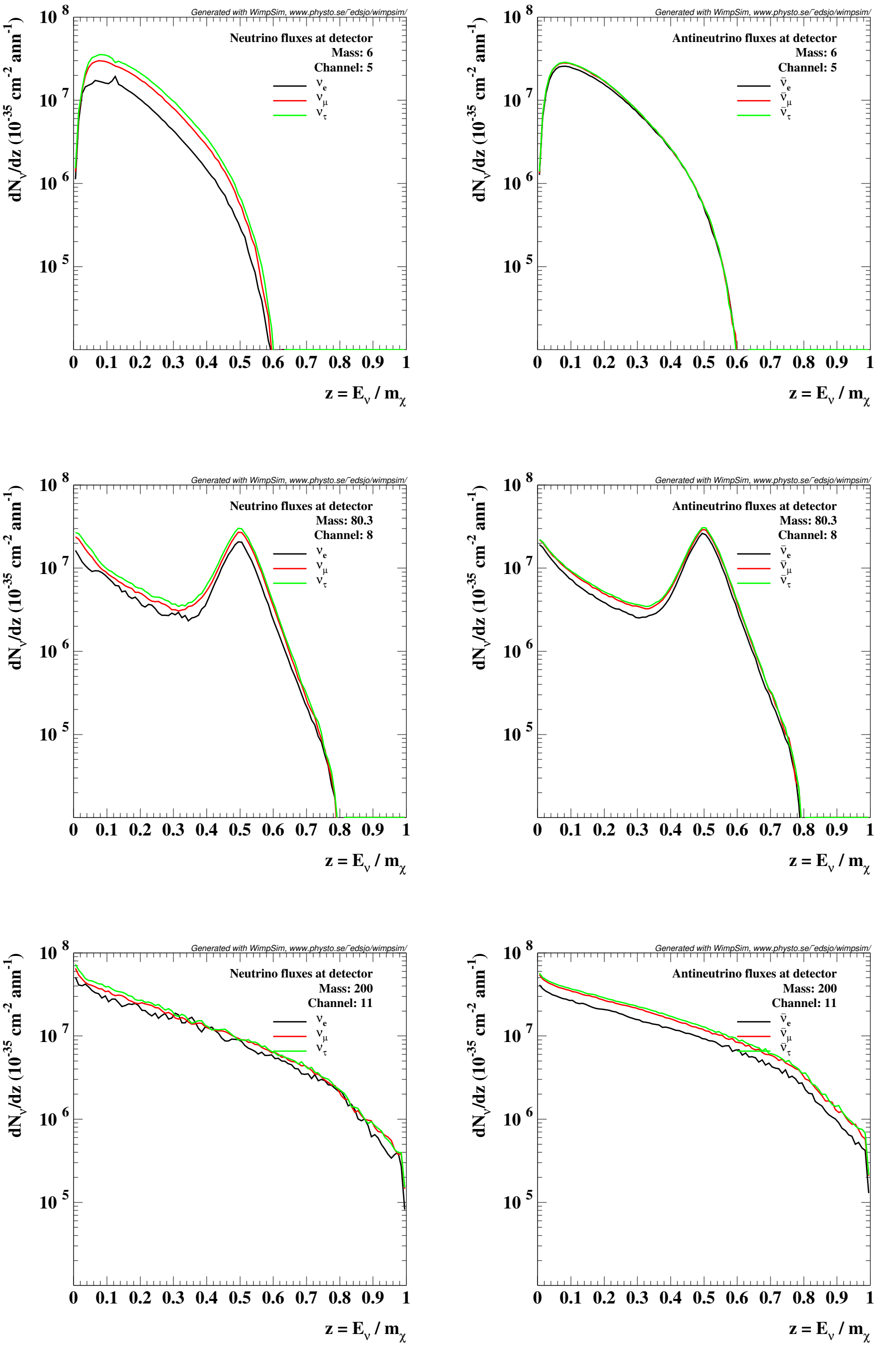

Figure 5.1: The WIMP-neutrino fluxes at the SK site for $m_\chi = 6$ GeV $b\bar{b}$ channel, 80.3 GeV W^+W^- channel, and 200 GeV $\tau^+\tau^-$ channel. The flux is shown as a function of neutrino energy normalized to WIMP mass (z) for neutrino (left column) and anti-neutrino flux (right column).

In this analysis, the neutrino flux before their interactions at the detector or at the surrounding rocks was used to simulate SK events with NEUT and detector simulation.

In summary, the input parameters we used for WIMPsim are:

- Number of annihilation simulated for each hypothesis of WIMP mass and channel: 10,000,000,
- Oscillation parameters: Three-flavor oscillation with parameters: $\theta_{12} = 33.461°, \theta_{13} = 9.097°, \theta_{23} = 40.686°, \delta = 300, \Delta m^2_{21} = 0.766 \times 10^{-4}$ eV^2, $\Delta m^2_{32} = 0.274 \times 10^{-2}$ eV^2 are used assuming normal mass hierarchy, and
- Location of the detector: at SK site (36°25'N, 137°18'E).

Figure 5.1 is an example of neutrino fluxes used in this analysis; the time-averaged differential neutrino flux for six neutrino and anti-neutrino flavors at the SK location. The information of angular distribution is not used because the WIMP-neutrino flux can be regarded to be point-like.

5.3 The WIMP-induced neutrino events at Super-Kamiokande

When the neutrinos from WIMP annihilations arrive at SK, it will produce leptons and hadrons by interaction inside the detector and in the surrounding rocks and water, which can be detected by Cherenkov radiation reaching to PMTs in SK. The existing atmospheric neutrino Monte Carlo simulation (MC) samples which have been already produced in large statistics (500 years for each SK era) to predict atmospheric neutrino induced events in SK were used to simulate WIMP events by reweighting method. We randomly divided the MC samples into two sets which equally have 250 years statistics for each SK era and used for BG and signal MC, respectively.

To have information of the direction of the Sun at event time, date and time information are stored for data. For MC events, date and time are randomly distributed. In the MC set to be used for signal MC, events whose angle between the true neutrino direction and the direction from the Sun at the event time are $< 10°$ and whose true neutrino energies is in the range of $0 \sim$ WIMP mass (GeV) are used to mimic WIMP-induced neutrino events. This choice of the angle ($< 10°$) does not introduce any bias to produce WIMP neutrino MC sample, because the collection of the events inside 10° cone doesn't have a preference of certain direction in the detector coordinate system, also the averaged location of the Sun is almost uniformly distributed in the SK coordinate. We also checked it by MC simulation by making a signal MC with difference choices of angular selection such as 5° and 15°. The result of the analysis shows consistency within the MC statistical limit.

We used all ν_μ, $\overline{\nu}_\mu$, ν_e, $\overline{\nu}_e$, ν_τ and $\overline{\nu}_\tau$ flavors. Table 5.1 shows the number of SK I-IV events used for signal MC compared to the total number of events in atmospheric neutrino MC (500 years, SK I-IV) for each mass and annihilation channel of WIMPs.

	WIMP event	fraction to total event(%)
4 GeV	19228	0.29
6 GeV	20797	0.31
10 GeV	22075	0.33
20 GeV	23112	0.35
50 GeV	23951	0.36
80 GeV	24234	0.36
100 GeV	24336	0.37
200 GeV	24605	0.37

Table 5.1: Number of SK I-IV events used for signal MC, and the fraction to total event number of atmospheric neutrino MC sample (6643287), for each mass and annihilation channel of WIMP.

In the atmospheric neutrino MC, there's a variable "hondaflx" assigned to each MC event, which represents absolute atmospheric neutrino flux defined for each flavor in dimension of $[1/\mathrm{Sr}/\mathrm{GeV}/\mathrm{m}^2/\mathrm{s}]$. This value is interpolated from original Honda flux calculation which has been updated since 2011 by Honda et al. (129). To produce the neutrino spectrum from WIMP annihilations, we reweight the hondaflx value event by event with the weighting factors calculated from the ratio of original hondaflx to the WIMP neutrino flux. For WIMP neutrino flux, the output fluxes from WIMPsim for six neutrino flavors are tabulated in 1000 energy bins whose sizes are $m_\chi/1000$. This procedure was repeated for each WIMP mass and annihilation channel. For the absolute normalization of the total WIMP ν_μ flux set to be $1/\mathrm{km}^2/\mathrm{yr}$, the weight factor is defined to be

$$1/(\pi \sin^2(10^\circ))/(\mathrm{m}_\chi/1000)/10^6/(365 \times 24 \times 3600), \tag{5.1}$$

which is multiplied by 'WIMP neutrino flux' in a bin size

$$[1/10^\circ/(m_\chi/1000\mathrm{GeV})/\mathrm{km}^2/\mathrm{yr}] \tag{5.2}$$

divided by hondaflx$[1/\mathrm{Sr}/\mathrm{GeV}/\mathrm{m}^2/\mathrm{s}]$. The normalization factor for other five flavor fluxes are calculated to hold the relative normalization to ν_μ flux by the additional normalizing factor.

The energy spectrum of original atmospheric neutrino flux and WIMP neutrino fluxes are shown in Fig. 5.2. The atmospheric neutrino fluxes originally have large variance in 3D angular distribution, therefore they are shown after averaging in each energy bin. The WIMP neutrino fluxes are shown for representative samples which is expected to have the softest (6 GeV $b\bar{b}$) and the harder (200 GeV $\tau^+\tau^-$) spectrum among tested hypotheses.

The reconstructed momentum distributions for the signal MC sample before and

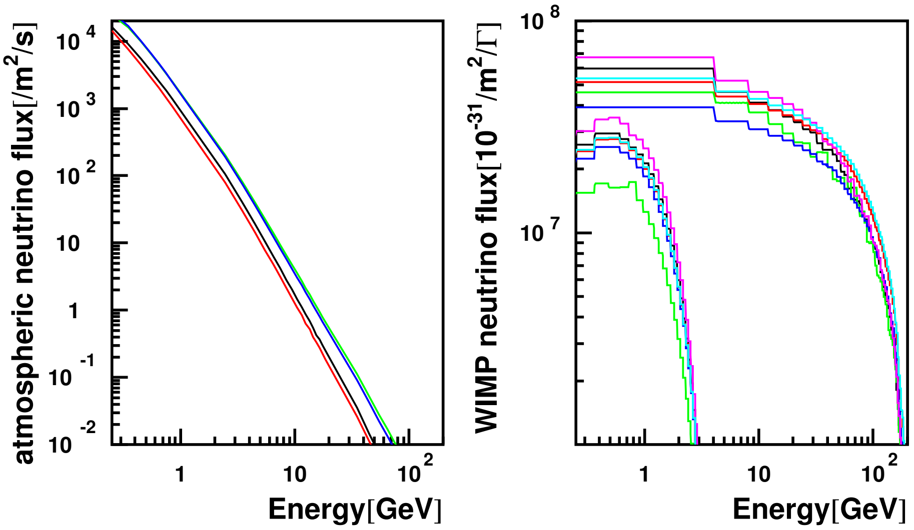

Figure 5.2: Left: True energy spectrum of unoscillated atmospheric muon-neutrino (ν_μ) (black), $\overline{\nu}_\mu$ (red), ν_e (green) and $\overline{\nu}_e$ (blue). Right: True energy spectrum of WIMP neutrinos per annihilation for 6-GeV $b\bar{b}$ channel, and 200-GeV $\tau^+\tau^-$ channel shown together (colors are the same as on the left, and ν_τ (magenta) and $\overline{\nu}_\tau$ (cyan)).

after weighting are shown in Fig. 5.3 for 6 GeV $b\bar{b}$ and 200 GeV $\tau^+\tau^-$ hypotheses, respectively.

5.4 atmospheric neutrino flux

The flux model calculated by M. Honda et al. (126) (127) (128) (129)(the Honda flux) is mainly used to predict the atmospheric neutrino flux coming in SK. For the higher energy neutrinos which the Honda model doesn't predict, the Volkova flux (132) is applied for energy above 10 TeV.

Figure 5.4 shows the primary cosmic ray flux model used in the Honda model (solid line) together with experimental measurements.

Primary protons and nuclei may interact with molecules in the Earth's atmosphere and produce secondary particles such as pions and kaons through hadronic interactions. In the Honda model, the US standard atmosphere model (145) is used to reproduce the density structure of the atmosphere.

Atmospheric neutrinos are produced by decays of pions and kaons:

$$\pi^+ \to \quad \mu^+ \quad +\nu_\mu \tag{5.3}$$

$$\hookrightarrow \; e^+ + \nu_e + \bar{\nu_\mu}, \tag{5.4}$$

$$\pi^- \to \quad \mu^- \quad +\bar{\nu_\mu} \tag{5.5}$$

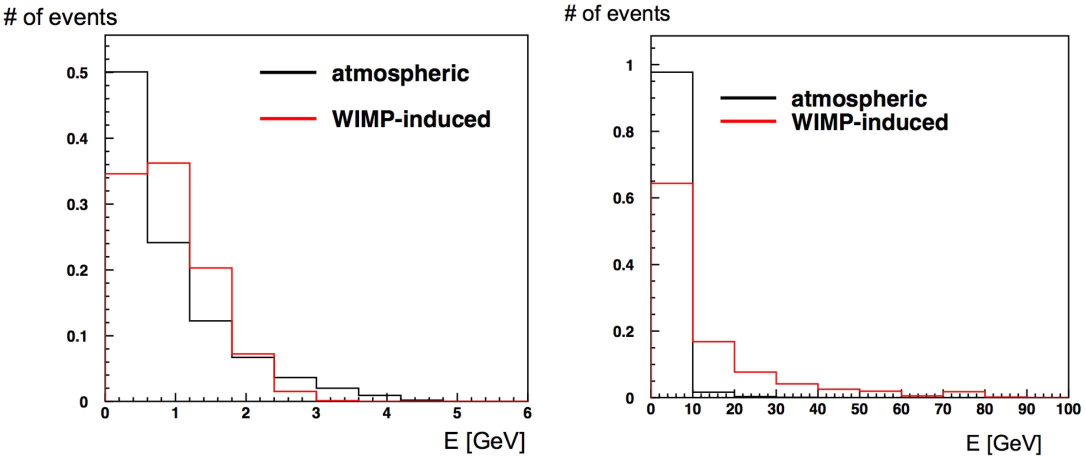

Figure 5.3: The reconstructed momentum distributions of signal MC before (black) and after (red) weighting for 6 GeV $b\bar{b}$ channel (left) and for 200 GeV $\tau^+\tau^-$ (right) channel are shown. Y axis shows the number of WIMP events whose normalization is arbitrary.

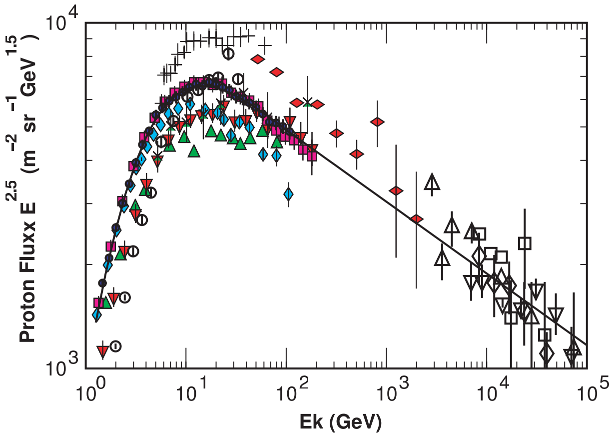

Figure 5.4: Primary cosmic ray flux used in Honda model (black solid). Also shown are the results from observations: Webber (133) (crosses), LEAP (134) (upward triangles), MASS1 (135) (open circles), CAPRICE (136) (vertical diamonds), IMAX (137) (downward triangles), BESS98 (138) (circles), AMS (139) (squares), Ryan (140) (horizontal diamonds), JACEE (141) (downward open triangles), Ivanenko (142) (upward open triangles), Kawamura (143) (open squares) and Runjob (144) (open diamonds). Figure is taken from (126).

$$\hookrightarrow \quad e^- + \bar{\nu}_e + \nu_\mu \tag{5.6}$$

The flavor ratio between $\nu_\mu + \bar{\nu}_\mu$ and $\nu_e + \bar{\nu}_e$ is about 2 for neutrino energies below a few GeV and becomes larger as neutrino energy increases, as more secondary muons reach the ground before decaying.

The energy spectrum of atmospheric neutrinos at the SK site is shown in Fig. 5.5 for the Honda model in comparison to other models as well as previous version of the Honda model. The flux is calculated in the 3-dimensional way and shown in average over the 3-dimensional directions.

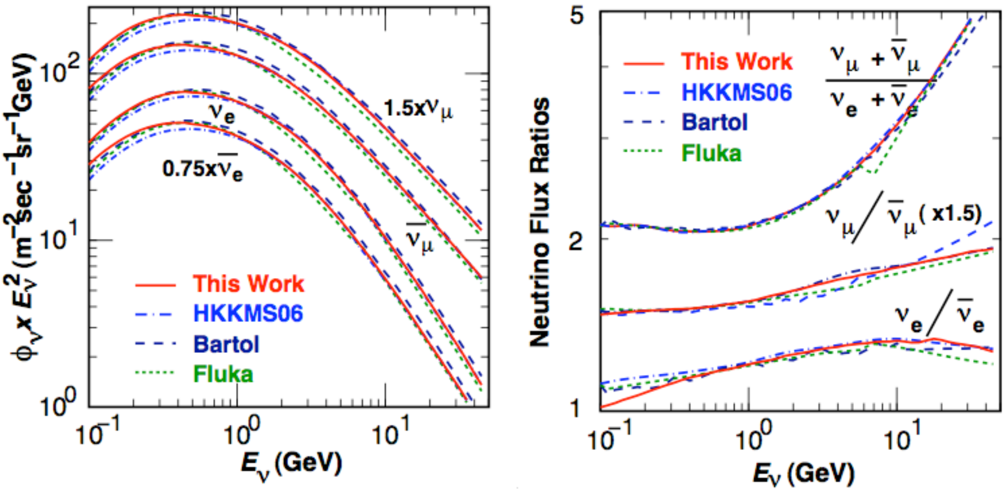

Figure 5.5: The energy spectrum of atmospheric neutrinos at the SK site for the Honda model (left) and the flavor ratio and neutrino/anti-neutrino ratios (right). Also shown are the calculations from other models: the Bartol model (146) (dashed line) and the FLUKA model (147) (dotted line). The previous version of Honda model (126) is shown as well (dot-dashed line). Figure is taken from (129).

5.5 Atmospheric neutrino oscillation

As quarks mix themselves in weak interaction, the leptons would do the same; differently from quarks, the definition of neutrinos is set on weak eigen states. The phenomena of neutrino oscillations were first proposed by Maki, Nakagawa, Sakata (148) and Pontecorvo (149). It was proposed for three lepton flavors, and the full three-flavor mixing is observed by the recent experiments.

A flavor eigenstate of neutrino can be written as a superposition of three mass eigenstates:

$$\mid \nu_\alpha\rangle = \sum_{i=1}^{3} U_{\alpha i} \mid \nu_i\rangle \tag{5.7}$$

where $\mid \nu_\alpha\rangle$ is the flavor eigenstate with the α corresponds to e, μ or τ, and $\mid \nu_i\rangle$ is the mass eigenstate, where i corresponds to 1,2 and 3. The unitary mixing matrix U is generally parameterized by three mixing angles (θ_{12}, θ_{23} and θ_{13}) and a single phase δ relating to charge-parity (CP) violation as:

$$U = \begin{pmatrix} 1 & 0 & 0 \\ 0 & \cos\theta_{23} & \sin\theta_{23} \\ 0 & -\sin\theta_{23} & \cos\theta_{23} \end{pmatrix} \times \begin{pmatrix} \cos\theta_{13} & 0 & \sin\theta_{13}e^{-i\delta} \\ 0 & 1 & 0 \\ -\sin\theta_{13}e^{i\delta} & 0 & \cos\theta_{13} \end{pmatrix} \times \begin{pmatrix} \cos\theta_{12} & \sin\theta_{12} & 0 \\ -\sin\theta_{12} & \cos\theta_{12} & 0 \\ 0 & 0 & 1 \end{pmatrix}. \tag{5.8}$$

The time evolution of the flavor eigenstate is represented as:

$$\begin{aligned} \mid \nu_\alpha(t)\rangle &= \sum_i U_{\alpha i} exp(-iE_i t) \mid \nu_i(0)\rangle & (5.9) \\ &= \sum_i \sum_{\alpha'} U_{\alpha i} U^*_{\alpha' i} exp(-iE_i t) \mid \nu_{\alpha'}(0)\rangle, & (5.10) \end{aligned}$$

where $\mid \nu(t)\rangle$ is a neutrino state at time t, E_i is the energy of the mass eigenstate $\mid \nu_i\rangle$. The probability of the initial state ν_α to oscillate to state ν_β at t is:

$$\begin{aligned} P(\nu_\alpha \to \nu_\beta) &= \mid \langle \nu_\beta(t) \mid \nu_\alpha(0)\rangle \mid^2 & (5.11) \\ &= \mid \sum_i U_{\beta i} U^*_{\alpha i} exp(-iE_i t) \mid^2 & (5.12) \\ &= \sum_i \mid U_{\alpha i} U_{\beta i} \mid^2 + \sum_{i \neq j} U_{\alpha i} U^*_{\beta i} U^*_{\alpha j} U_{\beta j} exp(-i(E_i - E_j)t). & (5.13) \end{aligned}$$

5.5.1 Two-flavor oscillation in atmospheric neutrinos

As mentioned above, atmospheric neutrinos are produced by decays of mesons which are generated through the primary cosmic rays interactions in the atmosphere.

$\nu_\mu \to \nu_\tau$ 2-flavor oscillation is good approximation for predicting atmospheric neutrino flux detected on the ground base. The mixing matrix U can be simplified in two-flavor mixing case:

$$U = \begin{pmatrix} \cos\theta & \sin\theta \\ -\sin\theta & \cos\theta \end{pmatrix}, \tag{5.14}$$

and the transition probability in equation (5.13) can be simplified to:

$$P(\nu_\alpha \to \nu_\beta) = \sin^2(2\theta)\sin^2(\frac{(E_i - E_j)t}{2}). \tag{5.15}$$

In the relativistic limit, $|p| \gg m$, the following approximation is allowed:

$$\begin{aligned} E_i - E_j &= \sqrt{(m_i^2 + p_i^2)} - \sqrt{(m_j^2 + p_j^2)} && (5.16)\\ &\approx (p + \frac{m_i^2}{2p}) - (p + \frac{m_j^2}{2p}) && (5.17)\\ &\approx \frac{\Delta m_{ij}^2}{2E}, && (5.18) \end{aligned}$$

where $\Delta m_{ij}^2 \equiv m_i^2 - m_j^2$ is the difference in squared masses.

Combining equations 5.18 and 5.15, the survival probability of ν_α can be written as:

$$\begin{aligned} P(\nu_\alpha \to \nu_\alpha) &= 1 - \sin^2 2\theta \sin^2(\frac{\Delta m_{ij}^2 L_\nu}{4E_\nu}) && (5.19)\\ &= 1 - \sin^2 2\theta \sin^2(\frac{1.27\Delta m_{ij}^2(\text{eV}^2)L_\nu(\text{km})}{E_\nu(\text{GeV})}). && (5.20) \end{aligned}$$

Hence the oscillation probability depends on the mixing angle θ, the mass square difference Δm_{ij}^2, neutrino flight length L_ν and neutrino energy E_ν.

The atmospheric neutrino flux peaks at around 40 MeV and extends to above TeV. Atmospheric neutrino experiments usually have good sensitivity for neutrino energies above a few hundreds MeV. Neutrino flight length ranges from about 15 km to the diameter of the Earth (~13000 km, produced at the other side of the Earth). Therefore observation of atmospheric neutrinos can confine the oscillation parameter Δm^2, if it is lied within $10^{-1} \sim 10^{-4}$ eV^2 as well as the mixing angle θ. As the prediction of the flavor ratio $(\nu_\mu + \bar{\nu_\mu})/(\nu_e + \bar{\nu}_e)$ is about 2% accurate for neutrino energy below 10 GeV (126), the measured flavor ratio which was roughly one half of what was expected, led the discovery of neutrino oscillation in atmospheric neutrinos, and the precise measurement of the Δm^2 and θ values (150; 151; 152; 153; 154).

Super-Kamiokande (SK) reported in 1998 the zenith angle dependent deficit of neutrinos (155) (Figure 5.6). It was reported that the observation was consistent with the $\nu_\mu \leftrightarrow \nu_\tau$ oscillation hypothesis with $\sin^2(2\theta) > 0.82$ and $5 \times 10^{-4} < \Delta m^2 < 6 \times 10^{-3}$ eV^2 at 90% confidence level. Later SK provided a L/E analysis(156) as shown in Fig. 5.7.

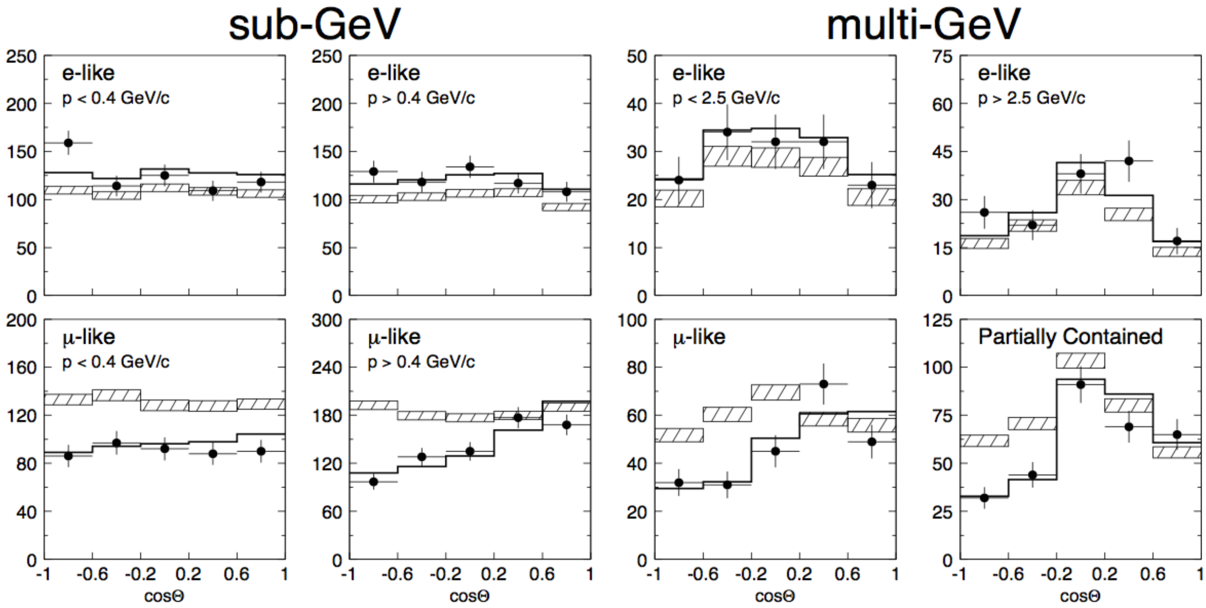

Figure 5.6: Zenith angle distributions of sub-GeV events (left) and multi-GeV events (right). The hatched regions show the MC expectation for no oscillations with statistical errors and the solid lines show the best-fit expectation for $\nu_\mu \leftrightarrow \nu_\tau$ oscillations. MCs are normalized to the data livetime. Figure is taken from (155).

5.5.2 Full three-flavor neutrino oscillation in atmospheric neutrinos

The discovery of non-zero neutrino mixing angle θ_{13} by the T2K and reactor experiments (157) excited the world by opening the possibility to measure CP violation in lepton sector. Equation 5.8 shows that, in order to access the leptonic CP violation phase δ, the mixing angle θ_{13} must be nonzero.

The SK atmospheric neutrino data doesn't have a good sensitivity to constrain θ_{13} solely, but as it covers a wide range of L/E_ν and can detect ν_e, it is possible to analysis the data in the three-flavor mixing framework in one mass scale dominance approximation.

The Earth contains a large number of electrons and ν_e interacts with them via CC while traversing the Earth. Therefore in three-flavor oscillation, matter effect (158; 159) plays an important role. In order to describe the oscillation effect due to these effects and the interference of them, full oscillation parameters are taken into account, including the CP violation phase δ.

When considering all oscillation parameters, $\nu_\mu \leftrightarrow \nu_e$ transition probability in constant matter density is:

$$\begin{aligned} P(\nu_\mu \leftrightarrow \nu_e) &= \cos^2\widetilde{\theta}_{13}\cos^2\theta_{23}P_{e2} \\ &\quad +\sin^2\widetilde{\theta}_{13}\cos^2\widetilde{\theta}_{13}\sin^2\theta_{23}(2-P_{e2}) \\ &\quad -2\sin^2\widetilde{\theta}_{13}\cos^2\widetilde{\theta}_{13}\sin\theta_{23}\cos\theta_{23}(\cos\delta R_2-\sin\delta I_2), \end{aligned} \tag{5.21}$$

where

$$P_{e2} = \sin^2 2\theta_{12,M}\sin^2\frac{\phi_m}{2} \tag{5.22}$$

$$R_2 = -\sin 2\theta_{12,M}\cos 2\theta_{12,M}\sin^2\frac{\phi_m}{2} \tag{5.23}$$

$$I_2 = -\frac{1}{2}\sin 2\theta_{12,M}\sin\phi_m. \tag{5.24}$$

ϕ_m is the phase of oscillation in matter, and $\widetilde{\theta}_{13}$ is the mixing angle in matter with $\widetilde{\theta}_{13} \approx \theta_{13,M}$ (160).

Figure 5.8 shows P($\nu_\mu \to \nu_e$) as a function of zenith angle and neutrino energy. The ratio between the expected electron events (N_e) and the non-oscillation electron events (N_e^0) is:

$$\frac{N_e}{N_e^0} = (P_{ee}-1)+rP_{e\mu} \tag{5.25}$$

$$\simeq \Delta_1(\theta_{13})+\Delta_2(\theta_{12},\Delta m^2_{21})+\Delta_3(\theta_{13},\theta_{12},\Delta m^2_{21},\delta), \tag{5.26}$$

where $r = N_\mu/N_e$, and $r \sim 2$ to 3.5 in ~100 MeV to ~10 GeV. The phenomenon of electron neutrino oscillation appears in wide range of energy as shown in Fig. 5.8.

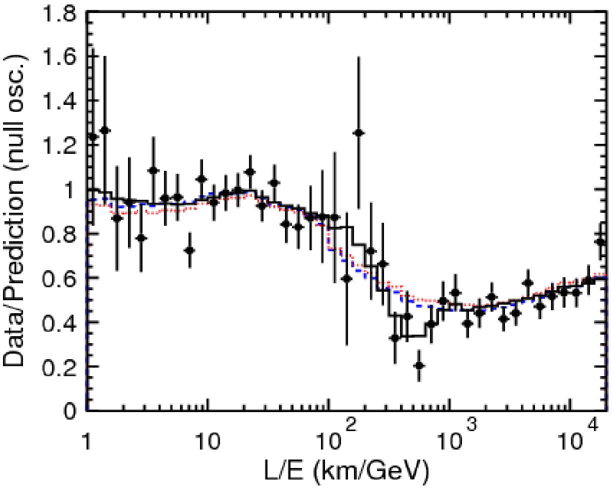

Figure 5.7: The ratios of data to unoscillated MC as a function of the L/E with statistical error (points) and the ratio of oscillated MC with the best-fit expectation for $\nu_\mu \leftrightarrow \nu_\tau$ oscillations to unoscillated MC (solid line). Also shown are the best-fit expectation for other scenarios such as neutrino decay (dashed line) and neutrino decoherence (dotted line). Figure is taken from (156).

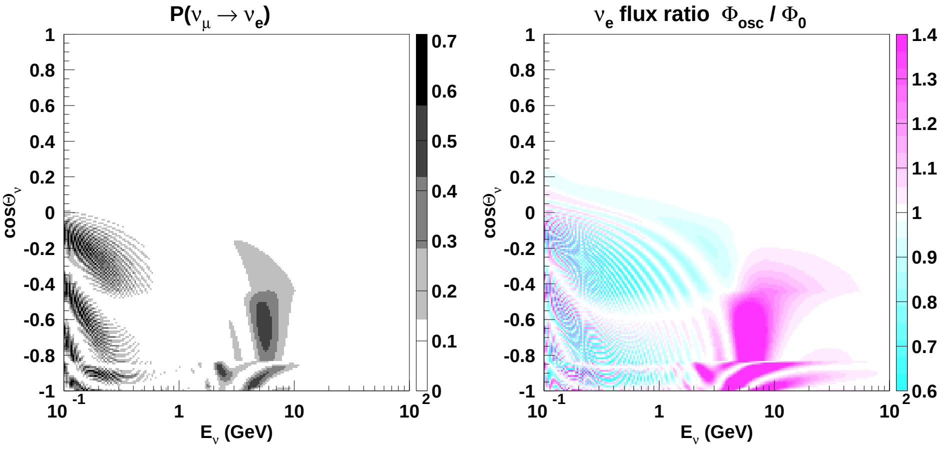

Figure 5.8: Left: Probability of $\nu_\mu \rightarrow \nu_e$ oscillation as a function of zenith angle and neutrino energy, in case of (Δm^2_{21}, Δm^2_{32}, $\sin^2\theta_{12}$, $\sin^2\theta_{23}$, $\sin^2\theta_{13}$, δ) = (7.7×10^{-5}, 2.1×10^{-3}, 0.3, 0.5, 0.04, 0). Right: The ν_e flux ratio Φ_{osc}/Φ_0 assuming the same oscillation parameters as the left figure. Figures are taken from (124).

The global best fit results of neutrino oscillation parameters used to oscillate atmospheric neutrino MC events assuming normal hierarcy in this analysis are summarized in Tab. 5.2 assuming normal hierarchy.

Parameter	used value
θ_{12}°	33.461
θ_{13}°	9.097
θ_{23}°	40.686
Δm^2_{32}	0.274×10^{-2} eV^2
Δm^2_{21}	0.766×10^{-4} eV^2
δ	300

Table 5.2: Summary of global fit values of neutrino oscillation parameters used in the analysis.

5.6 Neutrino interaction

The simulation library called "NEUT" (130) (131) is used to simulate the neutrino interactions with proton, oxygen and other nuclei. When a neutrino scatters off a nucleus, it actually interacts with a quark bound in a nucleon, which is bound in a nucleus by strong force. As a neutrino only interacts via weak force, charged current (CC) and neutral current (NC) weak interactions are to be considered. Figure 5.9 shows the Feynman diagrams of NC and CC interactions.

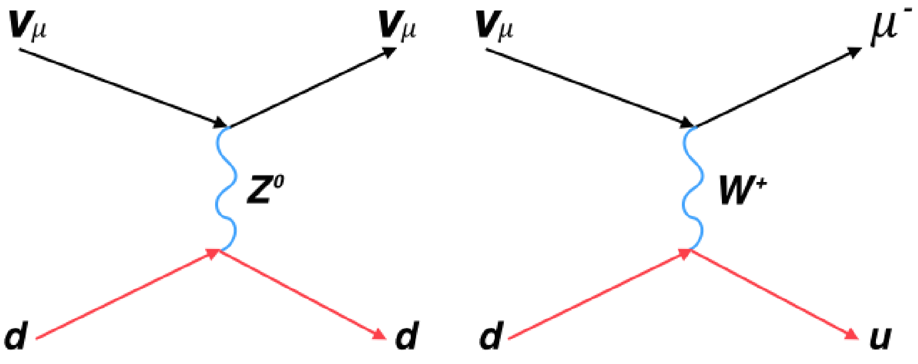

Figure 5.9: Feynman diagrams of neutrino-quark NC (left) and CC (right) interactions.

In the NC interaction, the neutrino scatters elastically off the quark where the outgoing neutrino cannot be detected in a water Cherenkov detector. In the CC interaction, the out-going particle is a charged lepton, which can be detected by Cherenkov radiation.

NEUT covers the neutrino interactions as following:

- CC/NC (quasi-)elastic scattering: $\nu + N \rightarrow l + N'$
- CC/NC resonance single meson production: $\nu + N \rightarrow l + N^* + meson$
- CC/NC deep inelastic interaction: $\nu + N \rightarrow l + N' + hadrons$
- CC/NC coherent pion production: $\nu +^{16} O \rightarrow l +^{16} O + \pi$,

where N and N' are the nucleons (proton or neutron), N^* is baryon resonance and l is a lepton.

5.6.1 Elastic and quasi-elastic scatterings

The differential cross section $d\sigma/dq^2$ for charged current quasi-elastic (CCQE) interaction of anti-neutrino off free proton can be written as (161):

$$\frac{d\sigma}{dq^2} = \frac{m_p^2 G_F^2 cos^2\theta_C}{8\pi E_\nu^2}[A(q^2) + B(q^2)\frac{s-u}{m_p^2} + C(q^2)\frac{(s-u)^2}{m_p^4}], \tag{5.27}$$

where m_p is the proton mass, G_F is the Fermi coupling constant, θ_C is the Cabibo angle, E_ν is the neutrino energy, q is the four-momentum transferred to the lepton, s and u are Mandelstam variables (161) and the form factors A, B and C are:

$$\begin{aligned} A(q^2) &= \frac{m_l^2 - q^2}{4m_p^2}[(4 - \frac{q^2}{m_p^2})|F_A|^2 - (4 + \frac{q^2}{m_p^2})|F_V^1|^2 \\ &\quad - \frac{q^2}{m_p^2}|\xi F_V^2|^2(1 + \frac{q^2}{4m_p^2}) - \frac{4q^2 F_V^1 \xi F_V^2}{m_p^2} \\ &\quad - \frac{m}{m_p}((F_V^1 + \xi F_V^2)^2 + |F_A|^2)], \qquad (5.28) \\ B(q^2) &= \frac{q^2}{m_p^2}(F_A(F_V^1 + \xi F_V^2)), \qquad (5.29) \\ C(q^2) &= \frac{1}{4}(|F_A|^2 + |F_V^1|^2 - \frac{q^2}{4m_p^2}|\xi F_V^2|^2), \qquad (5.30) \end{aligned}$$

where m_l is the outgoing lepton mass, $F_V^1(q^2)$ and $F_V^2(q^2)$ are vector form factors, $F_A(q^2)$ is axial vector form factor and ξ is the anomalous magnetic moment $\mu_p - \mu_n$ which is set to be 3.71. The form factors are determined from the experiments.

In the calculation of the cross sections of neutral current elastic scattering, $cos\theta_C$ in the Eq. 5.27 is replaced with unity, and the nucleon form factors are replaced by corresponding factors (162).

For the scattering off ^{16}O, as the protons are not free but are bound in nucleus, Fermi motion of the nucleon and Pauli principle are taken into account. The calculation is done based on the Smith and Moniz Fermi-gas model (163).

Figure 5.10 shows the total cross section of CCQE scattering as comparing the NEUT calculation with experimental data.

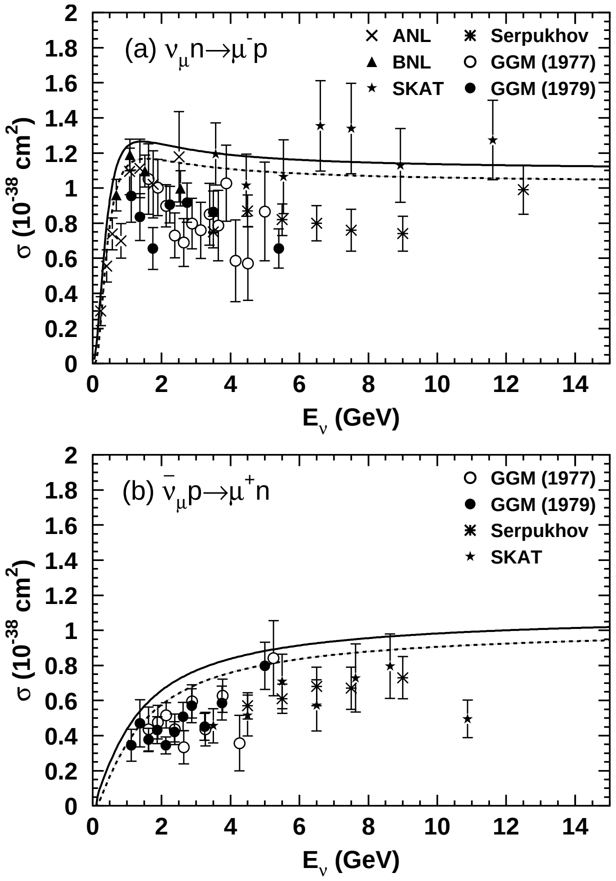

Figure 5.10: The CCQE scattering cross section of (a) ν_μ off neutron and (b) $\bar{\nu_\mu}$ off proton are shown as a function of neutrino energy. Solid line indicates the scattering off a free proton, the dashed line indicates scattering off a bound nucleon in ^{16}O. The experimental data from ANL (164), Gargamelle (165) (166; 167), BNL (168), Serpukhov (169) and SKAT (170) are shown together. Figure is taken from (125).

5.6.2 Resonance single meson production

The simulation of the resonance productions of single π, η and K is adopted from Rein and Sehgals model (171). The interaction process is separated into two parts as:

$$\nu + N \to l + N^* \tag{5.31}$$

$$N^* \to meson + N'. \tag{5.32}$$

Where the invariant mass of the intermediate resonance W is $\lesssim$ 2 GeV, resonance production of single meson often ($\sim$ 80%) occurs. In order to avoid double counting of the interactions, the W is restricted to be less than 2 GeV. As a result, eighteen resonances below 2 GeV are considered in the calculation. The angular distribution of the π in the final state for the $P_{33}(1232)$ resonance followed the Rein and Sehgal's method, and the angular distributions of the π in the other resonances are set to be isotropic in the resonance rest frame. Pauli-blocking effect for nucleons from Δ decays is taken into account by applying minimum momentum cut. Pion-less Δ decay is also considered which turns out to compose 20% of the Δ decay events.

Figure 5.11 and 5.12 show charged-current cross section of single meson production for ν_μ and $\bar{\nu_\mu}$ respectively.

5.6.3 Deep inelastic scattering

The cross section for charged-current deep inelastic scattering of neutrino or anti-neutrino off nucleon is given by integrating the following equation for the invariant mass W > 1.3 GeV (172):

$$\frac{d^2\sigma}{dxdy} = \frac{G_F^2 m_p E_\nu}{\pi}((1 - y + \frac{y^2}{2} + C_1)F_2(x, q^2) \pm y(1 - \frac{y}{2} + C_2)xF_3(x, q^2)), \tag{5.33}$$

where E_ν and E_l are the energy of incoming neutrino and outgoing lepton in the laboratory frame, respectively, $x = -q^2/(2M(E_\nu - E_l))$ and $y = (E_\nu - E_l)/E_\nu$ are the Bjorken scaling parameters and the factors C_1, C_2 are:

$$(5.34)$$

$$C_1 = \frac{yM_l^2}{4m_p E_\nu x} - \frac{xym_p}{2E_\nu} - \frac{m_l^2}{4E_\nu^2} - \frac{m_l^2}{2m_p E_\nu x}$$

$$C_2 = -\frac{m_l^2}{4m_p E_\nu x}. \tag{5.35}$$

F_2 and xF_3 are the nucleon structure functions taken from GRV98 (173) and from the A. Bodek and U.K. Yang's correction for the lower q^2 region (174).

In the region $1.3 < W < 2.0$ GeV, only pions are considered as outgoing mesons and in order to not overlap with the single pion production previously described, only

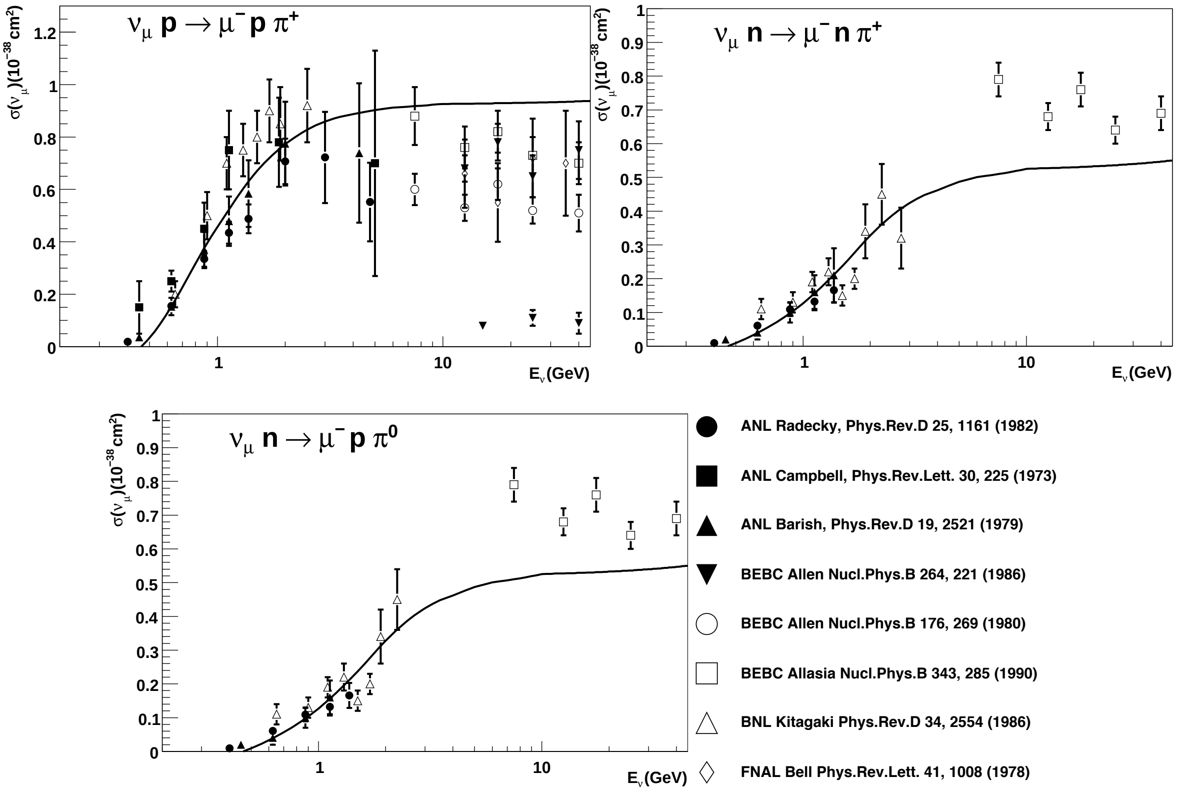

Figure 5.11: The charged-current single pion production cross sections for ν_μ as a function of neutrino energy. The solid lines show the NEUT calculations and the experimental data are shown together with error bars. Figure taken from (125).

multi-π production is considered. The mean multiplicity of produced charged pions is taken from the Fermilab 15-foot hydrogen bubble chamber experiment (175) result which was:

$$< n_\pi >= 0.09 + 1.83 ln W^2. \tag{5.36}$$

In the region $W > 2.0$ GeV, the PHYTIA/JETSET (176) simulations are used to treat π, K, η, ρ productions and so on.

The charged-current DIS cross section for ν_μ and $\bar{\nu_\mu}$ are shown in Fig. 5.13.

5.6.4 Coherent pion production

When the four-momentum transfer from neutrino to the oxygen nucleus is small, the nucleus recoils as a whole, unfragmented, which is called “coherent scattering”. When

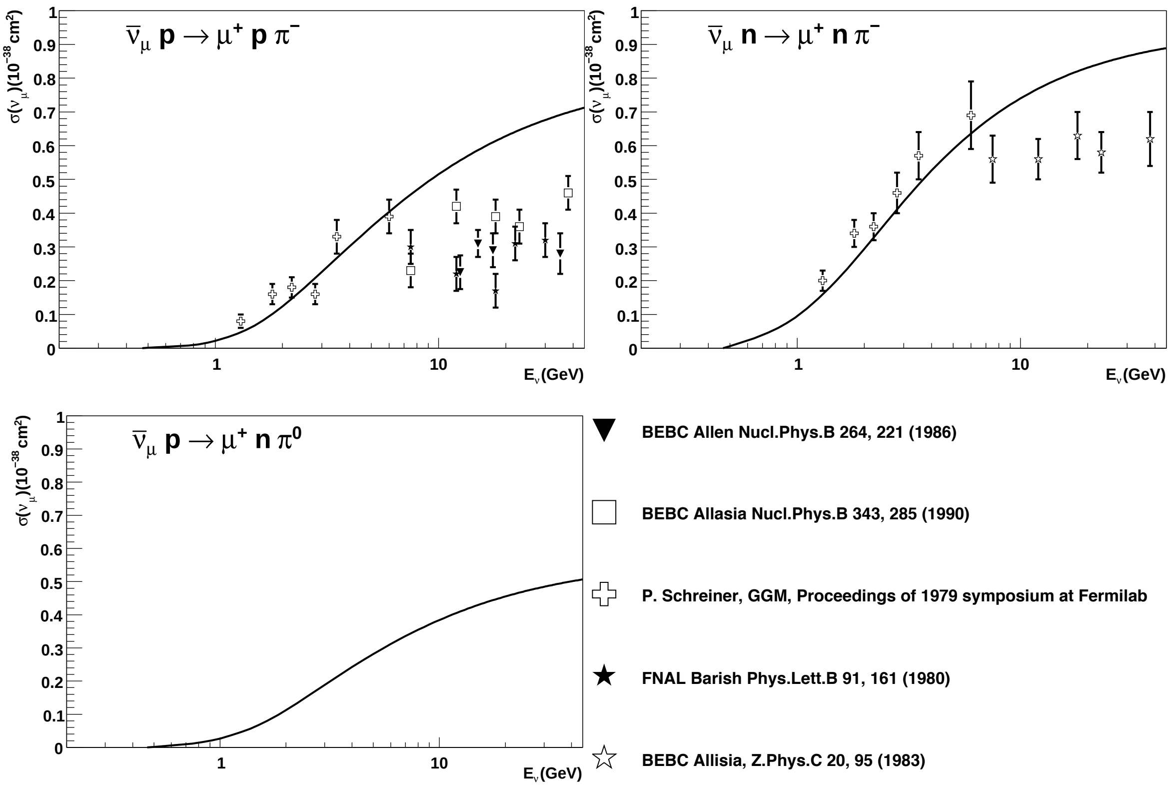

Figure 5.12: The charged-current single pion production cross sections for $\bar{\nu_\mu}$ as a function of neutrino energy. The solid lines are the NEUT calculations and the experimental data are shown together with error bars. Figure taken from (125).

neutrino energy is enough high, the coherent scattering results in the production of an additional particle such as a pion.

The simulation of the coherent pion production is based on the modified Rein and Sehgal model (177). The differential cross section is expressed as follows:

$$\frac{d^3\sigma}{dq^2dydt} = \frac{G^2 m_p}{2\pi^2} f_\pi^2 A^2 E_\nu (1-y) \times \frac{1}{16\pi}[\sigma_{tot}^{\pi N}]^2 \tag{5.37}$$

$$\times(1+r^2)(\frac{m_A^2}{m_A^2+q^2})^2 e^{-b|t|} F_{abs}, \tag{5.38}$$

$$\text{with} \tag{5.39}$$

$$r = \mathrm{Re} f_{\pi N}(0)/\mathrm{Im} f_{\pi N}(0), \tag{5.40}$$

where t is the square of the four-momentum transferred to the nucleus, m_A is the axial-vector mass, $f_\pi = 0.93 m_\pi$, $b = 80\mathrm{GeV}^{-2}$, G is the weak coupling constant, and

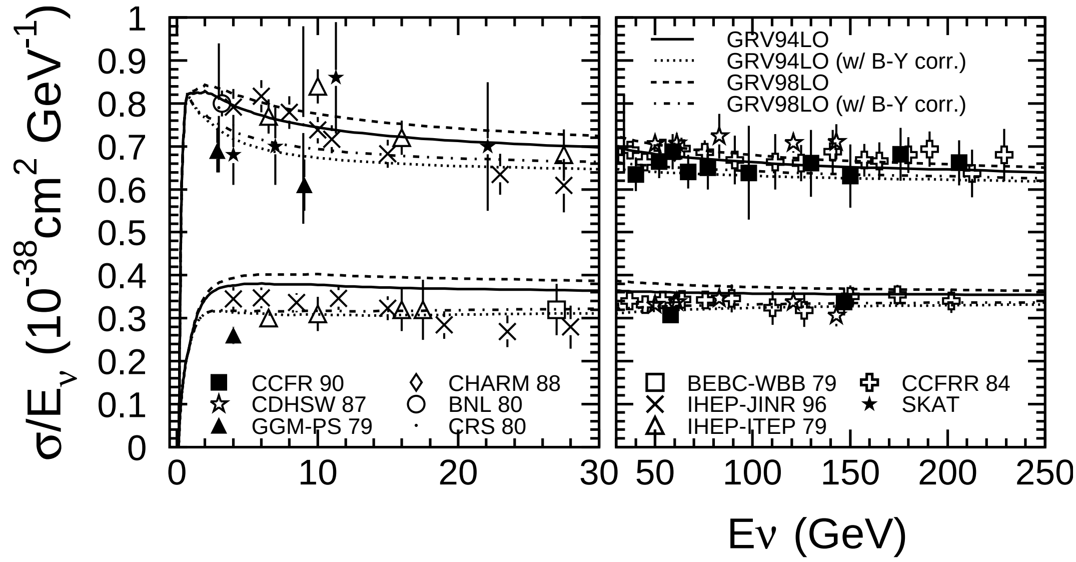

Figure 5.13: The charged-current DIS cross sections for ν_μ (upper lines and points) and $\bar{\nu_\mu}$ (lower lines and points) are shown as a function of neutrino energy.The current used one is the GRV98 model with the B-Y correction (dot-dashed lines). The experimental data are shown together with error bars. Figure taken from (125).

$A = 16$ is the atomic number of oxygen respectively. F_{abs}, which accounts for the absorption of pion in the nucleus, is as taken to be following form:

$$F_{abs} = e^{-<x>/\lambda}, \tag{5.41}$$

$$\text{with} \tag{5.42}$$

$$\lambda^{-1} = \sigma^{\pi N}_{inel}\rho, \tag{5.43}$$

where ρ is the nuclear density. $\sigma^{\pi N}_{tot}$ and $\sigma^{\pi N}_{inel}$ are the averaged total and inelastic cross sections respectively, taken from the experimental results.

Figure 5.14 shows the charged-current coherent pion cross-section used in NEUT together with experimental limits.

5.6.5 Nuclear effects

When secondary particles are produced through the neutrino interaction with a ^{16}O nucleus or other nuclei in the rock, the subsequent interactions of them within the nucleus are simulated. All of the mesons are tracked from the production points to either the exiting points or the absorption points in the nuclei. For pion interaction, inelastic scattering, charge exchange and absorption are considered. When pion scatters, the Fermi motion and Pauli blocking effect are taken into account. The interaction probabilities for pion momenta $p_\pi \leq 500$ MeV/c is calculated based on the model of

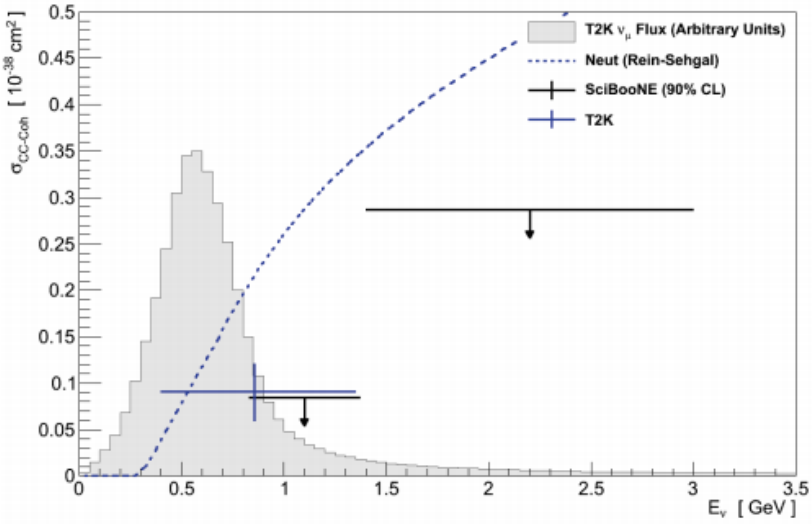

Figure 5.14: The flux-averaged ν_μ charged-current coherent pion cross-section from Rein-Sehgal model, used in NEUT is shown with measurements in SciBooNE (178) and in T2K (179) using the NEUT Rein-Sehgal model. Figure is taken from (179).

Salcedo et al. (180). For the case of p_π> 500 MeV/c, scattering cross section of $\pi^\pm$ off free proton is used. For kaon interaction, elastic scattering and charge exchange are considered by using the cross sections measured by $K^\pm - N$ scattering experiments (181) (182) (183). For η interactions, the absorption interaction $\eta N \rightarrow N^* \rightarrow \pi(\pi)N$ is considered (184). The secondary interactions of nucleons generated inside the oxygen are also treated. The nucleon-nucleon elastic scattering cross section bases on the measurements by Bertini et al. (185). A single or two delta(s) production is also considered and the pion production from decay of produced Δs is also taken into account using the isobar production model by Lindenbaum et al. (186). Total cross section calculated by using NEUT including quasi-elastic scattering, resonant single pion production, coherent pion production and deep inelastic scattering, together with individual components for ν_μ interaction with a nucleon bound in oxygen nucleus is shown in Fig. 5.15.

5.7 Detector simulation

The detector simulation, “SKdetsim” has been developed based on the GEANT3 program (188). In the SKdetsim, propagation of particles considering further interactions and production of secondary particles, generation and propagation of Cherenkov photons, and the response of PMTs and the detector electronics are considered. The simulation is tuned using calibration measurements.

Hadronic interactions in water are simulated with the CALOR package (189). In this package, pion interactions are well simulated until low energy region (about 1

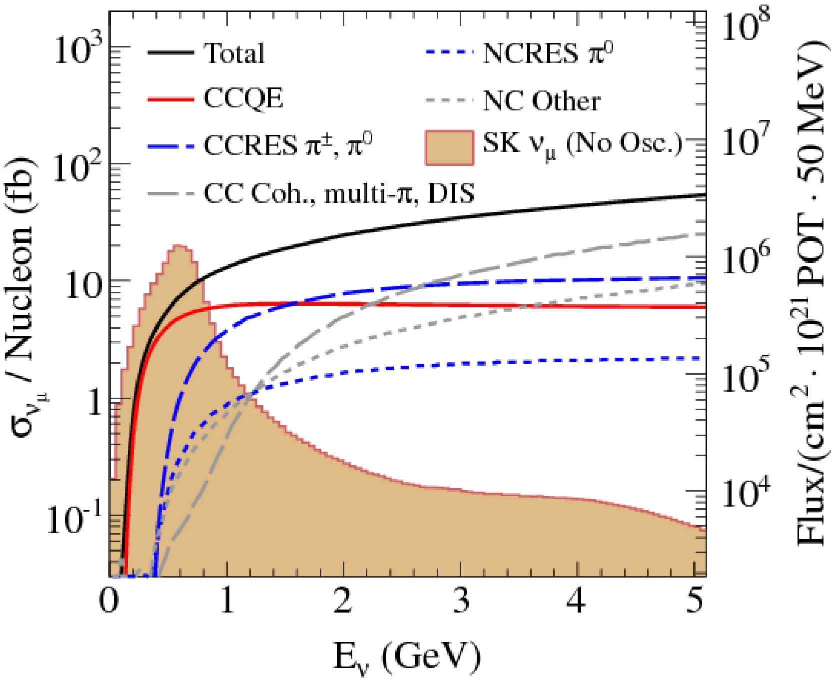

Figure 5.15: The NEUT total interaction cross section and individual components for ν_μ interaction with a nucleon bound in ^{16}O. The colored region shows the predicted ν_μ flux spectrum at SK without oscillation for comparison. Figure is taken from (187).

GeV/c). For lower energy region ($p_\pi \leq 500$ MeV/c), the NEUT cascade model is used.

GEANT3 controls the production and propagation of Cherenkov light, as well as processing any particle decays and interactions through the water that are required. For Cherenkov photons, Rayleigh scattering, Mie scattering and absorption are sumilated during propagation in the water. Also reflection and absorption at the detector surface are properly considered. The PMTs collect generated photons according to the quantum efficiency obtained by the calibration measurement. The detected charge of each hit PMT is decided according to the random number which are distributed following the measured average single-p.e. distribution as shown in Fig. 5.16.

Finally, the electronic response of the detector is generated considering the timing response of PMTs. The relation between timing and charge is measured using laser calibration. The timing of each PMT is smeared by a random variable distributed following Gaussian distribution. After HITSUM signal is calculated, the same software trigger which is applied to data is applied with dark noise being set at 5.8kHz.

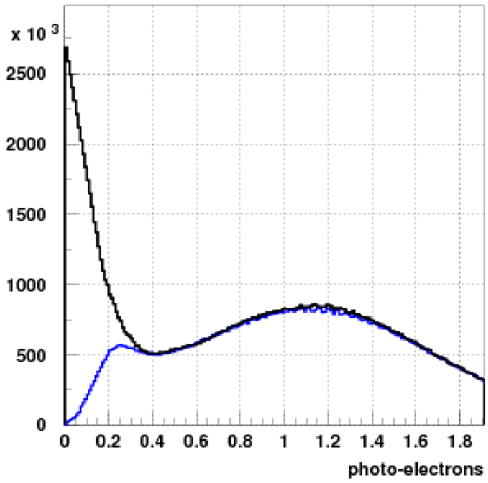

Figure 5.16: The single-p.e. distributions for the MC simulation (solid line). The blue line is obtained from the nickel data in SK-IV. The difference between them is due to the threshold function of the QBEE, and the ratio is also put into the MC simulation. Figure is taken from (121).

As up-going muon (up-μ) events are produced outside the Super-Kamiokande detector, they are independently simulated. The neutrino interactions occurring in the surrounding rocks and in the OD water were separately treated. After simulating neutrino interactions in the rocks, the propagation of produced muons through the rocks was simulated by considering energy loss at very high energy including radioactive process and multiple Coulomb scattering. Only the events in which muons can reach the detector are selected and considered for further detector simulation steps. The muon propagation range R_{eff} in the rock is shown in Fig. 5.17.

The neutrino interaction and the propagations are simulated in "standard rock" which has: $\rho = 2.65$ g/cm^3, Z = 11 and A = 22 ((190)).

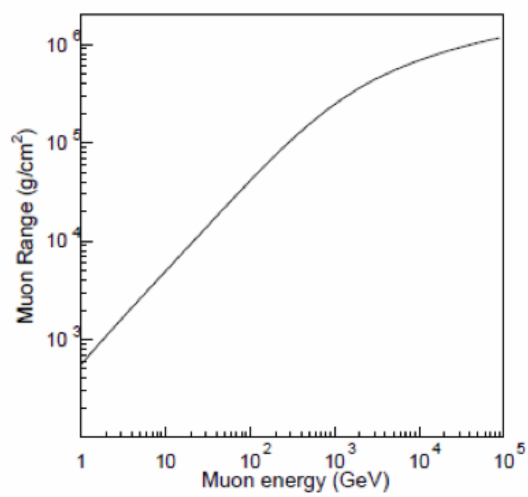

Figure 5.17: The muon propagation range in the in "standard rock". Figure is taken from (191).

The simulation covers the rocks within 4 km from the detector, which is the distance that muon produced from a few TeV neutrino event can travel.

As a result of the simulation, 85% of the total up-μ events turns out to be produced in the rocks and the remaining in the OD water.

Chapter 6

Description of Super-Kamiokande data used

6.1 Overview

High-energy neutrino events detected in the Super-Kamiokande are categorized into three types as shown in Fig. 6.1:

- Fully contained (FC)
- Partially contained (PC)
- Upward-going muon (Up-μ).

When the neutrino interacts inside the detector, it is called "contained event type". They are discriminated one to another by the OD activity; "fully-contained (FC) events" are in which all observed Cherenkov light is contained in the ID, "partially-contained (PC) events" additionally have an exiting particle that deposits energy in the OD. "Upward-going muons (up-μ)" are high-energy muons produced by neutrino interactions in the rocks and water surrounding the detector. To discriminate them from cosmic rays, muons going upward direction are only selected.

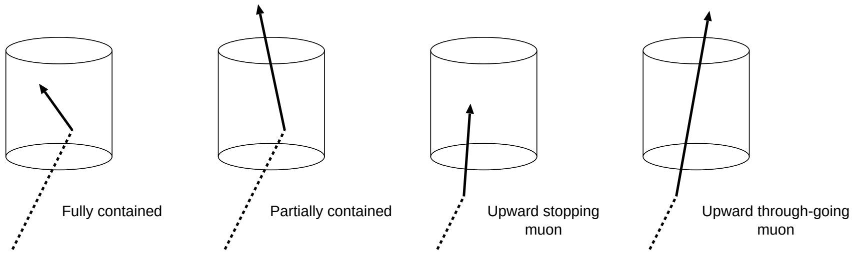

Figure 6.1: Schematic view of three types of high-energy neutrino events in SK.

This analysis uses data accumulated during the SK I-IV run periods. The SK-I (1996 to 2001) FC and PC samples correspond to 1489 live-days, and the up-μ sample corresponds to 1646 days of livetime. SK-II (2002 to 2005) had 799 live-days of FC and PC samples and 828 live-days of up-μ sample. SK-III (2006 to 2008) contains 518 live-days of FC and PC with 636 live-days of up-μ events. SK-IV (2008 to present) data-taking is ongoing; in this analysis we used the data collected until March 2012, containing 1096.7 live-days of FC, PC and up-μ events.

Events falling into each event category will experience independent back-ground events reduction process which will be explained in the following former three chapters (Chap. 6.2 to 6.4). In Chap. 6.5, the event reconstruction methods are explained. After reducing the back-grounds, data are further distributed into 18 event categories which are 13, 3 and 2 for FC, PC and up-μ respectively. The FC events are distributed in seven sub-GeV (visible energy $<$ 1.33 GeV) and six multi-GeV (visible energy $>$ 1.33 GeV) sub-categories, and then further divided based on particle identification (e-like, μ-like and π^0-like), number of reconstructed Cherenkov rings and number of decay electrons. PC events are sub-divided into “OD stopping” and “OD through-going” accoroding to their energy depoit in OD. Up-going muons either stop in the detector (stopping up-μ) or pass through the detector (through-going up-μ). Through-going up-μ events are further divided into “showering” and “non-showering” categories (192). The criteria for the event categorization will be given in the latter three chapters (Chap. 6.6 to 6.8).

6.2 Reduction for fully contained events

The FC reduction consists of five steps. Between third and fourth reduction steps, reconstruction fitters are applied. Since the number of ID PMTs was about half for SK-II period, reduction cut values differ from other period while sharing the concepts of the criteria.

6.2.1 First reduction

The first reduction applies rough cuts to reduce low energy and cosmic ray muon background events. An event is rejected, if one of these criteria is not satisfied:

1. $\mathrm{PE}_{tot} > 200$ p.e.s (100 p.e.s for SK-II),
   where PE_{tot} is number of total p.e.s observed by ID PMTs. This cut is to reject radioactive low energy background events. 200 p.e.s (100 p.e.s for SK-II) corresponds to 22 MeV/c of electron momentum, which is safely lower than the 30 MeV energy cut used for high energy neutrino analyses.

2. $\mathrm{NHITA}_{800} \leq 50$ or OD trigger is off,
   where NHITA_{800} is number of hit OD PMTs detected in a 800 nsec fixed time window. This criterion removes cosmic ray muon events.

If there was an event entered within 30 μsec window after a selected event by the above criteria, it is kept as attached to the previous events as 'sub-event's in order to search decay electrons. After the first reduction, the number of events decreases from 10^6 events/day to $\sim$1500 events/day.

6.2.2 Second reduction

The second reduction is composed of two cuts to give additional rejection of cosmic ray muons, and electric noise events respectively. An event is rejected if one of these criteria is not satisfied:

1. $\mathrm{NHITA}_{800} \leq 25$ (30 for SK-IV), if $\mathrm{PE}_{tot} < 100{,}000$ p.e.s (50,000 p.e.s for SK-II) or OD trigger is off, to reject more cosmic ray muons.

2. $\mathrm{PE}_{max}/\mathrm{PE}_{300} < 0.5$,
   where PE_{max} is the maximum number of p.e.s observed by an ID PMT, PE_{300} is the maximum number of p.e.s observed by total ID PMTs in a 300 nsec sliding time window. This criterion rejects low energy electric noise events, to whose signal a single PMT largely contribute.

Event rate further reduces to $\sim$200 events/day after the FC 2nd reduction.

6.2.3 Third reduction

Third reduction is composed of several cuts optimised to reduce various types of muons, flasher events and low energy radioactive and electric noise events.

Through-going muon cut

A specified fitter for the through-going muon is applied for the events who have more than 1000 PMTs which individually detect more than 230 p.e.s. The fitter first selects the entrance point by searching the earliest hit PMT with some neighboring hit PMTs, and selects the exit point by searching for the center of the hit ID PMTs. The cut criteria are following:

1. goodness of through-going muon fit > 0.75

2. $\mathrm{NHITA}_{in} \geq 10$ or $\mathrm{NHITA}_{out} \geq 10$
   where NHITA_{in} (NHITA_{out}) is number of OD hit PMTs located within 8 m from the entrance (exit) point in a 800 nsec fixed time window.

Stopping muon cut

A specified fitter for the stopping muon cut is applied to select the entrance point. The cut criteria are following:

- $\mathrm{NHITA}_{in} \geq 10$ (or if goodness of fit ≥ 0.5, $\mathrm{NHITA}_{in} \geq 5$ only for SK-I)

Cable hole muons

To pass the PMT cables through to the electronics huts, there are cable holes on the top of the tank. OD PMTs are not installed at the positions of these holes which occurs the missing information of the OD activities for the events occurring around these holes. To compensate the defect, 2 m × 2.5 m plastic scintillation counters are set as veto for four big cable holes (For eight smaller holes, back-ground rejection using software will be applied in 5th reduction).

The cut criteria related to the veto counters are:

1. One veto counter hit
2. $L_{veto} < 4$ m,
   where L_{veto} is the distance from the cable hole to the event vertex.

Flasher event cut

Flasher events are background events caused by PMTs emitting light from internal corona discharges. Typical flasher events would have broader hit timing distributions than neutrino events. Using this feature, following cut criteria is applied:

1. $NMIN_{100} \geq 15$ (or $NMIN_{100} \geq 10$ if the number of hit ID PMTs ≤ 800 (For SK-I),
   where $NMIN_{100}$ is the minimum number of ID PMTs hit in a 100 nsec sliding time window
2. $NMIN_{100} \geq 20$ (For SK-II to SK-IV)

Accidental coincidence events cut

Sometimes a cosmic ray muon event enters in the trigger gate which is activated by a low energy event. These events are removed by following cuts:

1. $NHITA_{off} \geq 20$,
   where $NHITA_{off}$ is the number of hit OD PMTs in a 500 nsec fixed off-time window (the timing window in which we do not expect a signal).
2. $PE_{off} > 5000$ p.e.s (2500 p.e.s for SK-II),
   where PE_{off} is the number of p.e.s observed ID PMTs in a 500 nsec fixed off-timing window.

Low energy events cut

The remaining low energy radioactive and electric noise events are removed by following criterion:

- $\mathrm{NHIT}_{50} < 50$ (25 for SK-II),
  where NHIT_{50} is the number of hit ID PMTs in a 50 nsec sliding time window.

Event rate becomes ∼35 events/day after the third reduction.

6.2.4 Fourth reduction

A pattern matching algorithm is used to remove the remaining flasher events because they usually show repeated hit patterns. The correlation factor of two events (A and B) is computed as follows:

$$r = \frac{1}{N}\sum_{i}^{N}\frac{(Q_i^A - \langle Q^A\rangle) \times (Q_i^B - \langle Q^B\rangle)}{\sigma_A \times \sigma_B}, \tag{6.1}$$

where N is the number of 2m × 2m patches of ID wall, $\langle Q^{A(B)}\rangle$ and $\sigma_{A(B)}$ are the average charge and its standard deviation for event A and event B. If the distance between the PMTs which have maximum pulse heights in the two events is smaller than 75 cm, an offset value 0.15 is add to r. Another matching parameter d_{ks} is introduced by KS (Kolmogorov-Smirnov) test. The normalised accumulated charge distributions of two events are compared and the maximum distance d_{ks} is picked up which is expected to be small, when two events have similar hit patterns.

A likelihood method is used to set a cut criterion:

$$\begin{aligned}\mathrm{Prob} = \frac{1}{2}(\mathrm{Prob}_r + \mathrm{Prob}_{dks}) = \frac{1}{2}\Bigg(&\frac{1}{10}\left[-2\sum_{i=1}^{top10} ln\,(\mathrm{Pr}(r_i, Q_i)) - 2\sum_{i=1}^{top10} ln(\frac{i}{N_\alpha})\right] + C_r + \\ &\frac{1}{10}\left[-2\sum_{i=1}^{top10} ln\,(\mathrm{Pr}(dks_i, Q_i)) - 2\sum_{i=1}^{top10} ln(\frac{i}{N_\beta})\right] + C_{dks}\Bigg)\end{aligned} \tag{6.2}$$

Pr is a probability density function (PDF), i is count for compared events up to ten of them, Q_i is average total charge of two compared events, N is number of combination and tunning parameters are set to be α=0.909, β=0.674, C_r=−0.31, C_{dks}=−3.39. Probabilities of getting r and d_{ks} are estimated from PDF made from MC, compared with expectation assuming neutrino event.

If Prob exceeds 3.0, events A and B are determined to be matched events. Figure 6.2 shows the Prob distribution for neutrino data and MC against flasher events.

The event rate after FC fourth reduction is ∼32 events/day.

6.2.5 Fifth reduction

The fifth (final) reduction step is composed of dedicated cuts for each background source.

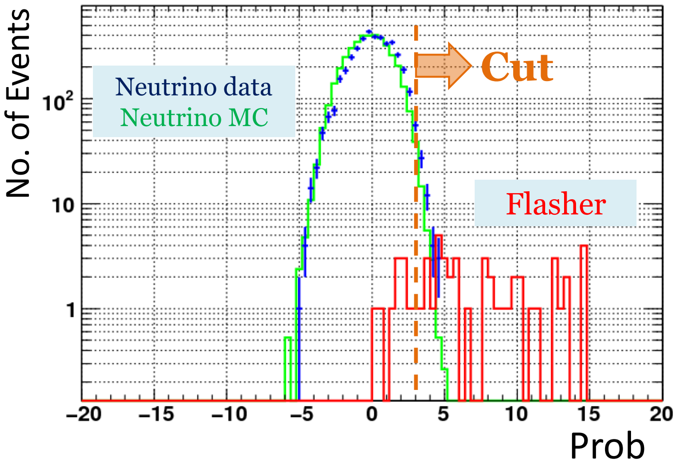

Figure 6.2: Prob distributions, regarding FC 4th reduction to reject flasher events for SK-III data and MC against flasher events inside fiducial volume. Figure is taken from a SK internal document generated by K. Okumura.

Invisible muon cut

If a cosmic-ray muon has momentum too low to generate Cherenkov radiation ("invisible") and accompanies a decay electron which is successfully tagged, the event may be misidentified as a neutrino event. Events fulfilling following cuts are recognized as invisible muon and are rejected:

1. $\mathrm{PE}_{tot} < 1000$ p.e.s (500 p.e.s for SK-II)
2. $\mathrm{NHITAC}_{early} > 9$,
   where NHITAC_{early} is the maximum number of hit PMTs in the OD hit cluster in a 200 nsec sliding time window in the range of 8900 ns. If there's a OD hit cluster within 500 cm from the early muon cluster in a 500 nsec fixed time window coming after the scanning for the early muon cluster, that number of hit PMTs (NHITAC_{500}) is added to NHITAC_{early}.

Coincidence muon cut

The coincidence muon events which are remaining after the third reduction are further removed by the following cuts:

1. $\mathrm{PE}_{500} < 300$ p.e.s (150 p.e.s for SK-II),
   where PE_{500} is the total number of p.e.s observed in the ID in a 500 nsec fixed time window

2. $\mathrm{PE}_{late} \geq 20$ p.e.s,
   where PE_{late} is the maximum number of hit OD PMTs in a 200 nsec sliding time window in the range of 1200 nsec starting after the earlier fixed time window.

Sub-cable hole muon cut

Besides the cable hole muon cut in the third reduction, another cut is introduced from SK-IV to remove cosmic ray muon events coming through eight sub-cable holes where veto counters are not set. The cut criteria are as following:

1. Goodness of stopping muon fit ≥ 0.4
2. $\mathrm{PE}_{tot} > 4000$
3. downward direction ($\cos\theta < -0.6$)
4. $\mathrm{L}_{veto} < 2.5$ m.

By this cut, the cosmic ray back-ground contamination in the final FC multi-GeV (will be defined soon after) data set decreased to 0.1% level.

Long-tail flasher cut

The additional flasher cut tighter than in third reduction is applied. Events satisfying the following criteria are regarded as flasher events and removed:

1. $\mathrm{NMIN}_{100} \geq 6$ if goodness of Point-fit < 0.4
   Point-fit will be explained in Chap. 6.5.

   From SK-II:

2. $\mathrm{NTMIN}_{100} \leq 5$ if the goodness of Point-fit < 0.3.

Stopping muon cut

The remaining stopping muons are rejected by the similar criterion with that in FC third reduction step:

- $\mathrm{NHITA}_{in_{FC5}} \geq 10$ (or if goodness of fit ≥ 0.5, $\mathrm{NHITA}_{in_{FC5}} \geq 5$).

Here $\mathrm{NHITA}_{in_{FC5}}$ is counted by applying 800 ns time window without TDC correction for event which has 8 or more sub event, which is made for third reduction.

After FC fifth reduction, FC event rate becomes ~30 events/day.

6.2.6 FC reduction summary

In the final FC data set after passing through five reduction steps, neutrino events which satisfy following criteria are finally selected to be used for this analysis:

1. Vertex of neutrino interaction locates inside the fiducial volume ($>$ 2m from the ID wall),
2. Number of hit PMTs in the OD cluster (NHITAC) $<$ 16 (10 for SK-II) and
3. $E_{vis} > 30$ MeV.

The second criteria ("fiducial volume cut") largely rejects the remaining background events such as cosmic-ray muons and flashers.

Detection efficiencies in each reduction step are estimated by atmospheric neutrino MC. The number of events per day in the final sample are 8.21±0.07, 8.24±0.10, 8.41±0.12 and 8.09±0.09 for SK-I, SK-II, SK-III and SK-IV respectively. Event rates are stable through all SK periods. The detection efficiencies, the number of events in the final sample and the event rates are summarised in Tab. 6.1.

FC	SK-I	SK-II	SK-III	SK-IV
reduction step	Detection efficiency (%)			
1st	100.0	99.97	100.0	100.0
2nd	100.0	99.92	99.98	99.99
3rd	99.93	99.78	99.81	99.82
4th	99.29	99.38	99.30	99.00
5th	99.26	99.30	99.24	98.95
5th (FV)	99.25	99.95	99.62	99.19
	Number of events			
MC	13461.3	7222.5	4753.6	10669.5
Data	12232	6584	4356	8929
	Event rate			
event rate/day	8.21±0.07	8.24±0.10	8.41±0.12	8.09±0.09

Table 6.1: Detection efficiencies, number of events and event rates of the FC neutrino events used in the analysis are summarised. Number of events for MC are normalized to data livetime without oscillation effect.

Background events remaining in the final FC data set are mostly cosmic-ray muons and flasher events. Flasher events is a background for e-like sample and cosmic-ray muons are a background for μ-like sample. After applying fiducial volume cut, remaining background events are checked by eye-scanning with a visual event display in real-time weakly base. The studied contamination rates of the final FC data set are summarized in Tab. 6.2.

	SK-I		SK-II		SK-III		SK-IV	
BG	cosmic ray	flasher	cosmic ray	flasher	cosmic ray	flasher	cosmic ray	flasher
Sub-GeV	0.2%	0.1%	0.2%	0.4%	0.3%	0.1%	0.1%	0.1%
Multi-GeV	0.3%	0.5%	0.2%	0.2%	0.3%	0.2%	0.1%	0.1%

Table 6.2: Summary of background contamination in FC final data set, estimated by eye-scanning.

6.3 Reduction for partially contained events

Partially contained events are distinguished from FC events mainly by looking at OD activities. In the elimination of cosmic ray backgrounds, cuts based on straightforward OD information used in the FC reduction are not as useful for PC events. Therefore the PC reduction is composed of more dedicated reduction means.

During the reconstruction between SK-II and SK-III, the OD segmentation was installed. As this change allows much efficient selection of PC events, the cut criteria from SK-III largely differ from the previous ones. Some cuts were removed in the second and third reduction, and the fourth reduction was completely modified. In the fifth reduction, several new cuts were added.

Here PC reduction corresponding to from SK-III is summarised. For the reductions applied for SK-I and SK-II, refer (193) for example.

6.3.1 First reduction

Events satisfying the following criteria are selected:

1. $\mathrm{PE}_{tot} \geq 1000$ p.e.s.
   Particles in PC events must travel at minimum 2m in the ID, which requires muons to have a momentum ≥ 500 MeV/c. A cut of 1000 (500 for SK-II) p.e.s in the ID is applied to reject events unable to reach the OD. 1000 p.e.s correspond to 310 MeV/c for muons, conservatively.

2. $\mathrm{NHITA}_{top} < 10$ or $\mathrm{NHITA}_{bottom} < 10$,
   where NHITA_{top} (NHITA_{bottom}) is number of OD hits at the top (bottom) of OD. This rejects muons through-going from top (bottom) to bottom (top).

3. $\mathrm{NHITA}_{endcap} < 25$ or $\mathrm{NHITA}_{side} < 70$,
   where NHITA_{side} is number of OD hits on the side region of the OD, and “endcap” refers to either top or bottom. This rejects corner clipping muons which leave hit PMTs in both endcap and side region of the detector.

4. $\mathrm{ODR}_{mean} < 2100$ cm, if OD hits < 20 in 500 nsec time window,
   where ODR_{mean} is the average distance between all hit pairs which is defined as

follows:

$$ODR_{mean} = \frac{1}{N_{pair}} \sum_{i=1}^{N-1} \mid \overrightarrow{x_i} - \overrightarrow{x_j} \mid . \tag{6.3}$$

This criterion is to reject through-going muons as their ODR$_{mean}$s are expected to be large.

Many through-going muons are rejected at this stage. The first reduction reduces the event rate to $\sim$ 9000 events/day.

6.3.2 Second reduction

The second reduction removes more corner clipping muons, and events with a large number of hits in the second largest cluster. From SK-III, events satisfying the following criteria are selected:

1. NHITA$_{endcap}$ < 20 or NHITA$_{endcap}$ $<$ MAX(NHITA$_{side}$), where MAX(NHITA$_{side}$) is defined as: $e^{(\alpha - \beta \times \text{NHITA}_{side})}$ with $\alpha = 5.8$, $\beta = 0.023$ if NHITA$_{side}$ < 75, $\alpha = 4.675$, $\beta = 0.008$ otherwise.
2. Nouter2 ≤ 10, where "Nouter2" is the number of hits in the second largest hit cluster. The clusters are formed based on the charge gradients between OD patches, which are composed of 11 × 11 PMTs.

Event rate after second reduction is $\sim$270 events/day.
After the second reduction, precise fit is applied and the event rate is reduced to $\sim$100 events/day.

6.3.3 Third reduction

At the 3rd reduction flashers are rejected using the same cut as the FC third reduction that used the flasher event's feature of broad timing distribution:

- NMIN$_{100}$ > 14 (if the number of hit ID PMTs < 800, > 9)

Event rate after PC third reduction is $\sim$2.6 events/day.

6.3.4 Fourth reduction

Because of OD segmentation introduced from SK-III, fourth reduction is completely rewritten based on the muon fitter "muboy" to powerfully identify remaining cosmic-ray muons which have survived so far due to limited OD activity. Muboy classifies each event as a stopping muon, a through-going muon, a multiple muon or a corner clipping muon.

Six variables and corresponding selection cuts which use the muboy information are defined as below, and if an event passes any of these selection cut for muon events, it is rejected from the PC sample.

Five selection criteria based on the results of the fitter are:

1. Muboy Angle $< 90°$,
   where Muboy Angle is the angle between the fitted direction and the direction between vertex fitted by the Point-fit and the center of the largest OD charge cluster. As for the Point-fit, see Chap. 6.5.

2. Muboy Dotprod $>$ -0.8,
   where Muboy Dotprod is the angle between the fitted direction and the direction between the Point-fit vertex and the earliest saturated ID PMT.

3. Muboy Track length $<$ 1750 cm,
   where Muboy Track length is the length of the fitted muon track.

4. Muboy Goodness $<$ 0.52,
   where Muboy Goodness is the goodness of fit by muon fitter.

5. Muboy Corner $\geq$ 300 cm,
   where Muboy Corner is the distance between fitted entrance point and the corner of the tank.

For stopping muons which are required to fulfill at least four of these criteria including the 2nd one, additional selection cut is applied:

- Muboy Goodness $<$ 0.5 or Muboy Ehit8m $<$ 10,
  where Muboy Ehit8m is number of OD hits within 8 m from the fitted entrance point in a 500 nsec fixed time window.

An additional cut is applied to all events to reduce more low energy back-ground events:

- $\mathrm{PE}_{tot} < 2900$ p.e.

2900 p.e. corresponds to $\sim$ 500 MeV/c, which is less than the minimum momentum which PC event needs to have to reach the OD, $\sim$ 700 MeV/c.

The event rate after the PC fourth reduction is $\sim$1.8 events/day.

6.3.5 Fifth reduction

Fifth reduction is composed of a series of dedicated cuts for each difficult remaining background source. There are two types of cuts: hard cuts and soft cuts. PC events are required to pass all hard cuts and allowed to fail soft cuts once. Hard cuts include through-going muon cuts, a stopping muon cut, a cable hole muon cut and a corner clipping muon cut. Soft cuts also include through-going muon cuts, stopping muon cuts, a corner clipping muon cut in a milder way, and a decay electron cut. The criteria of each cut is described elsewhere (193). The event rate after the PC fifth reduction is $\sim$1.2 events/day.

6.3.6 PC reduction summary

The final data set of PC events are selected by the following criteria:

1. Vertex of neutrino interaction locates inside the fiducial volume ($>$ 2m from the ID wall),
2. NHITAC $\geq$ 16 (10 for SK-II),
3. $E_{vis} > 350$ MeV
   (Total observed charge in ID $>$ 3000 p.e.s (1500 p.e.s for SK-II).

Detection efficiencies in each reduction step are estimated by atmospheric neutrino MC. The detection efficiencies, the number of events in the final sample and the event rates are summarised in Tab. 6.3.

Remained back-ground events, which are mainly due to cosmic ray muons, are checked by eye-scanning after applying fiducial volume cut. Contamination of background events is estimated by extrapolating vertex distribution of the OD-tagged muon sample into fiducial area. Table 6.4 summarizes the estimated contamination for each SK period.

6.4 Reduction for upward-going muon events

For the up-μ reduction, most background is cosmic ray muons and some radioactive radiations. Most tricky background comes from the cosmic rays coming from around horizontal direction, for which even-base selection is not able. The reduction composes of three reduction steps, eye-scanning and background estimation.

6.4.1 First reduction

Low-energy and very high energy events are rejected by requiring:
6000 p.e.s (3000 p.e.s for SK-II) $<$ PE_{tot} $<$ 1,750,000 p.e.s (800,000 p.e.s for SK-II). 6000 p.e.s corresponds to the muon momentum of 1 GeV/c and to the track length of

PC	SK-I	SK-II	SK-III	SK-IV
reduction step	Detection efficiency (%)			
1st	98.98	98.58	99.09	99.63
2nd	96.74	93.43	98.52	98.73
3rd	95.69	92.32	98.51	98.68
4th	89.86	84.60	97.87	97.42
5th	88.66	74.80	96.61	96.15
5th (FV)	80.98	74.80	88.80	86.30
	Number of events			
MC	913.8	448.6	356.0	744.9
Data	902	427	344	735
	Event rate			
event rate/day	0.66 ± 0.02	0.65 ± 0.04	0.62 ± 0.03	0.66 ± 0.02

Table 6.3: Detection efficiencies, number of events and event rates of the PC neutrino events used in the analysis are summarised. Number of events for MC are normalized to data livetime with two-flavor oscillation effect.

	SK-I	SK-II	SK-III	SK-IV
cosmic ray BG	0.2%	0.7%	1.8%	0.6%

Table 6.4: Estimated contamination in the PC final data set by cosmic ray muons.

3.5 m. Comparing to the requirement for final sample (tracklength $>$ 7 m), it is rather conservative cut applied at this stage. After that, an upmu fitter is applied and relect events whose goodness of fit is less than 0.3 or down-going. After first reduction, the event rate is ~9000 events/day.

6.4.2 Second reduction

To reject down-going cosmic-ray muons, dedicated fitting algorithms are used as following;

1. First muon fitter is applied to a event.
2. If the event is up-going and the goodness of fit is above the threshold, the event is save.
3. If the event is down-going and the goodness of fit is above the threshold, the event is rejected.
4. If the event is travelling horizontally and the goodness of fit is above the threshold, or if the goodness of fit is below the threshold, the judgement is postponed.
5. The event is brought to the first step for the next muon fitter.

The algorithm continues until the event is judged by criterion 2 or 3, or passes all fitters. Detailed description of the muon fitters and definition of goodness of fit can be found in (194). After second reduction, the event rate is reduced to be ~250 events/day.

6.4.3 Scanning

The remaining background corner clipper and cosmic ray muons are rejected by eye scanning (Note that FC and PC eye scannings are used for systematic study, not for reductions themselves). All the remaining events are checked one by one by two experts and efficiency of scanning is estimated to be ~100%. About remaining half of the events are rejected in this stage.

6.4.4 Background estimation for upward-going muon

Background cosmic-ray muons mostly come from around horizontal direction ($-0.1 < \cos\theta < 0$). Background contamination is estimated by extrapolating the distribution of downward events in $0 < \cos\theta$ with the exponential function with constant term.

The uncertainties on the background estimation is evaluated the maximum change on the number of background events fit parameters deduced from the fitting results. They are summarized in Tab. 6.5.

	SK-I	SK-II	SK-III	SK-IV
stop μ	16%	21%	20%	17%
through-going μ (non-shower)	11%	15$	19%	14%
through-going μ (shower)	18%	14%	24%	20%

Table 6.5: Uncertainties of up-μ background estimation in the zenith angle $-0.1 < \cos\theta < 0$.

6.4.5 Up-μ reduction summary

In the final up-μ data set after passing through three reduction steps, events which satisfy following criteria are finally selected to be used for this analysis:

For stopping muons;

1. Fitted momentum $\geq$ 1.6 GeV/c which corresponds to track length = 7 m,
2. NHITEX $<$ 10 (16 for SK-II),
   where NHITEX is number of hit OD PMTs within 8 m from the exit point.

For through-going muons;

1. Travelling in ID $\geq$ 7 m,
2. NHITEX $\geq$ 10 (16 for SK-II).

The detection efficiencies, the number of events in the final sample and the event rates are summarised in Tab. 6.6. Detection efficiencies in each reduction step are estimated by atmospheric neutrino MC.

6.5 Event reconstruction

A ring imaging Cherenkov detector Super-Kamiokande can derive various event information by reconstruction of the Cherenkov light cones detected at PMTs. From reconstructed ring shape, radius of the ring, i.e., the Cherenkov emission angle, the number of rings, the vertex position of the Cherenkov emission, and the directions and energies of particles can be obtained. Also the hit patterns allow to discriminate particle type and momentum.

For FC and PC events, the reconstruction process starts from fitting the vertex position of an event. With the vertex position, the ring fitting algorithm identifies other possible rings. After that, the particle type for each ring is identified. For single ring events, this particle identification (PID) is used to improve the vertex reconstruction. Finally, the momentum for each ring is determined and decay electrons are searched.

Up-μ events are also reconstructed by using some of the above processes. PC and up-μ events are basically treated as μ-like events.

	SK-I		SK-II		SK-III		SK-IV	
	stop	thru	stop	thru	stop	thru	stop	thru
	detection efficiency (%)							
	80.98	74.80	88.80	86.30	80.98	74.80	88.80	86.30
	number of events							
final sample (MC)	729.6	1892.4	364.6	926.2	286.0	725.1	474.0	1257.6
final sample (data)	462	1866	223	871	210	735	306	1345
BG subtracted	429	1835.6	210	833.4	193	722.9	284	1330.9
event rate (per day)	0.26 ±0.01	1.12 ±0.03	0.25 ±0.02	1.01 ±0.03	0.30 ±0.02	1.14 ±0.04	0.26 ±0.02	1.21 ±0.03

Table 6.6: Detection efficiencies, number of events and event rates of the up-μ neutrino events used in the analysis are summarized. “thru” means ’through-going’. Number of events for MC are normalized to data livetime with two-flavor oscillation effect. The number of events for “final sample” and “BG subtracted” are shown for before and after BG subtraction, respectively, where the event rate is calculated for the latter.

6.5.1 Vertex fitting

Vertex position is reconstructed by the hit timing information of PMTs. Assuming that all the PMT hits are created by photons coming from a single point, a fitter called “Point-fit” selects a point which gives the maximal goodness-of-fit of the timing residual, i.e., photon arrival time subtracted by the time of flight from a tested vertex, distribution of hit PMTs as a vertex of the event.

Using the vertex information reconstructed, the Cherenkov emission angle of the dominant ring is determined as an open angle giving the maximal goodness-of fit.

After that, using another fitter called “TDC-fit”, much precise vertex position is determined. This fitter assumes that photons are emitted along the particle track for the PMTs hit inside the opening angle. Fixing the Cherenkov ring, various vertex point is tested and the point with maximal goodness-of-fit is selected.

For single ring events, a more precise fitter called “MS-fit” is used. This fitter is applied after particle identification, that the fitter can use the information of the expected light pattern for each particle flavor. Performance of MS-fit is checked for the estimated resolution studied using MC. Table 6.7 summarises the vertex resolution, which is the difference between the true vertex and the reconstructed vertex, of FC and

PC samples for each SK period. Note that MS-fit is also used for up-μ reconstruction, assuming that the vertex locates at the ID surface.

Vertex resolution (cm)				
	SK-I	SK-II	SK-III	SK-IV
FC sub-GeV				
single-ring				
e-like	31.2	35.6	31.1	31.5
μ-like	23.8	30.3	23.9	23.5
FC multi-GeV				
multi-ring				
μ-like	67.4	111.8	73.8	87.8
PC	53.6	62.8	52.6	67

Table 6.7: Vertex resolutions of FC/PC samples for each SK period.

Figure 6.3 shows the vertex distributions of FC and PC events comparing the data and MC. Figure 6.4 shows the vertex distributions of FC and PC events comparing the data and MC.

6.5.2 Ring counting

Possibly existing other rings are searched for by a pattern recognition technique, "Hough transform method" (195) and likelihood technique. Figure 6.5 illustrates the method. For every hit PMT, a Cherenkov emission cone from the fitted vertex with opening angle 42° are drawn weighted with detected p.e.s after subtracting p.e.'s the dominant Cherenkov ring. The most probable direction of the ring is deduced from the maximum of the distribution are taken as ring candidates.

Ring candidates are tested whether they are true rings or not by likelihood technique to compare the (N + 1)-ring hypothesis to the N-ring hypothesis up to N = 5.

Figure 6.6 and Fig. 6.7 show the ring-counting likelihood distributions comparing the data and MC. Difference between the data and MC is taken as systematic uncertainty for ring counting. Among the reconstructed rings, rings with low momentum and overlapping with other energetic rings are discarded.

6.5.3 Particle identification

Each ring is classified as two types: "e-like" events which are supposed to be produced from $e^{\pm}$, γs have diffused ring pattern Electrons and positrons propagate in the water as generating electromagnetic shower through Bremsstrahlung ($e^- \rightarrow e^-\gamma$) and following photon pair production ($\gamma \rightarrow e^-e^+$), and multiple scatterings of low energy electrons. High-energy gamma rays also generate electromagnetic showers and

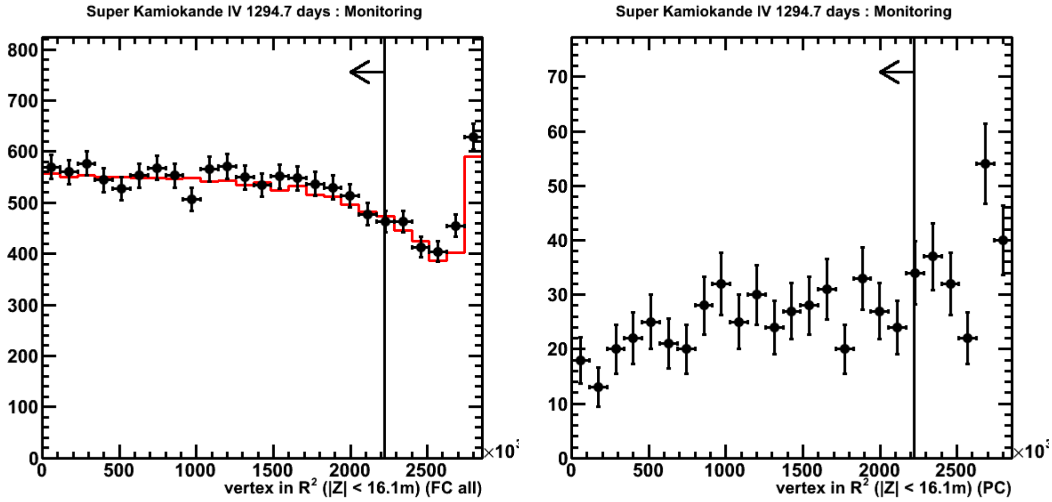

Figure 6.3: r^2 distributions in dimension of [cm^2] for SK-IV (left) FC and PC (right) events. For FC sample, Data (black dotted) is shown in comparison to MC (red solid) assuming two-flavor oscillation effect.

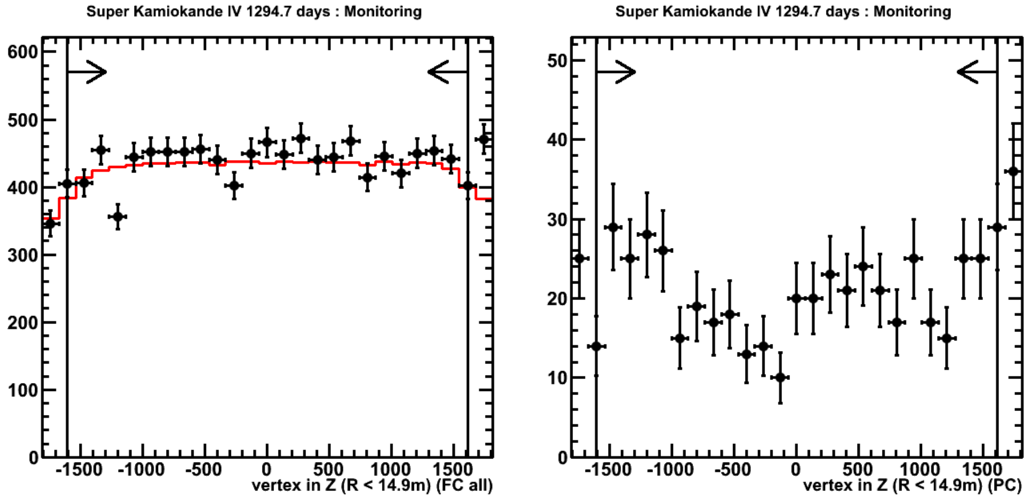

Figure 6.4: z distributions in dimension of [cm] for SK-IV (left) FC and PC (right) events. For FC sample, Data (black dotted) is shown in comparison to MC (red solid) assuming two-flavor oscillation effect.

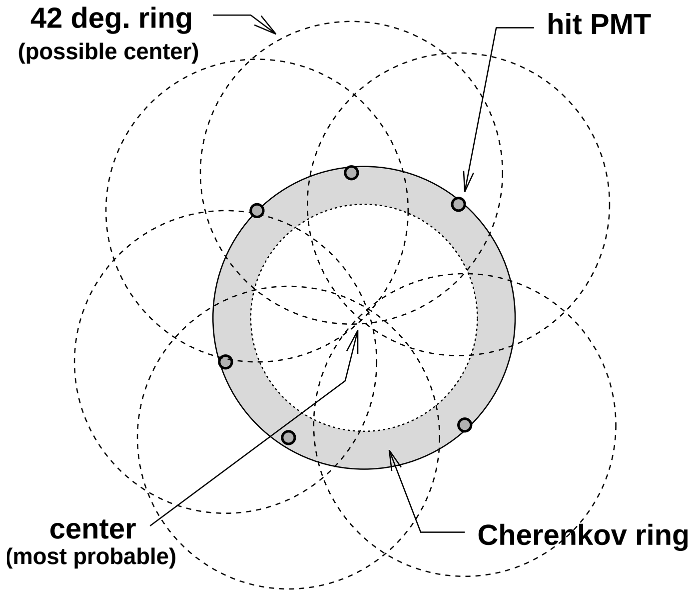

Figure 6.5: A drawing of basic idea of "Hough transform method". By drawing rings around the hit PMTs, center of the unknown Cherenkov ring can be revealed.

are indistinguishable from electrons. "μ-like" events have rings ring with sharper edge produced from $\mu^{\pm}$, $\pi^{\pm}$s. Figure 6.8 shows an example for event displays sample of ν_e and ν_μ MC events. A likelihood using Cherenkov ring pattern is defined and used for the particle identification.

Together with likelihood by hit pattern, the opening angle information is also used in PID algorithm. The Cherenkov rings from muons and charged pions would have smaller opening angle as they are less energetic than light electrons for the same neutrino energy.

Figures 6.9 to 6.12 show the PID likelihood distributions comparing the data and MC. Discrimination between multi-ring e-like and μ-like events suffers difficulty due to ring overlapping. Difference between the data and MC is taken as systematic uncertainty for ring counting.

π^0s can be identified due to its short lifetime (of 8.4×10^{-17} s) with 99% probability to two γs. By searching for two e-like rings, applying a cut on the invariant mass (to be within 85 MeV $\sim$ 215 MeV) and requiring no decay electron and sub-GeV momentum, NC single π^0 production event can be identified.

However, in case that one of the two rings is missed, the event can be misidentified as a single-ring e-like event. To compensate it, an algorithm called "POLfit" is applied for single-ring e-like events (196). Using the initially tagged ring, the best second ring candidate is searched for which maximizes the likelihood difference between two rings and single-ring assumptions. With the second ring candidate, the invariant π^0 mass is recalculated and if it exceeds 100 MeV and the likelihood passes an additional cut, the

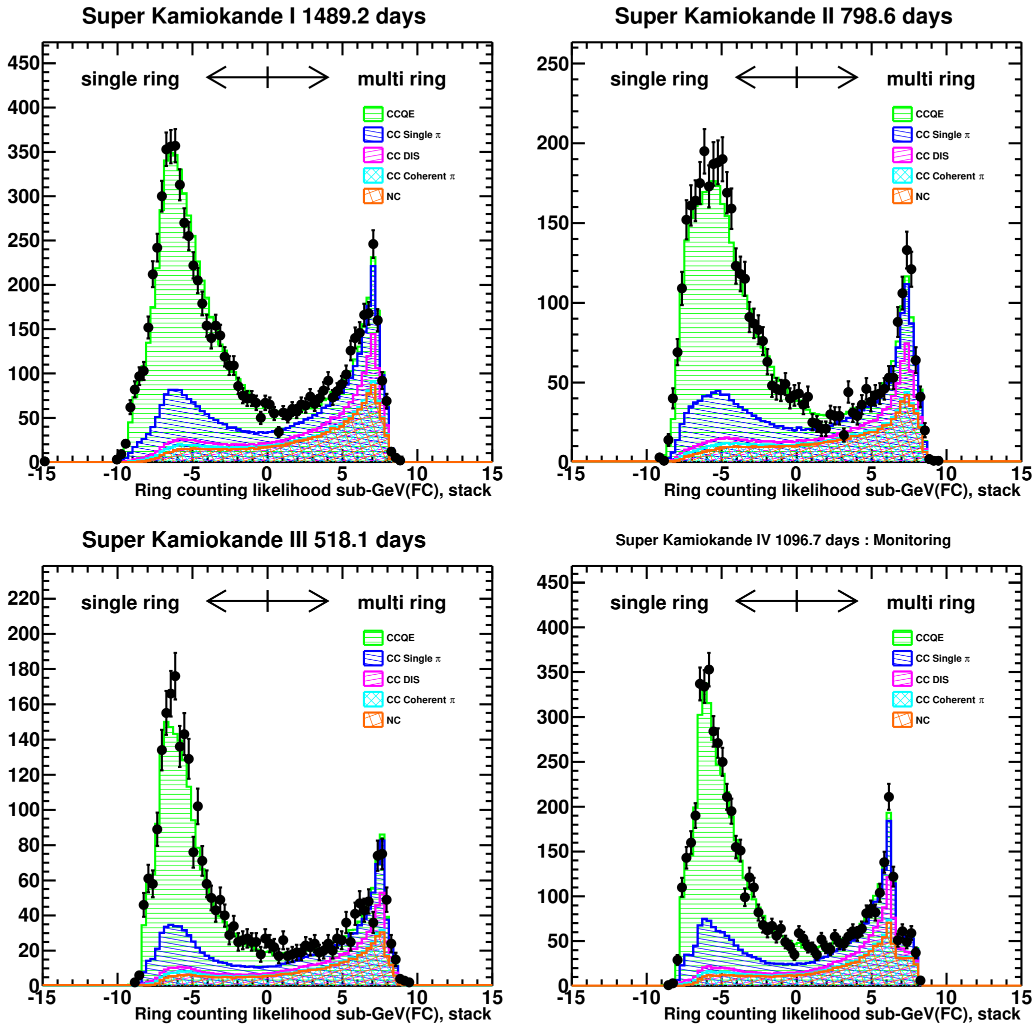

Figure 6.6: Ring-counting likelihood distributions for SK-I (top left), SK-II (top right), SKIII (bottom left) and SK-IV (bottom left) FC sub-GeV events. Data (black dotted) is shown in comparison to MC (shaded) for various interaction mode with two-flavor oscillation effect. The hatched regions indicate various neutrino interaction modes.

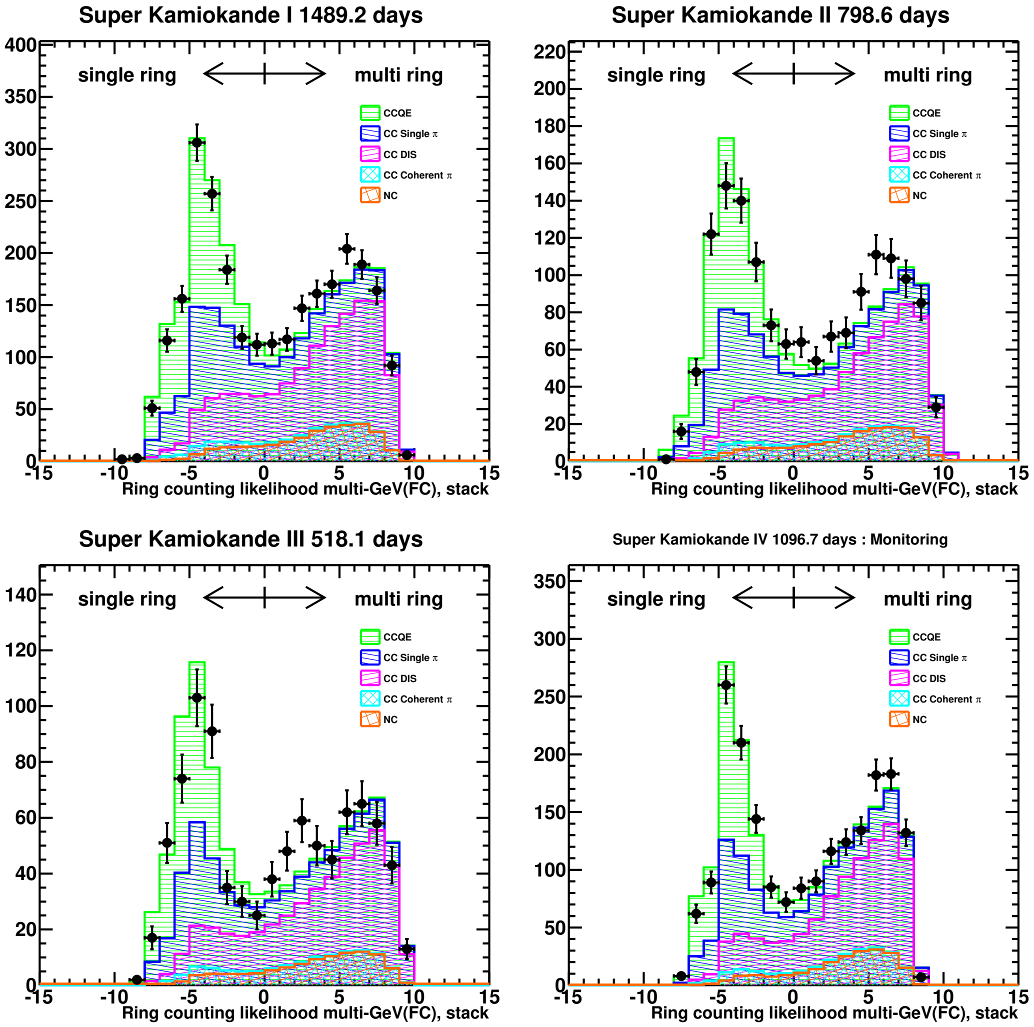

Figure 6.7: Ring-counting likelihood distributions for SK-I (top left), SK-II (top right), SK-III (bottom left) and SK-IV (bottom left) FC multi-GeV events. Data (black dotted) is shown in comparison to MC (shaded) for various interaction mode with two-flavor oscillation effect. The hatched regions indicate various neutrino interaction modes.

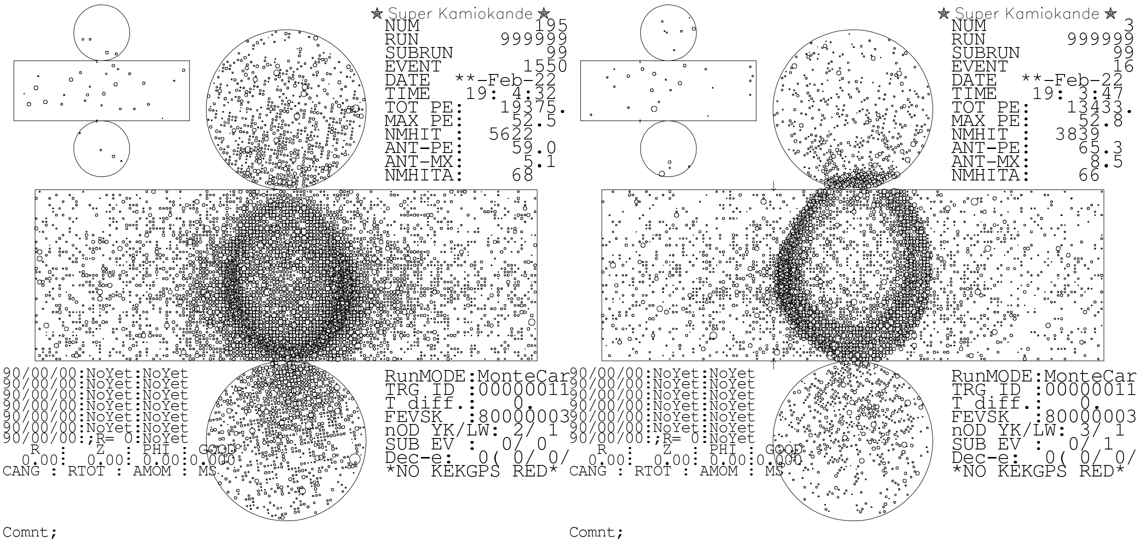

Figure 6.8: MC event displays of an electron produced from ν_e interaction (right) and a muon produced from ν_μ (left).

event is classified as an NC single π^0 event.

6.5.4 Momentum reconstruction

Number of p.e.s in each hit PMT is distributed to each ring according to an expected p.e. distribution. The q_i^{obs}, the observed p.e.s in the i-th PMT, is divided into the n-th ring as:

$$q_{i,n}^{obs} = q_i^{obs} \times \frac{q_{i,n}^{exp}}{\sum_{n'} q_{i,n'}^{exp}}, \tag{6.4}$$

where $q_{i,n}^{obs}$ is the fractional p.e.s from the n-th ring in the i-th PMT, $q_{i,n}^{exp}$ is the expected p.e. for the n-th ring in the i-th PMT.

The expectation is based on observation, estimated as a function of opening angle, assuming azimuthal angular symmetry.

For a momentum of a particle, the number of assigned fractional p.e.'s from all hit PMTs inside the Cherenkov cone with opening angle 70° in 300 nsec timing window, which is defined around the peak of the residual timing distribution, are summed.

In the summation, each hit PMT is corrected with the acceptance of PMTs, also considering light attenuation, scattering, reflection effects as:

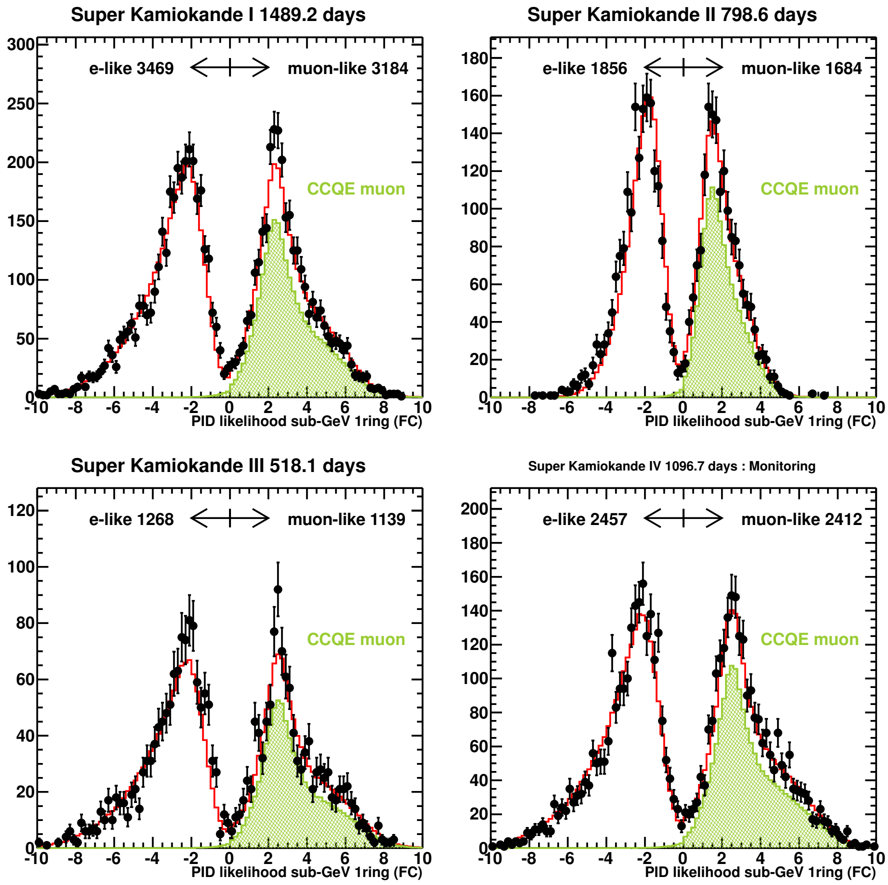

Figure 6.9: PID likelihood distributions for SK-I (top left), SK-II (top right), SKIII (bottom left) and SK-IV (bottom left) FC sub-GeV 1-ring events. Data (black dotted) is shown in comparison to MC (red solid) with two-flavor oscillation effect. The hatched histograms show CCQE ν_μ components.

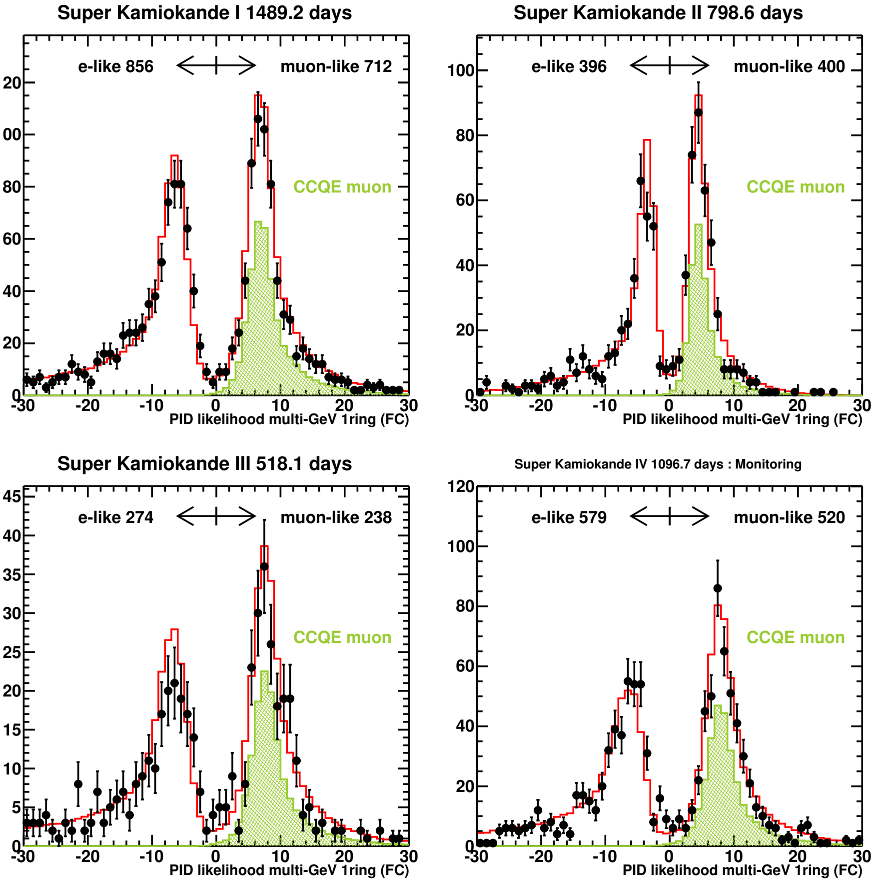

Figure 6.10: PID likelihood distributions for SK-I (top left), SK-II (top right), SKIII (bottom left) and SK-IV (bottom left) FC multi-GeV 1-ring events. Data (black dotted) is shown in comparison to MC (red solid) with two-flavor oscillation effect. The hatched histograms show CCQE ν_μ components.

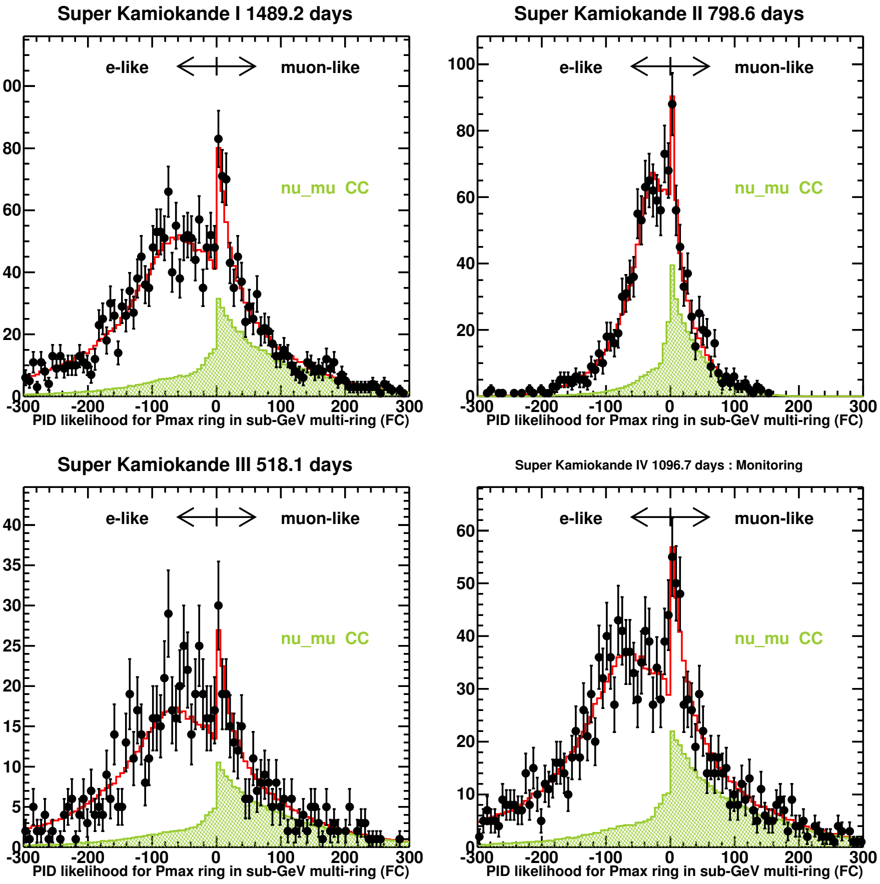

Figure 6.11: PID likelihood distributions for SK-I (top left), SK-II (top right), SKIII (bottom left) and SK-IV (bottom left) FC sub-GeV multi-ring events. Data (black dotted) is shown in comparison to MC (red solid) with two-flavor oscillation effect. The hatched histograms show CCQE ν_μ components.

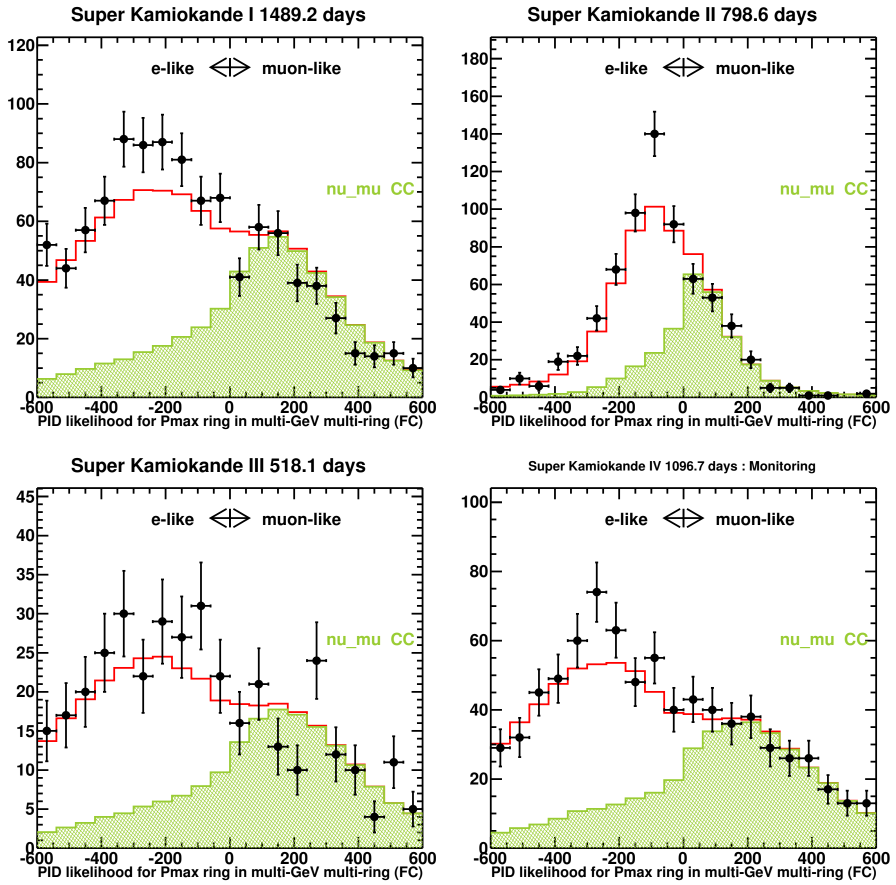

Figure 6.12: PID likelihood distributions for SK-I (top left), SK-II (top right), SKIII (bottom left) and SK-IV (bottom left) FC multi-GeV multi-ring events. Data (black dotted) is shown in comparison to MC (red solid) with two-flavor oscillation effect. The hatched histograms show CCQE ν_μ components.

$$RTOT_n = \frac{G_{MC}}{G_{data}}[\alpha \times \sum_i (q_i^{obs} \times exp(\frac{r_i}{L}) \times \frac{cos\theta_i}{f(\theta_i)}) - \sum_i S_i - \sum_i R_i], \tag{6.5}$$

where
α = normalization factor,
G_{data}, G_{MC} = relative PMT gain for data and MC,
L = light attenuation length in water, measured by using cosmic ray through-going muons,
r_i = distance between the vertex position and the i-th PMT,
$f(\theta_i)$ = correction function for the PMT acceptance as a function of photon incidence angle θ_i,
S_i = expected p.e.s for i-th PMT from scattered photons, and
R_i = expected p.e.s for i-th PMT from reflected photons on black sheets.

Then $RTOT_n$ is converted to a momentum using the MC simulation. As a result, the reconstructed momentum resolutions are estimated to be $1.7 + 0.7/\sqrt{P(\mathrm{GeV/c})}$ % and $0.6 + 2.6/\sqrt{P(\mathrm{GeV/c})}$ % for single-ring electron and single-ring muons, respectively.

Figure 6.13 show the momentum distributions of SK-IV events comparing the data and MC.

6.5.5 Direction reconstruction

The direction of single-ring event is decided by MS-fit as described before. Figures 6.14 and 6.15 show the angular resolution for single ring events from CCQE interactions, studied using MC single-ring events. The angular resolution is defined to be the difference between the true lepton direction and the reconstructed Cherenkov ring direction. Figure 6.16 shows the angular resolution for muon events. Table 6.8 summarises the angular resolution of FC and PC samples for each SK period. For multi-ring events, the directions are decided as the direction of the vector sum of the reconstructed momentum of each Cherenkov ring.

Figure 6.17 shows the angular correlation studied for all the categories using MC for SK-I events (197). The angular correlation is defined as the angle between the parent neutrino and the reconstructed direction for which 68 % of the events are included.

6.5.6 Decay electron search

Muons stopped in the detector may produce decay electrons which can be also observed. Decay-electrons ("decay-e") may be tagged within the timing window of the primarily triggered muon event ("in-gate"), or searched in a afterward-triggered 'sub-event' attached to the previous event ("sub-event"). Thanks to the improvement of electronics, the search criteria related to dead time have been removed, also tagging efficiency has increased for SK-IV.

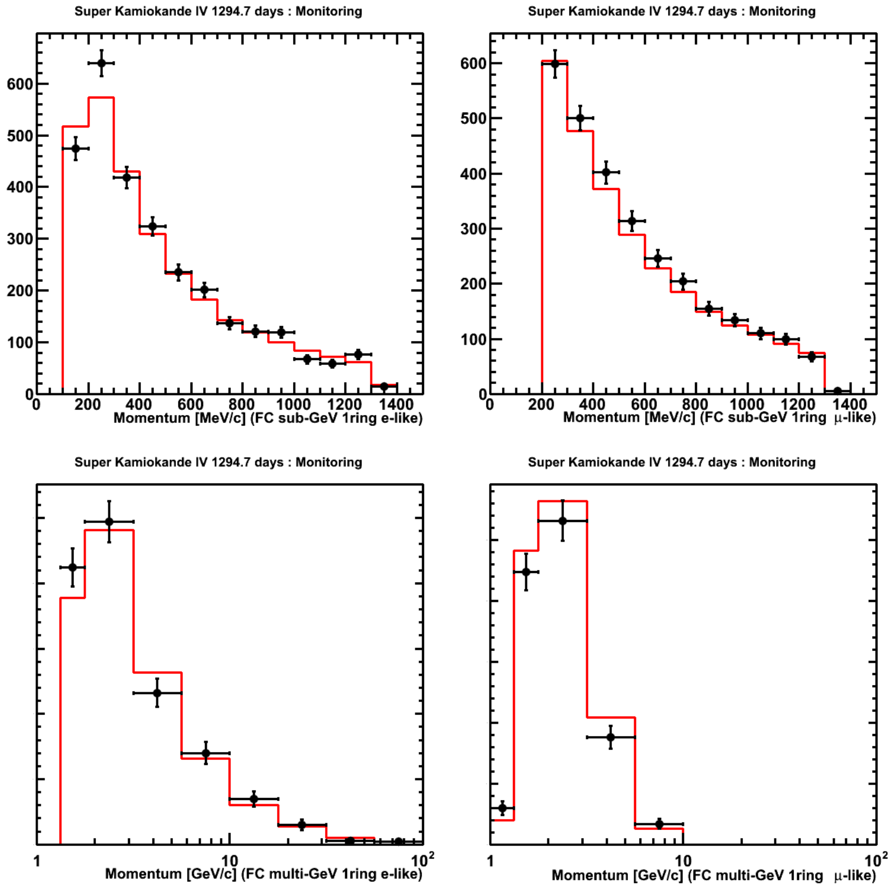

Figure 6.13: Momentum distributions for SK-IV FC 1-ring events for sub-GeV e-like (top left), sub-GeV μ-like (top right), multi-GeV e-like (bottom left) and multi-GeV μ-like (bottom right). Data (black dotted) is shown in comparison to MC (red solid) with two-flavor oscillation effect.

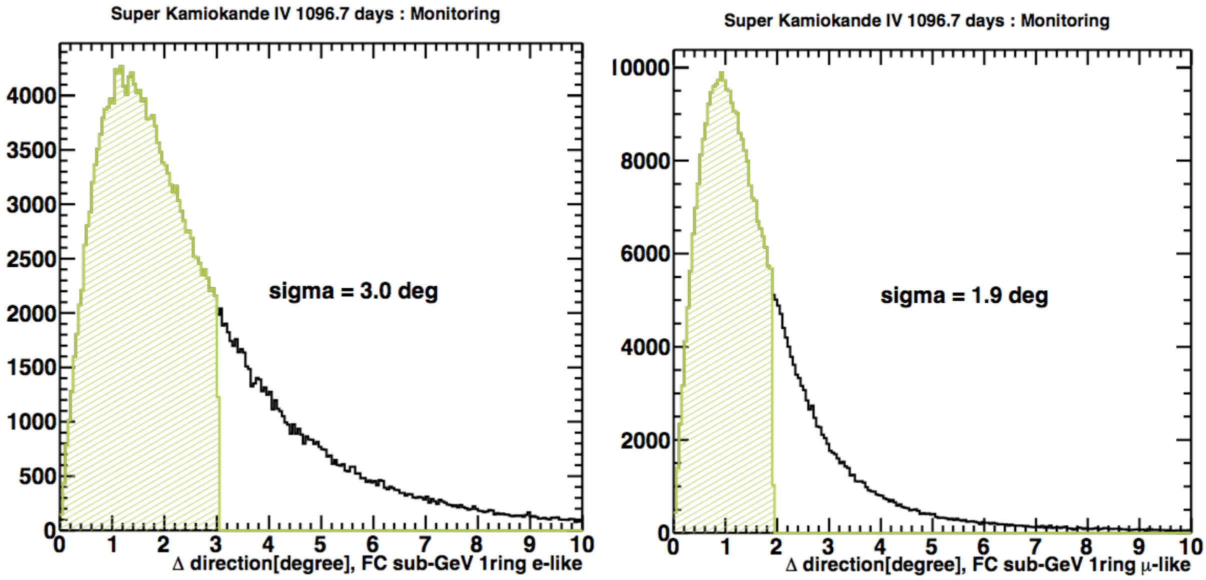

Figure 6.14: Angular difference between the true direction of out-going leptons and reconstructed direction of CCQE events in FC MC samples for SK-IV. Left: Sub-GeV 1-ring e-like. Right: Sub-GeV 1-ring μ-like. Figures are taken from (125).

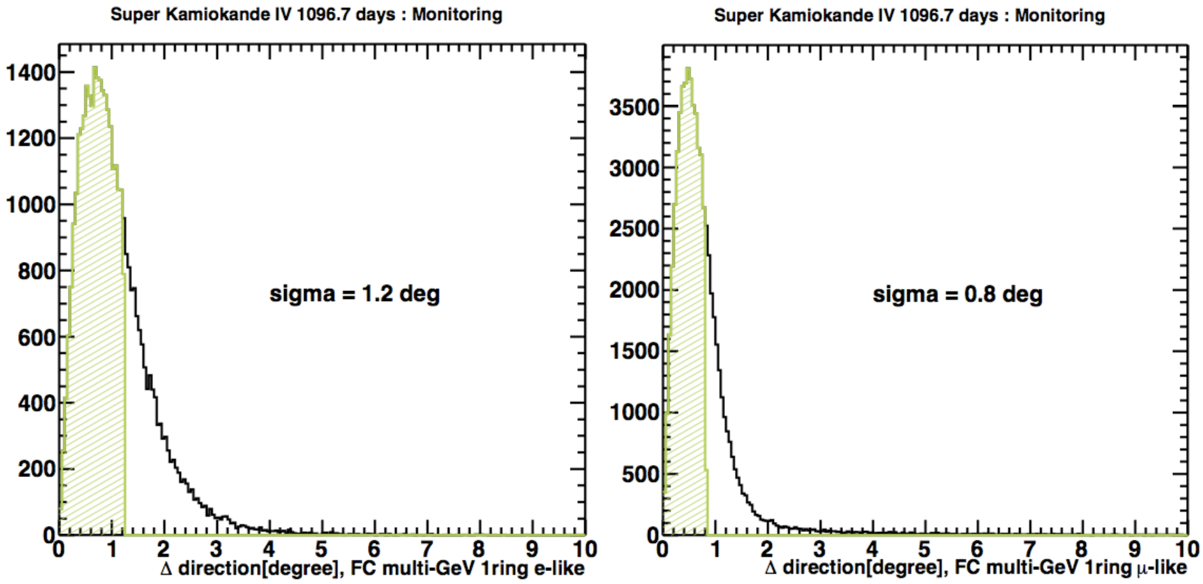

Figure 6.15: Angular difference between the true direction of out-going leptons and reconstructed direction for CCQE events in FC MC samples for SK-IV. Left: Mult-GeV 1-ring e-like. Right: Multi-GeV 1-ring μ-like. Figures are taken from (125).

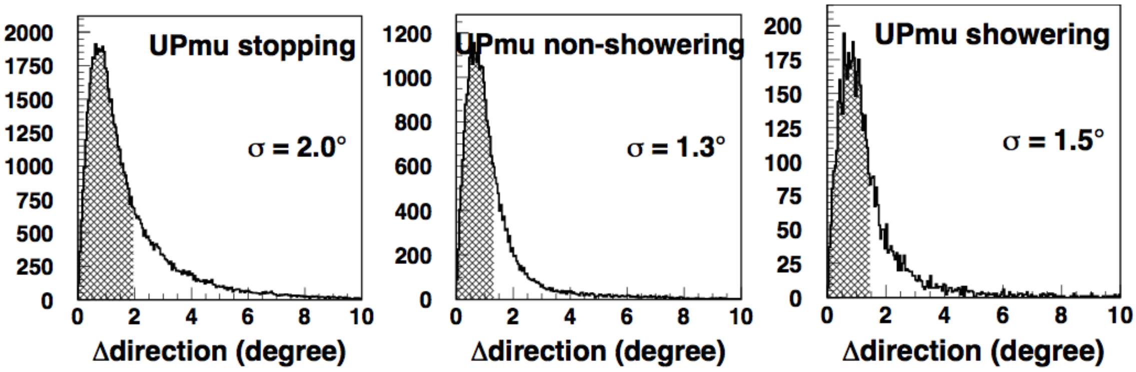

Figure 6.16: Angular difference between the true direction of out-going muon and the reconstructed direction for up-μ stopping event, up-μ non-showering events and up-μ showering events for SK-I. Figure is taken from (198).

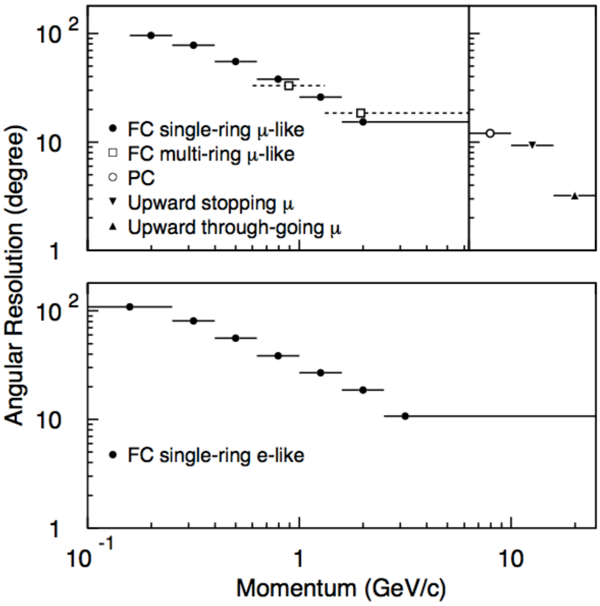

Figure 6.17: The angular correlation between neutrino direction and reconstructed ring direction as a function of the outgoing lepton momentum. Figure is taken from (197).

Angular resolution (degree)				
	SK-I	SK-II	SK-III	SK-IV
FC sub-GeV				
single-ring				
e-like	3.1	3.2	3.0	3.0
μ-like	1.9	2.1	1.9	1.9
FC multi-GeV				
single-ring				
e-like	1.2	1.3	1.2	1.2
μ-like	0.8	1.0	0.8	0.8
PC	1.0	1.2	0.9	0.9

Table 6.8: The angular resolutions of FC/PC samples for each SK period.

For "in-gate" type, another peak in the timing distribution after the primary event is searched and any peaks with more than 50 (25 for SK-II) hits in the 30 nsec window above the background level are identified as decay electron.

For "sub-event" type, the sub-events which fulfill the following criteria are identified as decay electron:

1. $\mathrm{NHIT}_{tot} > 50$ (25 for SK-II)
   where NHIT_{tot} is total number of hit PMTs (This cut is removed for SK-IV),
2. The goodness of vertex fit > 0.5,
3. $\mathrm{NHIT}_{50} > 30$ (16 for SK-II),
4. $\mathrm{PE}_{tot} < 2000$ (1000 for SK-II).

Tagging efficiency of decay electron is 80% for μ^+ and 63% for μ^- decays for SKI-III, since it is lower for μ^- as ~20% of μ^-s are captured by ^{16}O nuclei (199). For SK-IV, the tagging efficiency has been improved to be 96% for μ^+ and 83% for μ^- decays.

6.6 FC categorization

FC data is categorized into 13 sub samples - 7 sub-GeV ($E_{vis} < 1.3$ GeV) and 6 multi-GeV ($E_{vis} > 1.3$ GeV) samples.

Seven sub-GeV samples are as follows:

1. FC sub-GeV single-ring e-like 0 decay-e electron sample

2. FC sub-GeV single-ring e-like 1 decay-e electron sample
   with one or more decay electrons
3. π^0-like sample
   fitted as π^0-like by π^0-fitter and π^0 likelihood

4. FC sub-GeV single-ring μ-like 0 decay-e electron sample
5. FC sub-GeV single-ring μ-like 1 decay-e electron sample
6. FC sub-GeV single-ring μ-like 2 decay-e electron sample
   with two or more decay electrons

7. FC sub-GeV 2-ring π^0-like sample
   Two rings are recognized and both of them are identified as e-like
   No decay electrons

'Single-ring e-like (μ-like)' events are events who have a single ring identified as e-like (μ-like). e-like events has to satisfy the momentum cut $p_e > 100$ MeV/c, and for μ-like events it is $p_\mu > 200$ MeV/c.

FC sub-GeV single-ring e-like sample has events from ν_e CCQE interactions and also contains NC π^0 background events. A high fraction of CCQE events are contained in in the 0 decay-e sample. In case one of the two gamma rays produced in NC π^0 events is missed, the NC π^0 event could be misidentified as a single-ring e-like event. A specialized π^0 fitter is used to reconstruct the second gamma-ray ring based on the fitted first ring, a mass cut, as well as a likelihood method is used to separate π^0-like events.

After applying the π^0 likelihood method, remaining e-like events are divided into two categories by the detected number of decay electrons: 0 decay-e sample with no decay electrons and 1 decay-e sample with one or more decay electrons.

As ν_μ CCQE events are expected to produce one decay electron from a muon, the fraction of CCQE events is high in 1 decay-e single-ring μ-like sample. FC sub-GeV single-ring μ-like events are divided to three categories according to the number of decay electrons reconstructed: 0 decay-e, 1 decay-e and 2 decay-e (2 or more decay electrons).

Table 6.9 shows the summary of purities of FC sub-GeV single-ring samples.

Left sub-GeV events are π^0-like multi-ring events, which have two or more e-like rings recognized.

Six multi-GeV samples are as follows:

1. FC multi-GeV single-ring ν_e-like sample
   Number of decay electrons > 0

		FC sub-GeV single-ring e-like			FC sub-GeV single-ring e-like
		0 decay-e	1 decay-e	π^0-like	
MC events		1932.9	196.1	95.9	2224.9
CC $\nu_e + \overline{\nu}_e$	Q.E.	81.5%	3.7%	13.0%	72.2%
	single meson	12.5%	56.0%	6.0%	16.2%
	multi π	0.9%	10.4%	1.0%	1.0%
	coherent π	1.0%	8.4%	0.4%	1.6%
CC $\nu_\mu + \overline{\nu}_\mu$		0.2%	12.1%	1.3%	1.3%
NC		3.9%	9.3%	78.2%	7.6%

		FC sub-GeV single-ring μ-like			FC sub-GeV single-ring μ-like
		0 decay-e	1 decay-e	2 decay-e	
MC events		365.8	1651.9	130.2	2147.9
CC $\nu_\mu + \overline{\nu}_\mu$	Q.E.	63%	79.6%	5.4%	72.3%
	single meson	11.7%	15.1%	69.3%	17.8%
	multi π	0.9%	1.3%	14.8%	2.0%
	coherent π	0.4%	1.1%	7.5%	1.4%
CC $\nu_e + \overline{\nu}_e$		5.4%	0.1%	0.05%	1.0%
NC		18.5%	2.8%	3.0%	5.5%

Table 6.9: Number of FC sub-GeV single-ring events and the compositions of interaction modes in them, for SK-IV MC normalised to the SK-IV livetime assuming two-flavor oscillation.

2. FC multi-GeV single-ring $\overline{\nu}_e$-like sample
   Number of decay electrons = 0

3. FC multi-GeV single-ring μ-like sample

4. FC multi-GeV multi-ring ν_e-like sample
   Events that passed through the MME likelihood cut
   Events that have ν_e and $\overline{\nu}_e$ separation likelihood > 0

5. FC multi-GeV multi-ring $\overline{\nu}_e$-like sample
   Events that passed through the MME likelihood cut
   Events that have ν_e and $\overline{\nu}_e$ separation likelihood < 0

   Most energetic ring identified as μ-like
   Momentum $p_\mu > 600$ MeV/c
   $E_{vis} > 600$ MeV

Figure 6.18 shows the schematic diagram which summarizes the steps for division of multi-GeV samples.

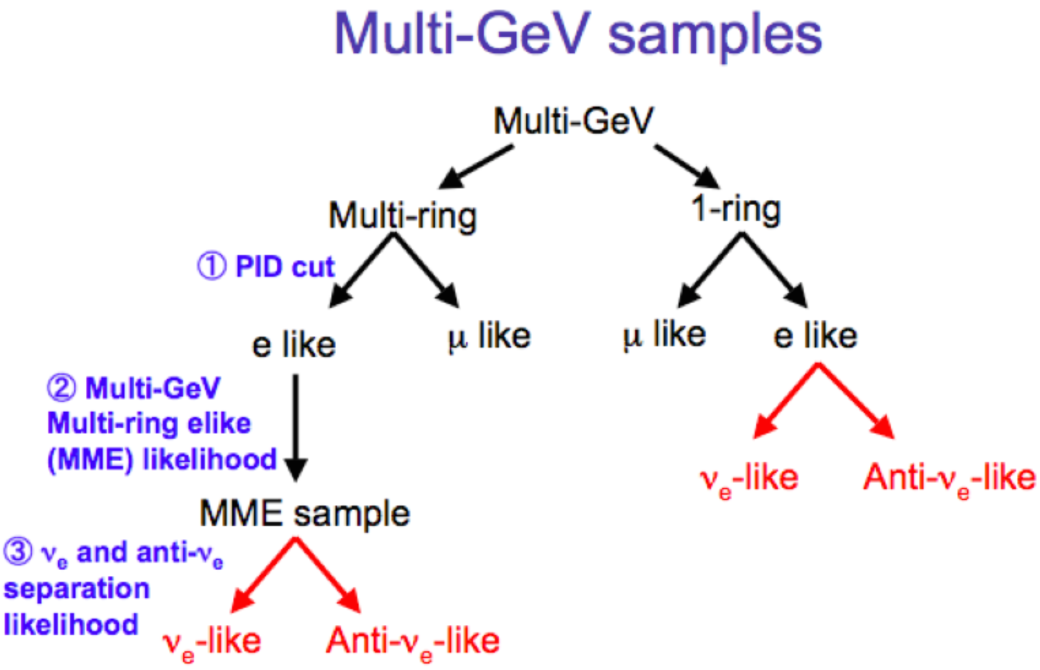

Figure 6.18: The schematic diagram of division steps for the multi-GeV samples. Figure is taken from (125).

Multi-GeV single-ring e-like sample is divided into ν_e-like and $\bar{\nu}_e$-like samples by the number of decay electrons. Table 6.10 shows the composition of interaction modes in the multi-GeV single-ring ν_e-like sample and $\bar{\nu}_e$-like sample, together with the case of without separation. By the $\nu_e/\bar{\nu}_e$ separation, the composition of CC interaction mode in ν_e-like ($\bar{\nu}_e$-like) sample has been increased by 5.2% (6.1%).

'Multi-ring $\nu_e/\bar{\nu}_e$-like (μ-like)' events are events whose most energetic ring is identified as e-like (μ-like). In order to make CC $\nu_e+\bar{\nu}_e$-enriched multi-GeV multi-ring e-like (MME) sample, a selection is applied based on likelihood method using variables such as PID likelihood, momentum fraction of the most energetic ring, number of decay electrons and the distance between the neutrino vertex and any muon decay electrons. This MME likelihood selection increases CC $\nu_e + \bar{\nu}_e$ purity significantly, as shown in Tab. 6.11.

Multi-GeV multi-ring e-like sample is sent through another cut to separate into ν_e-like and $\bar{\nu}_e$-like samples using a likelihood method using variables such as number of decay electrons, number of rings and transverse momentum of the most energetic ring, according to the fact that the outgoing electrons from CCν_e interaction with water nuclei tend to have smaller energy. Table 6.10 shows the composition of interaction

Interaction mode	Without separation	ν_e-like	$\overline{\nu}_e$-like
CC ν_e	57.6%	62.8%	55.9%
CC $\overline{\nu}_e$	30.6%	10.8%	36.7%
CC$\nu_\mu + \overline{\nu}_\mu$	3.2%	10.6%	8.1%
NC	8.8%	15.7%	6.6%
Total	568.7	135.9	432.8

Table 6.10: Interaction modes of multi-GeV single-ring sample for the cases without and with the $\nu_e/\overline{\nu}_e$ separation. The numbers are for SK-IV MC, normalised to data livetime with two-flavor oscillation effect.

Interaction mode composition	Without L_{MME}	With L_{MME}
CC $\nu_e + \overline{\nu}_e$	53.8%	75.5%
CC $\nu_\mu + \overline{\nu}_\mu$	21.5%	7.2%
NC	24.7%	17.3%
Total number of events	654.3	341.2

Table 6.11: Interaction modes of multi-GeV multi-ring sample for the cases without and with the MME likelihood. The numbers are for SK-IV MC, normalised to data livetime with two-flavor oscillation effect.

modes in the multi-GeV multi-ring ν_e-like sample and $\bar{\nu}_e$-like sample, together with the case of without separation. By the $\nu_e/\bar{\nu}_e$ separation, the composition of CC interaction mode in ν_e-like ($\bar{\nu}_e$-like) sample has been increased by 3.3% (1.5%).

6.7 PC OD stop/through separation

PC events are categorised to two samples - OD stopping and through-going events. OD stopping events deposit less charge in the OD compared to OD through-going events which travel through the OD into the rocks surrounding the detector. Selection criteria for OD stopping events are based on the energy deposited into the OD region.

1. PC OD stopping sample
   Maximum number of p.e.s observed in OD in a 500 nsec sliding time window (PE$_{anti}$) is less than PE$_{exp}$/1.5
   where PE$_{exp}$ is the expected number of p.e.s in the OD from the track length in the OD.
   The most energetic or the second most energetic ring is identified to be μ-like.

2. PC OD through-going sample

Interaction mode	Without separation	ν_e-like	$\overline{\nu}_e$-like
CC ν_e	56.1%	59.4%	53.1%
CC $\overline{\nu}_e$	19.5%	17.9%	21.0%
CC$\nu_\mu + \overline{\nu}_\mu$	7.2%	8.3%	6.1%
NC	17.3%	14.4%	19.8%
Total	341	161.9	168.1

Table 6.12: Interaction modes of multi-GeV multi-ring sample for the cases without and with the $\nu_e/\overline{\nu}_e$ separation. The numbers are for SK-IV MC, normalised to data livetime with two-flavor oscillation effect.

Remaining PC events after the OD stopping events are selected.

6.8 Up-μ separation

Up-μ events are further divided into stopping and through-going muon samples as described before. After stopping / through-going muons are separated by fitter and OD activities, the through-going up-μ data are further separated into showering muon sample and non-showering muon sample. Energetic muons produce electromagnetic shower while losing energy through processes such as Bremstrahlung, e^+ e^- pair production and photonuclear reactions. Selection of showering muons uses χ^2 technique based on expected charge (194). The through-goin muon events are categorized to be showering muons if they pass following criteria:

1. Difference between average corrected charge and the expected charge for non-showering muon ($\Delta(Q) = <Q> - q_l$) > 0.5 if χ^2 valuable for showering selection ≥ 50,
2. or $\Delta(Q) > 4.5$ - $0.08\chi^2$ if $\chi^2 < 50$,

otherwise they are categorised as non-showering through-going muons. Table 6.13 summarises the number of data and MC events in each eighteen samples used in this analysis, for each SK period.

	SK-I		SK-II		SK-III		SK-IV	
	Data	MC	Data	MC	Data	MC	Data	MC
FC sub-GeV								
single-ring								
e-like								
0-decay	2992	2705.4	1573	1445.4	1092	945.3	2098	1934.9
1-decay	301	248.1	172	138.9	118	85.3	243	198.4
π^0-like	176	160.0	111	96.3	58	53.8	116	96.2
μ-like								
0-decay	1025	893.7	561	501.9	336	311.8	405	366.3
1-decay	2012	1883.0	1037	1006.7	742	664.1	1833	1654.1
2-decay	147	130.4	86	71.3	61	46.6	174	132.2
2-ring π^0-like	524	492.8	266	259.8	182	172.2	380	355.9
FC multi-GeV								
single-ring								
ν_e-like	191	152.8	79	78.4	68	54.9	156	135.9
$\overline{\nu}_e$-like	665	656.2	317	349.5	206	231.6	423	432.8
μ-like	712	775.3	400	415.7	238	266.4	420	554.8
multi-ring								
ν_e-like	216	224.7	143	121.9	65	81.8	175	161.9
$\overline{\nu}_e$-like	227	219.7	134	121.1	80	72.4	212	179.1
μ-like	603	640.1	337	337.0	228	231.4	479	499.0
PC								
OD stopping	143	141.4	77	71.3	54	52.0	109	115.0
OD through-going	759	772.4	350	377.3	290	304.0	626	629.9
Up-μ								
stopping	435.9	388.3	241.2	210.1	193.7	210	286.7	248.7
non-showering	1564.4	1306.3	725.3	687.7	612.9	486.3	1047.6	847.6
showering	271.6	285.1	108.1	106.9	110	123.2	282.9	f 209.2

Table 6.13: Number of events for data and MC, in each SK run period. Number of events for MC are normalized to data livetime with two-flavor oscillation effect.

Chapter 7

Search for WIMP neutrinos in Super-Kamiokande

7.1 Overview

Light WIMPs whose masses are up to 200 GeV could produce neutrinos with energy of few MeV $\sim$ about 200 GeV, by pair-annihilations inside the Sun. For this energy range, the Super-Kamiokande (SK) data are dominated by atmospheric neutrino events produced by cosmic ray interactions with the atmosphere. To test the contribution of the WIMP-induced neutrino signal to the atmospheric neutrino BG, SK I-IV data are fitted against signal MC plus BG MC by pulled χ^2 method, using the information of direction, momentum and flavor of signal and BG. First we will introduce the strategy of the analysis in Chap. 7.2. After explaining analysis method in Chap. 7.3, the results of the sensitivity study will be given in Chap. 7.4. Finally, the result of the analysis using SK data will be given in Chap. 7.5 and interpreted to the WIMP-nucleon scattering cross-sections in Chap. 7.6. The resultant numbers will be shortly summarised in Chap. 7.7 before moving to discussions in the next Chapter.

7.2 Analysis strategy

The search for the light WIMPs using the Super-Kamiokande is motivated by recent observations as mentioned in Chap. 2. For scenarios with light WIMPs, most of the signal will end up in the contained neutrino event (FC+PC) categories. Tables 7.1, 7.2 and 7.3 show the expected fraction of WIMP-induced events in four event categories which span the energy range from the lowest to the highest, normalized to the total number of WIMP-induced events for candidate WIMP masses and for $b\bar{b}$, W^+W^- and $\tau^+\tau^-$ annihilation channels, respectively. Fig. 7.1 visualizes them. It can be seen that for 10 GeV $b\bar{b}$ WIMP, 98% of the signal goes into FC+PC categories.

Table 7.4 shows the fraction of the number of events from each flavor compared to the total number of events for signal MC, for 6 GeV $b\bar{b}$, 80.3 GeV W^+W^- and 200

GeV $\tau^+\tau^-$, respectively. Each flavor is shown for combination of ν and $\bar{\nu}$, and the ratio of the number of events produced through CC/NC type of interactions are separately shown. To show the statistical fluctuation in the signal MC, the mean values are shown together with 90% upper and lower values for 100 fluctuated MC samples. Note that electron neutrino and tau neutrino induced events make up about 44% of the signal for 6 GeV $b\bar{b}$ WIMP.

To increase signal acceptance, our analysis is updated to use FC and PC events as well. We also started using e-like events which only contribute to FC events. As a result, all e-like and μ-like high-energy events collected in SK are used. Compared to the up-μ only analysis, the signal acceptance is increased by 47 times for the 10 GeV $b\bar{b}$ channel WIMP hypothesis.

The main source of background is atmospheric neutrinos coming from all directions. The solar atmospheric neutrinos, originating from cosmic ray interactions in the Sun's atmosphere, is expected to be a source of background coming from the Sun. The calculation by Hettlage et al. shows that for a Cherenkov detectors with an effective area of 10^4 m^2 and a thickness of 500 m, the expected muon neutrino event rate with energies greater than 10 GeV is about $0.1 \sim 0.3$ events per year (200), therefore can be ignored. Figure 7.2 shows the expected event fraction of atmospheric neutrinos in SK event categories.

To reduce the overwhelming atmospheric neutrino BG events which increase as $\propto E^{-2.7}$, the angular cut approach used in the previous analysis is not as efficient, because the correlation of lepton direction and parent neutrino direction is worse for low-energy events.

	FC sub GeV	FC multi GeV	PC	up-μ
6 GeV	70	28	1.8	0.17
10 GeV	42	49	6.4	2.5
20 GeV	20	55	14	11
50 GeV	7.4	44	21	28
100 GeV	3.3	33	22	42
200 GeV	1.4	24	19	56

Table 7.1: The fraction(%)s of WIMP-induced events in four categories compared to the total WIMP-induced events in SK high energy data are shown for tested WIMP masses, for $b\bar{b}$ channel.

In this analysis, we adopt a fitting approach whose format was developed for SK atmospheric neutrino oscillation analyses. The different energy spectra of the atmospheric neutrino BG and the signal, the distinctive angular distribution of the signal peaking toward the direction of the Sun and the flavor composition information are fully used in the fitting approach. The details of the analysis will be described in next chapter.

	FC sub GeV	FC multi GeV	PC	up-μ
80.3GeV	0.32	25	19	56
100GeV	0.21	18	14	68
200 GeV	0.09	10	9.8	80

Table 7.2: Fraction(%)s of WIMP-induced events in four categories compared to the total WIMP-induced events in the SK high energy data are shown for tested WIMP masses, for W^+W^- channel.

	FC sub GeV	FC multi GeV	PC	up-μ
4GeV	46	49	4.1	0.97
6 GeV	26	60	9.4	4.3
10GeV	13	58	17	13
20GeV	5.3	44	22	29
50GeV	1.1	27	22	50
100GeV	0.26	17	15	68
200 GeV	0.09	10	11	79

Table 7.3: Fraction(%)s of WIMP-induced events in four categories compared to the total WIMP-induced events in the SK high energy data are shown for tested WIMP masses, for $\tau^+\tau^-$ channel.

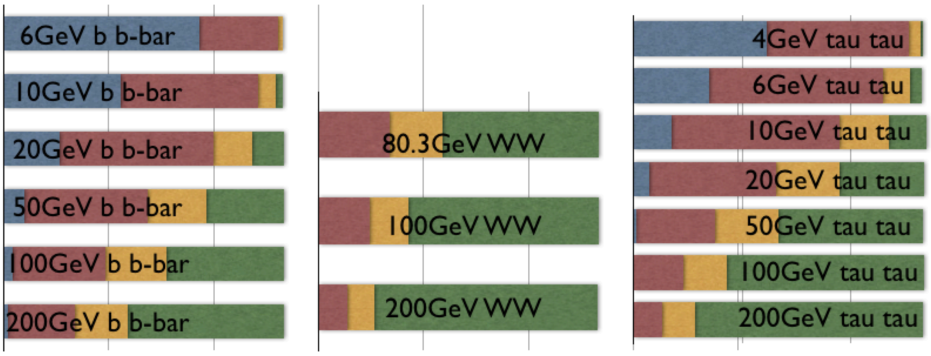

Figure 7.1: Visualized fractions of WIMP-induced events in four categories of SK high energy data are shown for assumed WIMP masses and annihilation channels; blue : FC sub GeV, red : FC multi GeV, yellow : PC, green : up-μ events.

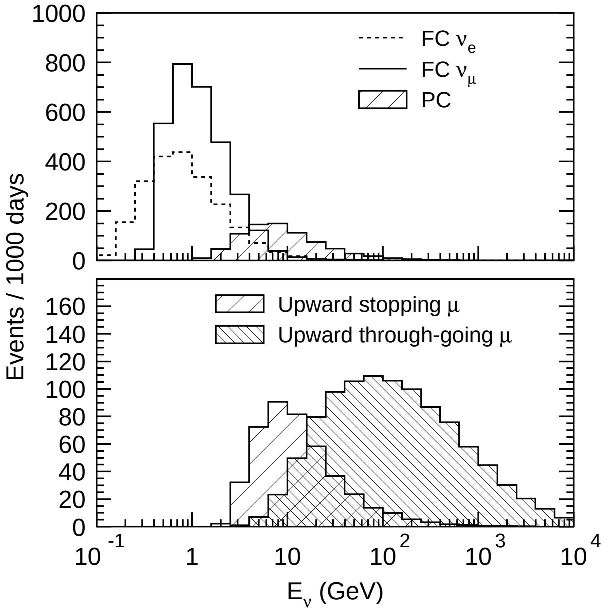

Figure 7.2: The expected event rates for FC ν_e, FC ν_μ, PC (top) and upward stopping μ, upward through-going μ (bottom).

m_χ (GeV)	annihilation channel	ν_e CC	ν_e NC	ν_μ CC	ν_μ NC	ν_τ CC	ν_τ NC
6 GeV	$b\bar{b}$	35.0 (34.2 +35.7)	3.37 (-3.02 +3.66)	50.9 (-50.2 +51.6)	5.04 (-4.76 +5.26)	4.37E-4 (-1.63E-4 +7.25E-4)	5.75 (-5.41 +6.01)
80.3 GeV	W^+W^-	12.6 (-9.05 +16.9)	2.30 (-0.645 +5.41)	68.4 (-63.8 +73.7)	3.27 (-2.20 +4.44)	8.95 (-7.48 +10.73)	3.60 (-2.44 +4.85)
200 GeV	$\tau^+\tau^-$	7.32 (-4.48 +10.2)	1.39 (-0.368 +3.50)	78.7 (-75.9 +82.0)	1.88 (-1.43 +2.52)	8.35 (-7.18 +9.75)	2.00 (-1.54 +2.67)

Table 7.4: Fraction (%) of the number of signal events from each flavor compared to the total number of events for three representative WIMP masses and channels. Each flavor is for combination of ν and $\bar{\nu}$, and further shown are the ratio of the number of events produced through CC / NC type of interactions. The mean values of 100 fluctuated signal MC sets are shown together with 90% lower and upper values in the parentheses.

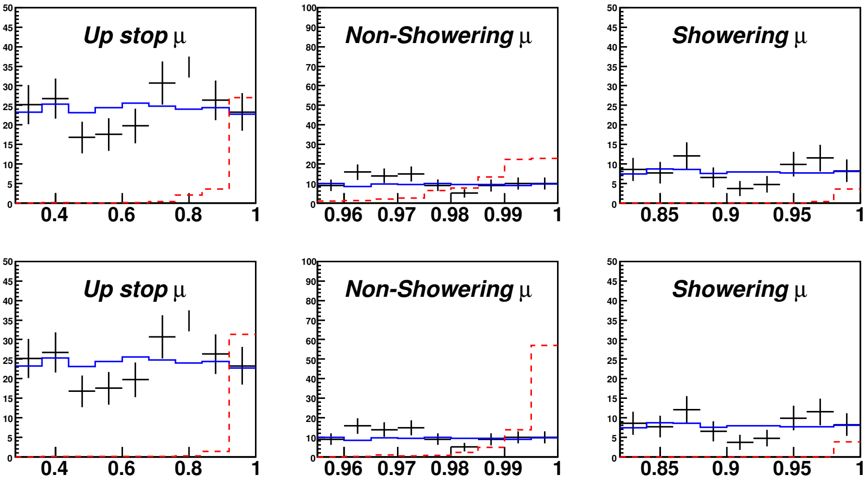

Figure 7.3: Angular distributions for 50 GeV $\tau^+\tau^-$ channel are shown in three up-μ samples. Red dashed : WIMP-induced neutrino signal magnified, in 'the cosine value between the direction from the Sun and the reconstructed direction' (top) and 'cosine value between the true direction of the parent neutrino and the reconstructed direction' (bottom, used in the analysis).

7.3 Analysis method

The data and BG/signal MC events in 18 event categories are distributed to finer bins. The visible energy and reconstructed angle are used to define bins. For angular binning, the cosine value between the angle from the Sun and the reconstructed direction, $cos\theta_{sun}$ is used, by reading solar position relative to the SK tank for each event time from SK low energy solar oscillation analysis library. In the $cos\theta_{sun}$ distribution, we can check for example in Fig. 7.6 that BG event are almost evenly spread, because of the mixing of zenith angular bins into $cos\theta_{sun}$ bins due to the location of the SK(36°25'N), which smears the original anomaly in zenith bins introduced by atmospheric neutrino oscillation. Because of the sample size of 10° open angle we took, the signal events are not perfectly coming from the direction of the Sun, therefore the angular distribution for the signal will be more spread than they are supposed to be. To correct this, instead of the cosine value between the direction from the Sun and the reconstructed direction, we used the angle between reconstructed direction and the true direction of the parent neutrino as the definition of $cos\theta_{sun}$ for signal MC events. Figures 7.3 and 7.4 show the angular distributions of the three up-μ samples for these two different definitions.

For PC, FC multi-GeV samples and sub-GeV CC samples, 10 equally-sized angular bins which span from $cos\theta_{sun} = -1$ to 1 are used. For FC sub-GeV μ-like 2 decay electron, Sub GeV e-like 1 decay electron, Sub GeV π^0-like 1-ring, Sub GeV

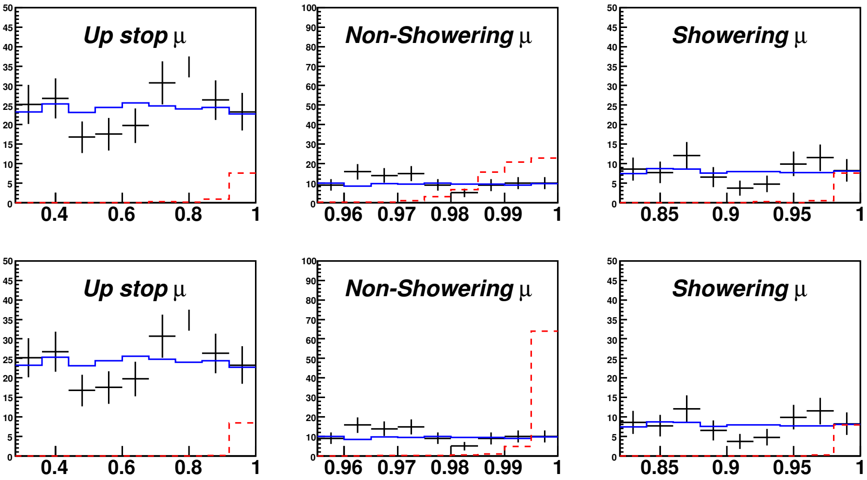

Figure 7.4: Angular distributions for 200 GeV $\tau^+\tau^-$ channel are shown in three up-μ samples. Red dashed : WIMP-induced neutrino signal magnified, in 'the cosine value between the direction from the Sun and the reconstructed direction' (top) and 'cosine value between the true direction of the parent neutrino and the reconstructed direction' (bottom, used in the analysis).

π^0-like multi-ring samples, angular information are not used. For up-μ samples, signal is expected to highly concentrate around $cos\theta_{sun} = 1$. Referring T.Tanaka's previous analysis (56) which calculated open angle containing 90% of WIMP-induced up-μ events for stopping, non-showering and showering through-going samples separately, assuring at least 6 BG events to be remained in each bin, we optimized the bin sizes to be {-1, 0.28, 0.36, 0.44, 0.52, 0.6, 0.68, 0.76, 0.84, 0.92, 1.0}, {-1, 0.955, 0.96, 0.965, 0.97, 0.975, 0.98, 0.985 , 0.99, 0.995, 1.0}, {-1, 0.82, 0.84, 0.86, 0.88, 0.9, 0.92, 0.94, 0.96, 0.98, 1.0} for stopping, non-showering and showering through-going up-μ samples, respectively. As discussed in previous chapter, the contamination from the cosmic-ray events left around horizontal direction are estimated and subtracted from the first and second closest bins to the horizon for 3 up-μ categories respectively. Assuming this contamination will spread evenly in $cos\theta_{sun}$ distribution, we take the fraction of contaminating events versus total up-μ events, and reduced the normalizations of all up-μ bins according to it.

All sub-GeV samples are further divided into 5 momentum bins. For multi-GeV samples in FC, PC, up-μ, 1 $\sim$ 6 energy bins are defined considering energy range of each sample. As a result, events will be distributed in 684 two-dimensional (angle & energy) bins for each SK run period respectively, in total 2736 bins for SK I-IV. After that, bins whose number of BG events in a bin are less than 6 are merged with

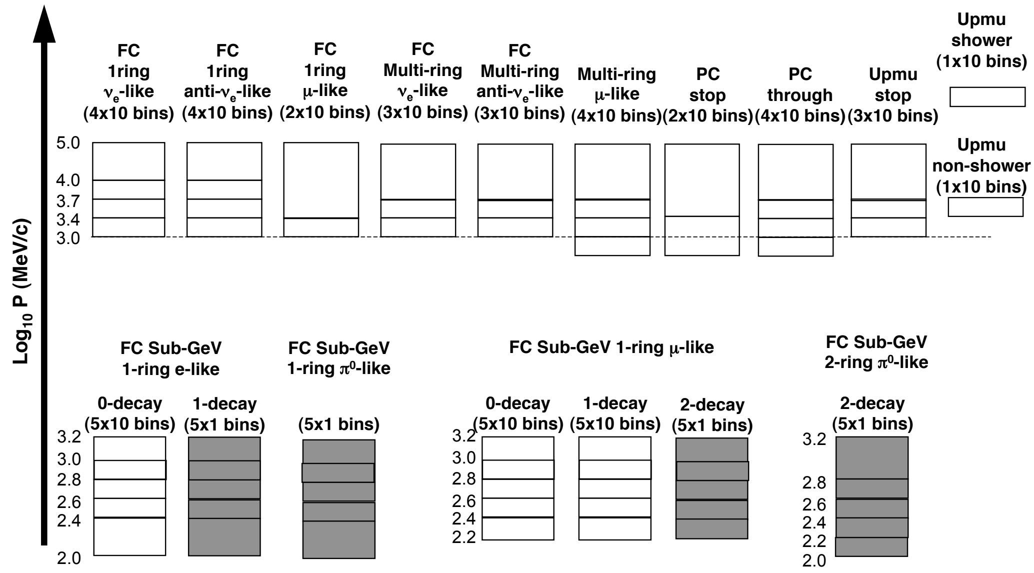

Figure 7.5: Illustration of the binning used in this analysis : FC: 370 bins, PC: 60 bins, up-μ: 50 bins are used. White boxes indicate that a momentum bin is divided into 10 angular bins between -1 < $cos\theta_{sun}$ < 1. Shaded boxes indicate that a momentum bin is not further divided into angular bins (FC single-ring e-like 1-decay, π^0-like, μ-like 2-decay samples and 2-ring π^0 samples).

neighboring bins, also SK-I, SK-II, SK-III, SK-IV bins are merged together as:

$$\begin{aligned} N_n^{data} &\to \sum_n N_{m,SKm}^{data} \\ (N_n^{exp})(1+\sum_j f_j^n \epsilon_j) &\to \sum_m N_{n,SKm}^{exp}(1+\sum_j f_{j,m}^n \epsilon_{j,m}) \end{aligned} \tag{7.1}$$

As a result, total 480 bins are used for fitting and they are illustrated in Fig. 7.5.

Figures 7.6 to 7.7 show the $\cos\theta_{sun}$ and reconstructed momentum distributions, for 6 GeV $b\bar{b}$ WIMP hypothesis as an example.

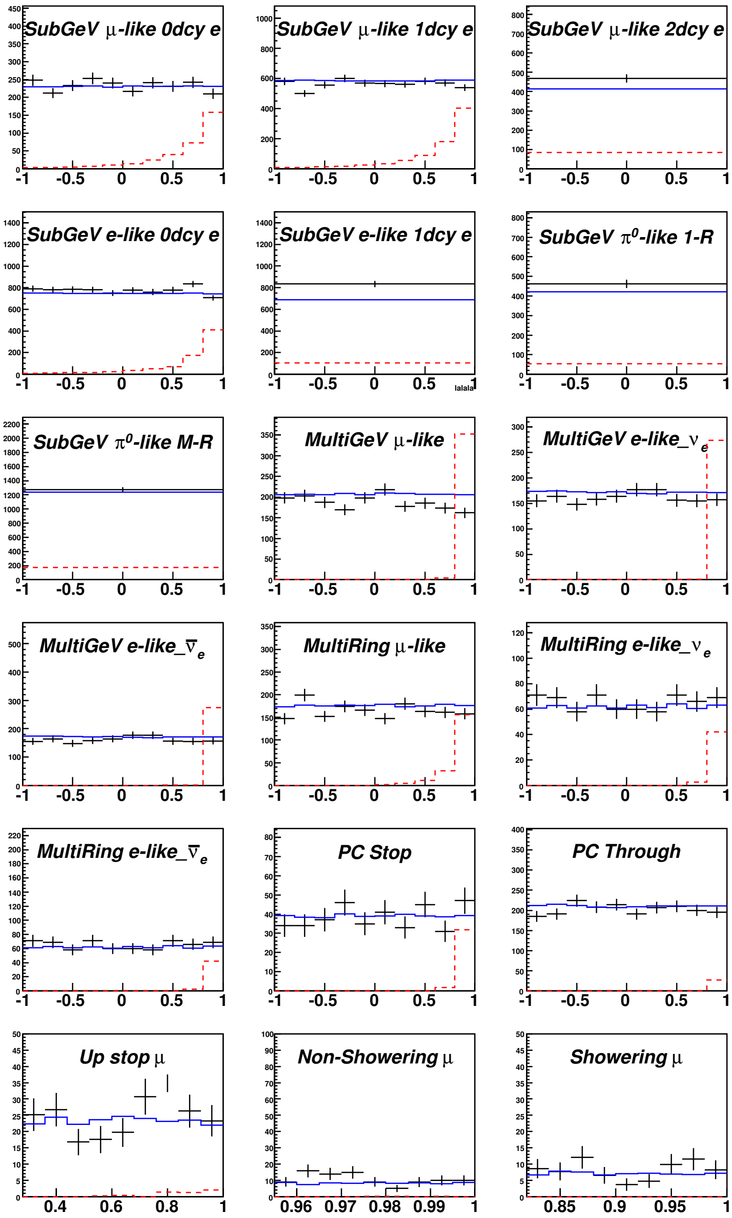

Figure 7.6: $\cos\theta_{sun}$ distributions of signal MC for 6 GeV $b\bar{b}$ are shown in the 18 event categories. Black cross: SK I-IV data, blue solid: atmospheric neutrino backgroundnormalized to livetime of data), red dashed: signal MC events in arbitrary normalization.

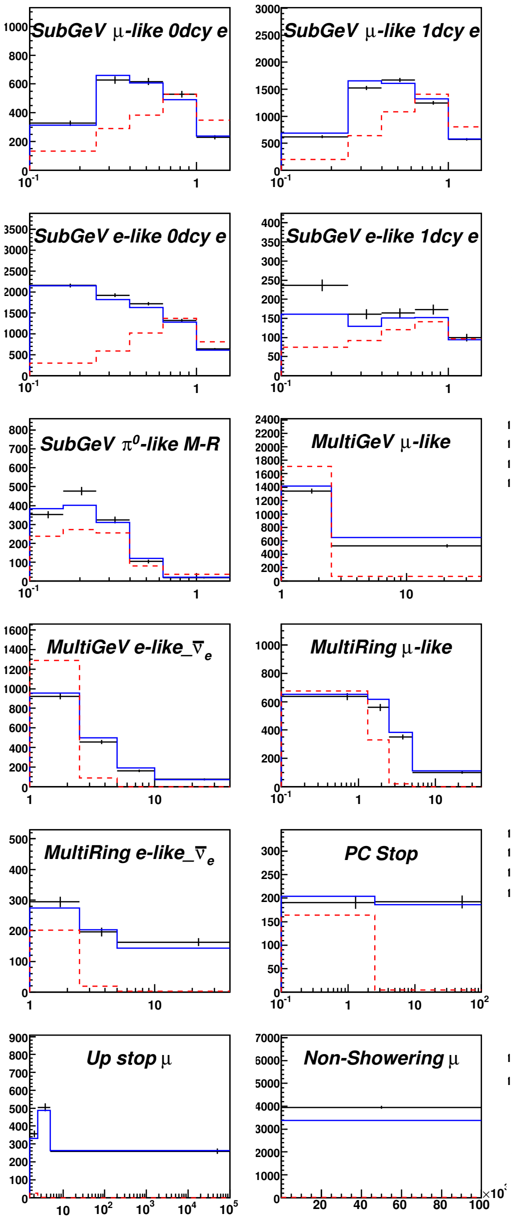

Figure 7.7: Reconstructed momentum [GeV] distributions of signal MC for 6 GeV $b\bar{b}$ are shown in the 18 event categories. Black cross: SK I-IV data, blue solid: atmospheric neutrino background normalized to livetime of data, red dashed: signal MC events in arbitrary normalization.

If the expected number of events in each bin is low, the number of events in each bin follows Poisson distribution, therefore the natural logarithm of the joint probability to obtain the observed data, i.e. the log-likelihood $-2lnL$ is used for fitting. The data is compared against signal plus BG using the maximum log-likelihood method, particularly with "pulled technique". In this approach, χ^2 is defined where $\partial\chi^2/\partial\epsilon_j = 0$ for every j as :

$$\chi^2 = \min_{\{\epsilon_j\}} \left[2\sum_{n=1}^{N} [N_n^{BG}(1+\sum_j^J f_j^n \epsilon_j) + \beta N_n^{\chi}(1+\sum_j^J g_j^n \epsilon_j) - N_n^{data} + N_n^{data} ln(\frac{N_n^{data}}{N_n^{BG}(1+\sum_j^J f_j^n\epsilon_j) + \beta N_n^{\chi}(1+\sum_j^J g_j^n\epsilon_j)})] + \sum_j^J (\frac{\epsilon_j}{\sigma_j})^2 \right], \tag{7.2}$$

where n is the index of the bins; N_n^{data} is the number of events observed in each bin; N_n^{BG} is the background expectation in the bin after oscillated and normalized; N_n^{χ} is the number of events of signal MC in the bin, where β, the global normalization parameter, stands for the allowed fraction of WIMP-induced events. β is the only parameter allowed to move free in the fitting, without prior regulation of the range. j is the systematic uncertainty index; σ_j is the 1σ value of the j-th systematic error; ϵ_j is the pull to it and f_j^n/σ_j (g_j^n/σ_j) is the predicted fractional change of the number of background (signal) events in the n-th bin due to 1σ change of the j-th systematic error.

148 systematic errors on neutrino flux, neutrino interaction, detector response are considered. List of the sources and some information about computation of the systematic errors will be presented in the next chapter.

The data could be fitted either in covariance approach or pull approach. The two approaches are equivalent for χ^2 distribution (201). In this analysis we can argue that our $-2lnL$ follows χ^2 distribution with sufficiently large degree of freedom (480 bins and a free parameter) and we extend the argument of (201) to maximum log-likelihood method and use the pull approach, because it is more practical than the covariance one when $J \ll N$; i.e. the minimization of the Eq. 7.2 leads to a $J \times J$ matrix inversion rather than the $N \times N$ covariance matrix inversion (201).

Differentiating χ^2 with respect to the systematic ϵ_j yields

$$\frac{\partial\chi^2}{\partial\epsilon_j} = 2\sum_n^N [A_{nj} - \frac{N_n^{data}A_{nj}}{B_{nj}}] + \frac{2\epsilon_j}{\sigma_j^2} = 0, \tag{7.3}$$

where

$$A_{nj} = N_n^{BG} f_j^n + \beta N_n^{\chi} g_j^n \tag{7.4}$$

and

$$B_{nj} = N_n^{BG}(1+\sum_j^J f_j^n\epsilon_j) + \beta N_n^{\chi}(1+\sum_j^J g_j^n\epsilon_j). \tag{7.5}$$

After arranging it to have the linear terms in left-hand side, the minimization problem is specified to solve $J \times J$ polynomial equations :

$$\sum_{l,n}\left(\frac{N_n^{data}A_{nj}A_{nl}}{C_{nj}^2}+\delta_{lj}\frac{1}{\sigma_l^2}\right)\epsilon_l=\sum_n\frac{N_n^{data}A_{nj}}{C_{nj}}\left(\frac{1}{1+\frac{\sum_j^J A_{nj}\epsilon_j}{C_{nj}}}+\frac{\sum_j^J A_{nj}\epsilon_j}{C_{nj}}\right)-A_{nj}, \tag{7.6}$$

where

$$C_{nj} = N_n^{BG} + \beta N_n^{\chi}. \tag{7.7}$$

Inverting this matrix allows one to solve for the set of ϵ_j that minimize χ^2. The χ^2 at each tested β is calculated by varying ϵ_j to minimize χ^2.

Again note that the merging is done such that it is predicted to have at least 6 BG events in each bin after scaling to data livetime, also the bins with no BG events are excluded from the fitting. Although our calculation is based on Poisson distribution, these will allow us to interpret the result with Gaussian error assumption and the χ^2 test.

We first run the fit for a wide range of β with rough gradation to find the range of β spanning about $-5\sigma \sim 5\sigma$, then run a fit again with more precise (about 0.1σ) gradation for that narrower range of β. In the resultant χ^2 distribution as a function of β, the best-fit β, or β_{min} is defined at the point with minimum-χ^2.

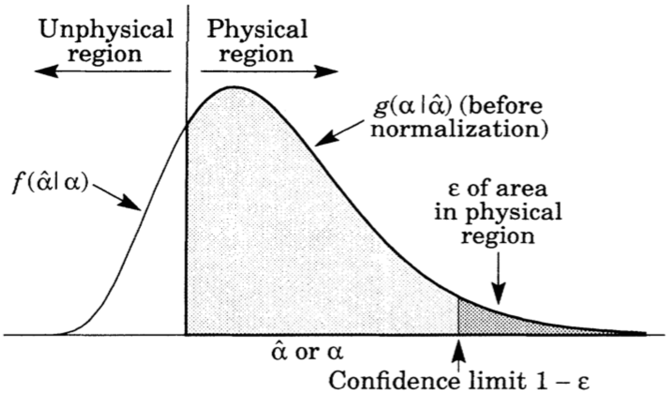

Figure 7.8: Bayes' theorem says that our new knowledge of the distribution of β, given our measurement $\hat{\beta}$, is given by the shaded function after appropriate renormalization. (α in this figure corresponds to β in this analysis. Figure is taken from Particle Data Group (PDG).)

In case where β_{min} is consistent with no WIMP hypothesis, we set 90% upper limit on β by drawing $\Delta\chi^2$ distribution; the definition of $\Delta\chi^2$ is the difference of the χ^2 value for each β compared to the χ^2 value at β_{min}, χ^2_{min}. Among the tested signal hypotheses, some of them results in negative value of β_{min}. To deal with these, we reveal the Bayes' theorem in the calculation of upper limit. The Bayes' theorem can be written as:

$$g(\beta|\hat{\beta}) = \frac{f(\hat{\beta}|\beta)\pi(\beta)}{\int f(\hat{\beta}|\beta)\pi(\beta)d\beta}; \tag{7.8}$$

In order to derive a confidence limit on β, one would like to know $g(\beta|\hat{\beta})d\beta$, which is the probability of β lies between β and $\beta + d\beta$, given our measurement $\hat{\beta}$. The conditional probability density function $f(\hat{\beta}|\beta)$ about experimental information $\hat{\beta}$ for a fixed and unknown value of β will be delivered from $\Delta\chi^2$ distribution.

If we assume that β cannot lie in the unphysical region but can lie anywhere in the physical region with constant probability, then a 'prior' $\pi(\beta)$ is assumed to be 0 when β has negative value, flat when β is positive. This leads to the following formula:

$$g(\beta|\hat{\beta}) = f(\hat{\beta}|\beta) / \int f(\hat{\beta}|\beta)d\beta; \tag{7.9}$$

if β is in the physical region,

$$g(\beta|\hat{\beta}) = 0;$$

otherwise.

It is known that at best fit maximum likelihood $-2lnL$ is asymptotically distributed as χ^2 distribution with $N - m$ degree of freedom, where m is the number of fit parameter which is 1 in our case. And χ^2 distribution for large degree of freedom can be approximated to follow normal distribution. We calculate the 90% upper limit on β, β_{90} above which the right tail of Gaussian distribution corresponds to 10% of physical region (colored) as in Fig. 7.8, in either case that β_{min} falls in physical region or unphysical region.

Fig. 7.9 shows an example of $\Delta\chi^2$ distribution versus β, for 6 GeV $b\bar{b}$ channel WIMP hypothesis.

7.4 Sensitivity study

7.4.1 Sensitivity study for null hypothesis

To understand the effect of the statistical fluctuation of the data in fitting, we generate the fake SK data by setting the number of events in each bin according to a Poisson distribution. We also make ϵ_j's fluctuated according to a Gaussian distribution and add $f_j^n \epsilon_j$ to the number of events in j-th bin to take into account the systematic fluctuations. By generating 500 sets of fake data for each WIMP mass and channel hypothesis and performing a pulled χ^2 test to each, we perform a toy MC study for the null hypothesis assuming data are composed of background only.

Fig.7.10 shows the distribution of β_{min} for the 10 GeV $\tau^+\tau^-$ WIMP hypothesis as an example. The two green lines show the 90% band within which 90% of the β_{min} values

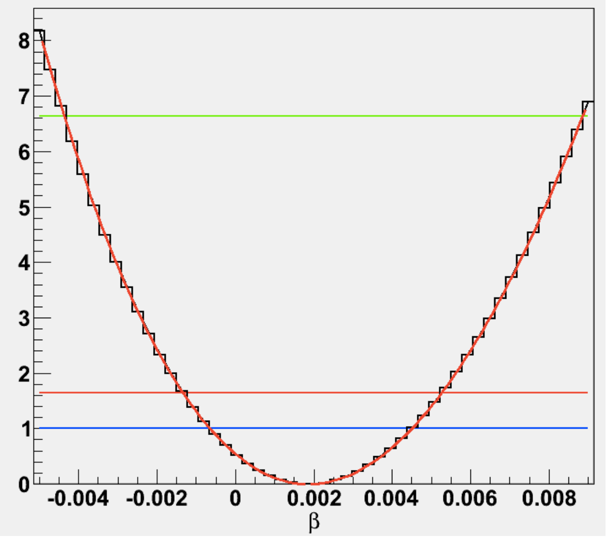

Figure 7.9: The $\Delta\chi^2$ distribution for 6 GeV $b\bar{b}$ channel. Blue line indicates $\Delta\chi^2 = 1.65\sigma$ which corresponds to 90% upper limit without Bayesian prior. Green line indicates $\Delta\chi^2 = 2.71\sigma$, which corresponds to 90% upper limit with Bayesian prior, if minimum was at $\beta = 0$. Finally red line indicates recalculated Bayesian 90% upper limit used in this analysis. For this example, $\Delta\chi^2$=4.9. The β_{min}, $\Delta\chi^2$ and β_{90}s for all test WIMP hypotheses will be summarized in Chap. 7.5.

of 500 toy MC sets are contained, and the result of the fit to the data is marked with red line. Figure 7.11 shows the distribution of β_{90} for 10 GeV $\tau^+\tau^-$ WIMP hypothesis. The guidelines indicate the mean value of β_{90} and the 90% upper and lower limits of β_{90}s, together with β_{90} from the data result.

Figure 7.12 shows the resultant best fit β_{min}s of data and toy MC for 16 tested WIMP hypotheses. Figure 7.13 shows the resultant 90% Bayesian upper limit β_{90}s of data and toy MC for 16 tested WIMP hypotheses.

7.4.2 Statistical fluctuation in the signal MC

The fluctuation of BG MC can be negligible as the statistics used is about 200 times that of data. However due to the statistical limitation of the events in the signal MC as shown in Tab. 5.1, larger fluctuation is expected for the MC. By testing 100 sets of signal MCs for 6 GeV $b\bar{b}$, 80.3 GeV W^+W^- and 200 GeV $\tau^+\tau^-$ hypotheses, the differences resulted in 90% upper limit are found to be about 2.8% for 6 GeV $b\bar{b}$, 9.6% for 80.3 GeV W^+W^- and 6.6% for 200 GeV $\tau^+\tau^-$ respectively. The 90% bands of the upper limit on flux of 100 sets of signal MC are shown in Tab. 7.5.

As the size of the difference coming from the signal MC is much smaller than the size of it in the data, it is not considered as a source of uncertainty in the final result.

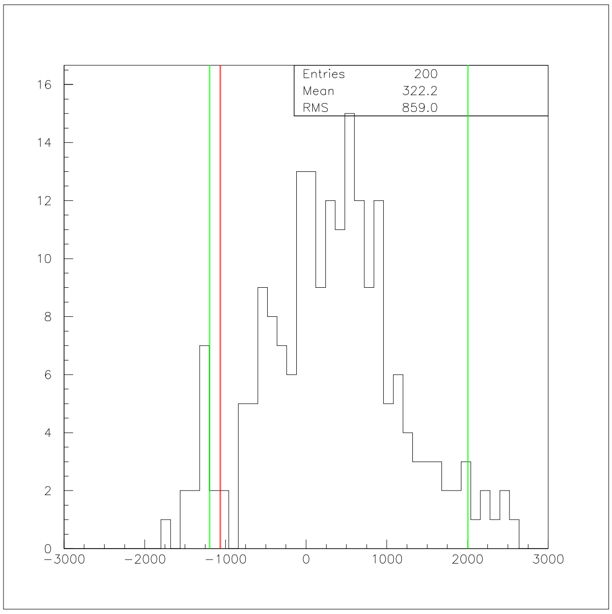

Figure 7.10: The distribution of β_{min} for the 10 GeV $\tau^+\tau^-$ WIMP hypothesis is shown. The green lines mark the 90% bands of β_{min}s from 500 toy MC sets, and the red line shows the β_{min} from the data result.

m_χ (GeV)	annihilation channel	ν_μ (mean value) (km^{-2}y^{-1})	ν_μ (lower) (km^{-2}y^{-1})	ν_μ (upper) (km^{-2}y^{-1})	fraction (%)
6 GeV	$b\bar{b}$	4.28×10^{14}	4.16×10^{14}	4.40×10^{14}	2.80
80.3 GeV	W^+W^-	8.59×10^{11}	8.00×10^{11}	9.41×10^{11}	9.55
200 GeV	$\tau^+\tau^-$	1.68×10^{11}	1.59×10^{11}	1.79×10^{11}	6.55

Table 7.5: The 90% upper limit on ν_μ flux from WIMP annihilations for the sensitivity study by 100 signal MCs are shown, for mean value (third column) and lower/upper values (fourth/fifth columns) of 90% band of it. The last column shows the fractional change in the 90% upper value compared to the mean value.

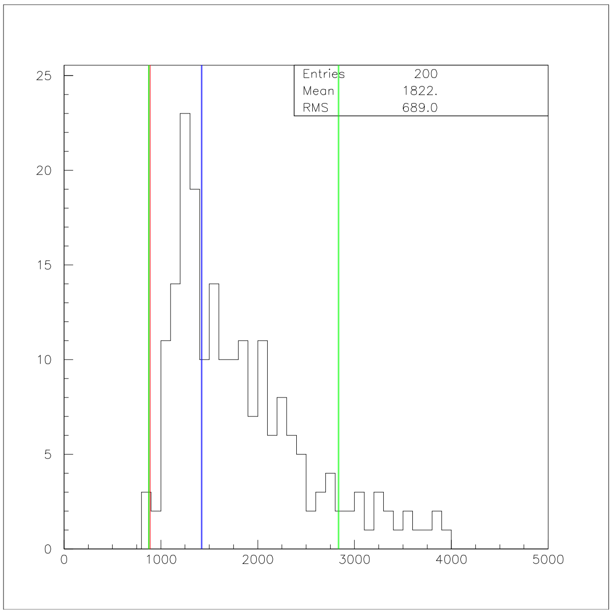

Figure 7.11: The distribution of β_{90} for 10 GeV $\tau^+\tau^-$ WIMP hypothesis is shown. The blue line shows the mean value of β_{90} and two green lines mark the 90% upper and lower limits of β_{90}s. The red line shows the β_{90} from the data result.

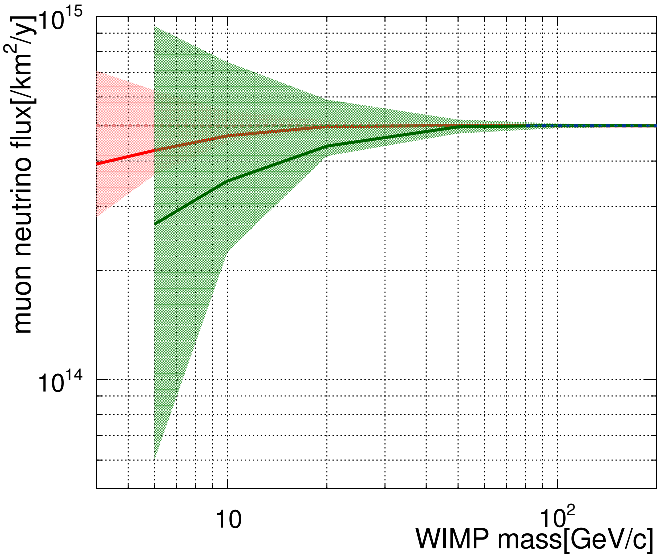

Figure 7.12: Fitted β_{min}s for data (solid), the 90 % bands of β_{min}s from 500 toy MC (band), and median value of β_{min}s from 500 toy MC (dashed) are shown as a function of WIMP mass for $\tau^+\tau^-$ (red), $b\bar{b}$ (green) and W^+W^- (blue) channels. We added $5{\times}10^{14}$ to all β_{min}s in order to plot in log scale.

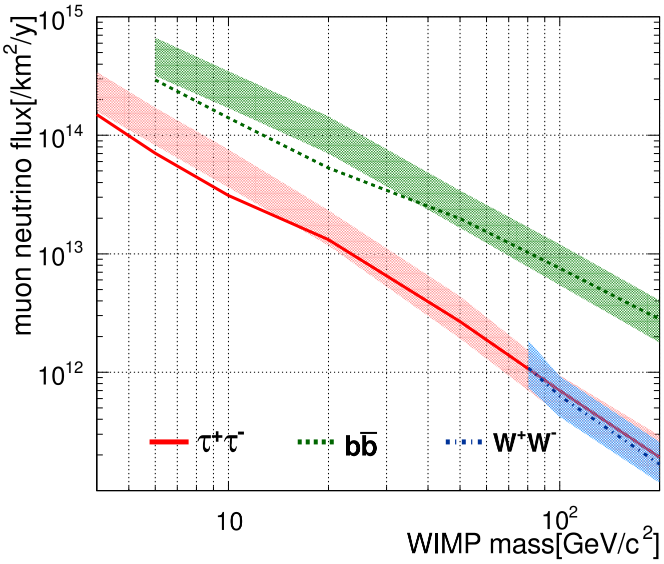

Figure 7.13: The 90% upper limit on muon-neutrino flux from WIMP annihilations in the Sun at SK for the $\tau^+\tau^-$ channel in red solid; $b\bar{b}$ in green dashed; W^+W^- in blue dot-dashed. The shaded regions show 1σ bands of the sensitivity study results (color scheme is the same as for data).

For example, for 10 GeV $\tau^+\tau^-$ hypothesis, the statistical fluctuation coming from the data shown as a band in Fig. 7.13 is found to be 15.6 times larger than the fluctuation coming from the signal MC.

7.5 Limits on WIMP-induced neutrino events and flux

When we perform the fit for only the point $\beta = 0$, it corresponds to the fitting of atmospheric neutrino three flavor oscillation without WIMP contribution in $cos\theta_{sun}$ distribution. The goodness of fit for null hypothesis is checked by sensitivity study explained in the previous chapter. But we also can quickly view the p-value obtained from Pearson's chi-squared test for no WIMP contribution. The χ^2 value for null hypothesis is 518.039, corresponding to χ^2/d.o.f = 518.039/479 = 1.08. The test p-value is 0.106, which is consistent with the conclusion of the sensitivity study.

Table 7.6 lists the χ^2 values at minimum or χ^2_{min}, $\Delta\chi^2$ at 0, Bayesian $\Delta\chi^2$ from the minimum, β_{90} (90% upper limit on WIMP-induced ν_μ flux in SK I-IV) for data and mean values of it for sensitivity study for all WIMP hypotheses tested.

The total number of WIMP-induced events in SK I-IV at the fitted minimum point, N_{min} and the number of total WIMP-induced events in SK I-IV at 90% upper limit, N_{90} for tested WIMP hypotheses are listed in Tab.7.7. Figure 7.14 visualizes N_{min}s

m_χ (GeV)	annihilation channel	χ^2_{min}	$\Delta\chi^2$ at 0	Bayesian $\Delta\chi^2$	ν_μ $(km^{-2}y^{-1})$	ν_μ sensitivity $(km^{-2}y^{-1})$
4 GeV	$\tau^+\tau^-$	508.1	0.87	4.4	1.50×10^{14}	2.43×10^{14}
6 GeV	$b\bar{b}$	507.8	1.24	4.9	2.94×10^{14}	4.67×10^{14}
	$\tau^+\tau^-$	507.8	1.25	4.9	7.08×10^{13}	1.19×10^{14}
10 GeV	$b\bar{b}$	507.4	1.65	5.4	1.40×10^{14}	2.50×10^{14}
	$\tau^+\tau^-$	507.6	1.40	5.1	3.10×10^{13}	5.30×10^{13}
20 GeV	$b\bar{b}$	507.4	1.65	5.4	5.31×10^{13}	1.01×10^{14}
	$\tau^+\tau^-$	509.0	0.06	2.4	1.32×10^{13}	1.63×10^{13}
50 GeV	$b\bar{b}$	509.0	0.04	3.0	1.98×10^{13}	2.29×10^{13}
	$\tau^+\tau^-$	508.9	0.14	2.3	2.67×10^{12}	2.97×10^{12}
80.3 GeV	W^+W^-	508.8	0.17	2.3	1.09×10^{12}	1.14×10^{12}
100 GeV	$b\bar{b}$	509.0	0.06	2.4	7.54×10^{12}	8.37×10^{12}
	W^+W^-	508.9	0.14	2.3	6.29×10^{11}	6.11×10^{11}
	$\tau^+\tau^-$	508.9	0.16	2.3	6.98×10^{11}	6.41×10^{11}
200 GeV	$b\bar{b}$	508.9	0.12	2.3	2.81×10^{12}	2.59×10^{12}
	W^+W^-	508.9	0.07	2.4	1.67×10^{11}	1.68×10^{11}
	$\tau^+\tau^-$	508.9	0.08	2.4	1.91×10^{11}	1.88×10^{11}

Table 7.6: χ^2 value at minimum (χ^2_{min}), $\Delta\chi^2$ at 0, Bayesian $\Delta\chi^2$ from the minimum, 90% upper limit on WIMP-induced ν_μ flux in SK I-IV for data and median value of it for 500 sets of sensitivity study are shown.

and N_{90}s for $b\bar{b}$, $\tau^+\tau^-$, W^+W^- channels, respectively.

m_χ (GeV)	annihilation channel	N_{min} (3903 days)	N_{90} (3903 days)
4 GeV	$\tau^+\tau^-$	-41.0	58.1
6 GeV	$b\bar{b}$	-55.2	74.2
	$\tau^+\tau^-$	-44.1	45.2
10 GeV	$b\bar{b}$	-56.1	54.6
	$\tau^+\tau^-$	-33.8	35.3
20 GeV	$b\bar{b}$	-43.9	40.9
	$\tau^+\tau^-$	-4.66	32.8
50 GeV	$b\bar{b}$	-5.01	35.5
	$\tau^+\tau^-$	4.17	23.4
80.3 GeV	W^+W^-	4.98	21.1
100 GeV	$b\bar{b}$	2.48	27.5
	W^+W^-	2.38	15.3
	$\tau^+\tau^-$	2.21	15.0
200 GeV	$b\bar{b}$	2.74	19.4
	W^+W^-	0.640	10.4
	$\tau^+\tau^-$	0.629	10.9

Table 7.7: Number of total WIMP-induced events in SK I-IV at fitted minimum (N_{min}) and 90% Bayesian upper limit of the number of total WIMP-induced events in SK I-IV (N_{90}) are listed.

Given no significant excess of WIMP-induced events, we can set upper limits on the WIMP-induced neutrino flux. We chose ν_μ flux for a simple representation of the results, but it can be also ν_e flux or total flux as it doesn't matter because we fix the relative normalization between them. Because we weight atmospheric neutrino events by the weight factor w_i and the fitting parameter β, the total number of WIMP-induced events N_χ can be calculated as:

$$\begin{aligned}&\sum_i (df_{atm}/dE)_i \times \beta \times w_i \times [(d\sigma/dE)_i \times N_T \times \eta] \times 3903\text{days}\\ &= \sum_i (df_\chi/dE)_i \times \beta \times [(d\sigma/dE)_i \times N_T \times \eta] \times 3903\text{days}, \qquad (7.10)\end{aligned}$$

where i is the index for energy bin whose size is $m_\chi/1000$ and $w_i = (df_\chi/dE)_i/(df_{atm}/dE)_i$, N_T is the number of target and η is the detection efficiency.

The differential signal flux in each energy bin is therefore $(df_\chi/dE)_i \times \beta$ and the total flux will be $\sum_i((df_\chi/dE)_i \times \beta) = (\sum_i(df_\chi/dE)_i) \times \beta = \beta$ because our initial signal flux before fitting was normalized to 1. Therefore the 90 % upper limit on total ν_μ flux from WIMP annihilations is simply β_{90}.

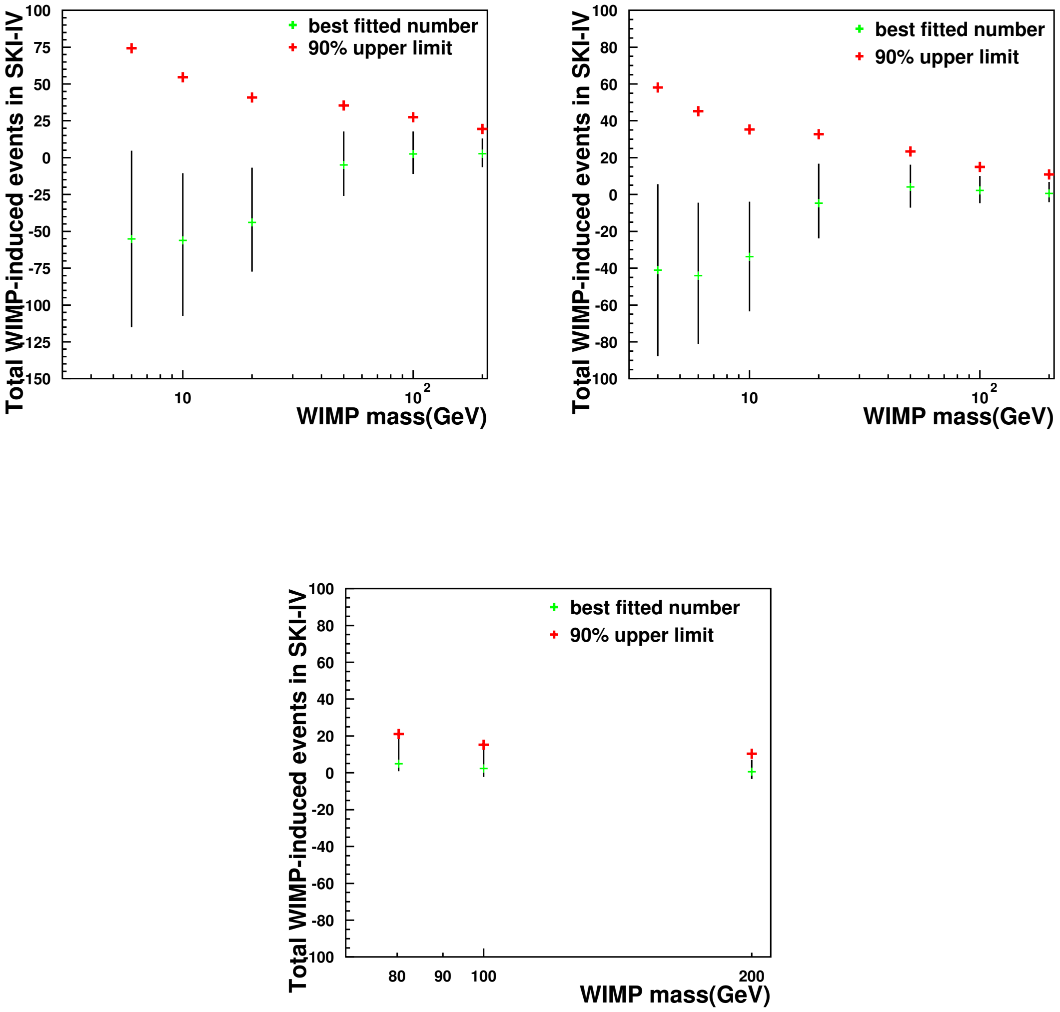

Figure 7.14: The best fitted number of total WIMP-induced events in SK I-IV for each WIMP mass, N_{min} for $b\bar{b}$ (top left) / $\tau^+\tau^-$ (top right) / W^+W^- (bottom) channel are shown in green crosses. 90% Bayesian upper limit of total WIMP-induced events, N_{90} are shown in red crosses. Black bars correspond to fitted 1σ from the fitted minimum as guidelines.

Tab. 7.6 lists the 90% upper limits on ν_μ flux from WIMP annihilations (β_{90}s) for data and mean value of it from toy MC study for all WIMP hypotheses tested. Figure 7.13 visualize the results.

The overall effect of the systematic errors is up to 10% on the WIMP sensitivity, where the largest contributions come from neutrino interaction and atmospheric neutrino flux uncertainties. Comparing to the case in which all systematic errors are turned off, the study shows the size of the effect for each group of the source of uncertainties:

- sensitivity wtih all systematic error ON: <10.4%,
- w/ only 16 neutrino interaction errors ON: <9.8%,
- w/ only 25 atmospheric flux errors ON: <7.1%,
- w/ only 14 × 4 reduction errors ON: <5.6%,
- w/ only 11 × 4 reconstruction errors ON: <1.5%,
- w/ only 7 WIMP neutrino flux errors ON: <1.0%.

The list of each source of uncertainties will be given in Chap. 8.

Among individual source of errors, the θ_{23} uncertainty on the signal flux is expected to affect the result up to $\sim$ 1%. For heavy (50 GeV$\sim$ for $\tau^+\tau^-$, 100 GeV$\sim$ for $b\bar{b}$ channel) WIMP hypotheses, the Q^2 spectrum in deep inelastic scattering for invariant mass W >1.3 GeV is expected to be a source of $\sim$ 1% uncertainty.

In overall, the 1σ statistical uncertainties in the data, determined by 500 toy MC sets are about 74.7% for 6 GeV $b\bar{b}$, 97.8% for 80.3 GeV W^+W^- and 89.0% for 200 GeV $\tau^+\tau^-$ respectively. The systematic uncertainties in BG and signal flux, neutrino interaction, data reduction and reconstruction are about 10.4% for 6 GeV $b\bar{b}$, 2.2% for 80.3 GeV W^+W^- and 1.4% for 200 GeV $\tau^+\tau^-$ respectively. The 90% systematic uncertainty in the generation of signal MC (statistical flucuation) is about 2.8% for 6 GeV $b\bar{b}$, 9.6% for 80.3 GeV W^+W^- and 6.6% for 200 GeV $\tau^+\tau^-$ respectively.

7.6 Limits on WIMP-nucleon elastic scattering cross-sections

The amount of neutrino flux at SK is directly proportional to the WIMP annihilation rate inside the Sun, and to capture rate under the equilibrium condition, and then to WIMP-nucleon scattering cross-section.

As discussed in Chap. 2, we used DarkSUSY to compute the neutrino flux for the assumed WIMP mass, annihilation channel and WIMP-nucleus scattering cross section $\sigma_0^{SD/SI}$. The ratio between the DarkSUSY-outcome neutrino flux and WIMP-nucleon scattering cross sections is used to convert the 90% C.L. upper limit on the ν_μ flux calculated in the previous chapter to the 90% C.L. upper limit on the WIMP-nucleon scattering cross sections.

Table 7.8 shows the conversion factor from the ν_μ flux to SD, SI and IVDM SI scattering cross-sections used in the analysis. Figure 7.15 shows them graphically, for SD, SI and IVDM SI scattering coupling WIMPs, respectively. The explanation of IVDM will be given in the next chapter.

The 90% upper limit on SD WIMP-proton and SI WIMP-nucleon cross-section are listed in Tab. 7.9 and shown in Figures 7.16 and 7.17 together with other experimental limits.

$m_\chi(GeV)$	annihilation channel	$\sigma_{SD,p}$ (km^2× yr/cm^2)	$\sigma_{SI,p}$ (km^2× yr/cm^2) (fn/fp=1)	$\sigma_{SI,p}$ (km^2× yr/cm^2) (fn/fp=−0.7)
4 GeV	$\tau^+\tau^-$	1.44E-18	6.62E-20	3.15E-19
6 GeV	$b\bar{b}$	5.84E-18	1.79E-19	8.53E-19
	$\tau^+\tau^-$	2.25E-18	7.11E-20	3.38E-19
10 GeV	$b\bar{b}$	1.06E-17	2.02E-19	9.63E-19
	$\tau^+\tau^-$	4.10E-18	8.06E-20	3.84E-19
20 GeV	$b\bar{b}$	2.70E-17	2.72E-19	2.27E-18
	$\tau^+\tau^-$	1.05E-17	1.09E-19	9.10E-19
50 GeV	$b\bar{b}$	1.19E-16	5.58E-19	1.05E-17
	$\tau^+\tau^-$	4.65E-17	2.26E-19	4.27E-18
80 GeV	W^+W^-	2.80E-16	9.45E-19	3.05E-17
100 GeV	$b\bar{b}$	4.27E-16	1.18E-18	4.91E-17
	W^+W^-	4.30E-16	1.24E-18	5.16E-17
	$\tau^+\tau^-$	1.71E-16	4.91E-19	2.05E-17
200 GeV	$b\bar{b}$	1.65E-15	2.86E-18	2.97E-16
	W^+W^-	1.74E-15	3.21E-18	3.34E-16
	$\tau^+\tau^-$	6.75E-16	1.24E-18	1.30E-16

Table 7.8: Conversion factors from ν_μ flux to SD WIMP-proton scattering cross-section, SI and SI (IVDM) WIMP-nucleon scattering cross-sections are listed.

7.7 Summary

In this analysis, we increased the signal acceptance by using fully-contained and partially-contained neutrino events, and all three flavors of neutrinos added to up-going muons in Super-Kamiokande. We also used minimum-χ^2 method to use energy, direction and flavor informations. We fitted Super-Kamiokande I-IV data to find the allowed contribution of WIMP-induced neutrino events added to large background of atmospheric neutrino events.

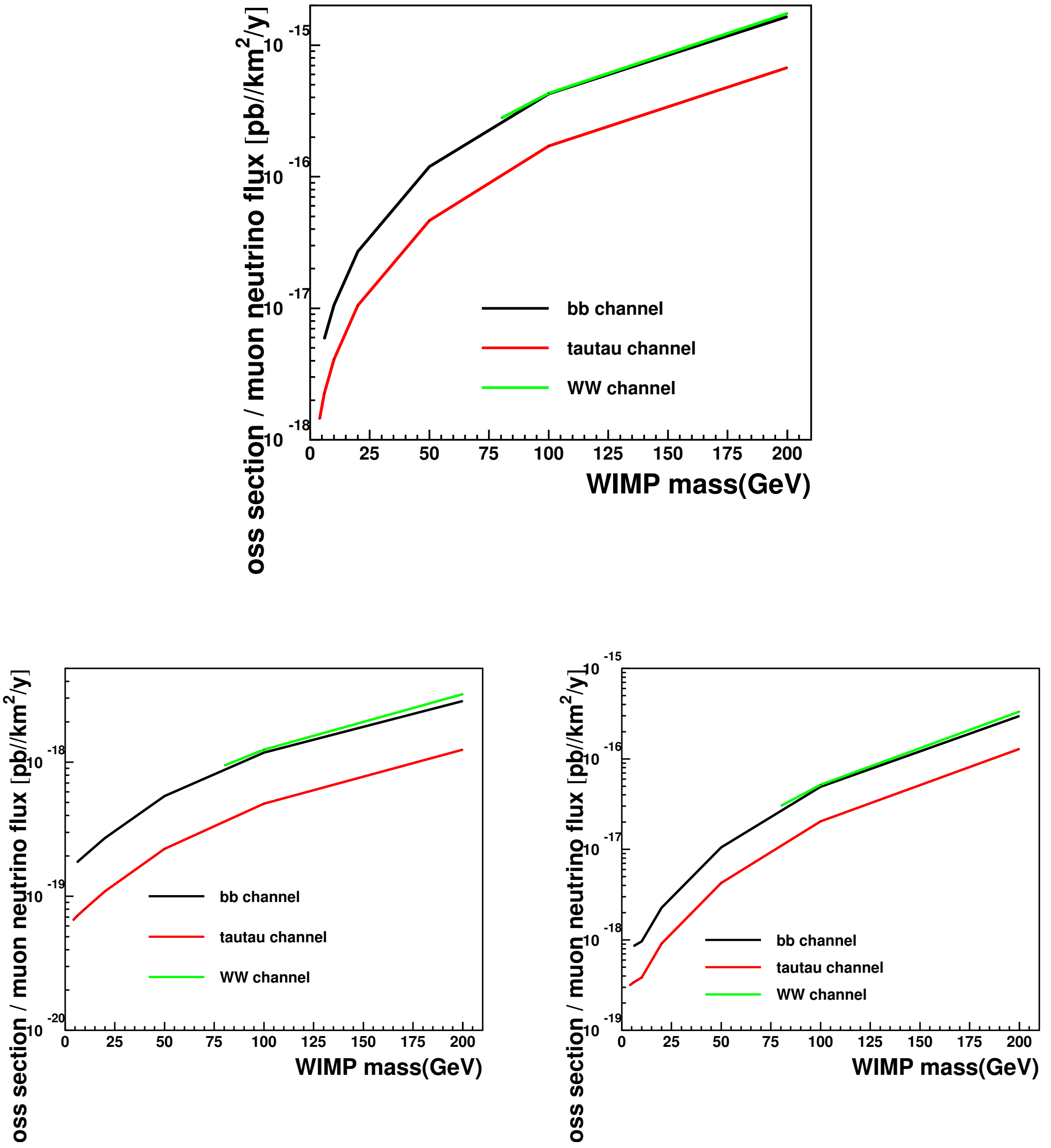

Figure 7.15: Conversion factor from ν_μ flux to SD (top), SI (bottom left) and IVDM(bottom right) scattering cross-section.

m_χ (GeV)	annihilation channel	$\sigma_{SD,p}$ (cm^2)	$\sigma_{SI,p}$ (cm^2) (fn/fp=1)	$\sigma_{SI,p}$ (cm^2) (fn/fp=-0.7)
4 GeV	$\tau^+\tau^-$	2.22×10^{-40}	8.73×10^{-42}	2.45×10^{-40}
6 GeV	$b\bar{b}$	1.72×10^{-39}	4.56×10^{-41}	1.28×10^{-39}
	$\tau^+\tau^-$	1.63×10^{-40}	4.35×10^{-42}	1.22×10^{-40}
10 GeV	$b\bar{b}$	1.49×10^{-39}	2.40×10^{-41}	6.75×10^{-40}
	$\tau^+\tau^-$	1.31×10^{-40}	2.12×10^{-42}	5.95×10^{-41}
20 GeV	$b\bar{b}$	1.43×10^{-39}	1.20×10^{-41}	4.48×10^{-40}
	$\tau^+\tau^-$	1.42×10^{-40}	1.19×10^{-42}	4.47×10^{-41}
50 GeV	$b\bar{b}$	2.34×10^{-39}	8.99×10^{-42}	3.90×10^{-40}
	$\tau^+\tau^-$	1.28×10^{-40}	4.92×10^{-43}	2.14×10^{-41}
80.3 GeV	W^+W^-	3.13×10^{-40}	8.26×10^{-43}	3.73×10^{-41}
100 GeV	$b\bar{b}$	3.19×10^{-39}	7.13×10^{-42}	3.27×10^{-40}
	W^+W^-	2.80×10^{-40}	6.26×10^{-43}	2.87×10^{-41}
	$\tau^+\tau^-$	1.24×10^{-40}	2.76×10^{-43}	1.26×10^{-41}
200 GeV	$b\bar{b}$	4.49×10^{-39}	6.34×10^{-42}	3.04×10^{-40}
	W^+W^-	3.00×10^{-40}	4.23×10^{-43}	2.03×10^{-41}
	$\tau^+\tau^-$	1.33×10^{-40}	1.88×10^{-43}	9.03×10^{-42}

Table 7.9: The 90% upper limits on SD WIMP-proton scattering cross-section, SI and SI (IVDM) WIMP-nucleon scattering cross-sections are listed.

As a result, we found no signal observed and the null result was interpreted as upper limit on the SD and SI WIMP-proton elastic scattering cross-section for $\chi\chi \rightarrow b\bar{b}$ and $\chi\chi \rightarrow \tau^+\tau^-$ WIMP annihilation channels. The result of the study is consistent with no signal from 10 GeV WIMP with SD coupling of 1.31×10^{-40}cm^2 (1.49×10^{-39}cm^2) to proton where $\tau^+\tau^-$ ($b\bar{b}$) annihilation channels are assumed respectively, and consistent with no signal from 10 GeV WIMP with SI coupling of 2.12×10^{-42}cm^2 (2.40×10^{-41}cm^2) to proton where $\tau^+\tau^-$ ($b\bar{b}$) annihilation channels are assumed respectively. We set current best limit on SD cross-section for WIMP mass below 200 GeV and ruled out some fraction of signal-claimed region in SI parameter space.

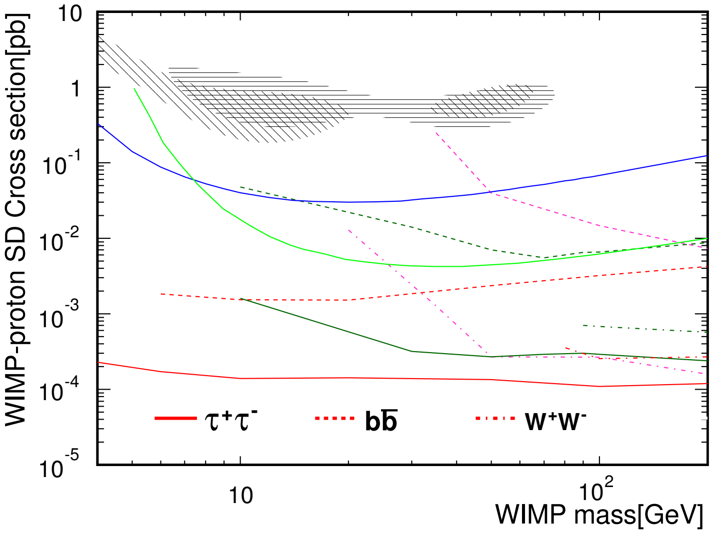

Figure 7.16: 90% C. L. upper limits on SD WIMP-proton cross section calculated for the DarkSUSY (83) default are shown for the $\tau^+\tau^-$ channel in red solid; $b\bar{b}$ in red dashed; W^+W^- in red dot-dashed. Also shown are limits from other experiments: IceCube (54) $b\bar{b}$ (brown dashed) / W^+W^- (brown dot-dashed); BAKSAN (59) $\tau^+\tau^-$ (pink solid) / $b\bar{b}$ (pink dashed) / W^+W^- (pink dot-dashed); PICASSO (202) (blue solid); SIMPLE (203) (green solid). The black shaded regions are the 3σ C.L. signal claimed by DAMA/LIBRA (62; 204).

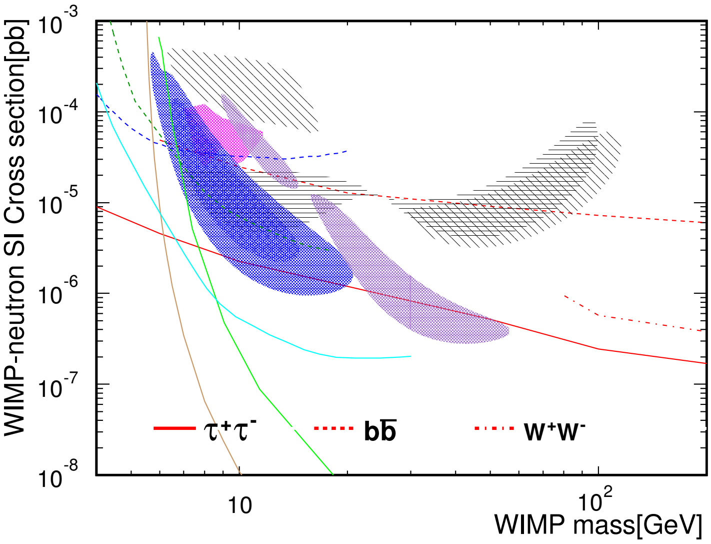

Figure 7.17: 90% C. L. upper limits on the SI WIMP-nucleon cross section calculated using the DarkSUSY (83) default are shown for the $\tau^+\tau^-$ channel in red solid; $b\bar{b}$ in red dashed; W^+W^- in red dot-dashed. Also shown are signal claims from other experiments: DAMA/LIBRA (black shaded regions, 3σ C.L.); CoGENT (48) (magenta shaded region, 90% C.L.); CRESSTII (45) (violet shaded regions, 2σ C.L.); CDMS II Si (46) (blue shaded region, 90% C.L.); and limits: SuperCDMS (51) (cyan solid); CDMSlite (205) (blue dashed); XENON10 S2-only (52) (dark green dashed); XENON100 (49) (green solid); LUX (50) (brown solid).

Chapter 8

Discussions: On the uncertainties in solar WIMP search

8.1 Overview

In order to set upper limits on cross sections appropriately from searches for the neutrinos coming from the WIMP annihilation in the Sun, we have to consider various sources of uncertainties which can be grouped into three categories:

- A) uncertainties in annihilation in the Sun,
- B) uncertainties in neutrino propagation from the Sun to a detector,
- C) uncertainties related to detector response and background.

The last category C is detector specific and hence need to be studied by the corresponding experiments. In this chapter, we focus on the Super-Kamiokande detector. The errors in category B is location specific and the DarkSUSY (83) and WimpSim (88) packages can, for example, be utilised to obtain precise neutrino flux at the given detector site.

These uncertainties are treated with the "pulled" method and included in the result shown in the previous chapter. Total 73 sources of systematic errors are considered in the predictions of atmospheric neutrino flux, WIMP neutrino flux, neutrino interaction, event reduction, event selection and reconstruction. The best fit systematic uncertainties, ϵ_j's, and the estimated 1σ errors, σ_j's together with the brief description of the estimation of the errors are summarized in the following chapters; for errors in the background atmospheric neutrino flux and detector response, and in the signal WIMP neutrino propagation in Chap. 8.2 and Chap. 8.3, respectively.

The category A includes astrophysical uncertainties as well as particle- and nuclear-physics uncertainties. These errors don't alter the energy spectrum nor the flavor composition of the neutrino flux but only alter the normalization of the flux. Therefore they are common for searches at all neutrino detectors. These errors are considered in the conversion from the neutrino flux to the capture rate. To provide the reliable interpretation of the result of solar WIMP neutrino searches in comparison to direct detection experiments, these uncertainties are quantified and the new result of the SK solar WIMP search is shown with the “uncertainty band” at the end of this chapter. On the uncertainties which are not reflected in the result, a short comments will be given.

Chapter 8.4 briefly explains and summarizes the uncertainties related to nuclear physics and Chap. 8.5 discusses the uncertainties in particle physics assumptions made. The final summary is given in Chap. 8.6.

8.2 Uncertainties related to detector response and background

The systematic error tables for 480 bins are generated for BG and signal, respectively. For simplicity, MC events are weighted for 2D atmospheric oscillation scenario for BG, and to have 1:1:1:1:1:1 flavor fatio for three-flavor neutrino and anti-neutrinos for signal.

8.2.1 Uncertainties in background atmospheric neutrino flux

Twenty-five systematic errors corresponding to the uncertainty in BG atmospheric neutrino flux are summarized in Tab. 8.1, where ϵ_j's at the best fit are shown for three representative WIMP hypotheses. Most of the systematic errors considered in oscillation analysis are commonly used except those certainly related to zenith angle distribution. Uncertainties in atmospheric neutrino oscillations are introduced as varying five neutrino oscillation parameters by 1σ deviation taken from PDG (206) and considering the matter effect in the Earth.

The uncertainty in the absolute atmospheric neutrino flux includes the uncertainty of π production in the hadronic interaction model and the hadronic interaction cross sections. Calculations done by Honda et al. (126) are used:

- $E_\nu < 1$ GeV: it linearly decreases with log E_ν from 25% at 0.1 GeV to 7% at 1 GeV,
- $E_\nu > 1$ GeV: 7% in $1 \sim 10$ GeV, and it linearly increases with log E_ν from 7% at 10 GeV to 12% at 100 GeV, then it linearly increases with log E_ν from 12% at 100 GeV to 20% at 1 TeV.

As the differences in absolute normalization of flux models become large above ∼10 GeV, additional 5% is assigned for normalizations of FC multi-GeV, PC and UPMU-stop samples.

The uncertainty in the flavor ratio $(\nu_\mu + \overline{\nu}_\mu)/(\nu_e + \overline{\nu}_e)$ of the atmospheric neutrino flux is estimated from the difference in the flavor ratio of the FLUKA (147) and Bartol (146) flux models normalized to the Honda flux (126), as shown in Fig. 8.1. They are;

Systematic error related to BG neutrino flux		σ(%)	Fit value	(ϵ/σ)	
			6 b	80.3 W	200 τ
Absolute Flux Normalization	$E_\nu < 1$ GeV	25^a	0.89	0.90	0.90
	$E_\nu > 1$ GeV	15^a	0.75	0.72	0.73
$(\nu_\mu + \overline{\nu}_\mu)/(\nu_e + \overline{\nu}_e)$ ratio					
	$E_\nu < 1$ GeV	2	-0.90	-0.90	-0.90
	$1 < E_\nu < 10$ GeV	3	-0.95	-0.94	-0.94
	$E_\nu > 10$ GeV	5^a	0.52	0.54	0.52
$\overline{\nu_e}/\nu_e$ ratio					
	$E_\nu < 1$ GeV	5	1.19	1.19	1.19
	$1 < E_\nu < 10$ GeV	5	0.59	0.58	0.58
	$E_\nu > 10$ GeV	8^a	-0.02	-0.03	-0.03
$\overline{\nu_\mu}/\nu_\mu$ ratio					
	$E_\nu < 1$ GeV	2	-0.15	-0.14	-0.14
	$1 < E_\nu < 10$ GeV	6	0.31	0.30	0.30
	$E_\nu > 10$ GeV	15^a	0.07	0.08	0.07
K/π ratio		10^a	-0.62	-0.61	-0.61
Neutrino path length		10	-0.09	-0.10	-0.10
Sample-by-sample normalization	FC Multi-GeV	5	-1.13	-1.13	-1.13
	PC & stopping up-μ	5	-0.17	-0.16	-0.16
Solar Activity	SK-I	20	0.00	0.00	0.00
	SK-II	50	0.62	0.62	0.62
	SK-III	20	0.08	0.08	0.08
	SK-IV	10	-0.01	-0.01	-0.01
oscillation parameter θ_{13}		13.3	-0.23	-0.23	-0.22
oscillation parameter θ_{12}		3.6	0.01	0.01	0.01
oscillation parameter θ_{23}		14.0	-0.23	-0.23	-0.23
oscillation parameter Δm_{32}		6.6	0.11	0.13	0.12
oscillation parameter Δm_{21}		2.7	-0.08	-0.08	-0.08
Matter effect		6.8	-0.01	-0.01	-0.01

---

[a] They are energy dependent. See text for the detail.

Table 8.1: Systematic errors related to atmospheric neutrino flux calculation. They are common in all SK periods. The third column shows the estimated 1σ error size compared to nominal value, and the 4-6th columns show the best fit values of the systematic error parameter ϵ for three representative WIMP hypotheses; "6 b", "80.3 W", "200 τ" indicate 6 GeV $b\bar{b}$, 80.3 GeV W^+W^-, 200 GeV $\tau^+\tau^-$ channels, respectively.

- 2% for $E_\nu < 1$ GeV,
- 3% for $1 < E_\nu < 10$ GeV,
- 5% for $10 < E_\nu < 30$ GeV, and then it linearly increases with $\log E_\nu$ from 5% at 30 GeV to 30% at 1 TeV.

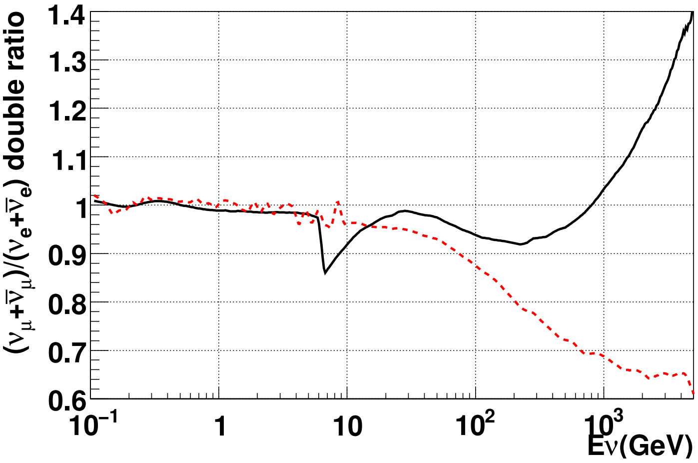

Figure 8.1: Double ratio of $(\nu_\mu + \overline{\nu}_\mu)/(\nu_e + \overline{\nu}_e)$ of the atmospheric neutrino flux for FLUKA flux/Honda flux (black solid) and Bartol flux/Honda flux (red dashed). Figure is taken from (125).

The uncertainty in the $\nu/\overline{\nu}$ ratio of the atmospheric neutrino flux is estimated from the difference in the flavor ratio of the FLUKA (147) and Bartol (146) flux models normalized to the Honda flux (126) as shown in Fig. 8.2. They are:
for $\overline{\nu}_e/\nu_e$,

- 5% for $E_\nu < 1$ GeV,
- 5% for $1 < E_\nu < 10$ GeV,
- 8% for $10 < E_\nu < 100$ GeV, and then it linearly increases with $\log E_\nu$ from 8% at 30 GeV to 30% at 1 TeV.

For $\overline{\nu}_\mu/\nu_\mu$,

- 2% for $E_\nu < 1$ GeV,
- 6% for $1 < E_\nu < 10$ GeV,
- 6% for $10 < E_\nu < 50$ GeV, and then it linearly increases with $\log E_\nu$ from 6% at 50 GeV to 60% at 1 TeV.

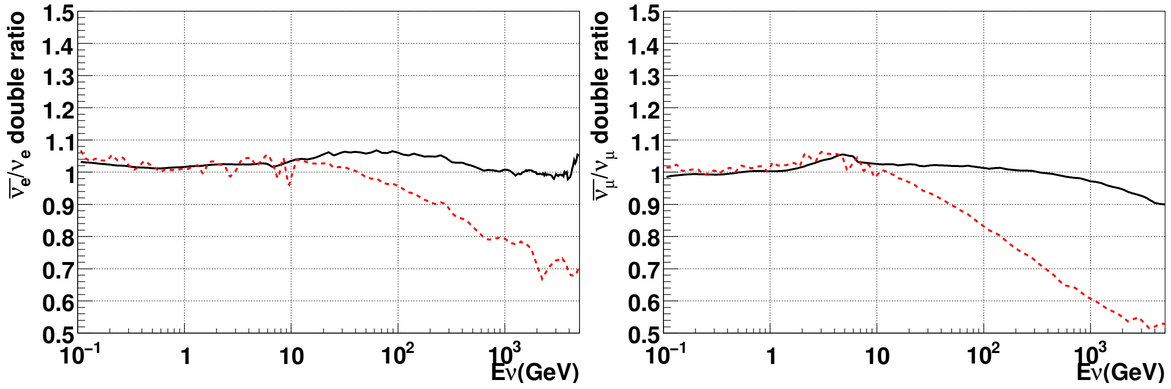

Figure 8.2: Double ratio of $\overline{\nu}_e/\nu_e$ (left) and $\overline{\nu}_\mu/\nu_\mu$ (right) of the atmospheric neutrino flux for FLUKA flux/Honda flux (black solid) and Bartol flux/Honda flux (red dashed). Figure is taken from (125).

Above a few tens of GeV, K's contribute to the production of the neutrinos in addition to π^+ and π^- decays. The uncertainty of K/π production ratio in cosmic ray interactions is estimated by using the SPY experiment measurement (207) as:

- 5% for $E_\nu < 100$ GeV, and it linearly increases with E_ν from 5% at 100 GeV to 20% at 1 TeV, then it is 20% for $E_\nu > 1$ TeV.

The uncertainty in the position of the neutrino production is related to the atmosphere density distribution. By varying the density distribution by 10 %, the difference in the resultant neutrino flux is taken as the systematic uncertainty.

For the uncertainty in solar activity, ±1 year is added on eleven-years solar activity cycle and accordingly altered primary cosmic ray flux takes the uncertainty of 20% for SK-I, 50% for SK-II, 20% for SK-III and 10% for SK-IV.

For the uncertainty in atmospheric neutrino oscillation, five neutrino oscillation parameters are varied by 1σ uncertainty based on the experimental results (206), as shown in Tab. 8.2.

The matter effect in the neutrino oscillation is affected by the electron density in the Earth, which depends on the chemical composition of the Earth. As the Earth's core is composed of heavier elements, the electron density in the core is expected to be less than other regions by $\sim 6.8\%$. Reduction of 6.8% electron density is taken as the uncertainty in the matter effect.

8.2.2 Uncertainties in detector response: Neutrino interactions

Sixteen systematic errors corresponding to neutrino interactions are considered. The results are summarized in Tab. 8.3 and briefly explained below.

Parameter	used value	-1σ	$+1\sigma$
$sin(2\theta_{12})$	0.873	-0.031	$+0.031$
$sin^2(2\theta_{13})$	0.098	-0.013	$+0.013$
$sin^2(\theta_{23})$	0.5	-0.07	$+0.07$
Δm^2_{32} [eV^2]	7.46e-5	$-$0.2e-5	+0.2e-5
Δm^2_{21} [eV^2]	2.44e-3	$-$0.15e-3	+0.17e-3

Table 8.2: Summary of 1σ variations of neutrino oscillation parameters taken as uncertainties.

CCQE interaction cross section between neutrino and nucleon is calculated based on the Smith and Moniz model as described in Chap. 5. The Smith and Moniz model is compared to the Nieves et al. model (208) and the difference is taken as the uncertainty. The uncertainties in total CCQE cross section, $\overline{\nu}/\nu$ ratio, and flavor ratio $(\nu_\mu + \overline{\nu_\mu})/(\nu_e + \overline{\nu}_e)$ are taken in this way. Figure 8.3 shows the calculated CCQE cross section ratio of Nieves model to Smith and Monitz model for total cross section and double ratios for $\overline{\nu}/\nu$ and flavor ratio.

Direction resolution becomes an issue in a search for point like signal; the uncertainty of axial mass M$_A$ is expected to be a large source of uncertainty in q^2 spectrum therefore in direction reconstruction. The size of the effect of the uncertainties from M$_A$ for CCQE and single pion production interactions are taken by comparing the differential cross section $d\sigma/dq^2$ with the M$_A$ = 1.4 and that with the fiducial value M$_A$ = 1.2. Figure 8.4 visualizes the change of angular resolution for two M$_A$ assumptions.

The Hernandez model (209) is compared to the Rein and Sehgal model for estimating the size of uncertainties relating to single meson production cross section. The cross section ratios between two models are shown in the left panel of Fig. 8.5. The ratio between the π^0 production interaction to the $\pi^\pm$ production interactions is about 40% and is taken as the systematic error. The double ratios of the $\overline{\nu}/\nu$ for two models are taken as the systematic uncertainties of the $\overline{\nu}/\nu$ ratio in the single meson production as shown in the right panel of Fig. 8.5 For the uncertainty in the cross section of single meson production itself, available experimental data of $\nu_\mu p \rightarrow \mu^- p \pi^+$ is used. By taking the difference between the MC expectation and data, the systematic uncertainty is estimated to be 20%.

The systematic uncertainty in deep inelastic scattering cross section is obtained by taking the difference between the reference model and the CKMT model (210).

The uncertainty of q^2 spectrum in deep inelastic scattering is taken into account by comparing the reference model with the original GRV98 model. It is separately calculated for the case W $<$ 1.3 GeV and W $>$ 1.3 GeV. Figure 8.6 visualizes the change of angular resolution for two models.

For NC and CC ν_e coherent pion production interactions, the Rein and Sehgal model is compared to the SciBooNE experimental measurement (211) and the uncertainty is

Systematic error in neutrino interaction	$\sigma(\sigma/\%)$	Fit value	(ϵ/σ)	
		6 b	80.3 W	200 τ
CCQE cross section	1.0[a]	0.33	0.34	0.35
CCQE $\overline{\nu}/\nu$ ratio	1.0[a]	2.07	2.05	2.05
CCQE $(\nu_\mu + \overline{\nu_\mu})/ (\nu_e + \overline{\nu}_e)$ ratio	1.0[a]	1.67	1.67	1.67
M_A in CCQE and single meson production	20	-0.98	-0.98	-0.98
Single meson production cross section	20	0.71	0.72	0.71
Single π production, $\pi^0/\pi^\pm$ ratio	40	-0.53	-0.53	-0.53
Single π production, $\overline{\nu}/\nu$ ratio	1.0[b]	-0.60	-0.57	-0.57
DIS cross section	5	0.71	0.72	0.74
Q^2 spectrum in DIS (W < 1.3 GeV)	1.0[c]	0.00	0.00	0.00
Q^2 spectrum in DIS (W > 1.3 GeV)	1.0[d]	0.51	0.51	0.51
Coherent π production	100	-0.27	-0.27	-0.28
NC/CC ratio	20	0.45	0.44	0.45
CC ν_τ cross section	25	0.26	0.26	0.26
NC in FC μ-like (hadron simulation)	10	-0.47	-0.46	-0.46
Decay electron tagging (π^+ interaction)[d]	10	-0.55	-0.54	-0.54
DIS model difference	10	-0.42	-0.41	-0.41

---

[a] Difference from the Nieves model is set to 1.0.

[b] Difference from the Hernandez model is set to 1.0.

[c] Difference from the GRV98 model is set to 1.0.

[d] Difference from the GRV98 model is set to 1.0.

Table 8.3: Systematic errors related to neutrino interactions. They are common in all SK periods. The second column shows the estimated 1σ error size compared to nominal value, and the 3-5th columns show the best fit values of the systematic error parameter ϵ for three representative WIMP hypotheses; "6 b", "80.3 W", "200 τ" indicate 6 GeV $b\bar{b}$, 80.3 GeV W^+W^-, 200 GeV $\tau^+\tau^-$ channels, respectively.

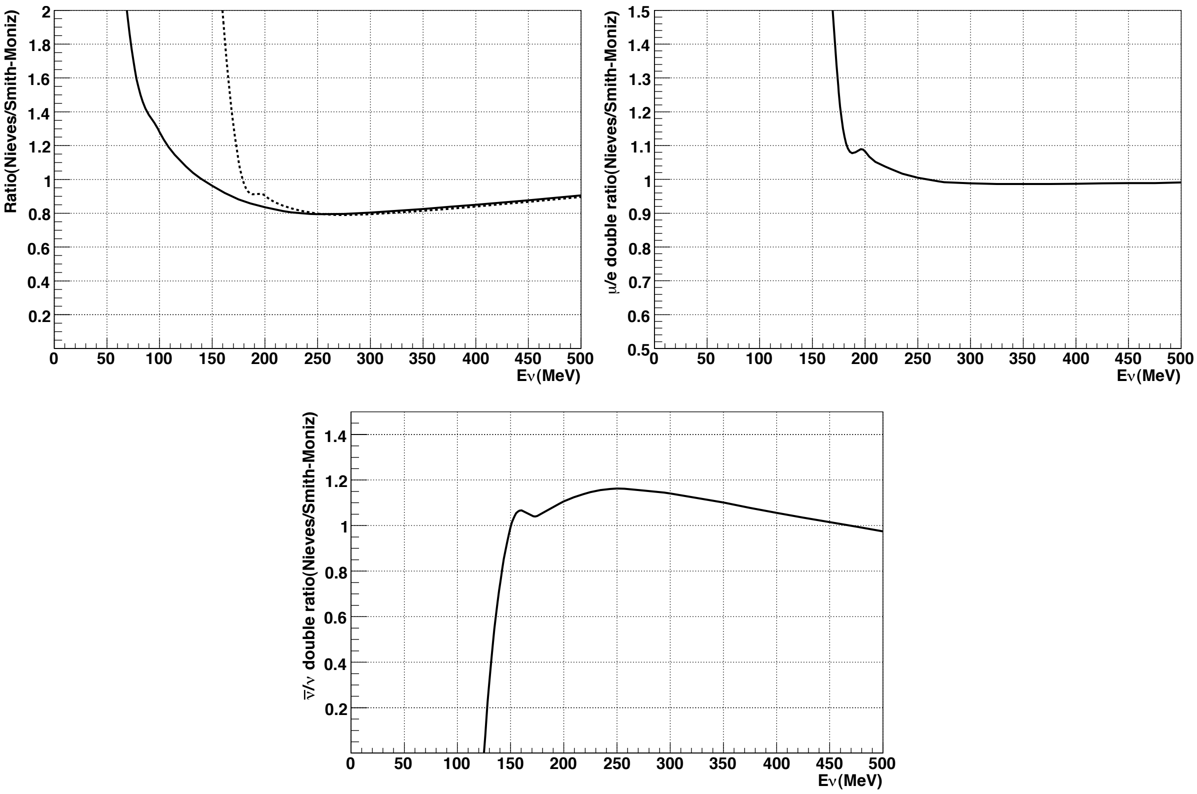

Figure 8.3: The CCQE cross section for $\nu_e + \overline{\nu}_e$ (solid line) and for $\nu_\mu + \overline{\nu}_\mu$ (dashed line) of Nieves model normalized by the Smith and Monitz model (top left), flavor ratio ($(\nu_\mu + \overline{\nu}_\mu)/(\nu_e + \overline{\nu}_e)$) of Nieves model normalized by the Smith and Monitz model (top right), $\overline{\nu}/\nu$ ratio of Nieves model normalized by the Smith and Monitz model (bottom) are shown as a function of neutrino energy. Figure is taken from (125).

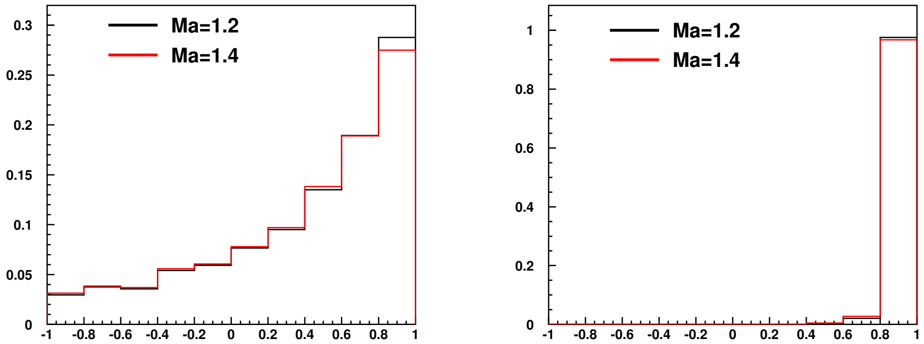

Figure 8.4: The angular distribution for two choices of M$_A$'s are compared for sub-GeV (left) and multi-GeV (right) signal MC events with arbitrary normalization, for 4 GeV $\tau^+\tau^-$ channel. The black line shows the angular distribution for default M_A=1.2, and the red line shows that for 20% increased M_A (=1.4). Note that the systematic error is applied only to the CCQE and single meson production events, but the plot is drawn for entire signal MC to visualize overall effect on angular distribution of the signal.

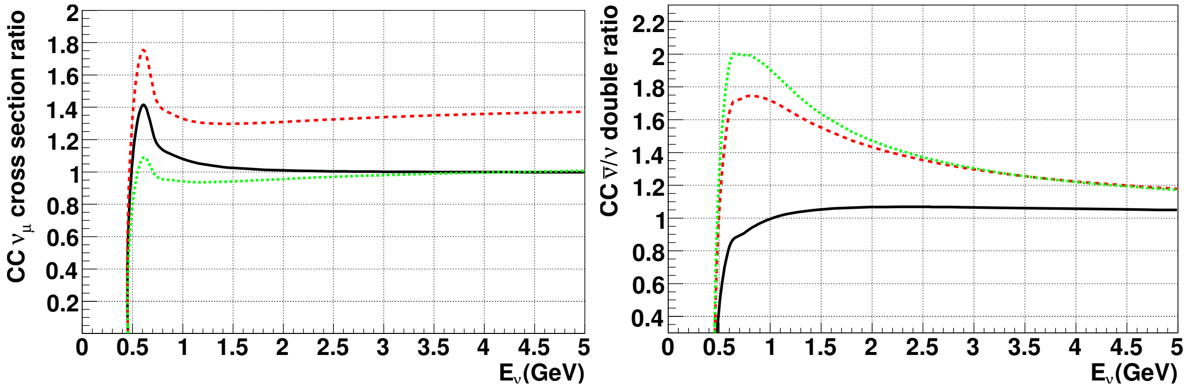

Figure 8.5: The Hernandez model normalized by that of the Rein and Sehgal model for $\nu_\mu p \to \mu^- p \pi^+$ (solid line), $\nu_\mu n \to \mu^- p \pi^0$ (dashed line) and $\nu_\mu n \to \mu^- p \pi^+$ (dotted line) are shown for the predicted cross section (left) and the double ratio for the $\overline{\nu}/\nu$ ratio (right). Figure is taken from (125).

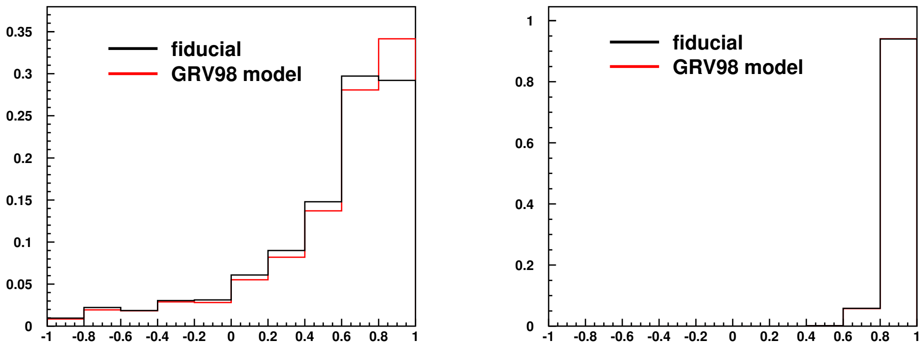

Figure 8.6: The angular distribution for two DIS models are compared for sub-GeV (left) and multi-GeV (right) signal MC events with arbitrary normalization, for 4 GeV $\tau^+\tau^-$ channel. The black line shows the angular distribution for default, and the red line shows that for the GRV98 model. Note that the systematic error is applied only to the DIS events, but the plot is drawn for entire signal MC to visualize overall effect on angular distribution of the signal.

taken to be 50%. For CC ν_μ coherent pion production interaction, the uncertainty is taken to be 100%.

The uncertainty in NC/CC ratio is taken to be 20%.

The uncertainty of the CC ν_τ cross section is estimated to be 25%, comparing to the Hagiwara model (212).

8.2.3 Uncertainties in detector response: event selections

Fourteen systematic errors correspond to event selections are summarized in Tab. 8.4 to Tab. 8.7 respectively for SK I-IV.

The systematic uncertainty for FC/PC separation is estimated to be 0.6% for SK-I, 0.5% for SK-II, 0.9% for SK-III and 0.02% for SK-IV from the difference of the NHITAC distribution between the data and MC.

The uncertainty in FC reduction efficiency is estimated by comparing the distributions of each cut variable for data and MC. They are 0.2%, 0.2%, 0.8% and 0.3% for SK I-IV, respectively.

The contamination of the background in the final FC data set are estimated to be 0.2%, 0.2%, 0.3% and 0.1% for sub-GeV μ-like sample for SK I-IV, respectively, 0.1%, 0.4%, 0.1% and 0.1% for sub-GeV e-like sample for SK I-IV, respectively, 0.3%, 0.2%, 0.3% and 0.1% for multi-GeV μ-like sample for SK I-IV, respectively, 0.5%, 0.2%, 0.2%

(SK-I) Systematic error		σ(%)	Fit value	(σ)	
in event reduction			6 b	80.3 W	200 τ
FC/PC separation		0.6	-0.06	-0.07	-0.07
FC reduction		0.2	0.02	0.02	0.02
PC reduction		2.4	-0.44	-0.43	-0.43
Non-ν BG (e-like)		1.0	0.16	0.16	0.16
Non-ν BG (μ-like)		1.0	-0.02	-0.02	-0.02
PC-stop/through separation	Top	46.1	-0.21	-0.21	-0.21
	Barrel	7.01	-0.16	-0.15	-0.15
	Bottom	22.7	-0.08	-0.08	-0.08
Fiducial volume		2.0	-0.16	-0.17	-0.17
up-μ reduction		1.0	-0.16	-0.16	-0.16
up-μ stop/through separation		0.4	0.00	0.00	0.00
up-μ through-going showering separation		3.4	0.00	0.00	0.00
Energy cut for up-μ stop		-0.9	0.00	0.00	0.00
Path length cut for up-μ through-going		-1.5	0.01	0.01	0.01

Table 8.4: Systematic errors related to event reduction for SK-I period. The second column shows the estimated 1σ error size and the 3-5th columns show the best fit value of the systematic error parameter ϵ_i for three representative WIMP hypotheses; “6 b”, “80.3 W”, “200 τ” indicate 6 GeV $b\bar{b}$, 80.3 GeV W^+W^-, 200 GeV $\tau^+\tau^-$ channels, respectively.

(SK-2) Systematic error in event reduction		σ(%)	Fit value 6 b	(σ) 80.3 W	 200 τ
FC/PC separation		0.5	0.16	0.16	0.16
FC reduction		0.2	0.04	0.04	0.04
PC reduction		4.8	-0.75	-0.74	-0.74
Non-ν BG (e-like)		1.0	0.05	0.05	0.05
Non-ν BG (μ-like)		1.0	-0.13	-0.12	-0.12
PC-stop/through separation	Top	19.37	-0.13	-0.13	-0.13
	Barrel	9.44	-0.60	-0.60	-0.60
	Bottom	12.9	-0.17	-0.17	-0.17
Fiducial volume		2.0	0.05	0.05	0.05
up-μ reduction		1.0	-0.23	-0.23	-0.23
up-μ stop/through separation		0.6	0.00	0.00	0.00
up-μ through-going showering separation		4.4	0.00	0.00	0.00
Energy cut for up-μ stop		-1.3	0.00	0.00	0.00
Pathlength cut for up-μ through-going		-2.3	-0.02	-0.02	-0.02

Table 8.5: Systematic errors related to event reduction for SK-II period. The second column shows the estimated 1σ error size and the 3-5th columns show the best fit value of the systematic error parameter ϵ_i for three representative WIMP hypotheses; "6 b", "80.3 W", "200 τ" indicate 6 GeV $b\bar{b}$, 80.3 GeV W^+W^-, 200 GeV $\tau^+\tau^-$ channels, respectively.

(SK-3) Systematic error		σ(%)	Fit value	(σ)	
in event reduction			6 b	80.3 W	200 τ
FC/PC separation		0.9	-0.02	-0.01	-0.02
FC reduction		0.8	0.06	0.05	0.05
PC reduction		0.5	-0.08	-0.08	-0.08
Non-ν BG (e-like)		1.0	-0.02	-0.02	-0.02
Non-ν BG (μ-like)		1.0	-0.39	-0.39	-0.39
PC-stop/through separation	Top	86.6	-0.17	-0.16	-0.16
	Barrel	28.7	-0.33	-0.33	-0.33
	Bottom	12.1	0.00	0.00	0.01
Fiducial volume		2.0	-0.19	-0.19	-0.19
up-μ reduction		1.0	0.16	0.16	0.16
up-μ stop/through separation		0.4	0.00	0.00	0.00
up-μ through-going showering separation		2.4	0.00	0.00	0.00
Energy cut for up-μ stop		2.0	0.00	0.00	0.00
Pathlength cut for up-μ through-going		-2.8	0.07	0.07	0.07

Table 8.6: Systematic errors related to event reduction for SK-III period. The second column shows the estimated 1σ error size and the 3-5th columns show the best fit value of the systematic error parameter ϵ_i for three representative WIMP hypotheses; "6 b", "80.3 W", "200 τ" indicate 6 GeV $b\bar{b}$, 80.3 GeV W^+W^-, 200 GeV $\tau^+\tau^-$ channels, respectively.

(SK-4) Systematic error		σ(%)	Fit value	(σ)	
in event reduction			6 b	80.3 W	200 τ
FC/PC separation		0.02	0.00	0.00	0.00
FC reduction		0.3	0.07	0.07	0.07
PC reduction		1.0	-0.26	-0.26	-0.25
Non-ν BG (e-like)		1.0	-0.01	-0.01	-0.01
Non-ν BG (μ-like)		1.0	-0.16	-0.16	-0.16
PC-stop/through separation	Top	40.33	0.11	0.11	0.11
	Barrel	8.54	0.13	0.13	0.13
	Bottom	6.8	0.02	0.02	0.02
Fiducial volume		2.0	-0.04	-0.04	-0.04
up-μ reduction		1.0	0.24	0.24	0.24
up-μ stop/through separation		0.6	0.00	0.00	0.00
up-μ through-going showering separation		3.0	0.00	0.00	0.00
Energy cut for up-μ stop		1.7	0.00	0.00	0.00
Path length cut for up-μ through-going		-1.5	-0.16	-0.16	-0.16

Table 8.7: Systematic errors related to event reduction for SK-IV period. The second column shows the estimated 1σ error size and the 3-5th columns show the best fit value of the systematic error parameter ϵ_i for three representative WIMP hypotheses; "6 b", "80.3 W", "200 τ" indicate 6 GeV $b\bar{b}$, 80.3 GeV W^+W^-, 200 GeV $\tau^+\tau^-$ channels, respectively.

and 0.1% for multi-GeV e-like sample for SK I-IV, respectively, as discussed in Chap. 6.

The systematic uncertainty of PC stopping/through-going separation is estimated by the difference of $\mathrm{PE}_{anti}/\mathrm{PE}_{exp}$ distributions between the data and MC. The estimations are done separately for OD bottom, barrel and top.

The systematic uncertainty of up-μ stopping and through-going separation is estimated by the difference of NHITEX distributions between the data and MC. The systematic uncertainty of up-μ non-showering and showering separation is estimated by comparing the $\Delta(Q)$ distribution between the data and MC.

8.2.4 Uncertainties in detector response: Event reconstructions

Eleven systematic errors correspond to FC/PC/up-μ reconstructions are summarized in Tab. 8.8 to 8.11 respectively for SK I-IV.

(SK-I) Systematic error	$\sigma(\%)$	Fit value	(σ)	
in event reconstruction and selection		6 b	80.3 W	200 τ
Ring separation	10	0.51	0.52	0.52
PID (single-ring)	1.0	-0.19	-0.19	-0.19
PID (multi-ring)	10	0.13	0.13	0.13
Energy calibration	1.1	0.00	0.00	0.00
Multi-GeV single-ring e-like non CCν_e BG	13.2	0.39	0.39	0.39
Multi-GeV multi-ring e-like non CCν_e BG	12.1	-0.10	-0.10	-0.10
Multi-GeV multi-ring ν_e and $\overline{\nu}_e$ separation	7.16	-0.45	-0.45	-0.46
Sub-GeV 1-ring π^0 selection	10	0.16	0.16	0.16
Sub-GeV 2-ring π^0 selection	5.6	-0.15	-0.15	-0.15
Decay-e tagging (μ-decay)	10	-0.36	-0.36	-0.36
Multi-GeV multi-ring e-like other separation	10	-0.14	-0.15	-0.14

Table 8.8: Systematic errors related to event reconstruction and selection for SK-I. The second column shows the estimated 1σ error size and the 3-5th columns show the best fit value of the systematic error parameter ϵ_i for three representative WIMP hypotheses; "6 b", "80.3 W", "200 τ" indicate 6 GeV $b\bar{b}$, 80.3 GeV W^+W^-, 200 GeV $\tau^+\tau^-$ channels, respectively.

For the ring seperation and the particle identification, the difference in the likelihood distribution between the data and MC are taken as the uncertainty for each event category.

The uncertainties for absolute energy scale are estimated to be 1.1%, 1.7%, 2.7% and 2.3% for SK I-IV, respectively, as discussed in Chap. 4.6.3.

(SK-2) Systematic error	σ(%)	Fit value	(σ)	
in event reconstruction and selection		6 b	80.3 W	200 τ
Ring separation	10	-1.06	-1.05	-1.05
PID (single-ring)	1.0	0.28	0.28	0.28
PID (multi-ring)	10	0.64	0.64	0.64
Energy calibration	1.7	0.00	0.00	0.00
Multi-GeV single-ring e-like non CCν_e BG	38.1	-0.37	-0.37	-0.37
Multi-GeV multi-ring e-like non CCν_e BG	11.1	0.12	0.12	0.12
Multi-GeV multi-ring ν_e and $\overline{\nu}_e$ separation	7.91	0.07	0.07	0.07
Sub-GeV 1-ring π^0 selection	10	0.19	0.19	0.19
Sub-GeV 2-ring π^0 selection	4.4	-0.39	-0.39	-0.39
Decay-e tagging (μ-decay)	10	-0.44	-0.45	-0.44
Multi-GeV multi-ring e-like other separation	10.	0.22	0.22	0.22

Table 8.9: Systematic errors related to event reconstruction and selection for SK-II. The second column shows the estimated 1σ error size and the 3-5th columns show the best fit value of the systematic error parameter ϵ_i for three representative WIMP hypotheses; "6 b", "80.3 W", "200 τ" indicate 6 GeV $b\bar{b}$, 80.3 GeV W^+W^-, 200 GeV $\tau^+\tau^-$ channels, respectively.

(SK-3) Systematic error	σ(%)	Fit value	(σ)	
in event reconstruction and selection		6 b	80.3 W	200 τ
Ring separation	10	0.29	0.29	0.29
PID (single-ring)	1.0	-0.14	-0.14	-0.14
PID (multi-ring)	10	0.31	0.31	0.31
Energy calibration	2.7	0.00	0.00	0.00
Multi-GeV single-ring e-like non CCν_e BG	26.7	0.14	0.14	0.14
Multi-GeV multi-ring e-like non CCν_e BG	11.4	-0.29	-0.29	-0.29
Multi-GeV multi-ring ν_e and $\overline{\nu}_e$ separation	7.68	-0.94	-0.94	-0.94
Sub-GeV 1-ring π^0 selection	10	0.22	0.22	0.22
Sub-GeV 2-ring π^0 selection	5.9	-0.12	-0.12	-0.12
Decay-e tagging (μ-decay)	10.	0.22	0.21	0.21
Multi-GeV multi-ring e-like other separation	10.	-0.42	-0.43	-0.43

Table 8.10: Systematic errors related to event reconstruction and selection for SK-III. The second column shows the estimated 1σ error size and the 3-5th columns show the best fit value of the systematic error parameter ϵ_i for three representative WIMP hypotheses; "6 b", "80.3 W", "200 τ" indicate 6 GeV $b\bar{b}$, 80.3 GeV W^+W^-, 200 GeV $\tau^+\tau^-$ channels, respectively.

(SK-4) Systematic error	σ(%)	Fit value	(σ)	
in event reconstruction and selection		6 b	80.3 W	200 τ
Ring separation	10	0.56	0.55	0.55
PID (single-ring)	1.0	0.08	0.08	0.08
PID (multi-ring)	10	0.59	0.59	0.59
Energy calibration	2.3	0.00	0.00	0.00
Multi-GeV single-ring e-like non CCν_e BG	17.6	0.06	0.06	0.06
Multi-GeV multi-ring e-like non CCν_e BG	11.6	0.61	0.61	0.61
Multi-GeV multi-ring ν_e and $\overline{\nu}_e$ separation	6.82	-0.28	-0.28	-0.28
Sub-GeV 1-ring π^0 selection	10	0.41	0.41	0.41
Sub-GeV 2-ring π^0 selection	5.6	-0.02	-0.02	-0.02
Decay-e tagging (μ-decay)	10	0.25	0.24	0.24
Multi-GeV multi-ring e-like other separation	10	-0.55	-0.55	-0.54

Table 8.11: Systematic errors related to event reconstruction and selection for SK-IV. The second column shows the estimated 1σ error size and the 3-5th columns show the best fit value of the systematic error parameter ϵ_i for three representative WIMP hypotheses; "6 b", "80.3 W", "200 τ" indicate 6 GeV $b\bar{b}$, 80.3 GeV W^+W^-, 200 GeV $\tau^+\tau^-$ channels, respectively.

For the multi-GeV multi-ring e-like non CC ν_e BG and ν_e and $\overline{\nu}_e$ separation, the cross section of the final state interactions of pions and the pion multiplicity are main expected source of the uncertainty (213). The cross sections of pions is compared to external experimental data, also the pion multiplicity is compared with the experimental data from the CHORUS experiment (214).

The uncertainties in the selection efficiency of π^0-like events in sub-GeV 1-ring π^0-like and 2-ring π^0-like samples are estimated by comparing the data with MC for each momentum region, and by shifting the absolute energy scale. The combined uncertainties are summarized in Tab. 8.12.

The uncertainty in decay electron detection efficiency is estimated to be 1.5% for SK I-III and improved to 0.8% for SK-IV, by using cosmic ray muons (215).

8.3 Uncertainties in WIMP neutrino propagation

For the uncertainties in the propagation of WIMP neutrino flux, seven systematic errors are considered for oscillation parameters and matter effect inside the Sun and the Earth. Five neutrino oscillation parameters are varied by 1σ deviation based on the experimental results (206), as shown in Tab. 8.13. The electron density inside the Sun and the Earth are varied by 10% in charge of the uncertainties in matter effects.

We simulate the neutrino flux using WIMPsim as varying each error source and

	1σ (%)			
	SK-I	SK-II	SK-III	SK-IV
100 < P_e < 250 MeV/c	11.2	7.5	7.7	10.8
250 < P_e < 400 MeV/c	11.5	8.9	26.4	11.6
400 < P_e < 630 MeV/c	23.4	17.5	12.5	10.1
630 < P_e < 1000 MeV/c	19.1	10.7	26.7	15.1
1000 < P_e < 1330 MeV/c	13.0	11.1	26.7	14.5

Table 8.12: 1σ values for systematic uncertainties of single-ring π^0-like events selection for SK-I, SK-II, SK-III and SK-IV.

compare to the original flux used in the analysis.

Parameter	used value	1σ
$\theta_{12}{}^\circ$	33.461	36
$\theta_{13}{}^\circ$	9.097	9.75
$\theta_{23}{}^\circ$	40.686	49
Δm^2_{32} [eV^2]	0.274×10^{-2}	0.289×10^{-2}
Δm^2_{21} [eV^2]	0.766×10^{-4}	0.726×10^{-4}

Table 8.13: Summary of 1σ variations of neutrino oscillation parameters taken as uncertainties.

The pulls for systematic errors related to signal flux are marginal except for θ_{23} which gives some contribution. Figure 8.7 shows fractional change in signal events due to 1σ increase of θ_{23}. The fit values of all signal flux errors are summarized in Tab. 8.14.

8.4 Uncertainties in nuclear physics and astrophysics

8.4.1 Form factor

In the spin-dependent coupling case, only hydrogen nuclei contribute, therefore form factor is not considered. However, the spin-independent coupling involves form factor correction, especially when WIMPs scatter off heavy elements.

The Helm-Gould nuclear form factor (82) for the momentum transfer q on the element i used in DarkSUSY has a form:

$$|F_i(q^2)|^2 = \exp(-\Delta E/E_i^0), \tag{8.1}$$

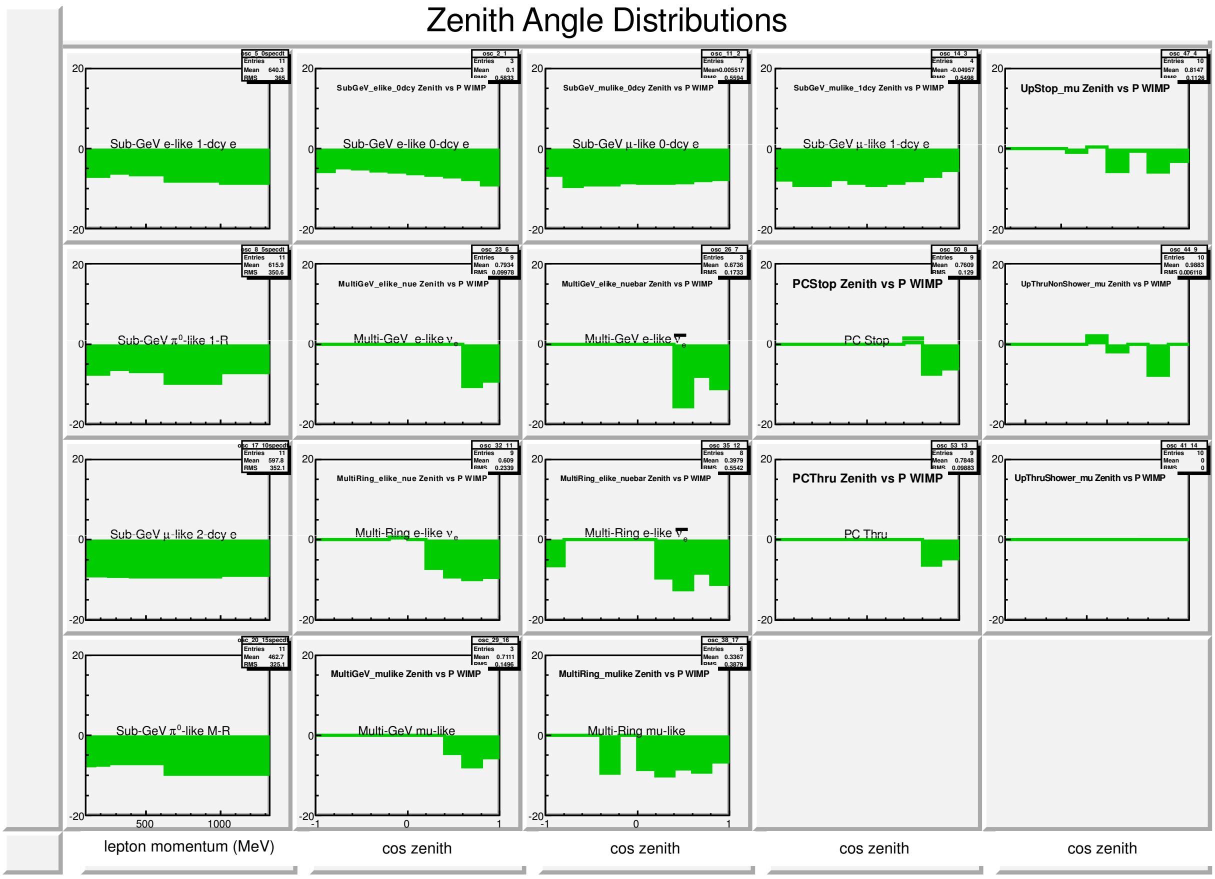

Figure 8.7: signal events with 1σ varied θ_{23} subtracted by signal events for nominal spectrum divided by signal events for nominal spectrum in percentage. They are shown for eighteen event categories used in the analysis.

Systematic error related to signal neutrino flux	$\sigma(\%)$	Fit value 6 b	(ϵ/σ) 80.3 W	 200 τ
oscillation parameter θ_{13}	13.3	-0.01	0.00	0.00
oscillation parameter θ_{12}	3.6	0.03	0.08	0.00
oscillation parameter θ_{23}	14.0	0.05	-0.02	0.00
oscillation parameter Δm_{32}	6.6	0.00	0.00	0.00
oscillation parameter Δm_{21}	2.7	0.00	0.00	0.00
Neutrino interaction in the Sun	10.0	0.00	0.00	0.00
Matter effect in the Earth	10.0	0.00	0.00	0.00

Table 8.14: Systematic errors related to WIMP neutrino flux calculation. They are common in all SK periods. The second column shows the estimated 1σ error size compared to nominal value, and the 3-5th columns show the best fit values of the systematic error parameter ϵ for three representative WIMP hypotheses; "6 b", "80.3 W", "200 τ" indicate 6 GeV $b\bar{b}$, 80.3 GeV W^+W^-, 200 GeV $\tau^+\tau^-$ channels, respectively.

where $\Delta E = q^2/2M_\chi$, $E_i^0 = 3\hbar^2/2M_\chi R_i^2$ with nuclear radius $R_i = [0.91(m_i/\mathrm{GeV})^{1/3} + 0.3] \times 10^{-15}$m are the used values.

The choice of parameters are compared to the choices in other works to estimate the size of the uncertainty. The effective radius $R_{eff,i} = [1.23 \times \exp(\log(m_i)/3) - 0.6] \times 10^{-15}$m as in Helm-Lewin-Smith form factor in (116) and (216; 217; 218) was used instead of nuclear radius used in (82) and DarkSUSY, and the difference was taken as upper error. The lower limit is taken by changing the factor 3/2 to 5/2 (219) as well as using the effective radius instead of the nuclear radius. It is a reasonable approximation to the more accurate Helm form factor for $\Delta E <\sim 2E_i^0$ (216; 217; 218). The sizes of the effects on the capture rate of WIMPs as a function of WIMP mass are shown in Tab. 8.15.

8.4.2 Solar model

The uncertainty on the composition of the Sun is calculated by comparing the DarkSUSY default choice, the BS2005-OP model, with the BS2005-AGS,OP model (220) with lower heavy element abundances. Table 8.16 shows the resultant numbers of change in the capture rate.

The effect is small for the SD-coupling case, about -3% lower capture rate is resulted. In the SI-coupling where heavier elements than hydrogen contribute, uncertainties are larger: 21% higher capture rate for 20 GeV and 26% of it for 500 GeV are resulted.

m_χ (GeV)		upper	lower
4	SI	0.3%	-1.4%
6	SI	1.0%	-2.8%
10	SI	3.1%	-6.6%
20	SI	8.8%	-17%
50	SI	16%	-33%
100	SI	19%	-41%
200	SI	22%	-47%

Table 8.15: Relative magnitudes of changes in the capture rate of WIMPs through SI coupling due to the form factor uncertainty are shown for several WIMP masses.

m_χ (GeV)		upper	lower
4	SD	-	-2.7%
	SI	14%	-
6	SD	-	-2.8%
	SI	16%	-
10	SD	-	-3.1%
	SI	18%	-
20	SD	-	-2.8%
	SI	21%	-
50	SD	-	-3.1%
	SI	23%	-
100	SD	-	-3.5%
	SI	24%	-
200	SD	-	-3.2%
	SI	26%	-

Table 8.16: Relative magnitudes of changes in the capture rate of WIMPs due to the uncertainty of the solar model, are shown for several WIMP masses, respectively for SD and SI coupling cases.

8.4.3 WIMP phase distribution

Large uncertainties on WIMP search comes from the understanding of the local dark matter phase space.

The uncertainty in local dark matter density is expected to be a factor of two (221; 222; 223; 224; 225), so do the uncertainties in the capture rate in the Sun and signal rate of direct detection searches, as scattering rate simply increases with the local density. Therefore it will make a similar overall shift of the limits for all direct and indirect detection experiments and doesn't effect the relative interpretation of them.

For the effect of the uncertainties in the velocity distribution of WIMPs, numbers determined in Chap. 3 are used. The uncertainties in the choice of the velocity distribution function, the orbital speed of the Sun and the high speed tail of the dark matter halo are summed in quadrature; They are $\sim \mathcal{O}(20)\%$ for 20 GeV WIMP and larger for heavier WIMP; $\sim \mathcal{O}(40)\%$ at 200 GeV. The possibility of co-rotating structure with the Sun can largely boost the signal by order of magnitude (73; 75; 116; 226). However, it is not considered as it makes the interpretation of solar WIMP search only conservative compared to direct detection searches.

8.4.4 Dynamics of solar system

The simplified dynamical history of WIMPs in Eq. 2.15 has several possible modifications.

As discussed in Chap. 3, the effects of the planets in the solar system on the capture rate, known as Jupiter depletion and solar gravitational diffusion, are canceled each other and determined to be negligible (109; 78) so not considered.

Solar evaporation is the process where captured WIMPs gain energy by rescatterings inside the Sun enough to escape out of the gravitational field of the Sun (227; 81; 228). This process can be important for the calculation of the density evolution of the light WIMPs inside the Sun, and is expected to drop rapidly for a WIMP mass of above 4 GeV (227; 81; 63; 229). Figure 8.8 shows the evaporation rate, $E_\odot$, as a function of WIMP mass (229). In the new SK analysis, WIMPs with masses above 4 GeV are studied in order to avoid the evaporation effect and to assume the equilibrium between the capture and the annihilation rates.

The evaporation mass, m_{evap}, which is defined as the mass with which the inverse of the evaporation rate, $E_\odot$, is equal to the age of the Sun $t_\odot = 4.7 \times 10^9$ yrs (228), can be approximated as (65):

$$m_{evap} = m_0 + 0.32 log_{10}(\frac{\sigma_0}{10^{-40}\mathrm{cm}^2})\mathrm{GeV} \tag{8.2}$$

with $m_0 = 3.02$ ($m_0 = 3.5$) for SD (SI) coupling case. As a result, for the cross-sections around new SK limits, which are about 10^{-40} cm^2 (10^{-41} cm^2) for SD (SI) couplings, the limits could be extended down to $m_{evap} \sim 3.02$ GeV for SD and $m_{evap} \sim 3.18$ GeV for SI coupling cases, and can be lowered further in future searches in neutrino detectors such as the Hyper-Kamiokande, with possible improvement of the sensitivity to cross sections by an order of magnitude.

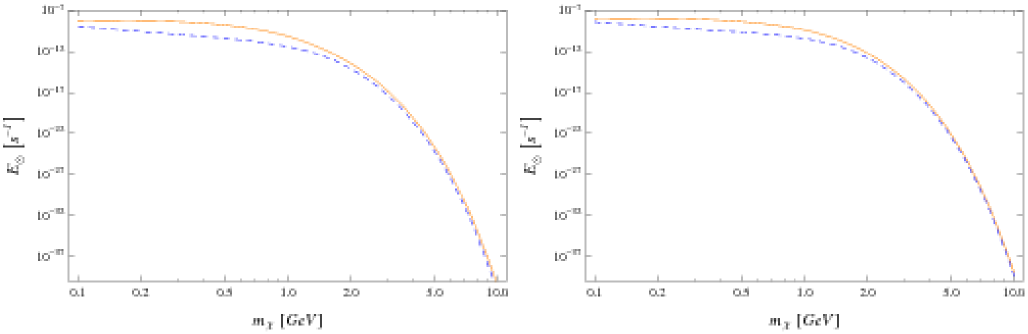

Figure 8.8: Evaporation rate versus WIMP mass for SD coupling (left) and SI coupling (right) cases. Figure is taken from (229).

Below the evaporation mass, the annihilation rate decreases and the evaporation rate increases. Therefore the capture rate of WIMPs with lighter mass may be set in equilibrium with evaporation rate, instead of annihilation rate. As a result, the annihilation rate, therefore the number of WIMP neutrinos detected in a neutrino detector, may become independent of the scattering cross section.

Recent theoretical work by Busoni et al. (229) points out that ven below evaporation mass, a neutrino detector can study the WIMP scattering property by solving the Eq. 2.14 with evaporation term. With the canonical value for the thermally-averaged annihilation rate $< \sigma v > = 3 \times 10^{-26}$ cm^3/s, one can find that for the WIMP with SD (SI) coupling cross-section of 10^{-41} cm^2 (10^{-42} cm^2), the minimum mass testable in a neutrino detector is as small as ∼2 GeV. Figure 8.9 shows the test-minimum mass versus cross-section (229).

8.4.5 Summary

In conclusion, the related uncertainties to the capture process are discussed. These errors are added in quadrature and the resultant numbers are shown in Tab. 8.17. The effects of them on the result from the SK analysis are indicated by the shadowed regions in Fig. 8.10 and Fig. 8.11. The combined effects of all errors loosen the upper limit of scattering cross-section maximally 42% for SD and 46% for SI coupling WIMPs.

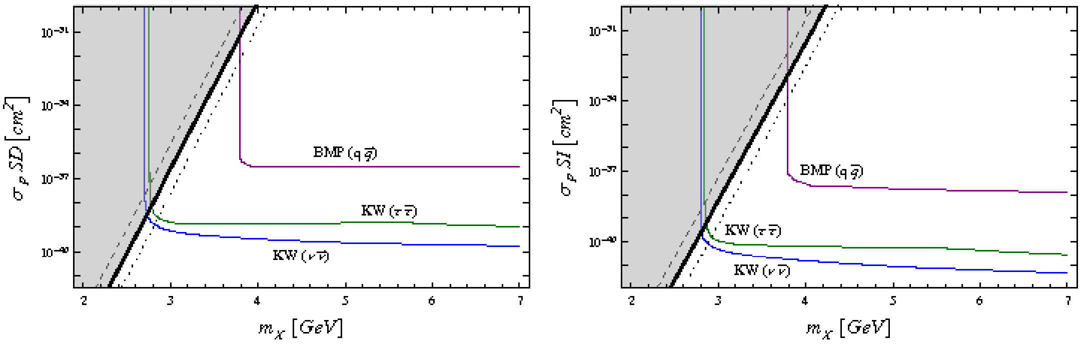

Figure 8.9: The test-minimum WIMP mass is shown on the parameter space of the WIMP mass versus the SD (left) and SI (right) scattering cross sections. The shaded regions are the parameter space which can not be tested by a neutrino detector. Figure is taken from (229).

m_χ (GeV)		upper	lower
4	SD	19%	−12%
	SI	22%	−11%
6	SD	19%	−12%
	SI	23%	−12%
10	SD	22%	−15%
	SI	25%	−13%
20	SD	30%	−20%
	SI	30%	−21%
50	SD	40%	−25%
	SI	35%	−36%
100	SD	41%	−20%
	SI	40%	−44%
200	SD	42%	−17%
	SI	46%	−51%

Table 8.17: Relative magnitudes of total changes in the capture rate due to uncertainties of form factor, solar model and astrophysics together are shown for several WIMP masses, respectively for SD and SI coupling cases.

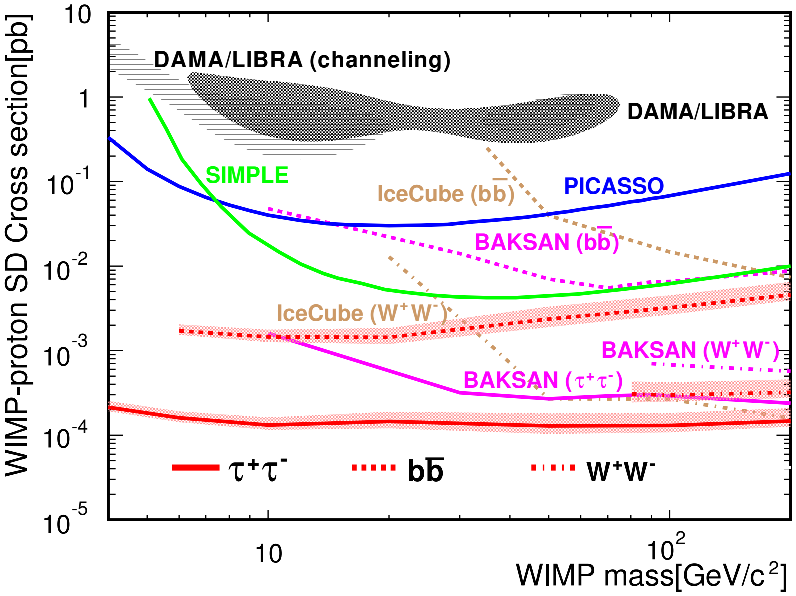

Figure 8.10: 90% C. L. upper limits on SD WIMP-proton cross section calculated for the DarkSUSY (83) default are shown for the $\tau^+\tau^-$ channel in red solid; $b\bar{b}$ in red dashed; W^+W^- in red dot-dashed with uncertainty bands to take account form factor, solar model and velocity distribution uncertainties. Also shown are limits from other experiments: IceCube (54) $b\bar{b}$ (brown dashed) / W^+W^- (brown dot-dashed); BAKSAN (59) $\tau^+\tau^-$ (pink solid) / $b\bar{b}$ (pink dashed) / W^+W^- (pink dot-dashed); PICASSO (202) (blue solid); SIMPLE (203) (green solid). The black shaded regions are the 3σ C.L. signal claimed by DAMA/LIBRA (62; 204).

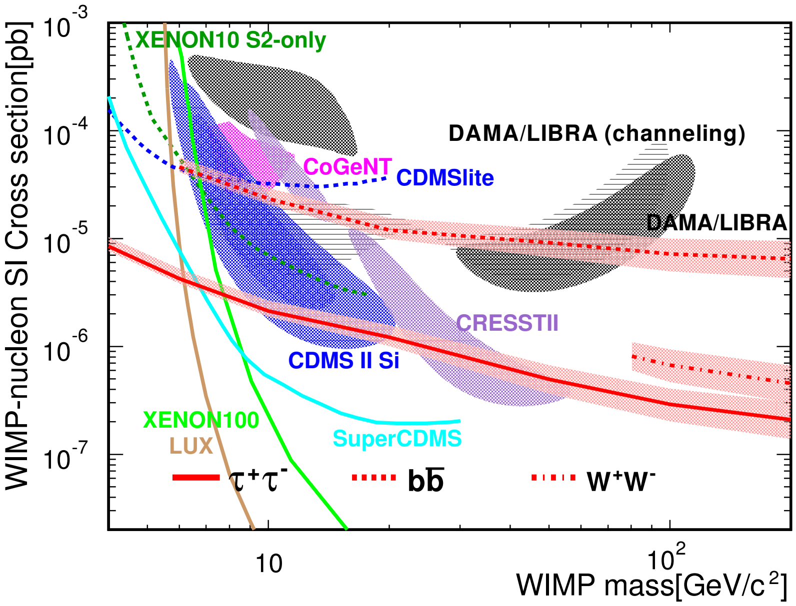

Figure 8.11: 90% C. L. upper limits on the SI WIMP-nucleon cross section calculated using the DarkSUSY (83) default are shown for the $\tau^+\tau^-$ channel in red solid; $b\bar{b}$ in red dashed; W^+W^- in red dot-dashed with uncertainty bands to take account form factor, solar model, form factor and velocity distribution uncertainties. Also shown are signal claims from other experiments: DAMA/LIBRA (black shaded regions, 3σ C.L.); CoGENT (48) (magenta shaded region, 90% C.L.); CRESSTII (45) (violet shaded regions, 2σ C.L.); CDMS II Si (46) (blue shaded region, 90% C.L.); and limits: SuperCDMS (51) (cyan solid); CDMSlite (205) (blue dashed); XENON10 S2-only (52) (dark green dashed); XENON100 (49) (green solid); LUX (50) (brown solid).

8.5 Uncertainties in particle physics

8.5.1 Overview

Throughout the majority of the WIMP searches including this work, we constrain a WIMP candidate to be a single type of WIMP which explains the entire signal detected solely, and to fulfill the observed local density 0.3 GeV/cm^3 of the WIMPs in the Milky way. Typically, no assumption is made on the WIMP mass and analyses test several WIMP masses. Annihilation cross-section is also free from particle-physics models under the condition that the equilibrium state of the WIMP is achieved; the uncertainty in the equilibrium condition itself will be discussed shortly. As mentioned before, typically solar WIMP searches make an assumption of the single-annihilation channel and test two or three channels, which are picked up to represent relatively "soft" and "hard" expected neutrino spectra.

The scattering properties of WIMPs have several uncertainties highly depending one the particle physics model. A common way to interpret the signal usually makes following assumptions for the scattering interaction:

A) contact interaction,
B) single type of interaction: SD couping only or SI couping only,
C) for SD coupling case, 'odd group assumption' for amplitudes of S_p and S_n,
D) for SI coupling case, isospin invariance for amplitudes of σ_p and σ_n.

In the literature, there have been discussions on long-ranged interactions of dark matter with nuclei, in elastic and inelastic scatterings. To some of them a neutrino detector is expected to have a strong sensitivity but in this dissertation, we restraint our discussion in contact interaction.

The assumption B) is left as a pure assumption, that we interpret the signal as if it is from pure SD or pure SI coupling.

The SD capture in the Sun is effectively governed by hydrogen, therefore we neglect the contribution from heavier elements. This allows the situation to be extremely simple compared to direct detection experiments using heavy elements in two ways; first, for heavier nuclei than hydrogen, in many cases the "odd-group" model is used, which assumes that total nuclear spin is carried by either protons or neutrons, whichever are more unpaired. So only one of either $a_p < S_{p(N)} >$ or $a_p < S_{n(N)} >$ in the WIMP-nucleon scattering cross-section at zero momentum transfer (1.5.2) is assumed to be non zero. However, for the SD scattering of WIMP to hydrogen, $a_n < S_{n(N)} >$ is naturally not needed to be considered. Secondly we don't have to take the decoherence into account by introducing a nuclear form factor suppression, as mentioned in the previous chapter. As a result, for the solar WIMP search, we can set upper limit on SD WIMP-proton cross-section without assumption on C).

8.5.2 Isospin violation

When the SI interaction is assumed, the further assumption D) that the f_p/f_n ratio to be 1, or "isospin conservation", is typically made. Although f_p/f_n is predicted to be very close to 1 in most of the WIMP models found in MSSM, it is not guaranteed in more general scenarios such as sneutrinos found in nMSSM. In these cases, an additional assumption on the ratio between f_p and f_n is needed to be made. As mentioned in Chap. 1, the phenomenologically motivated value $f_p/f_n = -0.7$ has interesting sensitivity for a neutrino detector. Thus, in addition to the conventional interpretation to isospin conserving model, we show our result on isospin-violating model as shown in Fig. 8.12.

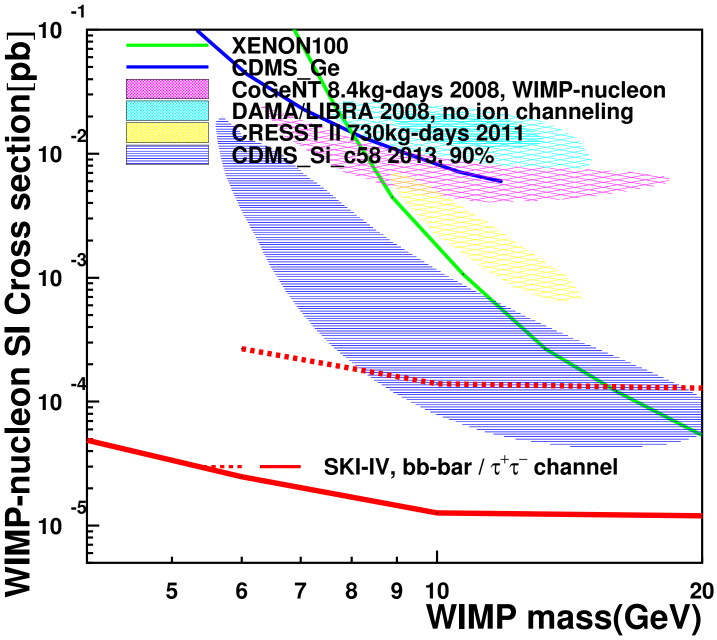

Figure 8.12: 90% upper limits on the SI IVDM-proton cross-section are shown for the $\tau^+\tau^-$ channel in red solid; $b\bar{b}$ in red dashed. Also shown are limits from other experiments: XENON100 (green solid); CDMS-Si (dark blue solid); CDMS-Ge (dark blue shaded region); CoGENT (pink shaded region); CRESSTII (yellow shaded region); DAMA/LIBRA (light blue shaded region).

8.5.3 Equilibrium condition

Given the age of the Sun, it is frequently assumed that the capture rate and the annihilation rate of WIMPs have been equilibrated. As discussed in Chap. 2, the instant thermalization assumption can be more easily achieved for low mass WIMPs with high scattering cross-section, and the relation of annihilation cross section to scattering cross section is well-defined but model dependent. With the typically assumed value 3×10^{-26} cm^{3}s^{-1} velocity-independent s-wave annihilation cross section, the capture rate of 10^{25} s^{-1} requires $<\sigma_\odot> \gg 10^{-30}$ cm^3 s^{-1} (65) and in this case equilibrium could safely be reached.

However, as several assumptions are involved in this scenario, for reliable usage of results from solar WIMP searches by neutrino experiments, the equilibrium condition needs to be evaluated for specific WIMP scenarios in individual studies (219; 66; 76). This has been done for example for cMSSM models (219; 66) and pMSSM models (76), and other scenarios in general can be scanned in future.

8.6 Summary

"Indirect" detection methods are in general regarded to suffer from uncertainties in backgrounds, astrophysics (effects are generally larger than direct detection) and propagation of annihilation products to detector. However, the detection of solar WIMP neutrino is not the case.

The backgrounds for WIMP search in neutrino detectors are in general atmospheric neutrinos, which are well understood enough to precisely constraint neutrino oscillation parameters as shown in Chap. 5. Also the propagation of the neutrinos produced inside the Sun to detector is straightforward (88). The detector response to both signal and the back-ground neutrinos are well studied as well.

A neutrino detector for solar WIMP search especially has a good sensitivity to spin-dependent coupling WIMP search. In this case, the nuclear physics- and particle physics-related uncertainties in the scattering process are negligible due to the simple structure of the hydrogen. Also the solar model is not a source for the uncertainty of WIMP-proton SD coupling as its uncertainty is more relevant to the distribution of the heavy nuclei inside the Sun. In a scenario of isospin-violating dark matter, the relative limit from a neutrino detector gets stronger as it gets weaker suppression, compared to direct detection experiments.

The dark matter phase distribution is regarded to be a large source of uncertainty for WIMP searches. However, the uncertainty in the local density will affect the indirect detection in the same size of the direct detection, and the result of the study of the uncertainties from the velocity distribution shows a mild change as the capture is given by an integral over wide range of the velocity distribution. Also because the capture process is more efficient from low-velocity region, it is insensitive to the critical uncertainty in high-velocity tail of the dark matter halo. Possibly existing co-rotating structure with the Sun can largely boost the signal and hence make the interpretation of solar WIMP search more conservative.

Chapter 9

Conclusion

Light WIMPs annihilating in the Sun were searched using the Super-Kamiokande I-IV 3903-days data. To increase signal acceptance for a few-GeV to a few tens of GeV WIMPs, the analysis used vertex-contained neutrino events in addition to neutrino-induced up-going muon events. Also ν_e, $\overline{\nu}_e$, ν_τ and $\overline{\nu}_\tau$ fluxes were used as well as ν_μ, $\overline{\nu}_\mu$ fluxes. As a result, the signal acceptance has increased 47 times compared to the previous analysis which used up-going muons only for example for 10-GeV WIMP annihilating to $b\bar{b}$. To discriminate the overwhelming atmospheric neutrino back-ground events which increase as $\propto E^{-2.7}$ at low energy, we performed a least-squares fit which makes full use of the energy, angle and flavor information. Under the assumption that SK data is composed of events from atmospheric neutrinos and WIMP neutrinos, we fit data to find the best contribution of WIMP-induced neutrino events.

As a result, we found no significant excess for 4–200-GeV WIMP hypotheses and the result is interpreted as upper limits on the WIMP-nucleon elastic scattering cross sections. The derived upper limit on the SD WIMP-proton cross section shows the most stringent constraint to date for WIMP masses below 200 GeV even with the conservative assumption of the $b\bar{b}$ annihilation channel. In the case that the branch of WIMP annihilation into $\tau^+\tau^-$ is 100%, we exclude the entire DAMA/CoGeNT-claimed signal regions and most parts of the CDMS signal region. This result is consistent with the recent null results from XENON100, LUX and SuperCDMS. We also exclude new region for WIMP masses below 6 GeV with $\tau^+\tau^-$ channel. If it is the case that WIMP violates isospin invariance and experiences destructive interference, our most conservative channel $b\bar{b}$ also becomes inconsistent with the CDMS Si signal.

We investigated how robust the limits were against astrophysical uncertainties using DarkSUSY simulation code. We have performed a detailed study of the effect of the velocity distribution of dark matter on capture rate in the Sun, therefore effect on indirect WIMP search using the neutrino flux from the Sun. We examined four sources of uncertainties: orbital speed of the Sun, escape velocity of dark matter from the halo, dark matter velocity distribution functions and the existence of a dark disc.

We found that even extreme cases currently discussed do not decrease the sensitivity of indirect detection significantly, because the capture is achieved over a broad range of the velocity distribution. The effect of the uncertainty in the high-velocity tail of dark matter halo is very marginal as the capture process is rather inefficient in this region. For a WIMP mass of 20 GeV, we found the uncertainties for SD (SI) coupling case are about 18 (14)% from local circular speed, 1 (1)% from high-velocity cut for the tested range, and 16 (10)% from the dark matter halos taken from cosmological simulations. The total sum of the uncertainties was found to be less then 24% (17%) for 20 GeV SD (SI) coupling WIMPs in the case absence of the dark disc. For heavier WIMPs, the uncertainty was larger but still below 50%; for SD (SI) coupling, they are 45 (32)% from local circular speed, 1 (1)% from high-velocity cut, 11 (16)% from deviation of the VDF from Maxwellian, in the case of 500 GeV WIMP. We concluded that the overall uncertainties from velocity distribution in solar WIMP searches were moderate. With the dark matter disc structure expected from ΛCDM cosmology, the impact could be significant as the low-velocity population, which is easy to be captured, is enriched. The signal could be enhanced as much as 6 (15) times for 100 GeV SI (SD) coupling WIMPs. However, the impact of a dark disc on direct detections, which had been previously shown, is expected to be milder. Hence the possible existence of a dark disc would only change the interpretation of the limits from the solar WIMP searches on the conservative side.

We also studied how the changes made by various source of uncertainties on the limits of solar WIMP search differ from that of direct detection. We found that the solar WIMP search and direct detection would have uncorrelated sensitivities to the sources of uncertainties in the tail of the VDF, and anti-correlated responses toward the uncertainties which shift the overall WIMP population. We confirmed that the solar neutrino search for light WIMP masses could be a good complementary method to break degeneracies among scattering cross section, WIMP mass and various astrophysical uncertainties that could significantly alter the interpretation of direct detection experiments. For high mass WIMP scenarios, sensitivity of solar WIMP searches to the low-velocity region can be exploited to understand properties such as the dark disc component to which direct detection experiments are rather insensitive.

For the first time the astrophysical uncertainties including the conclusion of the study of the velocity distribution was reflected on the derivation of upper limit in solar WIMP search. The upper limit on SD and SI WIMP-nucleon scattering cross sections obtained in this work carry an uncertainty of about 30% for 4 GeV WIMP, which increases for higher WIMP masses and resulting in up to 100% for 200 GeV WIMP. The new limits on cross sections by the Super-Kamiokande is shown together with the astrophysical uncertainty bands, which is relevant for precise comparison to direct detection experiment limits.

By quantitative study of uncertainties, it is possible to compare solar WIMP neutrino searches with direct detection. In terms of not only good sensitivity for signal but also unique sensitivities and insensitivities to astrophysical properties, the usefulness of this result and searches from future neutrino detectors such as the Hyper-Kamiokande and the PINGU upgrade are highlighted.

The uncertainties which are expected to decrease the sensitivity, for example the uncertainty of the Q^2 spectrum in deep inelastic scattering, could be studied more in future to improve the sensitivity. Also generating signal MC with larger statistics, or in different strategy, will improve the sensitivity. However, the sensitivity is governed by the statistical uncertainty as shown in Chap. 7.5. The future improvement of sensitivity to detection of WIMPs can be obtained by increasing statistics of data. With five-years data from the next generation neutrino detector Hyper-Kamiokande, which has about 25 times larger fiducial volume compared to the Super-Kamiokande, the sensitivity to $\sim$ 50 GeV WIMPs annihilating to $b\bar{b}$ channel (20 GeV WIMPs for $\tau^+\tau^-$ channel) will be improved by a factor 3.5 compared to this work. For heavier WIMPs, the 18 times enlarged effective area compared to the SK will give about 3 times improvement compared to this work.

In direct detection experiments, the sensitivity to WIMP mass is degenerated with that to the cross section. However, with the new SK WIMP analysis method, it is possible to distinguish the signals coming from WIMPs with different masses by their energy spectra. The SK, as well as future neutrino detectors sensitive to differential energy spectrum of WIMP neutrinos, will have power to determine the WIMP mass by performing a two-dimensional χ^2 test instead of making an assumption on WIMP mass. It will be so in particular for light WIMP scenario of WIMP mass below about 100 GeV, where the signal events are well accepted by contained event categories and spread over many energy bins.

The mass determination by solar WIMP search for light WIMP scenarios is not only expected to be powerful, but also important in terms of astrophysical uncertainties. In the light WIMP mass region, the uncertainty in the high-velocity tail of the velocity distribution of WIMPs will significantly affect the event rate of direct detection experiments, therefore entangling together with the mass and cross sections of WIMPs. However, solar WIMP search is affected less than 1% by the high-velocity tail. In case of multiple observations by direct detection experiments and solar WIMP searches, the solar WIMP neutrino detection will take important role in revealing the properties of WIMPs.

Bibliography

[1] Martin, S.P.: A Supersymmetry primer. Adv.Ser.Direct.High Energy Phys. **21** (2010) 1–153

[2] Appelquist, T., Cheng, H.C., Dobrescu, B.A.: Bounds on universal extra dimensions. Phys.Rev. **D64** (2001) 035002

[3] Zwicky, F.: Spectral displacement of extra galactic nebulae. Helv. Phys. Acta **6** (1933) 110–127

[4] van den Bergh, S.: The Early history of dark matter. Publ.Astron.Soc.Pac. (1999)

[5] Babcock, H.W.: The rotation of the andromeda nebula. Lick Observatory Bulletin **418** (1939) 41

[6] Rubin, V.C., Ford, W. Kent, J.: Rotation of the Andromeda Nebula from a Spectroscopic Survey of Emission Regions. Astrophys.J. **159** (1970) 379–403

[7] Roberts, M.S., Whitehurst, R.N.: The rotation curve and geometry of M31 at large galactocentric distances. **201** (October 1975) 327–346

[8] Clowe, D., Bradac, M., Gonzalez, A.H., Markevitch, M., Randall, S.W., et al.: A direct empirical proof of the existence of dark matter. Astrophys.J. **648** (2006) L109–L113

[9] Copi, C.J., Schramm, D.N., Turner, M.S.: Big bang nucleosynthesis and the baryon density of the universe. Science **267** (1995) 192–199

[10] Tytler, D., Fan, X.m., Burles, S.: The Cosmological baryon density from the deuterium abundance at a redshift z = 3.57. Nature **381** (1996) 207–209

[11] Schramm, D.N., Turner, M.S.: Big bang nucleosynthesis enters the precision era. Rev.Mod.Phys. **70** (1998) 303–318

[12] Hinshaw, G., et al.: Nine-Year Wilkinson Microwave Anisotropy Probe (WMAP) Observations: Cosmological Parameter Results. Astrophys.J.Suppl. **208** (2013) 19

[13] http://map.gsfc.nasa.gov/

[14] Cole, S., et al.: The 2dF Galaxy Redshift Survey: Power-spectrum analysis of the final dataset and cosmological implications. Mon.Not.Roy.Astron.Soc. **362** (2005) 505–534

[15] Kowalski, M., et al.: Improved Cosmological Constraints from New, Old and Combined Supernova Datasets. Astrophys.J. **686** (2008) 749–778

[16] Percival, W.J., et al.: Baryon Acoustic Oscillations in the Sloan Digital Sky Survey Data Release 7 Galaxy Sample. Mon.Not.Roy.Astron.Soc. **401** (2010) 2148–2168

[17] Weinheimer, C.: The Neutrino mass direct measurements. (2003) 335–344

[18] Peebles, P.: Large scale background temperature and mass fluctuations due to scale invariant primeval perturbations. Astrophys.J. **263** (1982) L1–L5

[19] Jenkins, A., et al.: Evolution of structure in cold dark matter universes. Astrophys.J. **499** (1998) 20

[20] Garrett, K., Duda, G.: Dark Matter: A Primer. Adv.Astron. **2011** (2011) 968283

[21] Houjun Mo, Frank van den Bosch, S.W.: Galaxy formation and evolution

[22] Lynden-Bell, D.: Statistical mechanics of violent relaxation in stellar systems. Mon.Not.Roy.Astron.Soc. **136** (1967) 101–121

[23] Kamionkowski, M., Kinkhabwala, A.: Galactic halo models and particle dark matter detection. Phys.Rev. **D57** (1998) 3256–3263

[24] Binney, J., Tremaine, S.: Galactic dynamics. (1987)

[25] Eddington, A.S.: The distribution of stars in globular clusters. Mon. Not. R. Astron. Soc. **76** (May 1916) 572–585

[26] Hansen, S.H., Egli, D., Hollenstein, L., Salzmann, C.: Dark matter distribution function from non-extensive statistical mechanics. New Astron. **10** (2005) 379

[27] Tsallis, C.: Possible Generalization of Boltzmann-Gibbs Statistics. J.Statist.Phys. **52** (1988) 479–487

[28] Plastino, A.R., Plastino, A. PLA,173:384,(1993)

[29] Primack, J.R.: Triumphs and tribulations of Lambda CDM, the double dark theory. Annalen Phys. **524** (2012) 535–544

[30] Guedes, J., Callegari, S., Madau, P., Mayer, L.: Forming Realistic Late-Type Spirals in a LCDM Universe: The Eris Simulation. Astrophys.J. **742** (2011) 76

[31] Governato, F., Zolotov, A., Pontzen, A., Christensen, C., Oh, S., et al.: Cuspy No More: How Outflows Affect the Central Dark Matter and Baryon Distribution in Lambda CDM Galaxies. Mon.Not.Roy.Astron.Soc. **422** (2012) 1231–1240

[32] Boylan-Kolchin, M., Bullock, J.S., Kaplinghat, M.: The Milky Way's bright satellites as an apparent failure of LCDM. Mon.Not.Roy.Astron.Soc. **422** (2012) 1203–1218

[33] http://www.mpa-garching.mpg.de/halo2013

[34] Ling, F., Nezri, E., Athanassoula, E., Teyssier, R.: Dark Matter Direct Detection Signals inferred from a Cosmological N-body Simulation with Baryons. JCAP **1002** (2010) 012

[35] Read, J., Lake, G., Agertz, O., Debattista, V.P.: Thin, thick and dark discs in LCDM. Mon.Not.Roy.Astron.Soc. **389** (2008) 1041–1057

[36] Read, J., Mayer, L., Brooks, A., Governato, F., Lake, G.: A dark matter disc in three cosmological simulations of Milky Way mass galaxies. (2009)

[37] Purcell, C.W., Bullock, J.S., Kaplinghat, M.: The Dark Disk of the Milky Way. Astrophys.J. **703** (2009) 2275–2284

[38] Kuhlen, M., Pillepich, A., Guedes, J., Madau, P.: The Distribution of Dark Matter in the Milky Way's Disk. Astrophys.J. **784** (2014) 161

[39] Goldberg, H.: Constraint on the Photino Mass from Cosmology. Phys.Rev.Lett. **50** (1983) 1419

[40] Ellis, J.R., Hagelin, J., Nanopoulos, D.V., Olive, K.A., Srednicki, M.: Supersymmetric Relics from the Big Bang. Nucl.Phys. **B238** (1984) 453–476

[41] Bertone, G., Hooper, D., Silk, J.: Particle dark matter: Evidence, candidates and constraints. Phys.Rept. **405** (2005) 279–390

[42] Jungman, G., Kamionkowski, M., Griest, K.: Supersymmetric dark matter. Phys. Rept. **267** (1996) 195–373

[43] Goodman, M.W., Witten, E.: Detectability of certain dark-matter candidates. prd **31** (June 1985) 3059–3063

[44] Schumann, M.: Dark Matter 2013. Braz.J.Phys. **44** (2014) 483–493

[45] Angloher, G., Bauer, M., Bavykina, I., Bento, A., Bucci, C., et al.: Results from 730 kg days of the CRESST-II Dark Matter Search. Eur.Phys.J. **C72** (2012) 1971

[46] Agnese, R., et al.: Silicon Detector Dark Matter Results from the Final Exposure of CDMS II. Phys.Rev.Lett. **111** (2013) 251301

[47] Bernabei, R., et al.: New results from DAMA/LIBRA. Eur.Phys.J. **C67** (2010) 39–49

[48] Aalseth, C., et al.: Results from a Search for Light-Mass Dark Matter with a P-type Point Contact Germanium Detector. Phys.Rev.Lett. **106** (2011) 131301

[49] Aprile, E., et al.: Dark Matter Results from 225 Live Days of XENON100 Data. Phys.Rev.Lett. **109** (2012) 181301

[50] Akerib, D., et al.: First results from the LUX dark matter experiment at the Sanford Underground Research Facility. (2013)

[51] Agnese, R., et al.: Search for Low-Mass WIMPs with SuperCDMS. (2014)

[52] Angle, J., et al.: A search for light dark matter in XENON10 data. Phys.Rev.Lett. **107** (2011) 051301

[53] Aprile, E.: The search for dark matter with XENON. (2011) 15–18

[54] Aartsen, M., et al.: Search for dark matter annihilations in the Sun with the 79-string IceCube detector. Phys.Rev.Lett. **110** (2013) 131302

[55] Feng, J., Ritz, S., Beatty, J., Buckley, J., Cowen, D., et al.: Planning the Future of U.S. Particle Physics (Snowmass 2013): Chapter 4: Cosmic Frontier. (2014)

[56] Tanaka, T., et al.: An Indirect Search for WIMPs in the Sun using 3109.6 days of upward-going muons in Super-Kamiokande. Astrophys.J. **742** (2011) 78

[57] Braun, J., Hubert, D.: Search for WIMP Dark Matter from the Sun with AMANDA. 31st ICRC Conf. Proc. (2009) 42–48

[58] Spiering, C.: The Baikal neutrino telescope: results and prospects. Nucl. Phys. Proc. Suppl. **138** (2005) 175–178

[59] Boliev, M., Demidov, S., Mikheyev, S., Suvorova, O.: Search for muon signal from dark matter annihilations inthe Sun with the Baksan Underground Scintillator Telescope for 24.12 years. JCAP **1309** (2013) 019

[60] Adrian-Martinez, S., et al.: First results on dark matter annihilation in the Sun using the ANTARES neutrino telescope. JCAP **1311** (2013) 032

[61] Desai, S., et al.: Search for dark matter WIMPs using upward through-going muons in Super-Kamiokande. Phys. Rev. **D70** (2004) 083523

[62] Bernabei, R., et al.: First results from DAMA/LIBRA and the combined results with DAMA/NaI. Eur.Phys.J. **C56** (2008) 333–355

[63] Hooper, D., Petriello, F., Zurek, K.M., Kamionkowski, M.: The New DAMA Dark-Matter Window and Energetic-Neutrino Searches. Phys.Rev. **D79** (2009) 015010

[64] Feng, J.L., Kumar, J., Learned, J., Strigari, L.E.: Testing the Dark Matter Interpretation of the DAMA/LIBRA Result with Super-Kamiokande. JCAP **0901** (2009) 032

[65] Kappl, R., Winkler, M.W.: New Limits on Dark Matter from Super-Kamiokande. Nucl.Phys. **B850** (2011) 505–521

[66] Rott, C., Tanaka, T., Itow, Y.: Enhanced Sensitivity to Dark Matter Self-annihilations in the Sun using Neutrino Spectral Information. JCAP **1109** (2011) 029

[67] Fitzpatrick, A.L., Hooper, D., Zurek, K.M.: Implications of CoGeNT and DAMA for Light WIMP Dark Matter. Phys.Rev. **D81** (2010) 115005

[68] Kumar, J., Sanford, D., Strigari, L.E.: New Constraints on Isospin-Violating Dark Matter. Phys.Rev. **D85** (2012) 081301

[69] Chen, S.L., Zhang, Y.: Isospin-Violating Dark Matter and Neutrinos From the Sun. Phys.Rev. **D84** (2011) 031301

[70] Gao, Y., Kumar, J., Marfatia, D.: Isospin-Violating Dark Matter in the Sun. Phys.Lett. **B704** (2011) 534–540

[71] McCabe, C.: The Astrophysical Uncertainties Of Dark Matter Direct Detection Experiments. Phys.Rev. **D82** (2010) 023530

[72] Green, A.M.: Astrophysical uncertainties on direct detection experiments. Mod.Phys.Lett. **A27** (2012) 1230004

[73] Bruch, T., Peter, A.H.G., Read, J., Baudis, L., Lake, G.: Dark Matter Disc Enhanced Neutrino Fluxes from the Sun and Earth. Phys. Lett. **B674** (2009) 250–256

[74] Peter, A.H.: Dark matter bound to the Solar System: consequences for annihilation searches. (2009)

[75] Ling, F.S.: Is the Dark Disc contribution to Dark Matter Signals important ? Phys.Rev. **D82** (2010) 023534

[76] Serpico, P.D., Bertone, G.: Astrophysical limitations to the identification of dark matter: indirect neutrino signals vis-a-vis direct detection recoil rates. Phys.Rev. **D82** (2010) 063505

[77] Kundu, S., Bhattacharjee, P.: Neutrinos from WIMP annihilation in the Sun : Implications of a self-consistent model of the Milky Way's dark matter halo. Phys.Rev. **D85** (2012) 123533

[78] Sivertsson, S., Edsjo, J.: WIMP diffusion in the solar system including solar WIMP-nucleon scattering. Phys.Rev. **D85** (2012) 123514

[79] Arina, C., Bertone, G., Silverwood, H.: Complementarity of direct and indirect Dark Matter detection experiments. Phys.Rev. **D88** (2013) 013002

[80] Press, W.H., Spergel, D.N.: Capture by the sun of a galactic population of weakly interacting massive particles. Astrophys.J. **296** (1985) 679–684

[81] Gould, A.: WIMP Distribution in and Evaporation From the Sun. Astrophys.J. **321** (1987) 560

[82] Gould, A.: Resonant Enhancements in WIMP Capture by the Earth. Astrophys. J. **321** (1987) 571

[83] Gondolo, P., et al.: DarkSUSY: Computing supersymmetric dark matter properties numerically. JCAP **0407** (2004) 008

[84] Yao, W., et al.: Review of Particle Physics. J.Phys. **G33** (2006) 1–1232

[85] Zentner, A.R.: High-Energy Neutrinos From Dark Matter Particle Self-Capture Within the Sun. Phys.Rev. **D80** (2009) 063501

[86] Peter, A.H.: Dark matter in the solar system II: WIMP annihilation rates in the Sun. Phys.Rev. **D79** (2009) 103532

[87] Baratella, P., Cirelli, M., Hektor, A., Pata, J., Piibeleht, M., et al.: PPPC 4 DMν: a Poor Particle Physicist Cookbook for Neutrinos from Dark Matter annihilations in the Sun. JCAP **1403** (2014) 053

[88] Blennow, M., Edsjo, J., Ohlsson, T.: Neutrinos from WIMP annihilations using a full three-flavor Monte Carlo. JCAP **0801** (2008) 021

[89] http://copsosx03.physto.se/wimpsim/

[90] Vogelsberger, M., et al.: Phase-space structure in the local dark matter distribution and its signature in direct detection experiments. (2008)

[91] Kuhlen, M., Weiner, N., Diemand, J., Madau, P., Moore, B., et al.: Dark Matter Direct Detection with Non-Maxwellian Velocity Structure. JCAP **1002** (2010) 030

[92] Mao, Y.Y., Strigari, L.E., Wechsler, R.H., Wu, H.Y., Hahn, O.: Halo-to-Halo Similarity and Scatter in the Velocity Distribution of Dark Matter. Astrophys.J. **764** (2013) 35

[93] Springel, V., Wang, J., Vogelsberger, M., Ludlow, A., Jenkins, A., et al.: The Aquarius Project: the subhalos of galactic halos. Mon.Not.Roy.Astron.Soc. **391** (2008) 1685–1711

[94] Teyssier, R.: Cosmological hydrodynamics with adaptive mesh refinement: a new high resolution code called ramses. Astron.Astrophys. **385** (2002) 337–364

[95] Wu, H.Y., Hahn, O., Wechsler, R.H., Mao, Y.Y., Behroozi, P.S.: Rhapsody: I. Structural Properties and Formation History From a Statistical Sample of Re-simulated Cluster-size Halos. Astrophys.J. **763** (2013) 70

[96] Bruch, T., Read, J., Baudis, L., Lake, G.: Detecting the Milky Way's Dark Disk. Astrophys.J. **696** (2009) 920–923

[97] McMillan, P.J., Binney, J.J.: The uncertainty in Galactic parameters. (2009)

[98] Vogelsberger, M., White, S.D.: Streams and caustics: the fine-grained structure of LCDM haloes. (2010)

[99] Schneider, A., Krauss, L.M., Moore, B.: Microhalos and Dark Matter Detection. PoS **IDM2010** (2011) 079

[100] Fantin, D.S., Green, A.M., Merrifield, M.R.: Ultra-fine dark matter structure in the Solar neighbourhood. Mon.Not.Roy.Astron.Soc. **418** (2011) 2648–2655

[101] Green, A.M.: Dependence of direct detection signals on the WIMP velocity distribution. JCAP **1010** (2010) 034

[102] Catena, R., Ullio, P.: The local dark matter phase-space density and impact on WIMP direct detection. JCAP **1205** (2012) 005

[103] Lisanti, M., Strigari, L.E., Wacker, J.G., Wechsler, R.H.: The Dark Matter at the End of the Galaxy. Phys.Rev. **D83** (2011) 023519

[104] Strigari, L.E.: Astrophysical Interplay in Dark Matter Searches. AIP Conf.Proc. **1534** (2012) 156–164

[105] Smith, M.C., Ruchti, G., Helmi, A., Wyse, R., Fulbright, J., et al.: The RAVE Survey: Constraining the Local Galactic Escape Speed. Mon.Not.Roy.Astron.Soc. **379** (2007) 755–772

[106] Fornasa, M., Green, A.M.: A self-consistent phase-space distribution function for the anisotropic Dark Matter halo of the Milky Way. (2013)

[107] McMillan, P.J.: Mass models of the Milky Way. Mon.Not.Roy.Astron.Soc. **414** (2011) 2446–2457

[108] Bhattacharjee, P., Chaudhury, S., Kundu, S., Majumdar, S.: Sizing-up the WIMPs of Milky Way : Deriving the velocity distribution of Galactic Dark Matter particles from the rotation curve data. Phys.Rev. **D87** (2013) 083525

[109] Gould, A.: Gravitational diffusion of solar system WIMPs. Astrophys.J. **368** (1991) 610

[110] Gould, A., Khairul Alam, S.: Can heavy WIMPs be captured by the earth? Astrophys.J. **549** (2001) 72–75

[111] Damour, T., Krauss, L.M.: A New solar system population of WIMP dark matter. Phys.Rev.Lett. **81** (1998) 5726–5729

[112] Lundberg, J., Edsjo, J.: WIMP diffusion in the solar system including solar depletion and its effect on earth capture rates. Phys.Rev. **D69** (2004) 123505

[113] Peter, A.H.: Dark matter in the solar system I: The distribution function of WIMPs at the Earth from solar capture. Phys.Rev. **D79** (2009) 103531

[114] Peter, A.H.: Dark matter in the solar system III: The distribution function of WIMPs at the Earth from gravitational capture. Phys.Rev. **D79** (2009) 103533

[115] Sivertsson, S., Edsjo, J.: Accurate calculations of the WIMP halo around the Sun and prospects for its gamma ray detection. Phys.Rev. **D81** (2010) 063502

[116] Wikstrom, G., Edsjo, J.: Limits on the WIMP-nucleon scattering cross-section from neutrino telescopes. JCAP **0904** (2009) 009

[117] Fukuda, Y., et al.: The Super-Kamiokande detector. Nucl. Instrum. Meth. **A501** (2003) 418–462

[118] Abe, K., et al.: Solar neutrino results in Super-Kamiokande-III. Phys.Rev. **D83** (2011) 052010

[119] Takeuchi, Y., et al.: Measurement of radon concentrations at Super-Kamiokande. Phys.Lett. **B452** (1999) 418–424

[120] Kume, H., Sawaki, S., Ito, M., Arisaka, K., Kajita, T., et al.: 20-INCH DIAMETER PHOTOMULTIPLIER. Nucl.Instrum.Meth. **205** (1983) 443–449

[121] Abe, K., Hayato, Y., Iida, T., Iyogi, K., Kameda, J., et al.: Calibration of the Super-Kamiokande Detector. Nucl.Instrum.Meth. **A737** (2014) 253–272

[122] Nishino, H., et al.: High-speed charge-to-time converter ASIC for the Super-Kamiokande detector. Nucl. Instrum. Meth. **A610** (2009) 710–717

[123] Yamada, S., et al.: Commissioning of the new electronics and online system for the Super-Kamiokande experiment. IEEE Trans.Nucl.Sci. **57** (2010) 428–432

[124] Ishihara, C. Ph. D. Thesis, University of Tokyo (2010)

[125] Lee, K.P. Ph. D. Thesis, University of Tokyo (2012)

[126] Honda, M., Kajita, T., Kasahara, K., Midorikawa, S., Sanuki, T.: Calculation of atmospheric neutrino flux using the interaction model calibrated with atmospheric muon data. Phys.Rev. **D75** (2007) 043006

[127] Honda, M., Kajita, T., Kasahara, K., Midorikawa, S.: Comparison of three-dimensional and one-dimensional schemes in the calculation of atmospheric neutrinos. Phys.Rev. **D64** (2001) 053011

[128] Honda, M., Kajita, T., Kasahara, K., Midorikawa, S.: A New calculation of the atmospheric neutrino flux in a 3-dimensional scheme. Phys.Rev. **D70** (2004) 043008

[129] Honda, M., Kajita, T., Kasahara, K., Midorikawa, S.: Improvement of low energy atmospheric neutrino flux calculation using the JAM nuclear interaction model. Phys.Rev. **D83** (2011) 123001

[130] Hayato, Y.: NEUT. Nucl.Phys.Proc.Suppl. **112** (2002) 171–176

[131] Mitsuka, G.: NEUT. AIP Conf.Proc. **981** (2008) 262–264

[132] Volkova, L.: Energy Spectra and Angular Distributions of Atmospheric Neutrinos. Sov.J.Nucl.Phys. **31** (1980) 784–790

[133] W. R. Webber, R.L.G., Stephens, S.A. In Proceedings of the 20th International Cosmic Ray Conference (1987)

[134] Seo, E.S., et al. Astrophys. J. **378** (1991) 763

[135] P., P., et al. In Proceedings of the 23rd International Cosmic Ray Conference (1993)

[136] Boezio, M., et al.: The Cosmic ray proton and helium spectra between 0.4-GeV and 200-GeV. Astrophys.J. **518** (1999) 457–472

[137] Menn, W., et al. Astrophys. J. **533** (2000) 281

[138] Sanuki, T., Motoki, M., Matsumoto, H., Seo, E., Wang, J., et al.: Precise measurement of cosmic ray proton and helium spectra with the BESS spectrometer. Astrophys.J. **545** (2000) 1135

[139] Alcaraz, J., et al.: Cosmic protons. Phys.Lett. **B490** (2000) 27–35

[140] Ryan, M., Ormes, J., Balasubrahmanyan, V.: Cosmic ray proton and helium spectra above 50 gev. Phys.Rev.Lett. **28** (1972) 985–988

[141] Asakamori, K., et al. Astrophys. J. **502** (1998) 985

[142] I.P.Ivanenko, et al. In Proceedings of the 23rd International Cosmic Ray Conference (1993)

[143] Kawamura, Y., Matsutani, H., Nanjo, H., Katsuya, T., Toda, K., et al.: 'Quasidirect' Observations of Cosmic Ray Primaries in the Energy Region 10**12-ev to Approximately 10**14-ev. Phys.Rev. **D40** (1989) 729

[144] Apanasenko, A., et al.: Composition and energy spectra of cosmic ray primaries in the energy range 10**13-eV/particle to approximately 10**15-eV/particle observed by Japanese Russian joint balloon experiment. Astropart.Phys. **16** (2001) 13–46

[145] http://ccmc.gsfc.nasa.gov/modelweb/atmos/us_standard.html

[146] Barr, G.D., Gaisser, T.K., Lipari, P., Robbins, S., Stanev, T.: A three-dimensional calculation of atmospheric neutrinos. Phys. Rev. **D70** (2004) 023006

[147] Battistoni, G., Ferrari, A., Montaruli, T., Sala, P.: The FLUKA atmospheric neutrino flux calculation. Astropart.Phys. **19** (2003) 269–290

[148] Maki, Z., Nakagawa, M., Sakata, S.: Remarks on the unified model of elementary particles. Prog.Theor.Phys. **28** (1962) 870–880

[149] Pontecorvo, B.: Neutrino Experiments and the Problem of Conservation of Leptonic Charge. Sov.Phys.JETP **26** (1968) 984–988

[150] Hirata, K., et al.: Experimental Study of the Atmospheric Neutrino Flux. Phys.Lett. **B205** (1988) 416

[151] Hirata, K., et al.: Observation of a small atmospheric muon-neutrino / electron-neutrino ratio in Kamiokande. Phys.Lett. **B280** (1992) 146–152

[152] Casper, D., Becker-Szendy, R., Bratton, C., Cady, D., Claus, R., et al.: Measurement of atmospheric neutrino composition with IMB-3. Phys.Rev.Lett. **66** (1991) 2561–2564

[153] Becker-Szendy, R., Bratton, C., Casper, D., Dye, S., Gajewski, W., et al.: The Electron-neutrino and muon-neutrino content of the atmospheric flux. Phys.Rev. **D46** (1992) 3720–3724

[154] Sanchez, M.C., et al.: Measurement of the L/E distributions of atmospheric neutrinos in Soudan 2 and their interpretation as neutrino oscillations. Phys.Rev. **D68** (2003) 113004

[155] Fukuda, Y., et al.: Evidence for oscillation of atmospheric neutrinos. Phys.Rev.Lett. **81** (1998) 1562–1567

[156] Ashie, Y., et al.: Evidence for an oscillatory signature in atmospheric neutrino oscillation. Phys.Rev.Lett. **93** (2004) 101801

[157] Abe, K., et al.: Indication of Electron Neutrino Appearance from an Accelerator-produced Off-axis Muon Neutrino Beam. Phys.Rev.Lett. **107** (2011) 041801

[158] Mikheyev, S., Smirnov, A. Sov. Jour. Nucl. **42** (1985) 913

[159] Wolfenstein, L. Phys. Rev. D. **17** (1978) 2369

[160] Peres, O., Smirnov, A.Y.: Atmospheric neutrinos: LMA oscillations, U(e3) induced interference and CP violation. Nucl.Phys. **B680** (2004) 479–509

[161] Llewellyn Smith, C.: Neutrino Reactions at Accelerator Energies. Phys.Rept. **3** (1972) 261–379

[162] Ueno, K. T2K Technical Note 58 v3.1 (2012)

[163] Smith, R., Moniz, E.: NEUTRINO REACTIONS ON NUCLEAR TARGETS. Nucl.Phys. **B43** (1972) 605

[164] Barish, S., Campbell, J., Charlton, G., Cho, Y., Derrick, M., et al.: Study of Neutrino Interactions in Hydrogen and Deuterium. 1. Description of the Experiment and Study of the Reaction Neutrino d –>; mu- p p(s). Phys.Rev. **D16** (1977) 3103

[165] Bonetti, S., Carnesecchi, G., Cavalli, D., Negri, P., Pullia, A., et al.: Study of Quasielastic Reactions of Neutrino and anti-neutrino in Gargamelle. Nuovo Cim. **A38** (1977) 260–270

[166] Pohl, M., et al.: EXPERIMENTAL STUDY OF THE REACTION neutrino N —> MU- P. Lett.Nuovo Cim. **26** (1979) 332–336

[167] Arimenise, N., et al. Nucl. Phys. B **152** (1979) 365

[168] Mukhin, A., Perelygin, V., Shestermanov, K., Volkov, A., Vovenko, A., et al.: Energy Dependence of Total Cross-sections for Neutrino and Anti-neutrino Interactions at Energies Below 35-GeV. Sov.J.Nucl.Phys. **30** (1979) 528

[169] Belikov, S., Bugorsky, A., Epshtein, V.S., Kalganov, N., Klimenko, L., et al.: Quasielastic Neutrino and Anti-neutrinos Scattering: Total Cross-sections, Axial Vector Form-factor. Z.Phys. **A320** (1985) 625

[170] Brunner, J., et al.: Quasielastic Nucleon and Hyperon Production by Neutrinos and Anti-neutrinos With Energies Below 30-GeV. Z.Phys. **C45** (1990) 551

[171] Rein, D.: Angular Distribution in Neutrino Induced Single Pion Production Processes. Z.Phys. **C35** (1987) 43–64

[172] Albright, C.H., Jarlskog, C.: Neutrino Production of m+ and e+ Heavy Leptons. 1. Nucl.Phys. **B84** (1975) 467

[173] Gluck, M., Reya, E., Vogt, A.: Dynamical parton distributions revisited. Eur.Phys.J. **C5** (1998) 461–470

[174] Bodek, A., Yang, U.: Modeling neutrino and electron scattering inelastic cross-sections in the few GeV region with effective LO PDFs TV Leading Order. Nucl.Phys.Proc.Suppl. (2003)

[175] Derrick, M., et al.: Properties of the Hadronic System Resulting from anti-Muon-neutrino p Interactions. Phys. Rev. **D17** (1978) 1

[176] Sjostrand, T.: Pythia 5.7 and jetset 7.4 physics and manual. (1994)

[177] Rein, D., Sehgal, L.M.: Coherent pi0 Production in Neutrino Reactions. Nucl.Phys. **B223** (1983) 29

[178] Hiraide, K., et al.: Search for Charged Current Coherent Pion Production on Carbon in a Few-GeV Neutrino Beam. Phys.Rev. **D78** (2008) 112004

[179] Scully, D.I.: Neutrino Induced Coherent Pion Production

[180] Salcedo, L., Oset, E., Vicente-Vacas, M., Garcia-Recio, C.: Computer Simulation of Inclusive Pion Nuclear Reactions. Nucl.Phys. **A484** (1988) 557

[181] Martin, B., Pidcock, M.: Anti-K n Interactions in the Resonance Region. 1. Analysis of Data. Nucl.Phys. **B126** (1977) 266

[182] Martin, B., Pidcock, M.: Anti-K n Interactions in the Resonance Region. 2. Amplitudes. Nucl.Phys. **B126** (1977) 285

[183] Hyslop, J., Arndt, R., Roper, L., Workman, R.: Partial wave analysis of K+ nucleon scattering. Phys.Rev. **D46** (1992) 961–969

[184] Sparrow, D.: Effects of the Nuclear Medium on the Observation of Baryon Number Violation. AIP Conf.Proc. **123** (1984) 1019–1025

[185] Bertini, H.: Nonelastic interactions of nucleons and pi mesons with complex nuclei at energies below 3 gev. Phys.Rev. **C6** (1972) 631–659

[186] Lindenbaum, S., Sternheimer, R.: Isobaric nucleon model for pion production in nucleon-nucleon collisions. Phys.Rev. **105** (1957) 1874–1879

[187] Abe, K., et al.: Evidence of Electron Neutrino Appearance in a Muon Neutrino Beam. Phys.Rev. **D88**(3) (2013) 032002

[188] Brun, R., Carminati, F., Giani, S.: GEANT Detector Description and Simulation Tool. (1994)

[189] Zeitnitz, C., Gabriel, T.: The GEANT - CALOR interface and benchmark calculations of ZEUS test calorimeters. Nucl.Instrum.Meth. **A349** (1994) 106–111

[190] Groom, D.E., Mokhov, N.V., Striganov, S.I.: Muon stopping power and range tables 10-MeV to 100-TeV. Atom. Data Nucl. Data Tabl. **78** (2001) 183–356

[191] Tanaka, T.: An indirect search for wimps in the sun and the earth using upward-going muon events in super-kamiokande. Ph.D. Thesis, Nagoya University (2011)

[192] Desai, S., et al.: Study of TeV Neutrinos with Upward Showering Muons in Super-Kamiokande. Astropart. Phys. **29** (2008) 42–54

[193] Irvine, T.J.: Development of neutron-tagging techniques and application to atmospheric neutrino oscillation analysis in super-kamiokande. Ph.D. Thesis, University of Tokyo (2014)

[194] Desai, S. Ph. D. Thesis, Boston University (2004)

[195] Davies, E.R.: Machine vision: Theory, algorithms, practicalities. Academic Press, San Diego (1997)

[196] Barszczak, T.: The efficient discrimination of electron and pi-zero events in a water cherenkov detector and the application to neutrino oscillation experiments. Ph.D. thesis (2005)

[197] Ashie, Y., et al.: A Measurement of atmospheric neutrino oscillation parameters by SUPER-KAMIOKANDE I. Phys.Rev. **D71** (2005) 112005

[198] Mitsuka, G.: Study of non-standard neutrino interactions with atmospheric neutrino data in super-kamiokande. Ph.D. Thesis, University of Tokyo (2008)

[199] Haenggi, P., Viollier, R., Raff, U., Alder, K.: Muon decay in orbit. Phys.Lett. **B51** (1974) 119–122

[200] Hettlage, C., Mannheim, K., Learned, J.G.: The Sun as a high-energy neutrino source. Astropart.Phys. **13** (2000) 45–50

[201] Fogli, G., Lisi, E., Marrone, A., Montanino, D., Palazzo, A.: Getting the most from the statistical analysis of solar neutrino oscillations. Phys.Rev. **D66** (2002) 053010

[202] Archambault, S., et al.: Constraints on Low-Mass WIMP Interactions on ^{19}F from PICASSO. Phys.Lett. **B711** (2012) 153–161

[203] Felizardo, M., Girard, T., Morlat, T., Fernandes, A., Ramos, A., et al.: Final Analysis and Results of the Phase II SIMPLE Dark Matter Search. Phys.Rev.Lett. **108** (2012) 201302

[204] Savage, C., Gelmini, G., Gondolo, P., Freese, K.: Compatibility of DAMA/LIBRA dark matter detection with other searches. JCAP **0904** (2009) 010

[205] Agnese, R., et al.: CDMSlite: A Search for Low-Mass WIMPs using Voltage-Assisted Calorimetric Ionization Detection in the SuperCDMS Experiment. Phys.Rev.Lett. **112** (2014) 041302

[206] Beringer, J., et al.: Review of Particle Physics (RPP). Phys.Rev. **D86** (2012) 010001

[207] Ambrosini, G., et al.: K / pi production ratios from 450-GeV/c protons on beryllium. Phys.Lett. **B420** (1998) 225

[208] Nieves, J., Amaro, J.E., Valverde, M.: Inclusive quasi-elastic neutrino reactions. Phys.Rev. **C70** (2004) 055503

[209] Hernandez, E., Nieves, J., Valverde, M.: Weak Pion Production off the Nucleon. Phys.Rev. **D76** (2007) 033005

[210] Suzuki, A., et al.: Improvement of 20-inch diameter photomultiplier tubes. Nucl. Instrum. Meth. **A329** (1993) 299–313

[211] Nakajima, Y., et al.: Measurement of inclusive charged current interactions on carbon in a few-GeV neutrino beam. Phys.Rev. **D83** (2011) 012005

[212] Hagiwara, K., Mawatari, K., Yokoya, H.: Tau polarization in tau neutrino nucleon scattering. Nucl.Phys. **B668** (2003) 364–384

[213] de Perio, P.: NEUT pion FSI. AIP Conf.Proc. **1405** (2011) 223–228

[214] Kayis-Topaksu, A., et al.: Charged Particle Multiplicities in Charged-Current Neutrino and Anti-Neutrino Nucleus Interactions. Eur.Phys.J. **C51** (2007) 775–785

[215] Fukuda, Y., et al.: Measurement of a small atmospheric muon-neutrino / electron-neutrino ratio. Phys.Lett. **B433** (1998) 9–18

[216] Smith, P., Lewin, J.: Dark Matter Detection. Phys.Rept. **187** (1990) 203

[217] Lewin, J., Smith, P.: Review of mathematics, numerical factors, and corrections for dark matter experiments based on elastic nuclear recoil. Astropart.Phys. **6** (1996) 87–112

[218] Duda, G., Kemper, A., Gondolo, P.: Model Independent Form Factors for Spin Independent Neutralino-Nucleon Scattering from Elastic Electron Scattering Data. JCAP **0704** (2007) 012

[219] Ellis, J., Olive, K.A., Savage, C., Spanos, V.C.: Neutrino Fluxes from CMSSM LSP Annihilations in the Sun. Phys.Rev. **D81** (2010) 085004

[220] Bahcall, J.N., Serenelli, A.M., Basu, S.: New solar opacities, abundances, helioseismology, and neutrino fluxes. Astrophys. J. **621** (2005) L85–L88

[221] Catena, R., Ullio, P.: A novel determination of the local dark matter density. JCAP **1008** (2010) 004

[222] Weber, M., de Boer, W.: Determination of the Local Dark Matter Density in our Galaxy. Astron.Astrophys. **509** (2010) A25

[223] Salucci, P., Nesti, F., Gentile, G., Martins, C.: The dark matter density at the Sun's location. Astron.Astrophys. **523** (2010) A83

[224] Pato, M., Agertz, O., Bertone, G., Moore, B., Teyssier, R.: Systematic uncertainties in the determination of the local dark matter density. Phys.Rev. **D82** (2010) 023531

[225] Garbari, S., Read, J.I., Lake, G.: Limits on the local dark matter density. Mon.Not.Roy.Astron.Soc. **416** (2011) 2318–2340

[226] Choi, K., Rott, C., Itow, Y.: Impact of Dark Matter Velocity Distributions on Capture Rates in the Sun. (2013)

[227] Griest, K., Seckel, D.: Cosmic Asymmetry, Neutrinos and the Sun. Nuclear Physics B **B283** (1987) 681

[228] Gould, A.: Evaporation of WIMPs with arbitrary cross sections. apj **356** (June 1990) 302–309

[229] Busoni, G., De Simone, A., Huang, W.C.: On the Minimum Dark Matter Mass Testable by Neutrinos from the Sun. JCAP **1307** (2013) 010